Engineering of Block Copolymer Nanotemplates for Optoelectronics

This thesis is submitted as a partial fulfilment of the Ph.D. programme in Physics

by

Lokesh Kumar Jangir

2012RPH9559

Department of Physics

Malaviya National Institute of Technology Jaipur

December 2017

Thesis is dedicated to my family

MALAVIYA NATIONAL INSTITUTE OF TECHNOLOGY JAIPUR
(Institute of National Importance under NITs Act, Established by Govt. of India)
मालवीय राष्ट्रीय प्रौद्योगिकी संस्थान जयपुर
JLN Marg, Jaipur-302017 (India)

Declaration

I herewith declare that I have produced this thesis without the prohibited assistance of third parties and without making use of aids other than those specified; notions taken over directly or indirectly from other sources have been identified as such. This thesis has not previously been presented in identical or similar form to any other Indian or foreign examination board.

The thesis work was conducted from January, 2013 to December 2017 under the supervision of Dr. Kamlendra Awasthi and Prof. K C Swami at Department of Physics, Malaviya National Institute of Technology Jaipur.

Lokesh Kumar Jangir

MALAVIYA NATIONAL INSTITUTE OF TECHNOLOGY JAIPUR
(Institute of National Importance under NITs Act, Established by Govt. of India)
मालवीय राष्ट्रीय प्रौद्योगिकी संस्थान जयपुर
JLN Marg, Jaipur-302017 (India)

Supervisor's Certificate

This is to certify that the thesis entitled ***"Engineering of Block Copolymer Nano templates for Optoelectronics"*** is being submitted by **Mr. Lokesh Kumar Jangir** (ID No. 2012RPH9559), to the Malaviya National Institute of Technology Jaipur for the award of the degree of Doctor of Philosophy in Physics, is a bonafied record of original research work carried out by his. He has worked under our guidance and supervision and has fulfilled the requirement for the submission of this thesis, which has reached the requisite standard.

The result contained in this thesis have not been submitted in part or full, to any other university or institute for the award of any degree or diploma.

(Dr. Kamlendra Awasthi)
Assistance Professor
Department of Physics
MNIT Jaipur (India)

(Prof. K C Swami)
Retd. Professor
Department of Physics
MNIT Jaipur (India)

Acknowledgements

At very first, I express my sincere gratitude and the best regards to my supervisor Dr. Kamlendra Awasthi, for his guidance during my Ph.D. His knowledge and dedication towards the work always motivates me. He was always available to solve my problems with his kind behaviour. I am very thankful to him to encourage and support me during my journey of research.
I am very thankful to my co-supervisor Prof. K. C. Swami who always supported and encouraged me for doing my research work. He is very knowledgeable and kindhearted person.
I wish to express my sincere gratitude to Dr. Manoj Kumar, Assistant Professor, MNIT Jaipur for his consistent valuable discussions.
I, sincerely thank to the Head, department of Physics for giving me this opportunity to work in this laboratory. I also thank to all the Faculty members, Department of Physics, MNIT Jaipur for their suggestions during my research work and for their kind support.
I would like to extend my sincere thanks to Dr. Anjali Awasthi, Mrs. Sarika Kashyap, Dr. Kumud Kant Awasthi and Dr. Garima Awasthi for their support and encouragement.
I express my heartiest thanks to my friends and labmates Anil Kumar, Yogita Kumari, Rajesh Jangir, Kamakshi, Rini Singh, Pooja Kumari, Anoop M D, Shivani Shishodia, Prashant Sharma, Ritesh Dadhich, Aakanksha, and Jyoti from Soft Materials & High Pressure Physics Lab., Department of physics, MNIT Jaipur specially Yogesh kumar, Manish Kumar, Karam Chand and Manoj Kumar for their co-operation and making the journey memorable.
I would also like to thank to all research scholars, Department of Physics, MNIT Jaipur for their moral support and always available with a solution to my problems.
I specially thank to Dr. K C Bhamu, NPDF fellow, National Chemical Laboratory, Pune, for being a friend, a senior and always having confidence in me for completing this journey.
I am thankful to all the staff members of Department of Physics and Material Research Centre (MRC), MNIT Jaipur for their kind support

From deep of my heart, I am thankful to my parents and my wife (Poonam Kumari) who always encouraged me to pursue my goals and for always being my strength to face every difficulty and challenge in my life.
I also acknowledge the Ministry of Human Resources and Development, New Delhi, for providing me financial assistance under Institute Fellowship to out my Ph.D. work.

(Lokesh Kumar Jangir)

Abstract

In the present investigations, different chemical routes were optimized for the synthesis of *ZnO* nanoparticles with and without doping of various rare earth elements. Supramolecular assembly of diblock copolymer PS-*b*-P4VP and additive HABA have been explored for the fabrication of well-ordered array of *ZnO* nanostructures for their optoelectronic applications. Synthesized *ZnO* nanoparticles were studied for their action against Bacillus subtilis biofilm formation.

Zinc oxide nanoparticles (*ZnO* NPs) were synthesized by chemical methods using different precursors (zinc chloride, zinc nitrate hexahydrate and zinc acetate) and media (water, ethanol, and methanol). An effort has been made to precisely control the particle size and optical band gap by various methods, while maintaining the crystal structure. Transmission Electron Microscopy (TEM) analysis confirmed that the particle sizes of the synthesized *ZnO* nanoparticles were in the range of 5 nm to 20 nm. X-ray diffraction (XRD) studies were in tandem with the TEM studies and confirmed the hexagonal crystal structure for all the samples. Absorption spectra of these nanoparticles exhibit broad peaks in the range of 274 to 376 nm. Optical band gap values of the synthesized *ZnO* NPs were found to be in the range of 3.2 eV to 3.32 eV. The photoluminescence (PL) spectra show two emission peaks; one at 393âĂŞ420 nm which corresponds to band gap excitonic emission, and another located at 520-550 nm, due to the presence of defects. Variations in peak positions of the emission spectra are due to changes in the defect densities on the surfaces of the nanoparticles which were synthesized with different precursors. The number of sub peaks obtained from Gaussian peak function fitting of PL spectra shows the possible energy levels, the types of defects present in the samples and also their influence on the optical properties.

The synthesis of size controlled *ZnO* and rare-earth (RE) (terbium (Tb), erbium (Er), Europium (Eu)) doped *ZnO* nanoparticles (NPâĂŹs) via simple chemical route have been done. The structural, morphological and optical characterization was done using x-ray diffraction (XRD), transmission

electron microscopy (TEM), diffuse reflectance spectra (DRS) and photo luminescence (PL) spectroscopy. The formation of almost spherical, wurtzite phase with average crystallite size 12 nm of *ZnO* and RE doped *ZnO* was confirm by XRD and TEM. Decrease in band gap was observed in RE doped *ZnO* as compared to pure *ZnO* NPâĂŹs. Photo luminescence (PL) measurements reveal enhancement of visible luminescence intensity in RE^{3+} *ZnO* as compared to pure *ZnO*. RE doped *ZnO* shows characteristic peaks along with broad visible luminescence of *ZnO* originates from multiple intrinsic or extrinsic defects. The luminescence from RE^{3+} is enabled by energy transfer from defect centers of the host nanocrystal lattice to dopant sites. *ZnO*-RE energy transfer facilitates efficient intra-4f orbital transitions ($^5D_4 - ^7F_j$ for Tb^{3+}, $^5D_0 - ^7F_j$ for Eu^{3+} and $^4F_{9/2} - ^4I_{15/2}$, $^4S_{3/2} - ^4I_{15/2}$ for Er^{3+}) related characteristic green or red emission. Modulation of energy transfer dynamics is imperative to use the *ZnO*-based phosphor materials in future applications like optoelectronics and multi-colour emission displays. This can be achieved by the manipulation of defects through bottom up techniques, which is most viable, as suggested by the above studies.

The preparation and characterization of PS-*b*-P4VP block copolymer nanotemplates have been discussed. Ordered nanotemplates have been prepared using supramolecular assembly from diblock PS-*b*-P4VP and low molar mass additive HABA. Solvent annealing in a selective solvent (1-4 dioxane) affects the mobility of each block and results in the ordering of blocks. The molecular weight and volume fraction of one of the blocks determines the morphology of templates. It has been found that the cylindrical nanotemplates changes to lamellar when the relative volume fraction of minority block (P4VP/HABA) increases from âĹij 0.3 âĹŠ 0.5. Ex situ approach were opt for deposition of *ZnO* nanoparticles in order to obtain the regular assembly of the nanoparticles for different optoelectronic applications.

With the advancements in medicine, technology and research strategies the world has witnessed a rise in spectrum of options available for treatment and prevention of diseases. By understanding the complex nature of interaction of pathogen with host and its environment, the focus has shifted from conventional therapy to modern improved preventive strategies. Nanoparticles have shown immense potential and have been effective in eradicating bacterial biofilm, which is the common cause of drug resistance development and repeated bacterial proliferation. Hence, in order to explore the same, in this study *ZnO* nanoparticles have been synthesized by different routes and their

action against Bacillus subtilis biofilm formation was evaluated. The dose dependent reduction in biofilm biomass and density was observed as a result of nanoparticle exposure. There was $\sim 86\%$ reduction in biofilm formation after treatment of ZnO NPs. Change in surface morphology of the Bacillus subtilis cells was observed which could be due to oxidative stress induced by ZnO nanoparticles. The oxidative stress was estimated by measurement of the catalyse activity that also showed dose dependent decrease.

List of Abbreviations

AFM Atomic force microscopy

DAPI 4',6-diamidino-2-phenylindole

EDX Electron diffraction x-ray spectroscopy

Er Erbium

Eu Europium

FITC fluorescein isothiocyanate

FFT Fast fourier transform

FTIR Fourier transform infrared spectroscopy

HABA 2-(4-hydroxyphenylazo) benzoic acid

OSC Organic solar cell

PC Polycarbonate

PET Polyethylene terephthalate

PS-b-P2VP Poly (styrene)-b-poly (2-vinylpyridine)

PS-b-P4VP Poly (styrene)-b-poly (4-vinylpyridine)

PS-b-PB Poly (styrene)-b-poly (butadiene)

PS-b-PDMS Polystyrene-b-polydimethylsiloxane

PS-b-PEB-b-PMMA Poly (styrene-b-(ethylene-co-butylene)-b-methyl methacrylate)

PS-b-PEO Poly (styrene)-b-poly (ethylene oxide)

PS-b-PFS Poly (styrene)-b-poly (ferrocenyldimethylsilane)

PS-b-PI Poly (styrene)-b-poly (isoprene)

PS-b-PMMA Poly (styrene-b-methyl methacrylate)

PSC Polymer solar cell

PL Photoluminescence

RE Rare earth

SEM Scanning electron microscopy

TEM Transmission electron microscopy

Tb Terbium

UV-Vis UV-Visible spectroscopy

XRD X-ray diffraction

ZnO Zinc oxide

Contents

List of Tables **xvii**

List of Figures **xix**

1 General Introduction **1**

1.1 Introduction 1

1.2 Block copolymers 2

1.2.1 Diblock copolymers 3

1.2.2 Triblock copolymers 3

1.2.3 Self assembly 3

1.2.4 Supramolecular assembly 5

1.3 Zinc oxide (ZnO) nanostructures 6

1.3.1 Crystal Structure 7

1.3.2 Native defects in ZnO 8

1.3.3 Synthesis of ZnO NP's 8

1.4 RE doped ZnO NP's 9

1.5 Applications of RE doped ZnO 10

1.6 Block copolymer nanotemplates directed nanostructures 10

1.7 Motivation & objectives of the work 11

2 Brief Review of Literature **13**

2.1 Introduction 13

2.2 ZnO NP's 14

2.2.1 Synthesis methods of ZnO NP's 15

2.2.2 RE-doping in ZnO 15

2.2.3 Optical properties of ZnO and RE-doped nanostructures 15

2.2.3.1 UV Visible spectra 15

2.2.3.2 Low temperature photoluminescence 18

2.2.3.3 Room temperature photo-luminescence 20
2.2.4 Antibacterial Properties of *ZnO* 22
2.2.5 Applications of RE doped *ZnO* nanostructures 24
2.3 Block copolymer thin films 25
2.4 Ordering in thin films 25
2.4.1 Thermal annealing 26
2.4.2 Solvent annealing 27
2.5 Block copolymer directed nanostructures 30
2.5.1 Preparation of porous nanotemplates 31
2.5.2 Deposition of inorganic material into the nanotemplates 31
2.5.3 Removal of remaining polymer matrix 34
2.6 Applications of ordered *ZnO* nanostructures 35
2.6.1 Light emitting diodes (LEDs) 35
2.6.2 Gas sensors 37
2.6.3 Field emitters 38
2.6.4 Photovoltaics 39
2.7 Conclusions 40

3 Materials and Methods 41
3.1 Introduction 41
3.2 Materials 41
3.2.1 Polymers and substrates 42
3.2.2 Precursors and solvents 42
3.3 Techniques used to prepare the samples 42
3.3.1 Co-precipitation method 43
3.3.2 Dip coating 43
3.3.3 Solvent annealing 44
3.4 Characterization techniques 45
3.4.1 X-Ray diffraction (XRD) 45
3.4.2 Scanning electron microscopy (SEM) 46
3.4.3 Transmission electron microscopy (TEM) 48
3.4.4 Ultra violet-visible diffuse reflectance spectroscopy (UV-vis. DRS) 49
3.4.5 Atomic force microscopy (AFM) 51
3.4.6 Photo-luminescence (PL) 52
3.4.7 *Bacillus subtilis* growth assay 53
3.4.8 Disc diffusion method 53
3.4.9 Biofilm growth and *ZnO* treatment 53

3.4.10 Crystal violet (CV) assay 54
3.4.11 Scanning electron micrograph for bacterial biofilm 54

4 Synthesis and Characterization of *ZnO* NP's 55
4.1 Introduction 55
4.2 Experimental details 56
4.2.1 *ZnO* by $ZnCl_2$ in water medium 56
4.2.2 *ZnO* by $ZnCl_2$ in methanol medium 56
4.2.3 *ZnO* by $ZnCl_2$ in ethanol medium 57
4.2.4 *ZnO* by $Zn(NO_3)_2.6H_2O$ in water medium 57
4.2.5 *ZnO* by green synthesis method 57
4.2.6 *ZnO* by Zinc acetate in DMSO medium 57
4.3 Results and discussion 57
4.3.1 X-ray Diffraction (XRD) 58
4.3.2 Transmission Electron Microscopy (TEM) 59
4.3.3 Diffuse Reflectance Spectroscopy (DRS) 62
4.3.4 Photo luminescence (PL) spectroscopy 64
4.4 Conclusion 68

5 Synthesis of RE doped *ZnO* NP's and their Characterization 69
5.1 Introduction 69
5.2 Experimental details 70
5.2.1 Synthesis of pure and RE doped *ZnO* NP's 70
5.2.2 Synthesis of RE doped *ZnO* NP's 70
5.3 Results and Discussion 70
5.3.1 X-ray Diffraction (XRD) 71
5.3.2 Scaning Electron Microscopy (SEM) 72
5.3.3 Transmission Electron Microscopy (TEM) 74
5.3.4 UV-Vis. Diffuse Reflectance Spectroscopy (DRS) 75
5.3.5 Photo luminescence (PL) spectroscopy 78
5.4 Conclusion 83

6 Block copolymer directed nanostructures 85
6.1 Introduction 85
6.2 Experimental details 86
6.2.1 Deposition of thin films of supramolecular assembly 87
6.2.2 Ordering in thin films and surface reconstruction 87
6.2.3 Deposition of NP's into the templates 88

6.3 Results and discussion 89
6.3.1 Vertically aligned cylindrical porous templates 89
6.3.2 Vertically aligned lamellar templates 93
6.3.3 Switching behavior of thin film 94
6.3.4 ZnO and RE doped ZnO NP's deposition in nanotemplates 95
6.4 Applications 97
6.5 Conclusions 97

7 Antibacterial activities of *ZnO* NP's 99
7.1 Introduction 99
7.2 Results and discussion 101
7.2.1 Antibacterial activity 101
7.2.2 Effect of *ZnO* NP's on *Bacillus subtilis* biofilm formation 102
7.2.3 Crystal Violet Assay 103
7.2.4 Scanning Electron Micrographs 104
7.3 Conclusion 106

8 Conclusion and future aspects 107
8.1 Introduction 107
8.2 Future scope of the work 109

Bibliography 111

List of Tables

2.1 Basic properties of ZnO 14
2.2 Various methods for synthesis of ZnO nanostructures. 16
2.3 Various methods for synthesis of RE doped ZnO nanostructures. 17
2.4 peak position and possible origin of bound exciton lines in ZnO 19
2.5 Positions and proposed origin of room temperature PL peaks in ZnO . . 21
2.6 Applications of RE-doped ZnO nanostructures. 24

4.1 Lattice parameters for all the samples and corresponding JCPDS card numbers 59
4.2 Summary of present work 62
4.3 Band position, relative intensities and bandwidth in individual band after Gaussian fitting of PL of ZnO NP's 67

5.1 Calculated Lattice parameter, crystalline size and optical band-gap of NP's 78

List of Figures

1.1 Schematic diagram of linear di-block (AB), triblock (ABA, BAB and ABC) and AB multi-block copolymers [1]. 2

1.2 (a) Equilibrium morphologies of the bulk of AB diblock copolymers: S and S' = sphere, L = lamellae, G and G' = gyroid, and C and C' = cylinder. (b) Theoretical phase diagram of AB diblocks and (c) Experimental phase portrait of polyisoprene-*block*-polystyrene copolymers, here f_A represents the volume fraction of block A, PL = perforated lamellae [2]. 4

1.3 Schematic representation of ZnO crystal structures: hexagonal Wurtzite (a) and cubic zinc blende (b). The shaded black and grey spheres represent oxygen and zinc atoms respectively 7

1.4 The schematic of calculated defect's levels in ZnO film 8

2.1 (a) UV-Vis spectra of pure and Eu^{3+} doped ZnO (0.1, 0.2 and 0.3 mole%) doped samples (b) Comparison of bandgap energies with the variation in concentration of Europium [3]. 18

2.2 Solid state PL measurements for ZnO nanorods at different temperature doped with Tb precursor; (a) Near band edge emission and (b) visible PL spectra due to distinct intra-4f transition [4]. 20

2.3 PL spectra of RE^{3+} doped ZnO nanorods synthesized using different concentrations (atom%) of (a) Tb^{3+} and (b) Eu^{3+} precursors. (c and d) Time delayed PL spectra of Tb^{3+} and Eu^{3+} doped ZnO [4]. 22

2.4 (a) Variation of correlation length with annealing temperature, (b) Time evolution of lateral ordering at an annealing temperature $270°C$, and (c) Thickness dependence of lateral ordering annealed at $270°C$ 27

2.5 AFM images of as-deposited PS-*b*-P4VP thin film (a), before (b) and after (d) surface reconstruction of thin film annealed in the vapours of solvent 1-dioxane, and before (c) and after (e) surface reconstruction of thin film annealed in the vapours of solvent toluene/THF 29

2.6 Process flow for the fabrication of ordered array of metal oxides NP's . . 33

2.7 Scheme for the fabrication of ordered array of nanodots (top) and SEM images of the ordered array of metal nanodots (a) Au, (b) Pt, and (c) Pd. Inset shows the FFT of the image. 33
2.8 SEM images of metal oxide NP's 34
2.9 I-V curves of the *ZnO*/GaN heterostructures 36
2.10 EL spectra of ZnO/p-GaN LED (a) and a ZnO film-based LED (b). The insets show the schematic of the respective LEDs [5]. 36
2.11 Gas response of different dia size *ZnO* nanowire sensors [6]. 38

3.1 Schematic for the synthesis of *ZnO* (left) NR's using different precurssors and solvents and RE-doped *ZnO* (right) NP's. 43
3.2 Process flow for the dip coating 44
3.3 Schematic for the solvent annealing of block copolymer thin film 45
3.4 Schematic diagram of X-ray diffractometer 46
3.5 Schematic diagram of SEM 47
3.6 Schematic diagram of TEM 48
3.7 Schematic diagram of UV-Visible. 49
3.8 Schematic for working of AFM (left), and Vander walls force variation with the distance between tip and sample. 51
3.9 Schematic for working of photoluminescence 52

4.1 XRD spectra of all *ZnO* NP's. 58
4.2 TEM image, diffraction pattern and HRTEM image of *ZnO* synthesized by method 4.2.1 (a, b & c) and 4.2.2 (d, e & f). 60
4.3 TEM image, diffraction pattern and HRTEM image of *ZnO* synthesized by method 4.2.3 (g, h & i), 4.2.4 (j, k & l), 4.2.6 (m, n & o) and 4.2.5 (p. q & r). 61
4.4 Room temperature diffuse reflectance spectra of *ZnO* NP's prepared by method 4.2.1 to 4.2.6 63
4.5 UV Vis absorption spectra of *ZnO* NP's prepared by method 4.2.1 to 4.2.6. 63
4.6 Kubelka-Munk function versus energy plots of all the *ZnO* samples. . . . 64
4.7 PL spectra of all the *ZnO* samples ($\lambda_{exc} = 325nm$) 65
4.8 Gaussian fitted Photo luminescence spectra and corresponding possible energy level diagram for all the *ZnO* samples ($\lambda_{exc} = 325nm$) 66

5.1 XRD patterns of undoped *ZnO* and Er, Eu and Tb doped *ZnO* NP's. . . 71
5.2 XRD patterns of undoped *ZnO* and 1.5 wt% RE doped (*Er, Eu, Tb*) *ZnO* NP's. (a) represents the enlarged peaks of the spectra , (b) indicates the shifting in most intense peaks towards lower angle. 71

5.3 SEM image Tb doped (a .5 wt% Tb, b 1.5 wt% Tb, c 2 wt% Tb and d 5 wt% Tb) *ZnO* NP's. 73
5.4 EDX spectra of different wt% Tb doped *ZnO* NP's. 73
5.5 TEM, HRTEM and SAED pattern of undoped(a) and 1.5 wt% RE (Tb (b), Er (c) and Eu (d)) doped *ZnO* NP's. 74
5.6 Room temperature DRS spectra of different wt% doped Er, Eu and Tb doped *ZnO* NP's. 76
5.7 UV-Vis absorption spectra of different wt% doped Er, Eu and Tb doped *ZnO* NP's. 76
5.8 Kubelka-Munk function versus energy plots of different wt% doped Er, Eu and Tb doped *ZnO* NP's. 77
5.9 DRS, UV-Vis absorption spectra and Kubelka-Munk function versus energy plots of undoped and 1.5 wt% RE (Er, Tb and Eu) doped *ZnO* NP's. 77
5.10 Room temperature PL spectra of different wt% doped Er, Eu and Tb doped *ZnO* NP's. ($\lambda_{exc} = 325nm$) 79
5.11 PL spectra of undoped and 1.5 wt% RE (Er, Tb and Eu) doped *ZnO* NP's. ($\lambda_{exc} = 325nm$) 81
5.12 Schematic of energy level diagram and possible transitions for RE (Tb, Er and Eu) doped *ZnO* NPs. 82

6.1 Chemical structure of PS-*b*-P4VP/HABA supramolecular assembly (left) and schematic for the fabrication of nanotemplates (right). 87
6.2 Scheme for the fabrication of ordered ZnO and RE doped ZnO nanostructures. 88
6.3 AFM height image of PS-*b*-P4VP/HABA ($M_n^{PS} = 35.5\ kg/mol$, $M_n^{P4VP} = 4.4\ kg/mol$) thin films 90
6.4 AFM height image of PS-*b*-P4VP/HABA ($M_n^{PS} = 35.5\ kg/mol$, $M_n^{P4VP} = 4.4\ kg/mol$) thin films after immersing in ethanol. 91
6.5 AFM height images of PS-*b*-P4VP/HABA ($M_n^{PS} = 130\ kg/mol$, $M_n^{P4VP} = 75\ kg/mol$) thin films, (left) without annealing and (right) annealed in 1-4 dioxane 92
6.6 AFM height images of PS-*b*-P4VP/HABA ($M_n^{PS} = 130\ kg/mol$, $M_n^{P4VP} = 75\ kg/mol$) thin films after immersing in ethanol 92
6.7 AFM height and phase images of PS-*b*-P4VP/HABA ($M_n^{PS} = 33\ kg/mol$, $M_n^{P4VP} = 8\ kg/mol$) thin films (left) without annealing and (right) annealed in the vapours of 1-4 dioxane. 93

6.8 (a, b) AFM images of PS-*b*-P4VP/HABA ($M_n^{PS} = 33\ kg/mol$, $M_n^{P4VP} = 8\ kg/mol$) thin films annealed in 1-4 dioxane and after immersing in ethanol. 94
6.9 AFM images of PS-*b*-P4VP/HABA ($M_n^{PS} = 33\ kg/mol$, $M_n^{P4VP} = 8\ kg/mol$) thin films annealed in chloroform and after immersing in ethanol. 95
6.10 AFM images of an array of ZnO nanostructures in nanotemplate. 96
6.11 AFM images of an array of RE doped ZnO nanostructures in nanotemplate. 96

7.1 Antibacterial activity of *ZnO* NP's on *Bacillus subtilis* at concentration of (a) 2mg/ml (b) 5mg/ml (c) 10mg/ml. 101
7.2 Fluorescence micrographs (a) Control (witout *ZnO* NP's) (b) at *ZnO* concentration of 1mg/ml (c) 2mg/ml (d) 5 mg/ml (e) 10 mg/ml. 102
7.3 Biofilm formation setup (a) before incubation and (b) after incubation with *ZnO* NP's. The concentration *ZnO* NP's in tubes: control (first 2 tubes from left), 0.5 mg ml^{-1} (2 tubes in mid) and 1 mg ml^{-1}(first 2 tubes from right). 103
7.4 (1) Dissolution of Crystal Violet Dye: (a) Acetic acid (b) Blank (c) Control (d, e), treated with *ZnO* NP's with concentrations 0.2 and 0.5 mg ml^{-1} respectively. (2) Graph showing crystal violet absorbance at 550 nm by blank, control and *ZnO* NP's treated samples. 103
7.5 Scanning Electron Micrographs of biofilm: (a, c, e, g) Control; (b, d, f, h) treated with *ZnO* with concentration 0.2 mg ml-1. The arrows indicate: Red: biofilm (a) Black: adhered cells (a, b) Gold: linear chain formation, initial stage (b, d) Blue: deformed cells (h, f) Green: viable cell (g, h) Dark Red: EPS (g, h, i) White: embedded NP's (d, h) 105

8.1 Schematic for the proposed LED device. 109

1

General Introduction

1.1 Introduction

Ordered nanostructures have attracted a great attention as they have wide range applications from optoelectronics to biomedicine. Various techniques are known for patterning in nanometer range, such as X-ray lithography, e-beam or electron beam lithography, imprint lithography and Photo lithography [7–9]. But it is very difficult to achieve ordered nano structures of size less than 30 nm over a large area with the lithographic techniques mentioned above. This calls for a simple and effective patterning technique to generate large area ordered nanostructures with dimensions less than 30 nm. Fabrication of ordered nanostructurs using block copolymer nanotemplate is an efficiant approach [10, 11]. Block copolymers are phase-separated and self-assembled into nanostructured morphologies due to the covalent linkage of the two blocks. These block copolymer thinfilms with micro-phase separated blocks involves several steps for best utilization [12, 13]. Furthermore block copolymers provides variety of morphology such as spherical, cylindrical, lamellar and gyroidal. The nanoparticles (NP's) incorporation into these self-assembled blocks is relatively simple since no external field is required for deposition of NP's [13]. It is a great challenge to get stable nanosturctures in an ordered fashion. The stability along with controlled arrangement of these NPs in an ordered fashion above substrate is a great challenge. Various methods have been adopted for selective deposition of metallic NP's into the desired block of the block copolymer domain by preloading or post-loading of NP's. Here pre-loading is the process of loading the block copolymer solution with NP's before deposition onto the surface. In this the pre-synthesized metallic NP's and block copolymer solution are mixed. Now these NP's selectively interact with blocks to form nanopatterned block copolymer arrays. Whereas post-loading is the process of loading the NP's after the fabrication of the thin

film of nanotemplates [14, 15]. Among these methods post-loading methods widely used for deposition of metallic NP's, since this approach is relatively simple. Moreover, this method can be easily extended to fabricate large area templates and hence samples. For example, E. Bhoje Gowd *et al.* and co-workers have used 4-vinyl pyridine (polystyrene-block-poly) (PS-*b*-P4VP) nanotemplates for the deposition of Au, Pt and Pd NP's [16]. Furthermore supramolecular assembly (SMA) plays a crucial role in the fabrication of metal-oxide nanostructures.

This thesis work is an effort to prepare an ordered nanostructure of optically active material via template method. Pure and rare earth (RE) doped *ZnO* NP's were synthesized via simple chemical route in the diameter regime 5-15 nm. The supramolecular assembled thin film of block copolymer PS-*b*-P4VP and low molecular mass aditive 2-(4-hydroxyphenylazo)benzoic acid (HABA) were deposited on silicon substrate using dip coating technique. These films were further annealed 1-4 dioxane atmosphere in order to get ordering. Further, these thin films were rinsed using ethanol for selective removal of the block P4VP which is bonded with HABA. The obtained nanoporous template were used for deposition of pre-synthesized *ZnO* and RE doped *ZnO* NP's. These prepared nanostructures has potential application in optoelectronics devices such as LED's, solar cells etc... Antibacterial activity and biofilm activity of *ZnO* were also studied.

1.2 Block copolymers

Polymers are long chain molecules and broadly they are categorized into two types of polymers; homo-polymer and co-polymer. Homo-polymers consists only one type of monomers where as block copolymer consists of two or more than two monomers. The arrangement of monomers in co-polymers may be random or periodic. If the arrangement is periodic then copolymer is known as block copolymer.

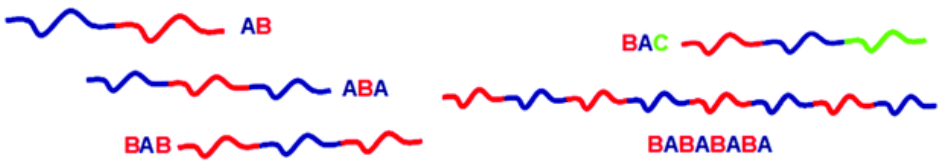

Figure 1.1: Schematic diagram of linear di-block (AB), triblock (ABA, BAB and ABC) and AB multi-block copolymers [1].

So, block co-polymers are the polymers comprising of the blocks of monomers repeating in a particular sequence and according to the number of blocks they are called di, tri or

multi block copolymers. Figure 1.1 represents the schematic representation of different block copolymers.

1.2.1 Diblock copolymers

Diblock copolymers consist of two monomers grouped together in a homogenous block of the polymer chains. The phase diagram for possible morphologies and their dependency on tha degree of polymerization (N), the volume fraction (f) and on the Flory-Huggins interaction parameter (χ) as well as schematic representation of the morphologies have been addressed in section 1.2.3. Diblock copolymers represents the simplest architectures rather than the other block copolymers (triblock and multiblock) and these are the most investigating block copolymers for the device applications. Most of diblock copolymers are consisting of PS, here are some examples for diblock copolymers; PS-*b*-PMMA, PS-*b*-P4VP, PS-*b*-P2VP, PS-*b*-PEO, PS-*b*-PI, PS-*b*-PB. Among them PS-*b*-PMMA and PS-*b*-P4VP have been extensively investigated for different structures, ordering, alignment and fabrication of nanostructures.

1.2.2 Triblock copolymers

Triblock copolymers consists of three dissimilar monomers (ABC triblock copolymer) grouped in homogenous blocks having repulsive interactions among them. The phase separation of microdomains in triblock copolymers not only depends on f, N and χ but also depends on the mutual interactions between the blocks A-B, B-C and C-A, and the blocks sequence. Therefore, they have more complexed morphologies as compaired to diblock copolymers. Zeng *et al.* have focused on the dependency of morphology on the sequence of block and strength of interactions between the blocks and theoretically calculated the phase diagram for the morphology of triblock copolymers [17].

1.2.3 Self assembly

Block copolymers are covalently bonded polymers. The formation of large domains restricted by connectivity between the polymers, leads to so called microphase separation. The theoretical descriptions of micro-phase separation has been developed by Helfand, Wassermann [18] and Leibler [19] and finally Matsen and Bates combined them in 1996 [20]. The appearance of micro-domains are determined by three principal factors the total degree of polymerization $N_{total}(= N_A + N_B)$, the Flory-Huggins interaction parameter χ, and volume fraction ((f_A and f_B) of the blocks A and B respectively (

$f_A + f_B = 1$) [21]. The degree of incompatibility of blocks is specified by the χ parameter, which drives the phase separation between the blocks, A and B. Equation (1.1) describes the relation between χ_{AB} and temperature (T)

$$\chi_{AB} = (\frac{z}{k_B T})[\varepsilon_{AB} - \frac{1}{2}(\varepsilon_{AA} + \varepsilon_{BB})] \tag{1.1}$$

where z is the number of nearest neighbors in the polymer, k_B is the Boltzman constant, T is the temperature in kelvin, ε_{AA}, ε_{BB} and ε_{AB} are the interaction energy of the repeated unit A-A, B-B, and A-B, respectively. The degree of polymerization predestinate the radius of gyration R_g which indirectly determine the size of the micro-domains. Characteristic stretching is associated with the polymer growth to fill the space, this N accommodates the entropic contribution towards the Gibbs free energy of the block copolymer.

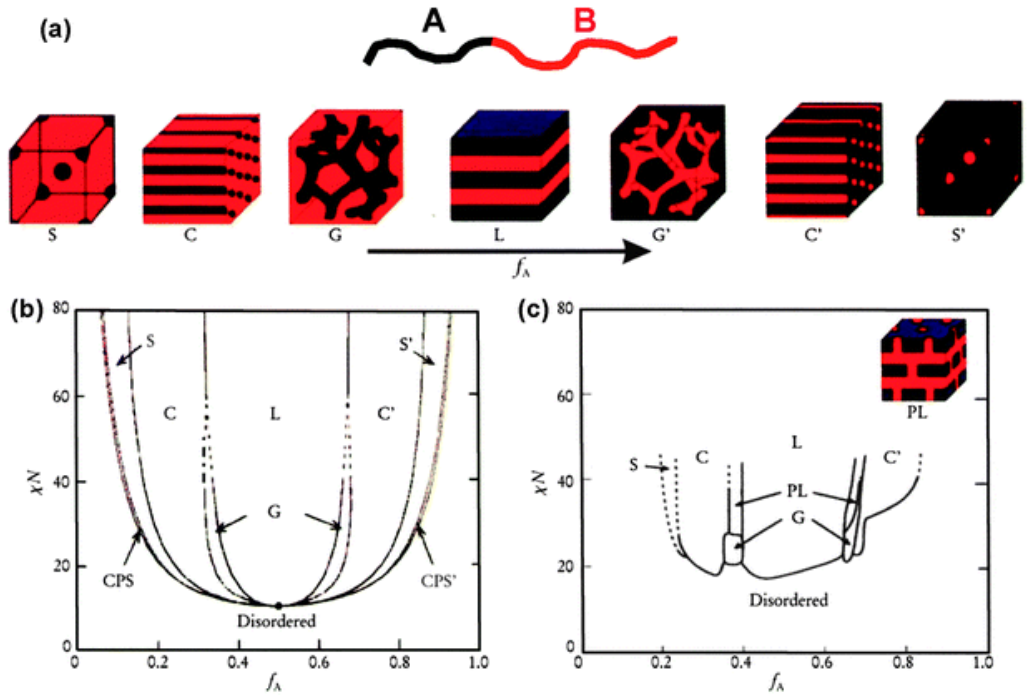

Figure 1.2: (a) Equilibrium morphologies of the bulk of AB diblock copolymers: S and S' = sphere, L = lamellae, G and G' = gyroid, and C and C' = cylinder. (b) Theoretical phase diagram of AB diblocks and (c) Experimental phase portrait of polyisoprene-*block*-polystyrene copolymers, here f_A represents the volume fraction of block A, PL = perforated lamellae [2].

Chemical incompatibility among the blocks causes repulsion between them which causes phase A to penetrate into phase B. The incompatibility is described by the χ parameter, which is a function of temperature, which inherently specifice the enthaplic contribution

towards the total Gibbs free energy. The curve between the product χN and f (the volume fraction of one of the blocks) expresses phase balance between entropy and enthalpy of the block. Hence this curve is considered as a phase diagram (figure 1.2). The mechanism for formation of the different morphologies is affected by two factors: one mediated by the chain stretching, the contribution towards entropy and other is the intefacial energy between the two blocks, the enthalpic contribution. During microphase separation, the blocks get separated in such a way that the interfacial lowered so that the total energy is minimized. minimize the interfacial area to lower the total interfacial energy. This phase separation results in the chain stretching, directed away from the preffered polymer chain conformation. The relative volume fraction wrt diblock is the major factor controlling the degree of stretching. The well known mechanism for the morphological transition 'the cone-column mechanism' is described in Figure 1.2. When there is a high asymmetry between the diblocks, the smaller block usually prefers to aggregate into spherical microdomain, hence allowing the other block to surround them "coronas" (figure 1.2 a). This process increases the configurational entropy by lowering the interfaciall area when compared to other morphologies making it energetically more favourable. As the effective volume fraction f_A increased at a fixed temperature, the corona volume fraction gets decreased resulting in the formation of less curved interfaces (figure 1.2 b and c). This changes forces the polymer chains to adopt new arrangements so as to reduce stretching. This leads to the morphological transformation of spheres to cylinders and then to lamellae(figure 4.2 b). The length scale of each domain is of the order of the corresponding radius of gyration [22], which results in structure sizes of $\sim 10 - 40$ nm. Block copolymers can be aligned in the bulk and thin films. Several reports have been proposed to make ordered block copolymers highly interesting for technological applications such as nanofabrication [23]. It is known that block copolymers films can be aligned by shear [24], or by exploiting surface properties such as the surface roughness, [25, 26] or else by using electric fields [27–29]. This way large-area ordered nanostructures can be processed cost-efficiently, without the use of lithography [30] which can be used as nanostructured templates.

1.2.4 Supramolecular assembly

Supramolecular assembly (SMA) is the process in which the small molecules called additives are attached with the one of the copolymer blocks via some specific interactions. The addition of these small molecules swells significantly one of the blocks and induces the interesting phase behavior of the block copolymers. These small molecules are associated with the co-polymer with weak interactions or noncovalent bonds. Generally,

they interact with co-polymer via hydrogen bond. These molecules attach with one of the block, resulting in the alteration of the relative volume fraction of that block which in-turn changes the morphology. Another advantage with the SMA is the readily removal of these small molecules by selective solvents which make them interesting for the fabrication of variety of functional nanomaterials. An example of the supramolecular complex system is PS-*b*-P4VP and pentadecylphenol (PDP) which has been widely investigated by Ikkala and co-workers [31]. The chemical structures and schematic representation of PS-*b*-P4VP and PDP are shown in figure 1.3 (a), PDP molecules possess the hydroxyl group which is bonded with pyridine group of P4VP via hydrogen bond. PDP molecules have polar backbone and non-polar alkyl tails with a sufficient repulsion between them. This repulsion is responsible to form the structures within structures with two length scale (figure 1.3 (b)). So, PDP molecules are microphase separated from P4VP and non-polar alkyl tails are aligned normal to the P4VP copolymer (shown in figure 1.3 (a)).

1.3 Zinc oxide (ZnO) nanostructures

An extensive research in the field of science and technology for nanomaterials has been going on since past decades. The structural, thermal, electronic and optical properties altered drastically when the size of the materials is reduced to the nanometer scale. ZnO, a II-VI compound semiconductor with a wide bandgap of $\sim 3.4\ eV$, is a versatile material with wide range of applications in optical devices (like light-emitting diodes (LEDs), UV laser, optical waveguides, solar cells etc...), field emission devices, photocatalysis, UV sensors, security printing, antibacterial and gas sensing [32–37]. Its vast and diverse morphology, easy and economic synthesis and thermal, mechanical as well as chemical stability of ZnO makes it a popular choice in optical devices. However, the promise of these nanocrystals as a technological material for such applications may ultimately depend on tuning their behavior by doping. Impurities can modify the properties of the material including optical, electronic, and magnetic properties [38–40]. It is required to control the size, shape, crystal structure and synthesis of novel nanostructures in order to design these properties of ZnO for practical applications. However, for some applications, such as nano-electronics and fluorescent imaging it has been noticed that tuning of band gap only by changing the morphology or size of nanocrystals is sufficient. Doping of appropriate impurity in semiconductor material plays an important role for desired optoelectronic and photovoltaic applications [41–43]. ZnO is considered as a unique host material for doping of optically active impurities which have luminescence

at room temperature [44]. Generally, semiconducting NP's are known to exhibit exotic physicochemical properties due to quantum confinement effect. Considering these advantages, there was a recent sruge in review articles, describing the progress in the growth and applications of various ZnO nanostructures having different morphologies [45, 46].

1.3.1 Crystal Structure

ZnO crystallizes in its thermodynamically stable wrutzite structure at ambient conditions. However, zinc-blend and rock-salt structures are also favorable crystal structures. In Schoenflies notation the wrutzite structure belongs to the class C6v4 (Space group) and to P63mc class in Hermann-Mauguin notation. The primitive unit cell of ZnO consist of two formula units, in which each zinc ion is surrounded by four oxygen ions in a tetrahedral coordination and vice versa [47]. The piezoelectric properties and crystallographic polarity of ZnO is due to the noncentrosymmetric tetrahedral coordination in ZnO which is a key factor in crystal growth and defect creation. Out of these the polar and the (1010) surfaces are found to be stable while the (1120) face is less stable [48]. For an ideal wrutzite structure, the lattice parameters derived from X-ray diffraction, at room temperature are $a = b = 3.25$Å and $c = 5.20$Å with a c/a ratio of 1.6. However, the lattice parameters $aandb$Å typically ranges from 3.2475 to 3.2501Å and c-parameter from 5.2042 to 5.2075Å. This variation is directly related to the concentration of foreign atoms, external strains, defects and temperature [47].

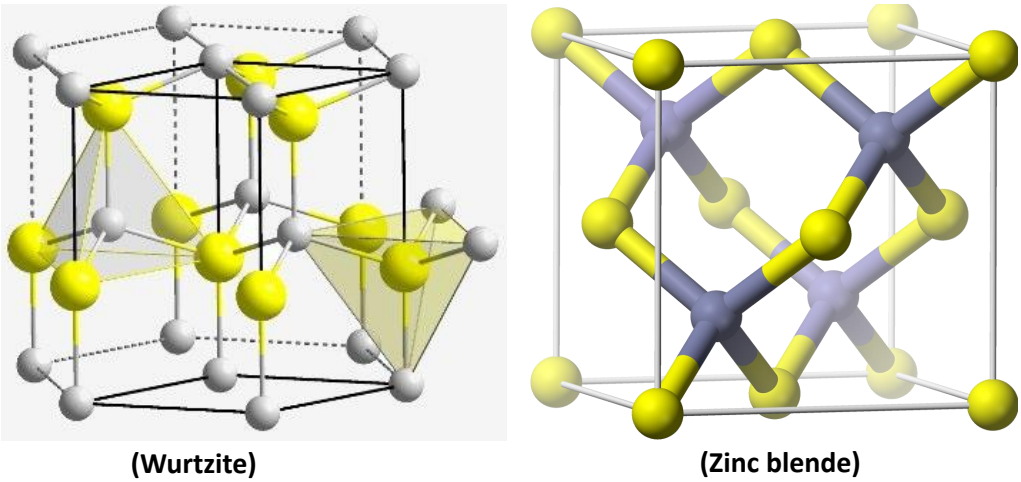

Figure 1.3: Schematic representation of ZnO crystal structures: hexagonal Wurtzite (a) and cubic zinc blende (b). The shaded black and grey spheres represent oxygen and zinc atoms respectively

1.3.2 Native defects in *ZnO*

It is of prime importance to control the defects and its associated charge carriers for the device applications of *ZnO* materials. The defects are directly correlated to doping which exploits the properties of *ZnO* materials, minority carrier lifetime and luminescence efficiency. This may be directly correlated to the diffusion mechanisms connected to growth, processing and devices degradation.

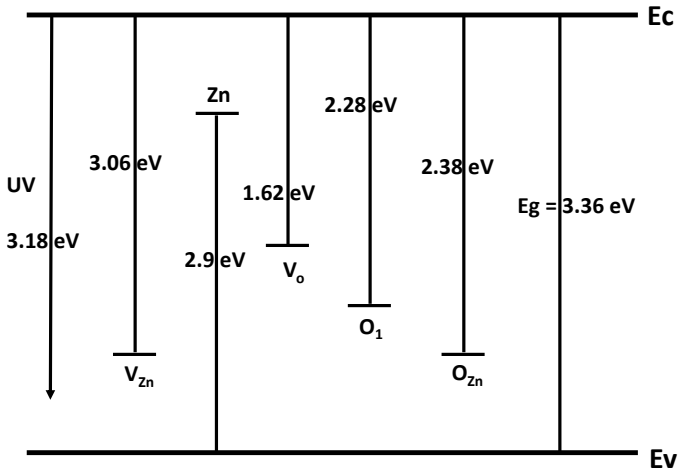

Figure 1.4: The schematic of calculated defect's levels in *ZnO* film

There are a number of intrinsic defects in *ZnO* with different ionization energies: oxygen vacancy (V_O), Zn vacancy (V_{Zn}), zinc interstitial (Zn_i), oxygen interstitial (O_i) and antisite oxygen O_{Zn}. The predominant ionic defect types are Zn interstitials and oxygen vacancies [49–51]. The energy levels of the native defects in *ZnO* film were calculated, as shown in figure 1.4. The atomic and electronic structures of the native defects in *ZnO* have been extensively investigated, both theoretically and experimentally [49–53].

1.3.3 Synthesis of *ZnO* NP's

There are several methods reported for the synthesis of *ZnO* nanostructures having different structures, shapes, and morphologies. Basically, the methods are chemical, physical, or mechanical, such as sol gel process [54], chemical vapor de-position [55], microwave synthesis [56], direct precipitation [57], homogeneous precipitation [58], micro emulsion synthesis [59], spray pyrolysis [60], plasma synthesis [61], ball milling [62], wet chemical synthesis [63], solvo-thermal and hydro thermal synthesis [64], pulsed laser ablation technique [65], combustion flame [66] etc... Out of these methods, the co-precipitation method is simple to implement, economically effective, and high yielding method for obtaining NP's at desired room temperature [67–69]. This method is steady,

fast, and spontaneous for the controlled growth of *ZnO* NPs by controlling the various parameters such as temperature, pH, and the type of solvent and reacting time of precursors to form co-precipitation.

1.4 RE doped *ZnO* NP's

For enhance the performance properties of *ZnO* without changing it's physio-chemical properties numerous studies are taking place by researchers to find the optimum solution. Thus, modifications are taking place by adding impurity or defect at the time of synthesis of NP's [70] The addition of impurities or foreign atoms to a compound by creating defect for enhancing its physical properties is termed as doping. Here, doping is required to modify the physical properties of nanostructures [71, 72]. Tuning of electrical conductivity, optical, luminescent, magnetic, and other physical properties of semiconductor material can be achieved by doping of impurities into the semiconductor lattices [73]. Due to wide band gap, pure *ZnO* is an insulator so electrical devices would not operate without having impurities. A small change in the concentrations of native or non-native defects can improve the conductivity of *ZnO* over 10 orders of magnitude. So, the doping is required for using *ZnO* in different devices. In *ZnO* nanostructures, there are basically two types of defects: intrinsic defects and extrinsic defects. The interstitial of zinc and oxygen, and vacancies at the bonding between zinc and oxygen are intrinsic or native point defects of *ZnO* NP's. Since the oxygen vacancies and zinc interstitials are dominant native or relevant donor, so the formation of donor levels are highly probable, if the Fermi energy band is at the valence band [74]. The zinc vacancies are the main native acceptor in *ZnO*. Oxygen anti-site has considered as deep acceptors because it has the highest defect formation energy even for oxygen rich conditions among the native point defects of *ZnO* NP's. Extrinsic defects are classified into two types: n-type and p-type. The n-type *ZnO* are obtained by doping with III Group elements (Al, In etc...), transition metal elements (Pb, Mn, Fe, Ni, Co etc...) and RE metals (Eu, Er, Gd, Tb etc...) [75–79]. These elements incorporate on the zinc lattice site and become shallower effective mass donors. With the help of hydrogen free electron concentration of n-type *ZnO* can be achieved. It is very difficult to formation of p-type *ZnO* because of the asymmetric doping limitations in *ZnO* nanostructures for practical as well as industrial applications [80]. The RE elements are considered as good dopants in *ZnO* due to their optical and high conductivity properties [75–77, 81]. RE doped wide band gap semiconductors has the importance for display applications involving UV, visible, and infrared light emission because of wide band gap that exhibits less thermal quenching of emissions than narrow gap semiconductors. Furthermore the

studies of RE (Tb, Eu, Gd etc...) doped ZnO suggest that these materials may useful in optoelectronic spintronic applications [82, 83]. Thus the doping of RE helps to modify the properties of ZnO nanostructures by modifying their crystal structure, morphology, size, and surface defects [78, 82].

1.5 Applications of RE doped ZnO

Due to their unique and versatile features and properties, the RE-doped ZnO nanostructures can be used in various industrial applications [84, 85]. They are used in the field of electronics and semiconductor industry for developing single electron transistors, photodetectors, fabricated LEDs, laser diodes, flat panel displays, transparent electrodes, nano-generators, solar cells, optical waveguides, PZT transducers, surface acoustic wave devices and optoelectronic devices [40, 84, 86–107]. They are used in the field of spintronics for making solid state devices for memory storage and electromagnetic devices. They are used in sensing applications and for photocatalysis. They show photocatalytic degradation of various anionic and cationic dyes [108–111]. With this, they are used for regulated and controlled drug release over sites and can be helpful in anticancer and antibacterial activities [84, 85, 112]. As a micronutrient, zinc can also be used as a supplement for plants and animals. The RE doped ZnO NP's have several other applications in printing inks, fire resistant materials, artificial fertilizer, fingerprint analysis, cigarette filters and bio-sensors for the detection of various enzymes and other bio-molecules.

1.6 Block copolymer nanotemplates directed nanostructures

The ordered block copolymers thin films can be used for fabrication of the nanostructures with higher aspect ratio. However, commercially available alumina nanotemplates have the high aspect ratio but block copolymer nanotemplates provide a denser array of pores with less size of pores and periodicity and it comes with variety of patterns because of their self-assembly into various morphologies on nanometer scale. Block copolymer nanotemplates with porous structures normal to the substrate are mainly used for the fabrication of ordered nanostructures. Mainly the cylindrical and lamellar block copolymer structures are used for the fabrication of nanorods, nanowires, nanodots and nanowalls [113–115]. The fabrication process mainly involves three steps;

1 Selective removal of one of the block and creation of nanoporous templates.

2 Backfilling of porous channels with inorganic materials

3 Removal of remaining polymer matrix via different techniques.

There are the different ways to remove the polymer block like UV etching, chemical etching, depending on the chemical nature of the block copolymer. Nanoporous channels can be filled by sol-gel method or direct deposition of NP's into the templates. In sol-gel method the reaction conditions have to be controlled carefully. Another way is the deposition of pre-synthesized inorganic NP's into the templates. It offers the flexibility to tailor the properties of NP's before deposition and can be controlled by their assembly time. Polymer templates/matrix can be removed by UV irradiation, pyrolysis and plasma etching.

1.7 Motivation & objectives of the work

Block copolymer nanotemplates using supramolecular assembly of diblock copolymer PS-*b*-P4VP and additive HABA have been explored for the fabrication of *ZnO* and RE doped *ZnO* nanostructures. The main objectives of the thesis are as follows;

- To synthesize *ZnO* NP's and optimization of their particle size.
- To synthesize RE doped *ZnO* NP's.
- To fabricate the block copolymer nanotemplates with different morphologies varying their molecular weight and the volume fraction.
- To fabricate the ordered *ZnO* and RE doped *ZnO* nanostructures using the prepared block copolymer nanotemplates.
- Antibacterial and biofilm activity of *ZnO*.

2

Brief Review of Literature

2.1 Introduction

The popularity of small length scale devices with high efficiency and low power consumption promotes the field of nanomaterials in the industrial applications. The low scale patterning with high resolution on the substrate is key factor for the rate of advancement in the semiconductor industry. The nanoscale patterning on a substrate with a 40 nm has been achieved by conventional UV photo lithography. Further improvement in the pattering structures in terms of scale makes the process complicated and increase the overall cost. The advance techniques for the nano patterning as nano-imprint lithography, extreme UV photo lithography, and interference lithography are still facing some difficulties for next generation device applications. These issues intensify the growing interest in self-assembly of materials which offers the well-ordered structures with a precise control at atomic or molecular level. For the device application of self-assembly, the nanomaterials, as a device component, are to be deposited on the substrate in a well-organized manner. Block copolymers have great interest over more than a decade for their use in semiconductor device applications because of their ability to self-assemble in the nanometer scale (typically 5 - 100 nm) with different morphologies [116, 117]. The block copolymer nano-lithography using spherical microdomain structure in 1995 was firstly demonstrated by Mansky *et al.*[118, 119]. The nano-patterning with block copolymers as an alternative for the polymeric photoresist offers the opportunity to explore the more benefits of self-assembly of block copolymers towards the optoelectronic applications. With this aim, enormous efforts have been dedicated to exploit the practical applications of block copolymer based nanostructures. Despite of ease of process and spatial scale of block copolymer pattering, still the work remains for the practical use of self-assembly in optoectronic applications. To combine the block copolymer

lithography with the current photolithography, important issues of domains orientation and lateral ordering must be focussed. The cylindrical domains are preferable than spherical domains for pattering or templating, owing to their stability or connectivity to the substrate and high aspect ratio. In this chapter, we have reviewed the literature for materials and methods for self-assembly of block copolymers along with the semiconductor material which is most suitable for fabrication of nanostructures using block copolymers nanotemplates for optoelectronic applications.

2.2 *ZnO* NP's

The efforts are being made by the researchers to prepare highly ordered nanostructures for the advancement of recent technology [120]. In the field of nanotechnology, different categories of nanostructures with unique characteristics are being processed and applied for a wide range of industrial applications [120].

Table 2.1: Basic properties of *ZnO*

1.	Appearance	White Solid
2.	Odor	Odorless
3.	Molecular Weight	81.38 g/mol
4.	Crystal Structure	Wurtzite
5.	Coordination Geometry	Tetrahedral
6.	Lattice Constant	a = 3.25Å, c = 5.2Å
7.	Band Gap	3.36 eV
8.	Solubility in Water	0.0004% (17.8°C)
9.	Refractive Index μD	2.0041
10.	Density	5.606 g/cm3
11.	Melting Point	1975°C
12.	Flash Point	1436°C
13.	Space Group	P63mc

Nano-sized semiconductor materials widely used in recent years due to their unusual thermal, structural, optical and electronic properties, and applications in different areas such as electronic industries, textile industries, medical industries, photo catalysts, gas sensors and photo electron devices [92, 120] . *ZnO* is a widely used material in recent years because of it's attractive features for catalytic, electrical, optoelectronic, and photochemical [120]. *ZnO* can be easily processed by different routes with variety of morphology along with excellent stability under high-energy radiation [120]. Furthermore, it can be grown on substrate in a variety of nanostructured morphologies, by low cost, low temperature methods and with less complex equipments [92]. These salient

feature motivated us to dig out more interesting properties of this novel compound. The remarkable basic properties of *ZnO* are summarized in table 2.1.

2.2.1 Synthesis methods of *ZnO* NP's

The morphology and size of *ZnO* NP's play an important role for observing the differences between the properties of nanostructures in comparison to bulk compound [121–124]. Many reports show that properties of nanomaterials depend on their morphologies and sizes. Relative luminescence intensity of *ZnO* varies with morphologies as nanowire > nanopowder > nanoneedle > nanoparticle. [124] Small changes in experimental condition like solvent, temperature, precursor, pH etc... may change the morphologies and properties of nanostructures. D Sridevi *et al.* synthesized *ZnO* NP's by hydrothermal method, x-ray diffraction confirmed crystalline nature and hexagonal structure of *ZnO* [125]. M. A. Shah *et al.* synthesized *ZnO* NP's by a chemical reaction of zinc metal with ethanol at 200°C. Morphology was change to nano rod with the addition of ethylenediamine to the reaction mixture [126]. *ZnO* flake structures were synthesized hydrothermally by D. Geetha *et al.* [127, 128]. Different synthesis methods of *ZnO* nanostructures and their morphologies are tabulated in table 2.2.

2.2.2 RE-doping in *ZnO*

Doping in *ZnO* are used to for devices application [103, 149–169]. The desired electronic properties can be achieve by doping of n type or p type. Furthermore RE doping is helpful for tuning the optical properties. The common problems with doping are that it change the morphology when dopant introduced during the growth, and the accurate determination of electronic properties. Therefore, most of the studies of doped *ZnO* are focused to the effect of dopant on the optical properties. The synthesis method and their morphologies are summarized in table 2.3.

2.2.3 Optical properties of *ZnO* and RE-doped nanostructures

2.2.3.1 UV Visible spectra

Generally bulk *ZnO* shows absorption peak at 370 nm in UV region. At nanometer scale, this peak shifts towards low wavelength side due to quantum confinement effect. The position of absorption peak varies with synthesis condition, precursor, solvent etc... [182, 183]. For example A.K. Singh *et al.* reported that the absorption peak shifted towards blue with concentration of Triethanolamine (TEA) [183].

Table 2.2: Various methods for synthesis of *ZnO* nanostructures.

Method	Chemical reagents	Synthesis condition	Properties	Reference
Mechano-chemical process	$ZnCl_2$, Na_2CO_3, NaCl, ethanol	Temp-350°C-450°C Calcination-1 hr.	Hexagonal and regular shape of particles, particle size of 51 nm	[129]
	$ZnCl_2$, Na_2CO_3, NaCl, ethanol	Temp-400°C Calcination-0.5 hr.	Hexagonal and regular shape of particles, particle size of 27-56 nm	[130]
	$ZnCl_2$, Na_2CO_3, NaCl, ethanol	Temp-600°C Calcination-1 hr.	Hexagonal structure, particle size of 21-25 nm	[131]
	$ZnCl_2$, Na_2CO_3, NaCl, ethanol	Temp-400°C-800°C	Hexagonal structure, particle size of 18-35 nm	[131]
Sol-gel method	Zinc acetate, ethanol, oxalic acid	Temp-60°C Drying 24 hrs., 60-80°C and calcinations at 500°C	Uniform, wurtize structure particle size of 100 nm	[132]
	Zinc acetate, oxalic acid, ethanol	Temp-50°C, time 60 min Dried at 80°C for 20 hrs.	Wurtize structure, spherically shaped particles, size of 50-200 nm	[133]
	Zinc accetate, diethanolamine, ethanol	synthesis at room temp. annealing: 500°C for 2 hrs.	Nanotubes of Hexagonal structure and	[134]
Hydrothermal process	Zinc acetate, NaOH, HMTA	Temp-100°-220°C for 5-10 hrs. and HMTA be of 0-200 ppm	Spherical shaped structures having particle size of 55-110 nm	[135]
	zinc acetate dihydrate, NaOH, PVP	stirring at 400 rpm at 60°C, thermally treated temp. up to 120°C, heating rate 2°C/min. for 72 hrs.	Hexagonal prismatic rods	[136]
	Zinc nitrate, deionized water, HMT	Microwave heating at 90° for 2 min and dried at 60°C, 2 hrs.	Hexagonal wurtize structure, nanorod and nanowire shape of 280 nm diameter	[122]
	Zinc acetylacetonate, n-tuboxyethanol and zinc oximate	Microwave heating of 800 W for 4 min and drying at 75°C	Crystallite size of 9-31 nm and particle diameter of 40-200 nm	[137]
	Zinc chloride, NaOH	Temp–100°-220 °C for 5-10 hrs.	Different types of structures are obtained: bullet like, rod like, sheet of size 50-200 nm	[138]
	Zinc acetate, Zinc nitrate, LiOH, KOH, NH_4OH	Temp-120°-250°C for 10-48 hrs.	Hexagonal wurtize structure of size greater than 100 nm	[139]
Co-precipitation process	Zinc nitrate, NaOH, Ionised water	Temp-100°C Stirring overnight at room temp.	Particles of spherical size of 40 nm	[121]
	zinc acetate dihydrate, DI water, tri-n-propylamine, NaOH	magnetic stirring at 80°C, pH 9, dried in hot air oven at 120°C for 4 h	Nano and micro-flowers, dumbbell shaped, rice flakes, and rings	[140]
	Zinc acetate, KOH, Ionised water	Temp-20°-20°C	Particle size of 160-500 nm	[141]
	Zinc acetate, NaOH, Ionised water	Temp-75°C Overnight drying at room temp.	Hexagonal structure, flower shape, particle size of 500-800 nm.	[142]
	Zinc nitrate, NaOH, Ionised water	Temp-100°C Cacination-2 hrs.	Particle size of 50 nm	[143]
	$ZnSO_4$, NH_4HCO_3, ethanol	Temp-100°C Cacination-2 hrs.	Wurtize structure, particle size of 12 nm	[144]
	$ZnSO_4$, NH_4HCO_3, ethanol	Temp-25°C Drying-80°C Cacination-1 hr.	Hexagonal structure, flower-like and rod-like shape, size of 15-25 nm	[123]
Green synthesis	Zinc acetate dihydrate, DI water, NaOH, [bmim][NTf_2]	domestic microwave oven (2.45 GHz, 850 W) in air, dried in vaccume at 40°C for 10 hrs.	Hexagonal wurtize structure and spherical shape size of 20-30 nm	[145]
Other methods	Diethylzinc, oxygen	Using helium as carrier gas	Hexagonal wurtize structure and size of 9 nm	[146]
	Zinc nitrate, NaOH, heptanes, hexanol, triton X-100, PEG	Temp. 140°C for 15 hrs. and dried at 60°C	Hexagonal wurtize structure and varying size of 50-200 nm	[147]
	Zinc acetate, NaOH, decane, water, ethanol	Temp.-90°C for 2 hrs.	Spherical and hexagonal particles, size of 100-230 nm	[122]
	Zinc acetate	Pyrolysis or thermal deposition around 800°C	Hexagonal wurtize structure and size of 20-30 nm	[148]

Table 2.3: Various methods for synthesis of RE doped *ZnO* nanostructures.

Method	Chemical reagents	Synthesis condition	Properties	Reference
Sol-gel	ZnA, $ErCl_2$, MEA	Stirring with temp.-60°C, for 1 hr. Annealing at 500-600°C for 1 hr.	Sphere like structures obtained on crystalline surfaces having size of 27.44 nm and 29.28 nm.	[82, 83]
	ZnA dehydrate, GdA hydrate, ethanol, NÁH	Stirring at 80°C for 6 hrs. and pH 8-11	NP's formed of size 9-22 nm.	[170]
	Zinc acetate, neodymium nitrate, CTAB, ammonium bromide,	Stirring and aged at room temp. for 48 hrs then dried at 60°C for 12 hrs.	NP's formed of size 22-33 nm	[109]
Hydrothermal	Zinc acetate, neodymium nitrate, water, HTMA	Constant stirring for 1 hr., then heated at 95°C for 16 hrs.	Hexagonal wurtzite structure having size of nearly 200 nm.	[171]
	ZnA, Eu_2O_3, methanol, NaOH	Temp.-150°C for 12 hrs. under stirring and dried at 60°C	Wurtzite structure NP's size of 9-12 nm.	[91]
Microwave assisted	ZnA, NaOH, Europium nitrate, water, ethanol, PVA	Constant stirring, room temp, pH-10, annealed at 200°C for 2 hrs.	Hexagonal crystal structure nanorods of size 25 nm.	[172]
Co-precipitation	Zinc nitrate, neodymium nitrate, NaOH, water and ethanol	Stirring at room temp. for 30 min, then temp.-80°C for 5 hrs. and drying at 120°C for 2 hrs.	The Hexagonal wurtzite structure having size of 29-35 nm	[136]
	ZnA, $NaBH_4$, Europium nitrate, water	Stirring for 4 hrs. at 60°C, dried at 200°C	NP's formed of size 1-60 nm	[173]
	ZnA, $Eu(CF3COO)_3Âů3H_2O$, ethanol, NaOH	Stirring for 2 hrs. at room temp, dried under vaccum for 24 hrs at 60°C	Quasi-spherical crystalline structures having size of 5-6 nm.	[174]
Diffusion process	ZnA, Eu, O_2	Temp.-900°C under vaccum and annealing for 1 hr.	Single crystal Eu-doped *ZnO* nanowire diameter appx. 200 nm.	[175]
Chemical route	ZnA, $ErCl_2$, dist. Water, octanol	Room temp.-25°-35°C	Spherical like structures having particle size of 15-50 nm and diameter of appx. 850 nm.	[79]
	$Zn(NO_3)_2$, $Er(NO_3)_3$, octanol	Solvothermal conditions, Temp-200°C for 10 hrs. and washed with ethanol	Nanocrystals are obtained having particle size of 23-30 nm.	[80]
	ZnA dehydrate, TMAH, GdA hydrate, ethanol, oleic acid	Constant stirring at room temp.	NP's formed of size 3-5 nm.	[176]
Sonochemical synthesis	ZnA dehydrate, GdNhexahydrate, PVP/CTAB, ammonia	Sonication 30 mins and dried at 320°C	Hexagonal wurtzite structure of size 10-70 nm	[177]
Combustion	*ZnO*, Eu_2O_3, nitric acid, water, NH_4OH	Temp.350°C for boiling, pH = 5, Annealed at 550°C	NP's obtained of size nearly 50 nm.	[178]
	Zinc nitrate, Europium nitrate, urea	Temp.-350°C, Annealed at 550°C	NP's obtained of size 28 nm	[179]
Thermal evaporation	ZnAdihydrate, GdNhexahydrate, O_2, ethanol	Temp-500°C for 2 hrs. Cacination-2 hrs.	NP's formed of size 10 nm.	[180]
Reverse micelle	$Zn(CH_3COO)_2Âů2H_2O$, $Eu(CH_3COO)_3Âů4H_2O$, CTAB, butanol and octane	Temp.-200°C for 10 hrs.	Nanocrystals of Eu-doped *ZnO* of size 50 nm,	[90]
Electrospinning calcinations	ZnA dehydrate, GdNhexahydrate, PAN, *N,N*-dimethyl formamide	Stirred at 35°C for 3 hrs., Voltage-22.5 kV, Calcinated at 500°C	Gd doped *ZnO* nanorods formed size of 73 nm.	[181]

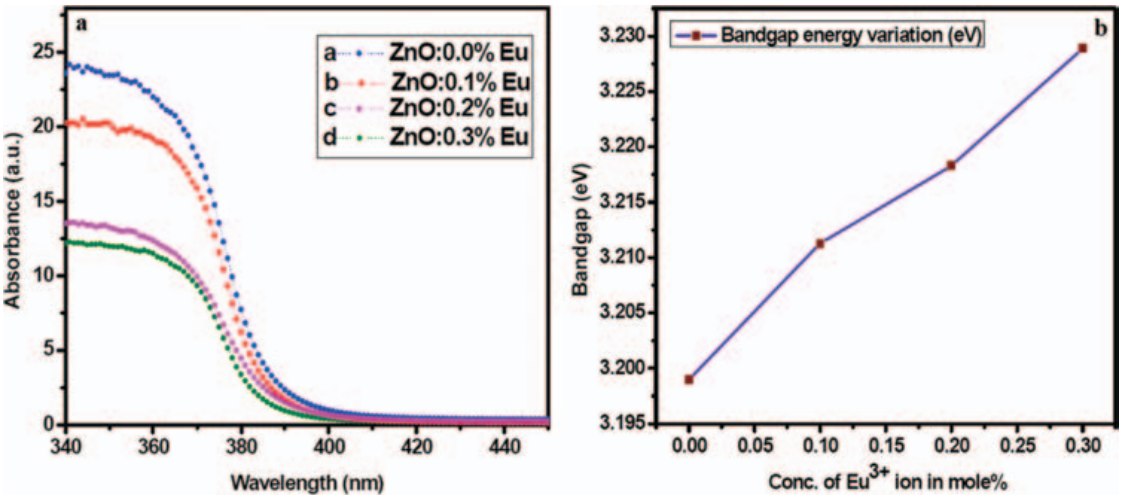

Figure 2.1: (a) UV-Vis spectra of pure and Eu^{3+} doped *ZnO* (0.1, 0.2 and 0.3 mole%) doped samples (b) Comparison of bandgap energies with the variation in concentration of Europium [3].

Shift in absorption peak also occurs by doping of RE elements. The absorption threshold of pure *ZnO* (373 nm) was shifted from UV range to visible range for RE doped *ZnO* products (Nd(2.0at%)/*ZnO*, Eu(2.0at%)/*ZnO* and Ce(2.0 at%)/*ZnO*) [184]. Moreover, Eu doped *ZnO* shows (figure 2.1a) that the absorbance decreases below 400 nm and optical band gap increases with increase in Eu doping [3]. The energy transfer from O atom to Eu^{3+} ion was observed in Eu doped *ZnO* samples [185]. Another study shows that with incorporation of Er in *ZnO*, the UV absorption bend shows shift in towards the lower energy side [186, 187]. Furthermore, the band edge was shifted to the shorter wavelength side for the La doped *ZnO* as compared to the pure *ZnO* [188]. The absorption study of Tb doped *ZnO* also shows an increase in the band gap as Tb is incorporated with *ZnO* NP's [107]. The UV absorption of Er-doped *ZnO* film was observed lower than annealed Er doped *ZnO* film because of the poor crystalline nature of as deposited film [189].

2.2.3.2 Low temperature photoluminescence

Low temperature photoluminescence (LTPL) studies are useful tool in order to examine the quality of *ZnO* nanostructures becouse room temperature photoluminescence does not detect the diffect emmition [190]. The information about impurity presents in the sample may also be extracted by high resolution measurements of LTPL spectra. In addition to neutral donor bound exciton peaks, free exciton emission in LTPL spectra

at 10 K for *ZnO* nanorods was also ditecteded which indicates the high optical quality of prepared *ZnO* nanorods [191].

Table 2.4: peak position and possible origin of bound exciton lines in *ZnO*

Position (eV)	Possible origin	Reference
3.332	Excitons bound to structural defects	[192]
3.31	Surface states	[193]
3.315	N_o acceptor	[194]
3.3725		[195]
3.3718		[195]
3.3679		[195]
3.3674, 3.3665	Ionized donor bound excitons	[195]
3.3660		[195]
3.3614, 3.3604, 3.3600, 3.3593	Neutral donor bound excitons	[195]
3.3628, 3.3630	H	[194, 195]
3.3608	Al	[195]
3.3598	Ga	[195]
3.3567, 3.3572	In	[195]
3.356	Na acceptors	[195, 196]
3.353	Li acceptors	[195, 196]
3.3531		[195]
3.3484		[195]
3.3481, 3.3530, 3.3564	Neutral acceptor bound excitons	[197, 198]
3.3484-3.3614	Neutral acceptor bound excitons	[199]
3.3562	Neutral acceptor bound excitons	[197, 200]
3.358	Neutral acceptor bound excitons	[195, 197]
3.3566	Neutral acceptor bound excitons	[197, 201]
3.3598-3.3693	Donor (neutralorionized) bound excitons	[195, 197, 200, 201]
3.3686, 3.302	Rotator states	[197, 198]
3.3670, 3.3664, 3.3702, 3.3714	Rotator states	[197, 200]
3.3724	B excitons bound to neutral donor	[197, 198]
3.3707, 3.3741, 3.3754, 3.3772	B excitons bound to neutral donor	[197, 202]

ZnO nanostructures shows the emission due to biexcitons in the LTPL spectra which may be indirect indication of the quality of sample[203]. S. Ozaki *et. al.* spotted the biexciton emission in LTPL spectra (Temp. up to 200 K) at 3.35 eV for *ZnO* nanowires synthesized via simple vapor transport route. The binding energy of biexciton was found to be 17 meV [204]. Further, the LTPL study of *ZnO* results the number of bound exciton peaks labeled from I_0 to I_{11} [199]. Mmagnetic field dependent analysisshows that the presence of exciton lines from I_5 to I_{11} are due to excitons bound to neutral acceptors [199]. While the bound exciton lines I_4 (3.3628 eV), I_6 (3.3607 eV), I_8 (3.3598 eV),and I_9 (3.3567 eV) have been attributed to donor bound excitons, namely excitons bound to hydrogen [195, 205].

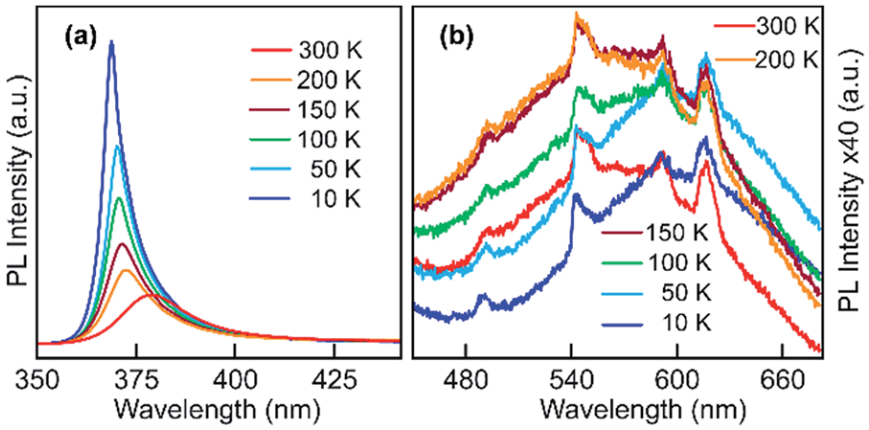

Figure 2.2: Solid state PL measurements for *ZnO* nanorods at different temperature doped with Tb precursor; (a) Near band edge emission and (b) visible PL spectra due to distinct intra-4f transition [4].

Annealing and surface modification can alter the PL spectra of *ZnO* nanostructures [190, 206]. K. H. Tam *et. al* reported the significant decrement in the defect emission was observed by annealing at 200°*C* while the *ZnO* nanorods was having large defect concentrations [190]. The LTPL study of NiO-*ZnO* shows enhansement in emission intensity of donor-bound exciton, which was corrosponds to oxygen deficiency [206]. On the other hand, Ni-*ZnO* shows enhancement in emission of acceptor-bound exciton due to diffusion of hydrogen into *ZnO* during the reduction process [206]. A. Layek *et. al.* investigated that intensity of UV peak related to donor-bound exciton decreases and shifted towards higher wavelength with the increase in temperature (10K to 300K) due to donor-bound exciton minimization as shown in figure 2.2 [4]. Reported bound exciton peak positions are listed in Table 2.4.

2.2.3.3 Room temperature photo-luminescence

Photoluminescence spectra of *ZnO* at room temperature generally shows two emmition peaks. First peak corrosponds to near band edge emission (NBE) and second broad emission band originated from defect emissions [207–209]. For example, RTPL spectra of *ZnO* NP's prepared by co-precipitation method showed an intense defect-related green emmision centered at 560 nm and a weak UV band-edge emmition centered at 373 nm[210]. Strong UV emission is not a sufficient proof of low defect density or good crystalline quality in the samples [190]. Green emission is the most commonly observed emission in PL of *ZnO* but the peak positions for green emission were found different from one study to another [211]. Many hypothesis have been proposed for the

explanations of green emission such as structured green emission is due to Cu impurities [212], Zn vacancies [213], oxygen antisite [214] and singly ionized oxygen vacancy [215].

Table 2.5: Positions and proposed origin of room temperature PL peaks in *ZnO*

Peak position(eV)	Proposed Origin	Reference
373-390	Near-and-edge emission	[216]
∼402 (77K)	OZn	[213]
∼446	Shallow donor-oxygen vacancy transition	[217]
∼459	Zinc interstitial	[218]
∼495	Oxygen vacancy	[218]
∼500-510	CuÃ¿/Cu2Ã¿	[212]
∼510	Surface defects/defect complexes	[211]
∼510	Singly ionized oxygen vacancy	[215]
∼520	Zinc vacancy	[213]
∼520	OZn	[214]
∼520	Oxygen vacancies and zinc interstitial	[219]
∼540	Vo	[220]
∼560	Surface defects	[221]
∼566	(10K) Shallow donor-deep acceptor(zinc vacancy containing complex)	[222]
∼580	Oxygen interstitials, Li impurities	[223]
∼590	Hydroxyl groups	[224]
∼626	Oxygen interstitials	[219]
∼750	Oxygen-related defects, zinc interstitials	[225]

Apart from green emission, broad yellow emission is also observed in *ZnO* samples prepared by solution methods [190, 224, 226, 227]. The possible reason for yellow emission are defects associated with excess oxygen [224], presence of hydroxyl groups [190] and Li impurities [223]. Some other emissions have been reported in addition to green and orange-yellow emission such as violet, blue, red and near infrared but there is no consensus on their origin [216]. The different growth conditions cause the variation of relative contribution of free excitons due to which position of the NBE varied significantly [210, 228]. Reported peak positions and their proposed origin are summarized in table 2.5. RTPL studies of *ZnO* nanostructures are mostly focused on the origin of defect emission. Partha P. Pal1 and J. Manam reported that the RTPL of Eu^{3+} doped *ZnO* nano phosphors showed bright red and orange emissions nearly at 618 and 594 nm, respectively along with efficient broad blue green emission spectrum due to *ZnO* lattice. Furthermore, a good energy transfer process from *ZnO* host to Eu^{3+} was observed in PL emission and excitation spectra of Eu^{3+} doped *ZnO* ions [229].

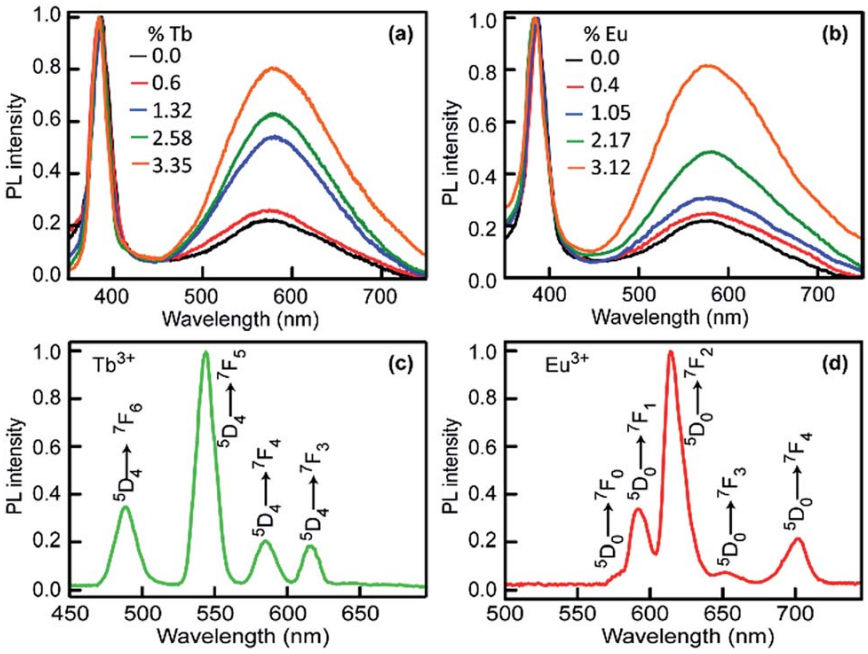

Figure 2.3: PL spectra of RE^{3+} doped *ZnO* nanorods synthesized using different concentrations (atom%) of (a) Tb^{3+} and (b) Eu^{3+} precursors. (c and d) Time delayed PL spectra of Tb^{3+} and Eu^{3+} doped *ZnO* [4].

The extra blue emission at 441 nm (2.81 eV) was observed along with emission bands from undoped *ZnO* in RTPL spectrum of Gd doped *ZnO* sample [230]. Eu^{3+} doped *ZnO* shows a sharp red emission due to the intra-4f transitions of Eu^{3+} ions at an excitation of 397 nm and 466 nm. At higher concentration of Eu^{3+}, luminescence quenching was observed [178]. The recent report by A. Layek *et al.* showed that the sharp UV emission due to the radiative annihilation of excitons with a maximum at $\sim$ 380 nm in solution phase RTPL spectra of pure and doped *ZnO* nanorods. A deep level defects related broad visible PL band (Fig. 6) was found in the wavelength rang from 500-750 nm. Moreover the excitonic absorption maxima was shifted twards blue with increasing doping concentration (figure 2.3) while there is no significant shift was observed ($\sim$ 2 nm) in NBE maxima [4]. By the direct excitation of *ZnO* host efficient energy transfer from *ZnO* host to guest RE ions has been revealed through the characteristic emissions of RE ions [231].

2.2.4 Antibacterial Properties of *ZnO*

ZnO is a II-VI semiconductor shows longer durability, higher selectivity, and heat resistance. Synthesis of variety of nano-sized *ZnO* has led to the investigation of its use as

new antibacterial agent. In addition to its unique antibacterial and antifungal properties, *ZnO* NP's possess high catalytic and high photo chemical activities. *ZnO* possesses high optical absorption in the UV-A (315-400 nm) and UV-B (280-315 nm) regions which is beneficial in antibacterial response and used as a UV protector in cosmetics [232]. In protein dysfunction and generation of Reactive Oxygen Species (ROS) mechanism, the particles bind to thiol groups in the protein hence changing their conformation. Also, through electron transfer reactions, they generate abnormal amount of ROS. In release of Metal Ions mechanism, for instance Ag or *ZnO* NP's release Ag^{+} or Zn^{+2} ions respectively that have ability to inhibit respiratory enzymes and cause protein dysfunction and influence DNA replication. Also, hydrophobicity is an essential feature of bacterial cells to adhere to surfaces and form biofilm, *ZnO* NP's have been reported to have enhanced cellular hydrophilic nature of Pseudomonas aeruginosa cells and reduce biofilm formation [233]. Delay in FtsZ (a cell division protein essential in initiating septation) ring formations and reduction in EPS production have been found to be responsible for slow growth and inhibition of biofilm. *ZnO* NP's synthesized by green method show more enhanced biocidal activity against various pathogens when compared to the one synthesized by chemical route. The use of *ZnO* NP's in functionalized or unfunctionalized forms have been tested for mammalian cytotoxicity vastly and it has been found that *ZnO* NP's show selective toxicity towards cancerous cells. NP's are taken up by the cell, after which dissolution takes place inside the cell. In-vitro results indicate that induction of oxidative stress is the most important or most likely mechanism underlying *ZnO* NP's toxicity other than changes in mitochondrial membrane potential, membrane integrity, apoptosis, etc... [234, 235]. Also HepG2 and MCF-7 cells when exposed to *ZnO* NP's showed the same fate. The cells showed dose-dependent decrease in cell-viability, increased cytotoxicity that was likely mediated through ROS generation and oxidative stress [236]. Cytotoxicity analysis of *ZnO* NP's against three types of cancer cells (human hepatocellular carcinoma HepG2, human lung adenocarcinoma A549, and human bronchial epithelial BEAS-2B) was done and it was found that cell viability was reduced specifically in transformed cells when compared to normal cells. ROS generation and oxidative stress was elevated, apoptotic and antiapoptotic genes where up-regulated and down-regulated respectively [237]. In-vitro and in-vivo study was conducted for effect of pH-sensitive, hollow *ZnO* nanocarriers loaded with paclitaxel in breast cancer. $\sim$75% of the paclitaxel payload was released within six hours in acidic pH and a dual cell-specific and pH-sensitive nanocarrier greatly improved the efficacy of paclitaxel to regress subcutaneous tumors in vivo [238]. Pure and Al-doped *ZnO* NP's synthesized via a simple sol-gel method had an IC50 of 44 μg ml^{-1} and 31 μg ml^{-1} for MCF-7 breast cancer cell line. Al-doped *ZnO* NP's induced apoptosis in

MCF-7 cells through mitochondrial pathway which was indicated by up-regulation of apoptotic genes (e.g. p53, bax/bcl2 ratio, caspase-3 & caspase-9) along with loss of mitochondrial membrane potential. Comparative analysis showed no effect on normal cells [239]. Porous and rod like structured *ZnO* NP's synthesized by green synthesis from Borassus flabellifer fruit extract with an average size of 55 nm had the inhibitory concentration (IC50) to be 0.125 μg ml^{-1} for MCF-7 and HT-29 cells. Nuclear staining by Hoechst 33258 showed induction of apoptosis. In murine model system DOX-*ZnO* NP's showed low systemic toxicity and further results proved that the DOX-*ZnO* NP's has low toxicity and high therapy efficacy providing convincing evidence for the green biosynthesized *ZnO* as a promising candidate for a drug delivery system [240].

2.2.5 Applications of RE doped *ZnO* nanostructures

Due to their versatile features and properties, *ZnO* nanostructures can be used in various industrial applications. *ZnO* NP's are used in FETs, LEDs and photo diodes [241–244].

Table 2.6: Applications of RE-doped *ZnO* nanostructures.

S. No.	Different areas	Applications	References
1.	Electronics	Photodetectors, transistors, LEDs, laser diodes, flat panel displays, transparent electrodes, nano-generators, solar cells, optical waveguides, PZT transducers, surface acoustic wave devices and optoelectronic devices, etc...	[79, 88, 96]
2.	Nanomedicine	Target and control release of drug, antibacterial and anticancer activities.	[94, 171, 245]
3.	Photocatalysis	Photocatalytic degradation of various organic and inorganic dyes.	[246–248]
4.	Computing	Energy as well as memory storage devices, optical imaging.	[180, 249, 250]
5.	Miscellaneous	Printing inks, fire resistant materials, artificial fertilizer, latent fingerprint analysis, cigarette filters, biosensors, etc...	[88, 89, 108, 122, 135, 147, 173, 251–254]
6.	Spintronics	Solid state devices, electro-magnetic devices and logic based devices.	[40, 92, 96]
7.	Sensors	Gas sensing and detection of different compounds, UV detectors.	[40, 80, 83]
8.	Textile industry	Removes UV radiation.	[122, 172]
9.	Rubber and Paint	Stabilization of latex, fire resistance, provides tensile strength, lubricating applications.	[122, 255]
10.	Pharmaceutical and cosmetics	Antiseptic healing creams, suntan lotions, source of micronutrient zinc.	[171, 173, 256]

The RE-doped *ZnO* nanostructures have various industrial applications compared with

pristine ZnO nanostructures [85, 257, 258]. They show photo-catalytic degradation of various anionic and cationic dyes. ZnO and RE doped ZnO have vast applications in the field of electronics. They are used by semiconductor industry for developing single electron transistors and photodetectors. Fabrication LEDs, laser diodes, flat panel displays, transparent electrodes, nano-generators, solar cells, optical waveguides, PZT transducers, surface acoustic wave devices and optoelectronic devices are another level of applications. They are also used in the field of spintronics for making solid state devices for memory storage. They are used in sensing applications and for photocatalysis. Moreover, these materials are used for regulated and controlled drug release in biological sites and can be helpful in anticancer and antibacterial treatments. Zinc is an important micro-nutrient, which enables its usage as a food supplement for plants and animals. The RE doped ZnO NP's have various other applications in printing (inks), fire resistant materials, artificial fertilizer, fingerprint analysis, cigarette filters and bio-sensors. It is also used for the detection of various enzymes and other bio-molecules. The applications of RE-doped ZnO Nanostructures are illustrated in the table 2.6.

2.3 Block copolymer thin films

The modern era of technology demands materials at the nanometer length scale. Advancement in technology is required to control the structure of these material and assemble them in a controlled manner. Many applications like membranes, templating etc... requires block copolymers in thin film of thickness $\sim$100 nm, where self-assembly is strongly depends on surface energies. Self-assembled block copolymer and supramolecular assembly of block copolymer being used as templates for nanofabrication as they provide nanotemplates with different morphologies and tunable sizes, are easily removed after reactions, and could be further modified with different functional groups to enhance the interactions. The self-assembly and supramolecular assemblies of block copolymer have been discussed in section 1.2.3 and section 1.2.4.

2.4 Ordering in thin films

To achieve well ordered nanostructures for optoelectronic device, applications the ordering in block copolymer thin films is a primary requirement. In general, the domains of block copolymer are self-assembled in to diverse morphologies in the as-deposited thin films. This is because of the fast evaporation of solvents, which does not provide the sufficient time to rearrange the molecules in the equilibrium. Two surface interactions,

polymer-substrate and polymer-air interaction, cause the ordering and the alignment of microdomains [259]. The block, interacts strongly with the substrate, prefers to stick parallel to the substrate. Annealing is an efficient approach to obtain the long-range ordering in the thin films. The ordering and the desired orientation of microdomains can be achieved by thermal annealing, solvent annealing, shear or electric field [29, 30, 260, 261].

2.4.1 Thermal annealing

The conventional method for ordering of block-copolymer thin films is thermal annealing in which the film have traditionally been ordered by heating them in a vacuum oven for extended periods (hours to days). It is usually done by elevating the temperatures of the thin films above the glass transition temperature (T_g) of both block compounds so that the material has sufficient mobility for rearrange the morphology. Annealing temperature is a crucial parameter for the ordering and alignment of microdomains in thin films. For the vertically aligned domains, the surface energies for both the copolymer blocks should be nearly equal. The surface energies and their difference is a function of temperature. In a special case of PS-*b*-PMMA, both the bocks PS and PMMA have the almost same surface energy over a broad range of temperature [262]. This property makes PS-*b*-PMMA a unique candidate for the self-assembly via thermal annealing. The diffusivity (D(T)) of the polymer chains is represented by Arrhenius equation as follows;

$$D(T) \sim \frac{1}{t} = Ae^{-\frac{\triangle E_a}{RT}} \tag{2.1}$$

Where t is annealing time, A is constant, R is ideal gas constant, T is annealing temperature, and $\triangle E_a$ represents activation energy of polymer. The above equation shows that on increasing the annealing temperature the diffusivity of the polymer chains increases which reduces the annealing time. The minimum annealing time for the self-assembled defect free lamellar forming PS-*b*-PMMA thin films was reported by Welander *et al.* [263]. The annealing time is a limitation for lithographic applications of block copolymer. However, the self-assembly of thin films has already been achieved within few minutes using hot plate or rapid thermal annealing process [264, 265]. Recently, Seshimo *et al.* have obtained sub-10 *nm* vertically oriented lamellae in modified polysiloxane-based block copolymers by thermal annealing at 130°C in atmospheric conditions for one minute [266]. Perpendicularly aligned PMMA cylinders in PS matrix with a high aspect ratio ($h/d \approx 7$) have been investigated with a thickness window of 5 nm to 400 nm under rapid thermal annealing at high temperatures (190°C $\leq T_a \leq$ 310°C) [267]. Initially, the annealing temperature was optimized by keeping the annealing time (900 s) and thickness of film (≈35 nm) same. Below and above 270°C, disorganized PMMA

cylinders were observed and this was correlated to orientational correlation (ξ) [268]. High temperatures speed up the kinetics of the block copolymer system and lead to a long-range ordering in orientational correlation which remarkably reduces the ordering time [263–265]. Further increasing the temperature results in the degradation of polymer chain and lead to the disarrangement of the blocks. Figure 2.4(a) shows the variation of ξ with annealing time and the maximum value is corresponding to 270°C. Once the annealing temperature was optimized, the optimization for annealing time and the thickness of film was carried out for the perfectly aligned (vertically) cylindrical domains (shown in figure 2.7 (b & c)). Annealing time $t < 300$s is sufficient to form organized cylinders without any defects. When the thickness $t < 10$ nm, the formation of droplets were observed. The reason may be attributed to the high surface tension of diblock copolymer which leads to the formation of droplets on annealing at high temperatures. On increasing the thickness, mixing of the droplets leads to the hexagonal arrangement of cylindrical domains up to ~ 200 nm and then increasing more thickness the disarranged cylinders were obtained, due to decrement in correlation length.

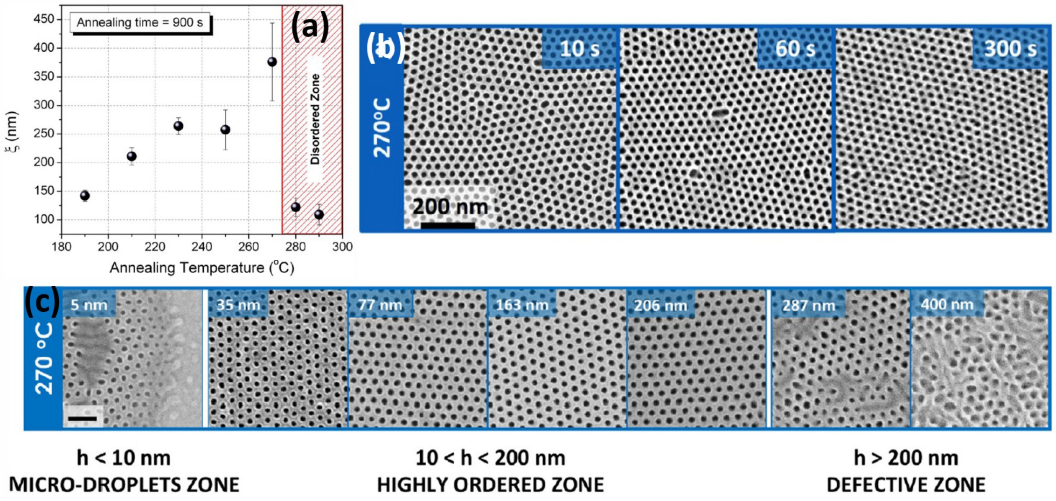

Figure 2.4: (a) Variation of correlation length with annealing temperature, (b) Time evolution of lateral ordering at an annealing temperature 270°C, and (c) Thickness dependence of lateral ordering annealed at 270°C [267]

.

2.4.2 Solvent annealing

Besides the thermal annealing, solvent annealing is another commonly used approach for the self-assembly of block copolymer thin films. In the solvent annealing, the thin films of block copolymer or supramolecules are placed in a closed glass jar having the reservoir

of solvent for a particular period of time [269, 270]. Annealing solvent in jar evaporates and eventually the vapours get saturated. Then, thin films are be removed from the jar and get dried in air. The thin films can be dried by purging N_2 also to remove the excess amount of solvent [70]. The copolymer blocks get swollen by the vapours of the annealing solvent and the thickness of block copolymer increases and copolymer blocks rearranged accordingly. After removing from the jar, it again comes to the original value. Many novel set ups for several purposes have been proposed; solvent annealing assisted by thermal or microwave to reduce the annealing time, set up for localized solvent annealing which could be done by using a vapour nozzle, use of polymer gel pad swelled by annealing solvent for the ultra-fast annealing over large areas [71–73, 271–273]. The reasons for adopting the solvent annealing over thermal annealing are; 1. it provides a path to reconcile the interfacial energies (polymer-substrate and polymer air) and promotes the perpendicular orientation of microdomains [269, 274–276], 2. it lowers the T_g of block copolymers, so, it induces the self-assembly even of the thermally unstable block copolymer [277], 3. it is appropriate for block copolymers with large molecular weights also. As it reduces T_g, that enhance the chain mobility and then the mass transport is obtained which is not possible in thermally annealed system [278, 279]. 4. provide an additional control to the process by varying the solvents with different selectivity, rate of evaporation of solvent, annealing time [280–283]. Additionally, for supramolecular assembled system, solvent annealing is preferable than thermal annealing because the thermal annealing may evaporate the small molecules. A little loss of small molecules may result the great variation in the morphology of supramolecular complex. The understanding of phase behaviour of block copolymer thin films is more complicated in solvent annealing than that of thermal annealing. Selectivity of the solvents is a key parameter that affects the phase behaviour. A non-selective solvent swells the copolymer with the same amount while the selective solvent swells the copolymers blocks differently which induces the change in relative volume fraction. The effective interaction parameter χ_{eff} will also be influenced in the presence of the selective solvent; it may be lower or higher than χ. Generally, the solvents are removed after the solvent annealing, and then dried. The process of removal of solvent may also affect the morphologies in the dried block copolymer thin films. So, basically, the solvent annealing process consists of two steps; swelling and drying. Phase segregation of microdomains may occur at any one of two stages; microdomains may be phase separated in a swollen state and gets affected by drying or microdomains may not be phase separated and are in disordered state and gets phase separated during drying.

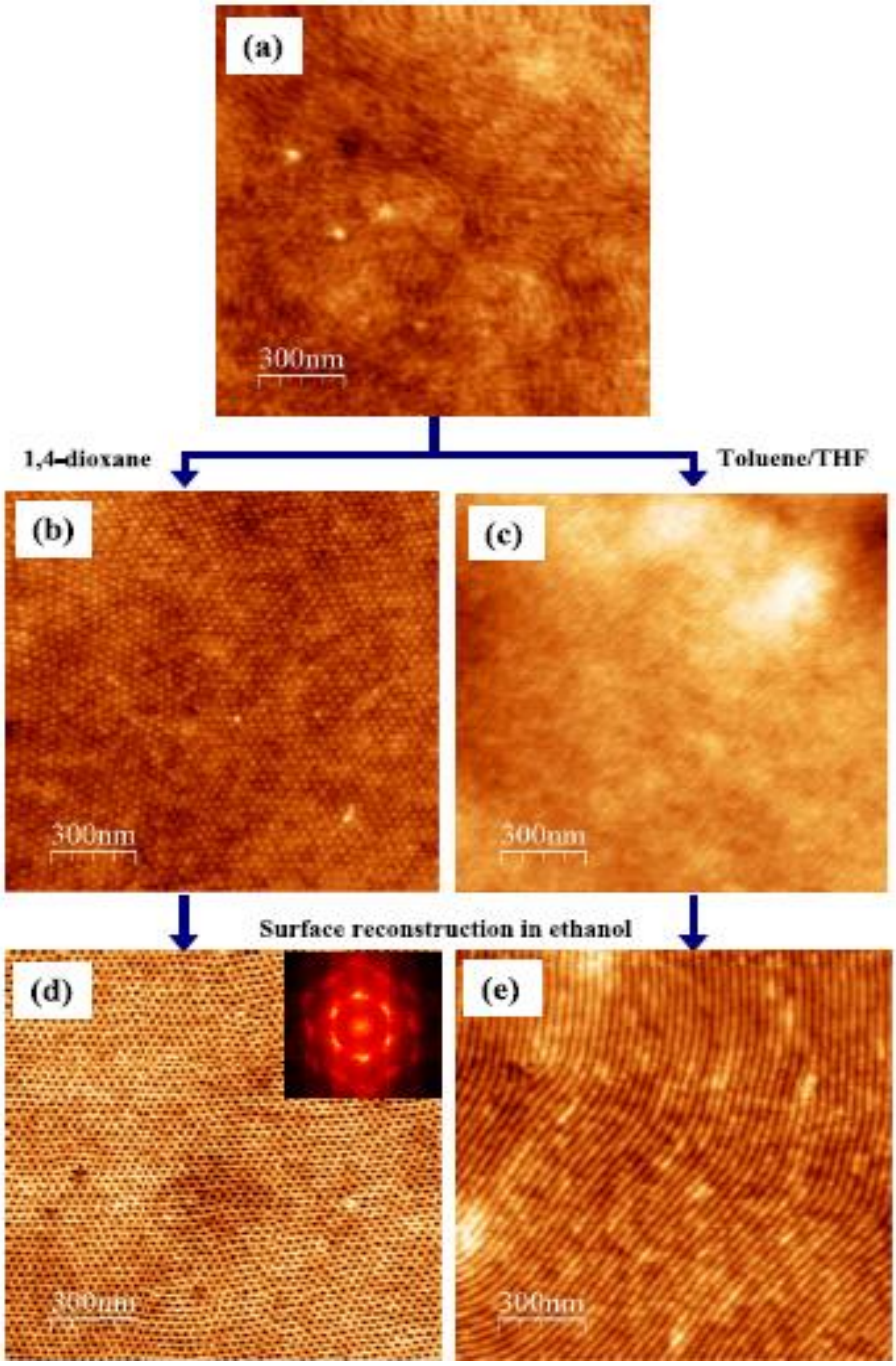

Figure 2.5: AFM images of as-deposited PS-*b*-P4VP thin film (a), before (b) and after (d) surface reconstruction of thin film annealed in the vapours of solvent 1-dioxane, and before (c) and after (e) surface reconstruction of thin film annealed in solvent toluene/THF [26]

However, the connection between the nanostructures formed in swollen state and dried state is not well-established [29]. Recently, Bai *et al.* have in-situ studied the swelling and the microdomain orientations in PS-*b*-PDMS 16 kg/mol (with a period of $\sim$18 nm)

thin films during solvent annealing using GISAXS [284]. Thin films were annealed in a non-selective solvent of a mixture toluene: heptane -5:1 and observed the swelling ratio with annealing time. The swelling ratio is defined as the ratio of the film thickness in swollen state to the thickness of as-deposited film. Cylindrical domains were obtained at lower swelling ratio and the in-plane cylindrical domains were promoted because of the preferential interaction of PDMS with the substrate. The transitions from short cylinders to out of plane cylinders and then in-plane cylinders with the annealing time were observed. They also observed the effect of vapour pressure on the swelling ratio and measured the critical value of swelling ratio (SRc) where the well-ordered cylinders were obtained at particular vapour pressure. Further the effect of thickness (28 nm -1141 nm) on the structural arrangement was investigated in the regime of swelling ratio below SRc. Thinner films led to the in-plane cylinders while thicker films show the well-ordered perpendicular cylinders. The selectivity of solvents causes the change in the orientation of the nanostructured domains [280, 285]. Stamm *et al.* have demonstrated the transition in the orientation of P4VP cylindrical domains from horizontal to perpendicular alignment. PS-*b*-P4VP/HABA thin films were annealed in the vapours of chloroform and 1-4 dioxane respectively [285]. Chloroform and 1-4 dioxane hydrogen bonded with P4VP by phenolic and carbonyl group respectively. The P4VP cylinders dispersed in PS matrix were aligned parallel to the substrate and switched the orientation to vertical to the substrate. This switching of orientation is attributed to the difference of substrate interfacial energy of P4VP/HABA in the presence of each solvent. They have shown the similar results for solvents 1-4 dioxane and mixture of toluene and THF (80:20) shown in figure 2.8 [286].

2.5 Block copolymer directed nanostructures

The preparation of ordered nanostructures requires ordering in block copolymer thin films which have been discussed in previous section. The ordered nanostructures are useful in many device applications. For this, following steps were followed.

- Creation of pores in block copolymer thin films by removing sacrificial polymer blocks.
- Backfilling of inorganic material (metal or metal oxide) in the porous nanotemplates.
- Removal of remaining polymer template.

2.5.1 Preparation of porous nanotemplates

Selective removal of polymer blocks from ordered block copolymer thin films is the primary requirement in order to prepare the nanotemplates. Depending on the chemical nature and stability of ordered block copolymer thin films various methods have been adopted to remove the sacrificing blocks. Amorphous component of crystelline-*b*-amorphous block copolymer (like polyethylene-*block*-polystyrene (PE-*b*-PS) or polystyrene-*block*-poly(vinylidene fluoride)-*block*-polystyrene (PS-*b*-PVDF-*b*-PS)) can be removed selectively by fuming nitric acid. The UV irradiation leads to degradation of PMMA block and provide cross-linking of the PS block so it is useful to remove PMMA block from the PS-*b*-PMMA block copolymer nanotemplets [287]. The nonporous structures can be generated from a blend of homopolymer PMMA and block copolymer PS-*b*-PMMA either by removing all PMMA blocks and PMMA homopolymer using irradiation or only PMMA block by using a selective solvent (acetic acid) [287]. Porous nanostructurs from block copolymer precursors with one etch-resistant block (increasing the oxygen or decreasing the carbon atoms in one of the blocks) can be generated using reactive ion etching [285]. Ozone treatment have been used for the removal of PI or PB block from PS-*b*-PI or PS-*b*-PB, respectively [288]. Chemical etching is the easy process and can be used for various copolymer blocks, for example; PDMS block from block copolymer PS-*b*-PDMS can be removed by the degradation using HF solution [289], hydrolysis process has been applied to PLA containing block copolymers to remove PLA block [290], and the rinsing in ethanol/methanol has been applied to remove the P4VP block from most commonly used block copolymer PS-*b*-P4VP [285, 291].

2.5.2 Deposition of inorganic material into the nanotemplates

Fabrication of 1-D conducting and semiconducting nanostructures have the increasing attention because of their potential applications in the optoelectronics. Electroless plating is an easy and cost-effective process to obtain the metallized nanowires from block copolymers. This process does not require any external current source, in this process a nanoporous block copolymer template is dipped into the electroless plating bath and metal is deposited via an autocatalytic process onto the surface of the template. Electroless deposition method describe as $M^{z+} + R^{n-} \rightarrow M^0 + R^{z-n}$., in which metal ions, M^{z+}, are reduced by the reducing agent R^{n-}. Moreover, non-conductive surfaces, such as polymers or ceramics can undergo electroless plating after the appropriate pre-treatment sensitization in $SnCl_2$/HCl followed by activation in $PdCl_2$/HCl. The Pd sites act as catalysts during the electroless metal plating procedure. Fahmi *et al.* used PS-*b*-P4VP block copolymer for fabrication of metallized nanowires, because the free pair of electrons

in the nitrogen of pyridine ring of P4VP may capture metal ions such as Pd, Ni, Fe, Au and others [292]. The intercalation of metals with pyridine works as inorganic-organic junction. Diameter of wire can be controlled by template size and reaction condition such that reaction time and concentration of coating solution. Electro-chemical deposition of metal inside the pores of a polymer template is also widely used technique in which the working electrode is usually coated by a template placed in the plating bath together with the counter and the reference electrode and connected to an external current source. The surface of the working electrode should be accessible to the plating bathe for completely plate the sample. Recently Chanchayya Gupta Chandaluri *et al.* deposited Au on polystyrene-*block*-poly(2-vinylpyridine), PS-*b*-P2VP, where the P2VP domains are quaternized with iodomethane and used for selective deposition of redox-active materials. It is well reported that PS domains insulate the conductive surface towards redox labels in solution and the quaternized P2VP domains electrostatically attract negatively-charged redox labels solubilized in the electrolyte solution. Which results in an effective electron transfer between the electrode and the redox label. This phenomenon is implemented for the selective deposition of Au on the nano-patterned surface [293]. Semiconducting nanostructures (especially ZnO) are of great interest for the optoelectronic applications. Sol-gel method has been widely used for the backfilling of the nanotemplates to develop the ordered semiconducting nanostructures. Song-Zhu Chu *et al.* synthesised metal oxide nanorods by alumina template-assisted sol-gel method [294]. For the fabrication of metal/metal oxide nanostructures, the metal/metal oxide precursor solutions need to be impregnated into the porous templates either by immersing the template into the sol or by using spin coating or dip coating technique. Raulet *et al.* have prepared the ordered array of metal oxides NP's (TiO_2, RuO_2, SiO_2, ZnO, MnO_2 and CeO_2) by spin coating the precursor solutions at a speed of 3000 rpm for 30 seconds [295]. Figure 2.6 shows the schematic representation for the fabrication of metal oxide nanostructures by block copolymer template assisted-sol-gel method. The filling of the templates can be tuned by the spinning speed and spinning time. Above-mentioned way of backfilling the pores might have an issue of forming a continuous layer over templates instead of the selective deposition. In that case, the overlayered metal oxide has to be removed by using ion etching techniques. So, in the same direction, another way of fabrication of ordered nanostructures by template assisted sol-gel method is the incorporation of metal ions of the precursors in one of the blocks of block copolymer solution. The metal oxide precursor selectively reacts with the P4VP phase. Deposition of thin film of composite solution followed by polymer removal left the the substrate decorated with metal oxide NP's [296].

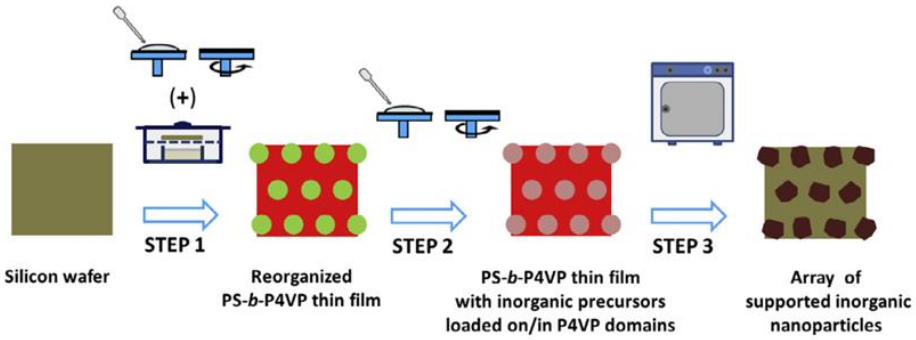

Figure 2.6: Process flow for the fabrication of ordered array of metal oxides NP's [295]

The ordering of the NP's deposited on the substrate can be tuned by varying the precursor concentrating loading to P4VP [297, 298]. Two dimensional array of TiO_2 strings have also been obtained by the micellar solution of block copolymer [299].

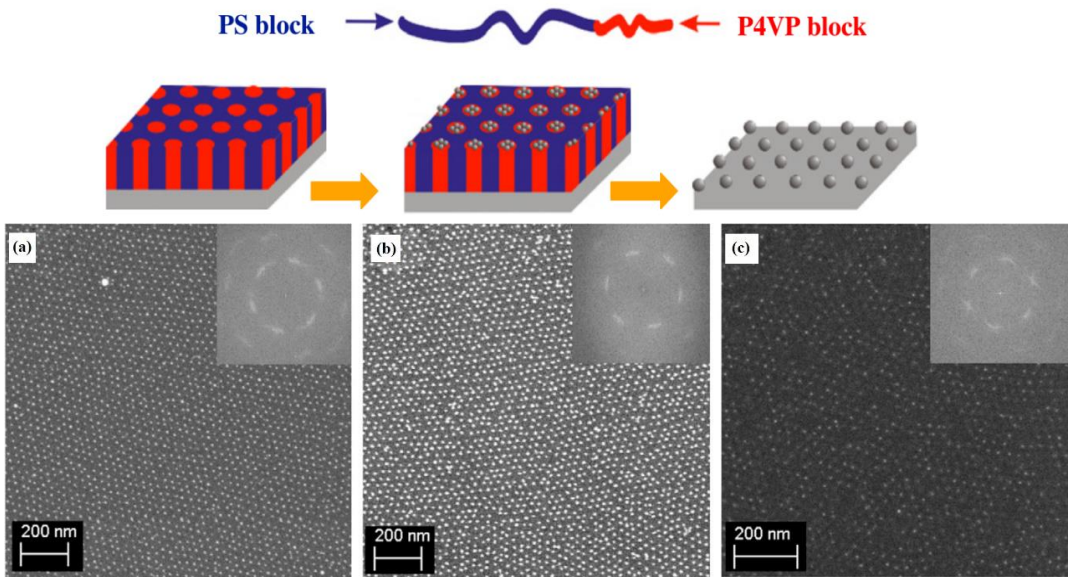

Figure 2.7: Scheme for the fabrication of ordered array of nanodots (top) and SEM images of the ordered array of metal nanodots (a) Au, (b) Pt, and (c) Pd. Inset shows the FFT of the image [16]

Direct deposition of the pre-synthesized NP's into the templates offers the flexibility to tailor the properties of NP's in advance. Moreover, the NP's can be selectively deposited into the pores and the formation of a layer of metal oxides over the template, (case of sol-gel method) can be avoided. This approach is easy as compared to sol-gel method because a number of the reaction parameters need to be optimized for the fabrication of well-ordered nanostructures in sol-gel method.

As the pores are functionalized with pyridine group of P4VP in the nanotemplates, the NP's can be directly deposited or may be functionalized depending on their reactivity with the pores. Stamm's group and the other researchers have published several reports on fabrication of metal NP's array by direct deposition of NP's into the pores [16, 300–304]. The whole process of the fabrication of well-ordered NP's array is depicted in figure 2.8. Magnetic NP's (Fe_3O_4) were also deposited by this approach without any surface modification to the NP's [305]. The deposition of nanomaterials on the substrate is also possible without removing one of the blocks. NP's can selectively bind with one of the blocks. The concentration of the NP's loading to the block copolymer solution governs the fidelity of the NP's deposited with the block copolymer morphology. Barandiaran *et al.* have synthesised the PS-*b*-P4VP/(Fe_2O_3) nanocomposites by using this approach [306]. However, the array of TiO_2 nanostructures by the deposition of pre-synthesized NP's is yet to be explored.

2.5.3 Removal of remaining polymer matrix

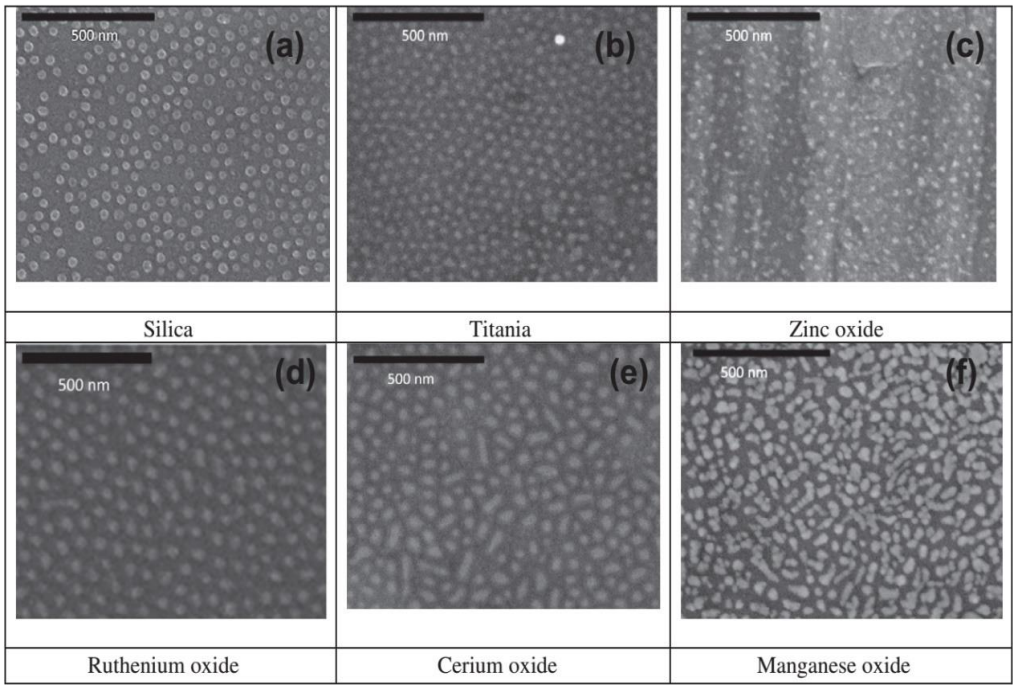

Figure 2.8: SEM images of metal oxide NP's after removel of polymer metrix [295].

Removal of polymer matrix is the last step of the process of the preparation of ordered nanostructures. Different techniques have been adopted to remove polymer matrix depending on the nature of copolymer and the deposited material like RIE, UV irradiation, chemical dissolution, plasma etching (oxygen or oxygen/ozone mixture), and pyrolysis

[13, 16, 301, 307, 308]. Removal of templates leads to the ordered metal oxide NP's (characterized by SEM) shown in figure 2.8. Pyrolysis involves the degradation of polymers at high temperatures. For TiO_2 nanostructures, heating at high temperature leads to the transformation from amorphous to crystalline behaviour (rutile, anatase, and brookite phase) while at high temperature Au NP's undergo the thermal coarsening due to recrystallization. So, the choice of method for removal of polymer matrix depends on the deposited materials and its application.

2.6 Applications of ordered *ZnO* nanostructures

Various ordered *ZnO* nanostructures are essential for variety of applications in nanoscience and nanotechnology over bulk metal-oxides due to presence of many better properties. In the following section, Some recent work on ordered *ZnO* nanostructure-based devices has been reviewed.

2.6.1 Light emitting diodes (LEDs)

Light-emitting diodes (LEDs) are normal p-n junctions that can emit light when supplied with electrical energy. In short, due to the electron hole recombination, a photon is emitted in visible range of electromagnetic spectrum. This phenomenon is called electroluminescence (EL). Direct band gap *ZnO* is good semiconductor which enables their use in LED applications. Compared to the bulk and thin films of *ZnO*, 1-D nanostructures have higher bandgap (3.37eV) and hence enhanced emission efficiency. The growth conditions of the *ZnO* largly affects the light emission, these materials are capable of emitting a wide range of colours [309–314] *ZnO* is capable of operating in high radiation field due to its wide bandgap [315, 316]. Light can escape easily from nanostructured materials, resulting in lesser heat generation. Figure 2.9 shows schematic diagram for the nanorod-array-based LED device, consisting n-*ZnO* nanocone/p-GaN heterostructures. From the I-V curve it is clear that there is no current delay in forward bias which indicates that the contacts are good and ohmic. The EL results shows emission of intense blue lines in the forward bias. Furthermore, there was enhancement of current on radiating UV light of 365 nm on heterostructures hence these structures can also be used as UV sensors [317].

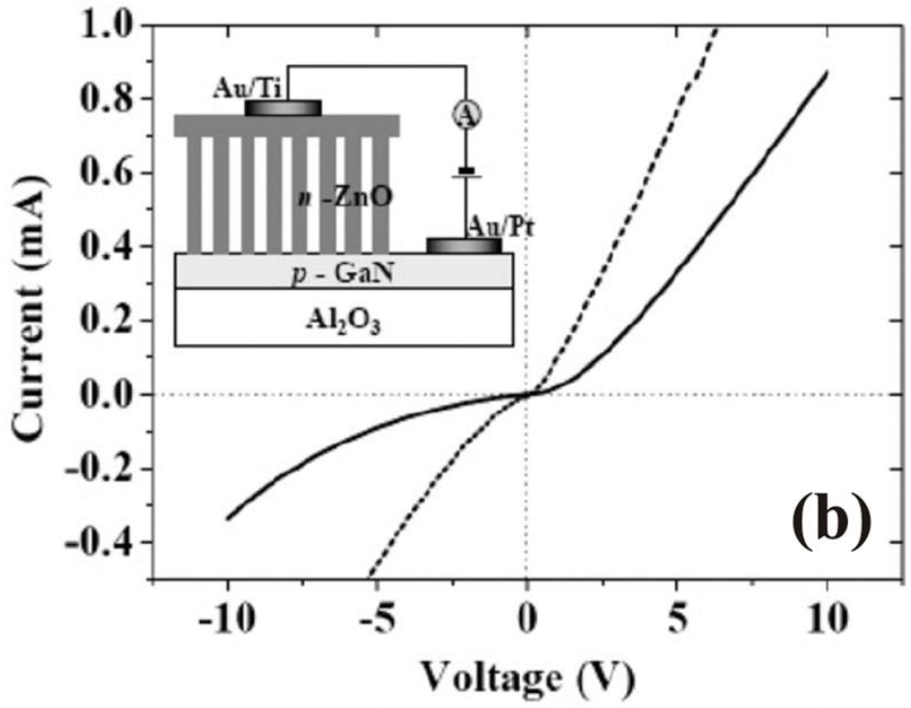

Figure 2.9: The inset shows a schematic of the ordered nanostructure based LED device [317]

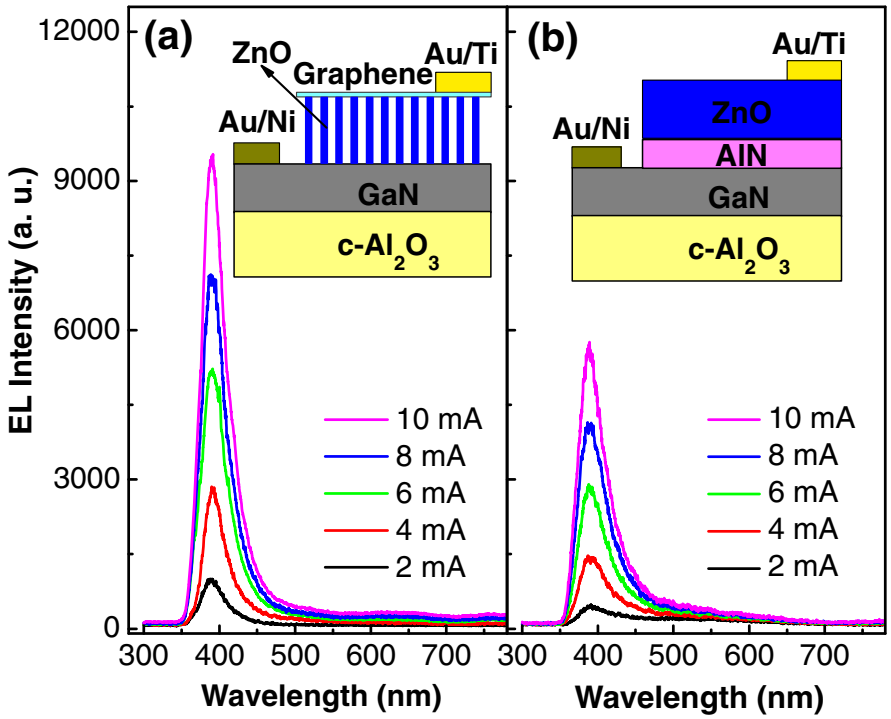

Figure 2.10: EL spectra of ZnO/p-GaN LED (a) and a ZnO film-based LED (b). The insets show the schematic of the respective LEDs [5].

The EL intensity spectra obtained from these arranged *ZnO* nanorode based LED device from 440 to 600 nm. The blue light is emitted from the p-GaN layer, hence the excited electrons originate from ordered *ZnO* nanorods, thus, the electrons from the n-*ZnO* nanorods are injected into the p-GaN layer with forward biasing, while no electrons can be injected into the p-GaN layer at the backward bias. So, the n-*ZnO* nanorods/p-GaN heterostructures are useful for optoelectronic applications [5]. It is demonstrated that highly ordered *ZnO* nanostructures based LED shows much stronger EL emission than *ZnO* thin film based LED. Insets of figure 2.10a and 2.10b shows schematic for LED device using highly oriented *ZnO* nanocone array on the p-GaN substrate and *ZnO* thin film based LED device respectively. The EL spectra for the *ZnO* nanorod/p-GaN LED and *ZnO* thin film based LED are also shown in 2.10a and 2.10b. Both spectra exhibit a unique peak centered at about 388 nm for the current ranging from 2-10 mA, which are attributed to the NBE emission from *ZnO* as shown in other studies [318–320]. It can be seen that the EL emission from the *ZnO* nanocone-based LED is much stronger than that from the *ZnO* film-based device at each injection currents, which can be attributed to the high carrier injection efficiency through the nano-sized junctions, low defect density and excellent waveguiding properties of the highly oriented *ZnO* nanocone array [5].

2.6.2 Gas sensors

A gas sensor is a device which is used to detect gases in the atmosphere. Some of the gases are very harmful to human-beings and animals, so sensing of these gases are critical part of safety measure. Functional materials are being used for absorption of active gases that changes electrical conductivity. Metal oxides are the most suitable material for this mechanism because the oxygen sites on their surfaces may perform gas adsorption. Gas sensors can detect combustible, flammable, toxic gases, and monitor oxygen depletion. High gas sensitivity for H_2 at different temperatures from upto 250°C with a detection limit of 20 ppm was observed for sensors fabricated with ordered *ZnO* nanorod arrays [321]. The smaller 1D *ZnO* nanorods shows higher sensitivity. Furthermore, the results shows the dependency of gas sensitivity on the diameters of the *ZnO* nanowires, as shown in figure 2.11 [6]. It was observed that for heavy isobutane gas, larger *ZnO* nanowire based gas sensors shows higher sensitivity and for light gases the smaller *ZnO* nanowires based sensors shows higher gas sensitivity. Moreover, the *ZnO* nanowire-based gas sensors for detecting H_2, NH_3, isobutene, and CH_4 gases, operate well at room temperature with high gas sensitivity. In fact, external heating systems are required for most of the gas sensors in order to achieve optimum sensitivity.

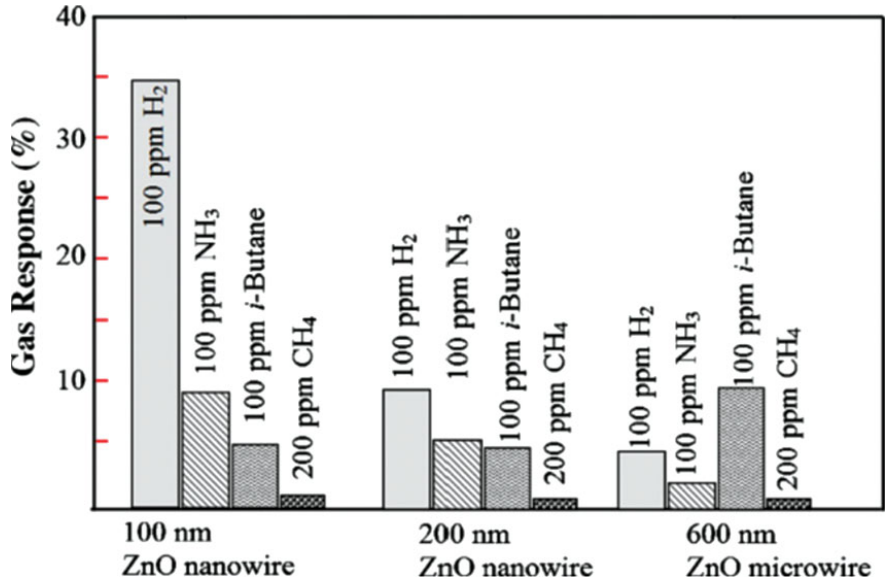

Figure 2.11: Gas response of different dia size *ZnO* nanowire sensors [6].

2.6.3 Field emitters

Emission of electrons into vacuum fro sharp featured samples on application of negative voltages is called a field emission. For this, a strong electric field is required because of tunneling of electrons can easily through the potential barrier between sharp-tip features and electrodes. The sharp-tip features can enhance the field emission properties, as the field emitters. The transition metal-oxides poses good thermal and chemical stability, hence can be used as potential field emitters. Furthe, in commercially produced flat displays of ordered 1-D nanostructures should be excellent for field emitters. A comparative study of ordered *ZnO* nanowires and random array of *ZnO* nanowires with nearly same density shows that the field enhancement factor (β) has higher value for ordered *ZnO* nanowires [322]. The higher value indicates higher field emission efficiency so the ordered array has a better field emission over random array because of screening effect in random array due to some *ZnO* nanowires grow closer together that reduces the field-emitting efficiency. Y. K. Tseng *et al.* grown needle-like *ZnO* nanowires with high density over a Ge doped conductive *ZnO* film which can be subjected to the field emission test at least ten times without change in the results by sweeping electric field from 0 to 30 V μm^{-1} [323]. Some other reports also show the field emission properties of *ZnO* nanostructures [323–327]

2.6.4 Photovoltaics

Solar energy is considered as the major renewable energy source which can eliminate the mankind's dependency on fossil fuels. However, current photovoltaic technology lacks the power to extract full potential of solar energy. Matt Law *et al.* described the construction and performance of dye-sensitized solar cells (DSCs- a low cost photovoltaic device) based on arrays of *ZnO* nanowires coated with thin shells of amorphous Al_2O_3 or anatase TiO_2 by atomic layer deposition. They found titania shells are better than alumina shells. Both acts as insulating barriers that improve cell open-circuit voltage (V_{OC}) but the former causes drastic reduction in short circuit current(J_{SC}). However, titania shells, 10-25 nm in thickness enhances V_{OC} sharply with an increased fill factor(FF) with small current fall off, which results an increased effeciency, up to 2.25% under 100 mW cm^{-2} AM 1.5 simulated sunlight. Further studies prove that the radial surface field in *ZnO*-TiO_2 core-shell reduces the rate of recombination in these devices to get an increased efficiency [328]. Use of efficient anti-reflection coating (ARC) is another method to increase the performance, since it increase the light coupling. Solution grown ordered *ZnO* nanostructures as ARCs for Si solar cells was compared with conventional single layer ARCs. It was found that nanoscale morphology had a great effect on the macroscopic ARC performance. *ZnO* nanorod arrays displays a broadband reflection suppression ranging from 400 to 1200 nm compared with a silicon nitride (SiN) single layer ARC [329]. Efficient charge transport has been demonstrated in DSSCs based on *ZnO* nanowires with 1.5% power conversion efficiency [330]. Ordered *ZnO* nanostructures also have vast application in polymer solar cells. Drastic increase in efficiency can be achieved by optimized treatment of dye and polymer in nanostrucutres. A photovoltaic device fabricated with nanorod structure when treated with dye before deposition of the P3HT polymer yielded four times higher efficiency than similar device based on the NP's [331]. Atomic layer deposition of TiO_2 can result encapsulated *ZnO* nanorods, this structure can significantly increase the V_{OC} and FF [332]. In a nutshell these studies compare the best achieved performance of organic solar cell and their hybrid solar cell counterpart. At present the organic solar cells are found to have higher efficiency. This could be due to the incomplete filling of the pores/gaps in the inorganic part and unfavorable band bending at the interface. Morphology and unfavorable organic/inorganic composite film-phase separation can also be considered as another reason. Surface modification of nanomaterials can be used to optimize these factors. Use of novel organic materials designed for hybrid device can also be a solution to this problem.

2.7 Conclusions

Literature survey about the variety of morphologies of block copolymers and their self-assembly have been discussed. The materials and the methods for the synthesis of block copolymer thin films were also introduced. The research reports published by many researchers revealed that the supramolecular assembly of block copolymer is an efficient approach for the nanopatterning and fabrication of functional nanomaterials. Functional nanomaterials have their own advantages in various applications. It was also revealed that the ordering in thin films of block copolymers can be improved by thermal and solvent annealing. There are several other factors that affect the morphological behaviour and orientation of domains like thickness of film, content of small molecules or additives, type of additives etc... Few applications of ordered ZnO nanostructures (gas sensor, field emitters, LED's and photovoltaics) have also been discussed. For the photovoltaic applications, block copolymers act as either active material or structure directors or both. In the end, it can be concluded that metal oxide nanostructures shows the improvement in the efficiency of solar cells and block copolymers provides the plenty of morphologies that can be used for the fabrication of metal oxide nanomaterials.

3

Materials and Methods

3.1 Introduction

The present thesis deals with the formation of ordered ZnO nanostructures using the block copolymer nanotemplates. Nanostructures have been potentially used in various area of applications like optoelectronics, photovoltaic devices, memory devices, batteries, field emitters and gas sensing [40, 79, 88, 321, 324]. Various routes have been employed to synthesize ZnO nanostructures such as sol-gel, hydrothermal, solvothermal, anodization and templating synthesis. Among them synthesis using block copolymer nanotemplates is a very efficient and easily controlled approach which gives the highly-ordered nanostructures with a tunability of their size and the periodicity. Block copolymer nanotemplates shows very interesting and easily tailored morphologies. Fundamental understanding of materials characteristics is important for it's potential use in optoelectronics. In this chapter, the materials and methods used for synthesis of ZnO, RE doped ZnO and block co-polymer nanotemplates have been discussed in detail. Disk diffusion method for testing of antibacterial properties of ZnO is also discussed. The detailed discussion of characterization techniques that were used for the overall analysis of the research work is also included in this chapter.

3.2 Materials

The following materials were used to carry out this research work.

3.2.1 Polymers and substrates

In order to prepare block copolymer nanotemplates of different morphology poly(styrene)-*b*-poly(4-vinylpyridine) (PS-*b*-P4VP) with the molecular weights of $M_n = 39.9\ kg/mol$, ($M_n^{PS} = 35.5\ kg/mol$, M_n^{P4VP} =4.4 kg/mol, polydispersity index (PDI) = 1.09), M_n =41 kg/mol, (M_n^{PS} =33 kg/mol, M_n^{P4VP} =8 kg/mol, PDI = 1.10) and M_n =205 kg/mol, (M_n^{PS} =130 kg/mol, M_n^{P4VP} =75 kg/mol, PDI = 1.25) were purchased from Polymer Source Inc. Canada. 2-(4-hydroxyphenylazo) benzoic acid (HABA) (> 98%, Sigma-Aldrich) and 1-4 dioxane (Merck) were used as additive and solvent respectively. 1-4 dioxane was used as annealing solvent also. 0.2 μm PVDF syringe filter (Whatmann) was used to filter the block copolymer as well as NP's solution. Si wafer (p-type (100), Macwin India) were used as substrates.

3.2.2 Precursors and solvents

For synthesis of *ZnO* and RE doped *ZnO* NP's via chemical route, Zinc chloride (Rankem ,Purity 98.0%), Zinc nitrate hexa hydrate (Merck, Purity > 96%), zinc acetate dihydrate (Merck, Purity ≥ 98%) were used as zinc precursor and Erbium(III) chloride hexahydrate (Alfa Aesar, Purity 99.9%), Terbium(III) chloride hexahydrate (Aldrich, Purity 99.9%), Europium(III) nitrate penta-hydrate (Aldrich, Purity 99.9%) were used as RE precursor. Potassium hydroxide (Merck, Purity ≥ 84%), Sodium hydroxide (Fisher scientific Purity, 97.0%), Ammonia solution (Rankem, Purity 95.0%) were used as precipitating agent. Polyvinyl pyrrolidone (Lobal chemie), Thioglycerol(Otto, Purity 98%) as a capping agent and Dimethyl sulphoxide (Himedia, Purity 99.5%), Ethanol(Changshu angyuan chemical), Methanol (Rankem, Purity 99.0%), Tea leaf (dry form) and Deionized (DI) Water were used as solvent. All the above chemical were used without further purification.

3.3 Techniques used to prepare the samples

In the present thesis co-precipitation method was used for the synthesis of *ZnO* and RE-doped *ZnO* NP's. Because it is steady, fast, cost effective, high yield and efficient to control the growth of *ZnO* and RE doped *ZnO* NP's by controlling various parameters like temperature, pH, and reaction time. For the preparation of nanotemplates, the thin films of block copolymer were deposited on the substrates by dip coating and spin coating techniques. Lateral ordering in the film was improved by solvent annealing.

3.3.1 Co-precipitation method

In the co-precipitation method, an inorganic metal compound dissolved in solvent is hydrolyzed by using a base solution of NaOH or NH_4OH, these compounds then condense to form a metal oxide precipitate by increasing the concentrations of OH ions. The precipitate obtained is then washed and dried to collect the crystalline metal oxide powder form. This process is advantageous over other processes as it is economical and widely used to synthesize a range of single and multi-oxide nanomaterials. But there is one disadvantage of agglomeration of NP's, which can be solved by using capping agents. These capping agents can neutralize the NP's in the solution and surface electronic states in semiconductor quantum particles. Thus, capping agents play a vital role in controlled growth of NP's and enhance the properties of NP's by capping them. Figure 3.1 shows the schematic for synthesis of ZnO NP's using different precursors and solvents(also the syntesis) and RE doped ZnO NPs(right).

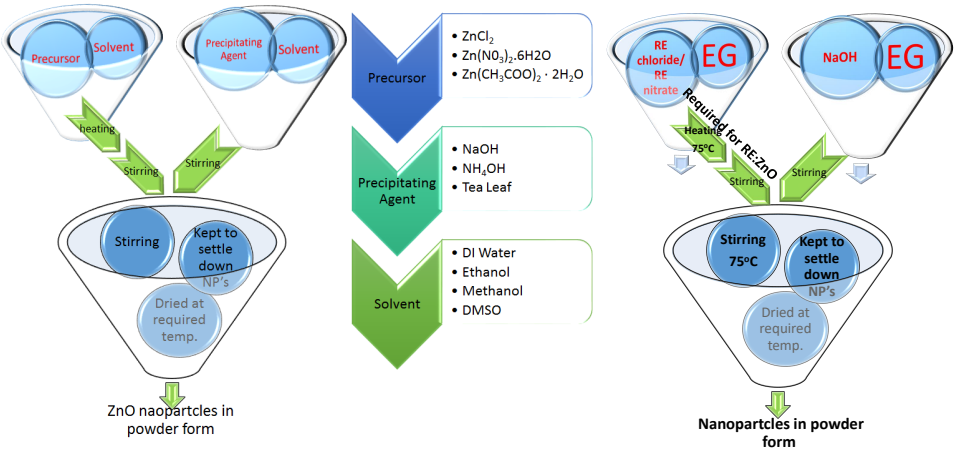

Figure 3.1: Schematic for the synthesis of ZnO (left) NR's using different precurssors and solvents and RE-doped ZnO (right) NP's.

3.3.2 Dip coating

Dip-coating is an affluent and fast method for the thin film deposition from the chemical solution. This method provides the great facility to deposit coating on large area with very good control for various technological applications. The working principle for the dip coating can be described as follows; the substrate is to be immerged in the solution tank with user controlled speed and left it for the particular time and then, it is to be withdrawn from the solution with a particular speed. The immerging and withdrawn speed can easily be controlled. During this dipping process, solution spreads out on the substrate homogeneously due to the basic physical effect of capillary rise

and viscous force. Then evaporation process occurs after coating which is responsible for the solidification of the final film which already grown on the substrate. Different evaporation conditions and withdrawal speed are the key parameters for the film quality as well film thickness. So, one has to take care of them carefully. The process flow for dip coating is shown in figure 3.2

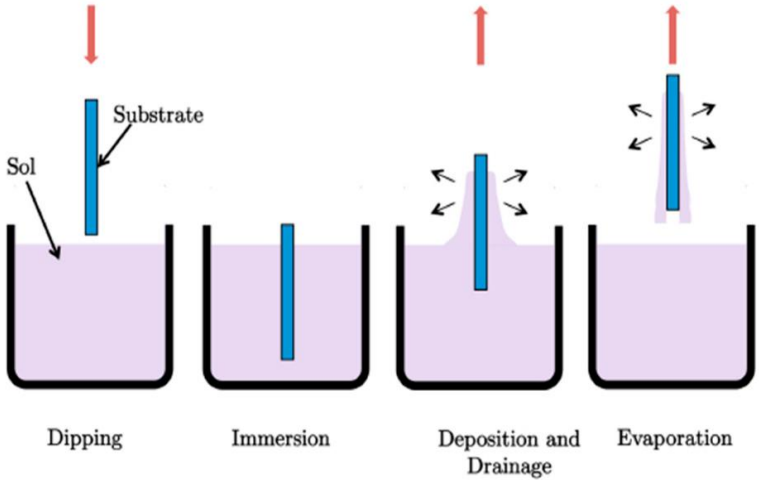

Figure 3.2: Schematic for the dip coating process [333].

The whole deposition process may be divided in the following three major steps:

(a) Immersion of the substrate into the solution tank.

(b) Dwell time for the film deposition.

(c) Withdrawal of the substrate from the solution tank.

We have used programmable dip coating system (XDIP-SV1, Apex) in this study with a withdrawn speed of 100 mm/min.

3.3.3 Solvent annealing

Thermal annealing and solvent annealing are the common process to improve the ordering in thin films of block copolymer. Solvent annealing is considered more advantageous and better than the thermal annealing because in thermal annealing small molecules in the supramolecular assembly may evaporate. Evaporation of small number of molecules may affect the morphology of thin films of block copolymer to a great extent. Solvent annealing is the process in which each copolymer interacts with the vapour of the solvent (selective/non-selective). Ordering in the thin films depends on the affinity of copolymers towards solvent molecules, rate of evaporation of solvent, volume of solvent and

container, and time of annealing. Depending on their affinity for the annealing solvent, the copolymers swell with different rate. Thin films were put in a tightly sealed glass chamber along with the annealing solvent in a bottle with some pinhole shown in figure 3.3. The thin films were removed from the annealing chamber after a particular time and solvents were allowed to evaporate.

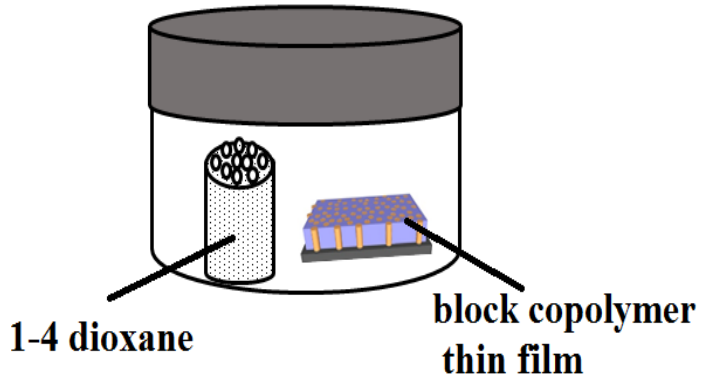

Figure 3.3: Schematic for the solvent annealing of block copolymer thin film

.

3.4 Characterization techniques

Many characterization methods were used to analyze the synthesized NP's and block copolymer thin films. Structural analysis were done by X-ray diffraction (XRD), transmission electron microscopy (TEM) and scanning electron microscopy (SEM). Energy dispersive X-ray (EDAX) was used for elemental composition of the RE doped ZnO NP's. The optical properties of pure and RE doped ZnO NP's were analyzed by UV-Vis spectroscopy and Photoluminescence spectroscopy. Whereas, atomic force microscopy (AFM) was used to determine surface morphology of prepared block copolymer thin films. The used methods are discussed as follows.

3.4.1 X-Ray diffraction (XRD)

X-ray diffraction is the fundamental tool for determining the structure of the material and widely used for material characterization. When a monochromatic X-ray beam incidents on the material at an angle θ, it gets scattered from the sample. The scattered beam is detected by the detector and give the crystallographic information about the lattice structure. The wavelength of the beam is nearly comparable to the atomic size which leads to collect the information about atomic arrangement of the material. If

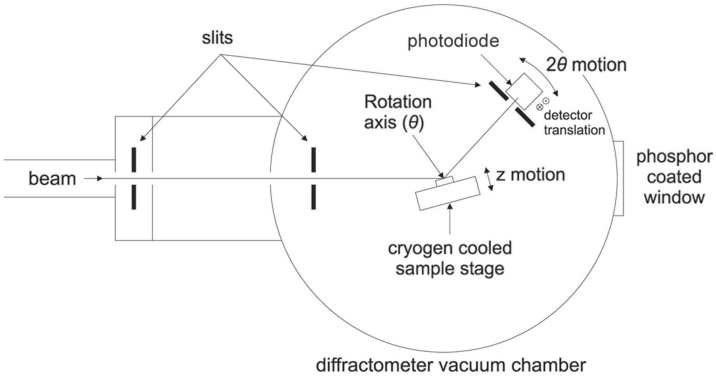

Figure 3.4: Schematic diagram of X-ray diffractometer

the arrangement of the atoms in the material is in regular manner, then diffracted beam interfere constructively or destructively with each other depending on the path difference. A well-known formula Bragg-relation [334, 335] holds for the condition of constructive interference as in following manner:

$$2dsin\theta = n\lambda \tag{3.1}$$

Where, n = order of reflection, λ = wavelength of incident X-rays, d = interatomic spacing between lattice plane and θ = diffraction angle. The average crystallite size of the nanoparticles can be calculated by the following equation known as Debye-Scherrer's formula [335]

$$D = \frac{0.9\lambda}{\beta cos\theta} \tag{3.2}$$

Where, λ = wavelength of X-rays, β = full width at half maxima (FWHM) of diffracted peak, θ = diffraction angle. Furthermore the lattice parameter were calculated with unit cell refinement technique. The crystallographic information related to pure and RE doped ZnO was collected with the help of X-ray Diffractometry (XRD; PaNalytical X'Pert Pro, Cu k_α radiation, wavelength $\lambda = 1.54$Å). The XRD data for pure and RE doped ZnO was recorded in the 2θ range from 20° to 90°; scan step size 0.02° with a scanning step rate of $0.5s$ (in some case it was varied). The schematic diagram of X-ray diffractometer is shown in figure 3.4.

3.4.2 Scanning electron microscopy (SEM)

Electron microscope are very advantageous microscopy tool due to high magnification and resolving power in comparison of light microscope. The highly energetic focused electron beam interacts with sample surface instead of light to get the image and structural information of the sample. The whole system of the imaging must be vacuum

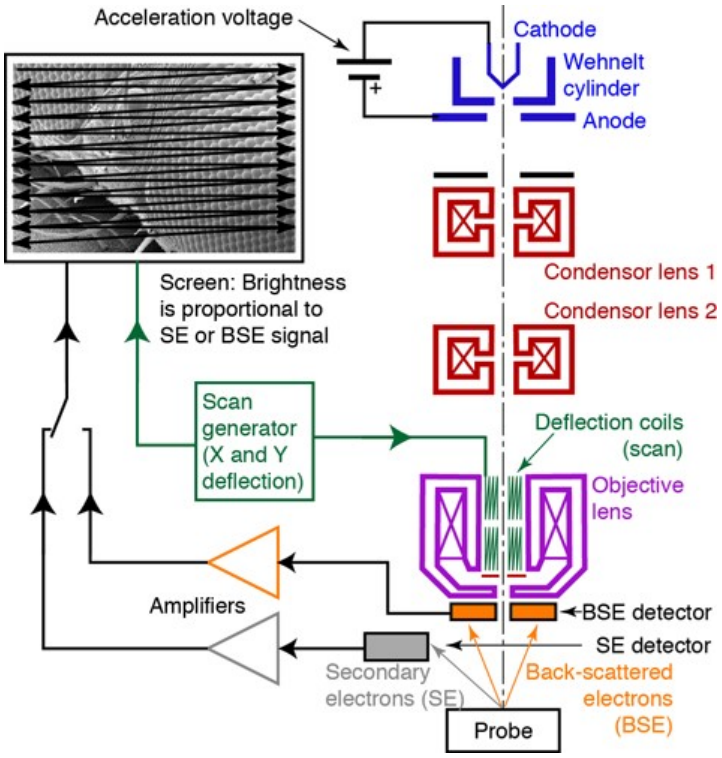

Figure 3.5: Schematic diagram of SEM

shielded for the prevention of the scattering of the electrons during experiment. The wavelength of the beam can be easily controlled with the operating voltage which leads to acceleration of the electrons toward the sample. SEM gives following information regarding the specimen. (i) Topography (ii) Morphology (iii) Compositions and (iv) Crystallographic information [336]. The schematic diagram of SEM is shown in figure 3.5. At the top of instrument, there is source of electron beam which produces a very fine scale monochromatic electron beam (diameter $\sim$ 0.01 mm) in the range of 2-40 kV. The first condenser lens is used for controlling the beam. To eliminate the high-angle electrons from the beam, condenser lens works in conjunction with condenser aperture. The second condenser lens utilized to form the very thin, tight and coherent beam and is controlled by the "fine probe current knob". A set of scan coils used for the scan or sweep the electron beam during imaging in a grid fashion. The various components are placed in the system to observe the interaction of electron beam with specimen and displayed pixel on a CRT monitor. The electron beam interacts with specimen in various ways with the surface of the sample. On the basic of these interactions the mainly two types of the signal are considered for the imaging in SEM and operated in following two modes; (a) Secondary electron mode (b) Backscattered mode. Secondary electron mode is the most common mode for the high-resolution imaging with detailed

information about the surface. In this thesis, Tb doped ZnO NP's were characterized by SEM (Model: Nova Nano FE-SEM 450 FEI) with an accelerating voltage of 15 kV. To take high quality SEM images, all the samples were made conductive by applying a thin coating of platinum/gold using sputter coater.

3.4.3 Transmission electron microscopy (TEM)

To know the internal structural information of *ZnO* NP's and RE doped *ZnO* NP's, TEM is very important technique.

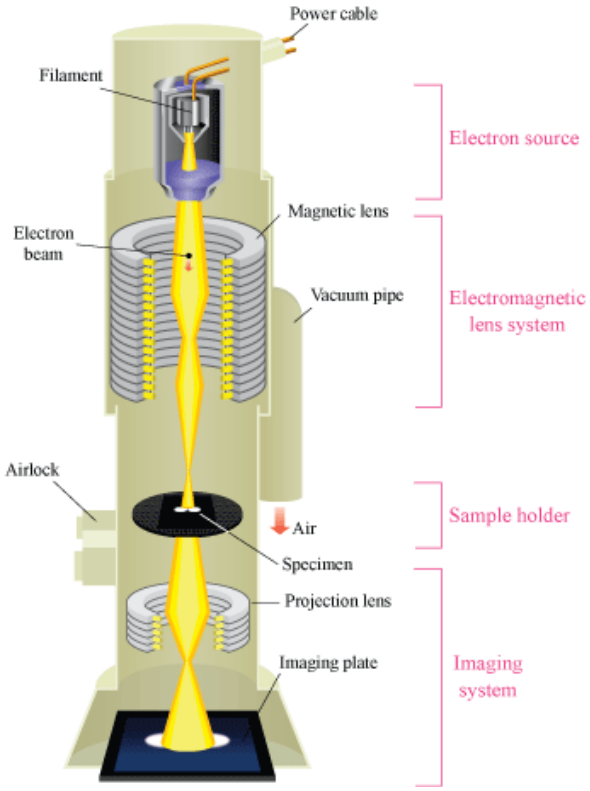

Figure 3.6: Schematic diagram of TEM

In this technique, electron beam is generated by electron gun was collimated by different magnetic lens. These were accelerated by high potential anode with potential ∼100-400 kV. After transmitted through the sample, beam made to fall on charge-coupled device (CCD) sensor which response to form a very high-resolution image of the sample. The image is detected by the CCD and displayed in real time on computer screen [337]. In general, TEM is working with two imaging mode: (a) Bright-field image mode and (b) Dark-field image mode. In dark field image mode, direct beam is blocked by the aperture and pass one or more diffracted beam. Here we used most commonly used

bright-field mode which is commonly used for microstructural analysis while The lattice planes and interplanar distances can be easily observed with the help of selected area diffraction pattern (SEAD) mode [338]. The wavelength of incident electron beam can easily be controlled by accelerating voltage. The schematic of TEM is shown in figure 3.6.

$$\lambda = \frac{h}{p} = \frac{12.25 \times 10^{-10}}{\sqrt{V}} \tag{3.3}$$

The morphology of ZnO and RE doped ZnO were investigated by TEM and high-resolution TEM (HRTEM) [Model: FEI: TECNAI G2 operated at 200 kV]. For sample preparation, small amount of pure and RE doped ZnO was dispersed in isopropyl alcohol, a few drops of this dispersed sample were dropped on a carbon coated grid with 300 mesh. SAED pattern and HRTEM was used to investigate the characteristic features of the NP's.

3.4.4 Ultra violet-visible diffuse reflectance spectroscopy (UV-vis. DRS)

When the light of wavelength 200-800Åfalls on the sample then atom or molecules of the material absorbed the energy from incident light and goes to excited state from ground state. UV-visible spectroscopy is greatly used for quantitative analysis of the materials and using for determine of the band gap of the material.

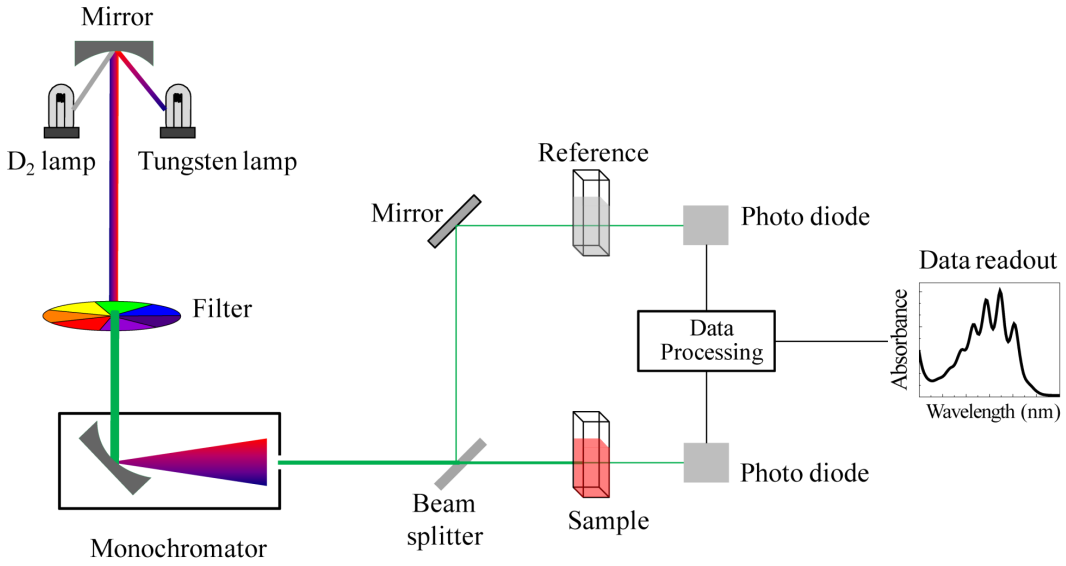

Figure 3.7: Schematic diagram of UV-Visible.

The principle of absorption spectroscopy is based on Beer's and Lambert law [339]; it states that fraction of incident radiation absorbed is proportional to the number of absorbing molecules in its path which is described in as follows:

$$A = -log_{10}\frac{I}{I_o} = \varepsilon.b.c \tag{3.4}$$

Where, ε = wavelength dependent absorptive coefficient, b = path length, I = intensity of incident light, I_o = intensity of transmitted light and c = concentration. Figure 3.7 shows the ray diagram of duel beam UV-vis spectrometer. The diffuse reflectance spectra of pure and RE doped ZnO pallets were recorded using UV-vis spectroscopy (Model: C60, Agilent Technologies, 300-900 nm). The absorbance has been calculated using the Kubelka-Munk equation

$$\frac{K}{S} = \frac{(100-R)^2}{2R} \equiv F(R) \tag{3.5}$$

Where $F(R)$ is the remission or Kubelka-Munk function. The K-M absorption coefficient K then becomes equal to $2\alpha(K = 2\alpha)$ when the sample scatters in a perfectly diffuse manner. Furthermore, In the parabolic band structure, the band gap E_g, and coefficient α of a direct band gap semiconductor are related through the following equation [340]

$$\alpha h\nu = B(h\nu - E_g)^{1/2} \tag{3.6}$$

where α is the linear absorption coefficient of the material, $h\nu$ is the photon energy and B is a proportionality constant. In this case, considering the K-M scattering coefficient S as constant with respect to wavelength, and using the remission function in Eq. (3.6) we obtain the expression:

$$[F(R)h\nu]^2 = B(h\nu - E_g) \tag{3.7}$$

The photons of UV-vis light have sufficient energy to excite the electrons of the sample to higher energy states. Therefore, it can be used to probe the electronic and optical properties of the materials. Usually, it is used for semiconductors and metallic NP's. In semiconductors we use it to measure their bandgap and obtain information about their optical properties. Figure 3.7 illustrates the various components of the dual beam UV-vis spectrometer. The incident beam from the source lamp is passed through the monochromator that splits the beam into two parts using a half mirror. One beam passes through the sample and the other through the reference. The intensities of these light beams are then measured and compared by electronic detectors. The intensity of the reference beam, which should have suffered a little or no light absorption, is defined as Io. The intensity of the sample beam is defined as I. Over a short period of time, the spectrometer automatically scans all the component wavelengths. The region normally

scanned for UV is 200 to 400 nm, whereas the visible region is from 400 to 800 nm. The deuterium lamp is used as a source of UV light, whereas tungsten lamp is taken into account for the visible light. Spectra are obtained by scanning the wavelengths for quantitative measurements.

3.4.5 Atomic force microscopy (AFM)

AFM has been widely used for the fundamental research, material science, medical science and technology applications. It is suitable characterization tool to investigate the various technological materials including membranes, thin films of polymers and semiconductors etc... [341]. In the AFM, sharp metallic tip interacts with the surface of the material and produce the Vander-Waals force between tip and surface of the sample. This Vander-Waals force could be generated due to short-range repulsive force (in contact mode) or longer-range attractive force (in non-contact mode). In the contact mode (repulsive force), the instrument slightly connects with a tip at the end of cantilever which scan over the sample surface during imaging. During the raster-scan, metallic tip goes along the surface of the material and found the vertical deflection of the cantilever.

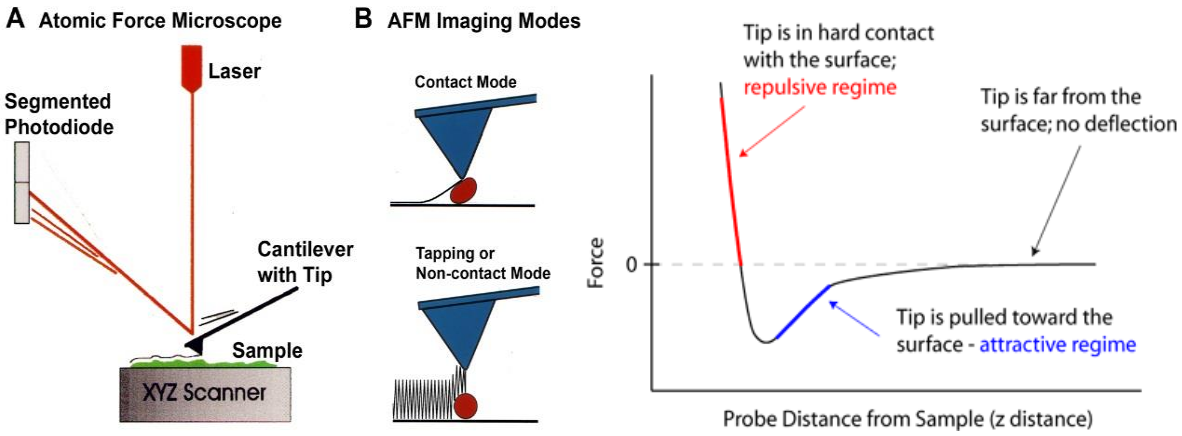

Figure 3.8: Schematic for working of AFM (left), and Vander walls force variation with the distance between tip and sample.

These deflections indicate the undulation in the surface of the film. In non-contact mode (attractive force), the metallic tip does not touch the sample surface and gives the topographic images of the material due to attractive forces. In the tapping mode, the cantilever is driven to oscillate up and down close to the resonance frequency due to presence of piezoelectric material which is mounted on the scanner. This mode is very much effective for the scanning of the soft material like polymer and membranes due to its non-destructive nature in comparison of contact mode. Surface damage possibilities

are reduced in this mode because tip does not drag across the sample during scanning [342]. Figure 3.8 shows the schematic diagram for the working of the AFM and the force variation with distance between tip and sample. When the cantilever bends due to the surface of the sample, the path of laser beam also deflected which leads to deviation at different angle and these variations perceived by the photodiode. The force between the tip and sample is responsible for the fluctuations in cantilever.

$$F = ks \tag{3.8}$$

Where, k = spring constant and s = bending distance for the cantilever during imaging [341]. The cantilever of the AFM is made up of silicon nitride or silicon material with a very sharp tip (width of few $\sim$10 nm) which provide the facility to observe very high-resolution image on nanometer scale. In the present study, the thin films were characterized by AFM (Bruker) in tapping mode.

3.4.6 Photo-luminescence (PL)

PL is a widely used technique for characterization of the optical and electronic properties of semiconductors and molecules. In this technique, light is fall on the material, atoms get excited by absorbing photons from incident light, the spontaneous emission of light by de excitation of atoms is known as PL.

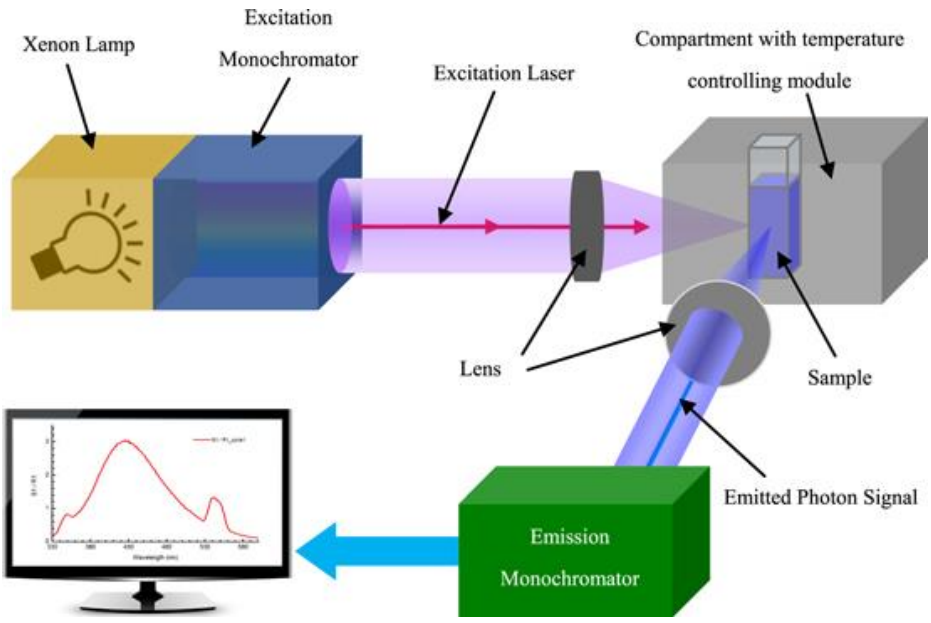

Figure 3.9: Schematic for working of photoluminescence

Lasers with different wavelength have used for PL. For this thesis work, in order to investigate luminescence properties and possible defect present in pure and RE doped

ZnO NP's room temperature photoluminescence spectra were recorded by LABHR-UV-EVO using He-Cd laser with 30 mW power at excitation wavelength (lexc) 325 nm. Figure 3.9 represents the Schematic for working of PL.

3.4.7 *Bacillus subtilis* growth assay

Bacillus subtilis strain was obtained from MTCC, Chandigarh. The bacteria was revived on Nutrient Broth. For growth assays bacterial culture was grown on nutrient agar medium overnight at 37°C.

3.4.8 Disc diffusion method

ZnO NP's solutions of 2mg/ml, 5mg/ml, and 10mg/ml concentrations were made in micro centrifuge tubes and UV sterilized Whattman paper discs were added to them. The solutions were kept overnight and sonicated for 30 minutes before using. Autoclaved agar plates were taken and marked with 4 quadrants. 250ml of test culture was spread over agar plate. Then a disc from each concentration of NP's was kept over their respective quadrant and in the 40°C quadrant, control was kept i.e. the disc of autoclaved water. After this, the plates were kept in incubator at 37°C overnight. Zone of inhibition was observed and measured in mm. The test suspension cultures with and without (control) NP's were prepared as earlier. Cells were pelleted down by centrifugation at 10,000 rpm for 5 min at 40°C, cells were washed twice and re-suspended in PBS and stored at 40°C for further use. For staining assay, the 1:100 dilution of overnight cell suspension was incubated with 20 ml PI at 37°C for 1h and later with 40 ml FITC (10 mg/ml FITC stock solution) at 37°C for 1 hour with endover-end rotation in dark accompanied with intermediate washing and resuspension in PBS. After double staining, the stained cells were washed, resuspended in PBS and 1:100 dilution of final cell suspension was spread on a standard glass slide, air-dried and visualized under fluorescence microscope (Leica DM1000, Leica Microsystems).

3.4.9 Biofilm growth and *ZnO* treatment

An overnight culture of the *Bacillus subtilis* strain was grown and diluted to 1:100 into fresh medium for biofilm assays. The coverslips were washed, rinsed with sterile distilled water, air-dried and then UV sterilized for 30 mins. The coverslips were placed in the tubes with media and autoclaved. For each set of tubes there was one blank (no inoculation, no nanoparticle), control (only bacterial inoculation), 2 test samples (each with inoculation and 0.5 mg/ml and 1 mg/ml *ZnO* NP's). Tubes were incubated for 24

hrs at 37°C. At the end of incubation period, coverslips were aseptically removed from the broth culture for biofilm visualization by phase contrast microscope and scanning electron microscope and quantification by crystal violet binding assay. The experiment was repeated in triplicate.

3.4.10 Crystal violet (CV) assay

The assay was performed according to the method described by O'Toole [] [37]. After incubation, the cover slips with adhered film (control and treated) were washed with distilled water. The process was repeated twice to remove unattached cells and media components which may otherwise cause background staining. The coverslips were submerged in a 0.1% solution of crystal violet and incubated at room temperature for 10-15 mins. The coverslips were dried overnight. For qualitative assays, the dried coverslips were photographed when dried. In order to quantify the biofilm formed, coverslips were placed in 2.5 ml of 30% acetic acid in water and incubated at room temperature for 10-15 mins to solubilize the CV. The solubilized CV was transferred to clean eppendorf tubes and later quantified by measuring absorbance spectrophotometrically at 550 nm using 30% acetic acid in water as the blank. By analysing the absorbance values, biofilm biomass can be estimated. The reduction in biofilm biomass was calculated by:

$$\%reduction = \frac{Abs.(control) - Abs(sample)}{Abs.(control)} \times 100 \tag{3.9}$$

Where Abs. = Absorbance at 550 nm

3.4.11 Scanning electron micrograph for bacterial biofilm

The test suspension cultures with and without (control) NP's were inoculated with fresh culture and incubated at 37°C, ∼100 rpm for 12 hrs. The sample preparation for SEM analysis was done as follows. Sterilized coverslips were dipped in 1% agar solution and left horizontally allowing a thin agar film to materialize. Diluted cell suspensions were spread on coverslips and then incubated overnight at 37°C. The fixed samples were dehydrated in ascending alcoholic series (10, 30, 50, 75, 90 and absolute 99.99%) for ∼ 30 minutes each. The sample was dried at 37°C for about 2 hrs and coated with a thin gold film before observing under SEM (Zeiss).

4

Synthesis and Characterization of *ZnO* NP's

4.1 Introduction

Semiconductors with dimension in nanometer scale have gained remarkable interest because of their optical electrical and chemical properties desirable for various applications [343]. Optical properties of these materials are specifically being investigated for their use in optoelectronics, photovoltaic and sensing [344]. *ZnO* is a direct band gap (3.37 eV) and large exciton binding energy (60 meV) semiconductor [345]. Moreover, it's relatively higher thermal and mechanical stability makes it ideal candidate for device applications [346–349]. Further, due to more resestance to UV rays, high electrical conductivity and strong ferromagnetic properties it is more useful then conventional materials like phosphorus and sulfur [350]. The size of the NP's, temperature and defects in crystalline structure affects the photo luminescent properties of *ZnO* NP's. Because of photo luminescent property it is used in field emission display devices such as LCD's, LED's and OLED's [122]. The *ZnO* nanorod provids short response and recovery time for NO_2 gas as a highly sensitive gas sensor [351]. *ZnO* nanostructures have large surface area, low toxicity and long life-span [352] and being use as promising material for antibacterial [353], chemical absorbents [354], polymer additives [355] and photocatalytic [356, 357]. Interestingly *ZnO* NP's have tunable optical and electrical properties due to large band gap [358] suitable wide range of applications like UV detectors [359, 360], solar cells [361], light emitting diode [362, 363], gas sensing materials [364] in addition, *ZnO* is also suitable for generating UV light [365] and Bio sensing [366]. In the last few decades researchers have reported various methods for synthesizing of *ZnO* NP's which are dis-

cussed in section 1.3.3. From these methods, chance of impurity in ball milling method is more while others are either more expensive or required complex equipment so it is required to search for a simple route with less equipment required yet giving high yield. There are several reports on size and morphology dependent green luminescence intensity of *ZnO* NP's but in their synthesis method size variation or morphology variation occurs by varying only particular parameters like solvent, solvent concentration, temperature etc... In our modified synthesis methods we take arbitrary solvent, precursor and temperature.

In the present chapter, we are reporting synthesis of *ZnO* NP's using different precursors and solvents via chemical route. The possible energy levels and defects have been investigated in detail from the optical characterization of *ZnO* NP's. In addition, the detailed structural investigation of different sized *ZnO* NP's has been also done.

4.2 Experimental details

4.2.1 *ZnO* by $ZnCl_2$ in water medium

1.1g of $ZnCl_2$ was dissolved in 20 mL DI water under constant stirring at 90°C (solution A). Another solution was prepared by dissolving 4g NaOH in 20 mL DI water (solution B). 4 mL of solution B was drop wise added in solution A and resultant milky white solution without any precipitation was left for 2 hours of stirring. This solution was then kept for sufficient time to settle down the NP's. The supernatant was removed, washed 5 times with DI water and dried at 100°C for 30 minutes. *ZnO* NP's obtained in white powder form [367].

4.2.2 *ZnO* by $ZnCl_2$ in methanol medium

1.090g of $ZnCl_2$ was dissolved in 20 mL methanol and 0.96g of NaOH was dissolved in 30 mL methanol both solution were kept under constant stirring for 40 minutes. NaOH solution was added drop wise in zinc chloride solution for 20 minutes and stirred for 2 hours then kept in dark chamber overnight. The obtained precipitate was centrifuged for 5 minutes then washed 5 times with DI water and annealed in air atmosphere at 300°C. The white powder of *ZnO* NP's was obtained [368].

4.2.3 *ZnO* by $ZnCl_2$ in ethanol medium

ZnO NP's were synthesized by the same procedure as discussed in section 3.2 but using ethanol in place of methanol medium. All the experimental parameters and condition was the same. The *ZnO* NP's was obtained in light brown color powder form [368].

4.2.4 *ZnO* by $Zn(NO_3)_2.6H_2O$ in water medium

Wet chemical method was used to synthesize of *ZnO* NP's by dissolving 2.9747g of $Zn(NO_3)_2.6H_2O$ in 100 mL DI water (solution A) and 0.8924g of polyvinyl pyrrolidone in 50 mL DI water (solution B). Both solution were stirred for 30 minutes at 60°C then NH_4OH was added drop wise in solution A till the pH reached to 7.5 (solution C) and kept stirring for 15 minutes. Solution B was added in solution C and resultant solution was kept at 60°C for 1 hour. The mixture was then cooled at room temperature and kept overnight in dark chamber. The precipitate was filtered with 0.2 μm filter and washed 2-3 times with DI water and dried at 60°C for 12 hours [63].

4.2.5 *ZnO* by green synthesis method

0.2M of zinc acetate dehydrate was dissolved in 70 mL of distilled water and stirred for 30-40 minutes. Another solution of 5g dried green tea leaf powder in 100 mL of distilled water was prepared with stirring for 2 hours at 80°C then cooled to room temperature and filtered through whatman filter paper. 30 mL of this green tea extract was mixed homogeneously with the zinc acetate solution. The solution was filtered and dried at room temperature. The obtained powder was annealed at 300°C for 1hour [369].

4.2.6 *ZnO* by Zinc acetate in DMSO medium

Zinc acetate (0.4M), potassium hydroxide (2.4M) were separately stirred in 40 mL dimethyl sulfoxide and 20 mL ethanol. Potassium hydroxide solution was added drop wise in zinc acetate solution. Thioglycerol (0.25 mL) was added to the above solution which turned milky. White filtrate was washed three times with methanol and DI water followed by drying at room temperature [370].

4.3 Results and discussion

The *ZnO* NP's are synthesized by modified methods and the characterization of the NP's are done by XRD, TEM, UV-Vis and PL. The discussion of obtained results are

as follows.

4.3.1 X-ray Diffraction (XRD)

The XRD patterns of *ZnO* NP's prepared by methods 4.2.1 to 4.2.6 are shown in figure 4.1. These XRD patterns of NP's show single phase crystalline nature corresponding to wurtzite hexagonal crystal structure. Morphological studies by TEM (figure 4.2 and 4.3) confirms single phase. Spurious low intensity peaks in range 20-35 degree in XRD (figure 4.1, Method 4.2.2) are observed which can be attributed to the multi phase product or the impurity in the sample. However, the occurrence of multiphase induces the change in the morphology of NP's [371, 372] which is not observed in our case (figure 4.2d). So, the extra peaks can be assigned to the impurity in the sample. *ZnO* NP's synthesized by method 4.2.1-4.2.6 have all characteristic peaks of *ZnO*. It can be concluded from characteristics peaks that *ZnO* have hexagonal crystal structure and matches to the space group P63mc. The relative intensity of XRD peaks corresponding to a particular plane depends on the morphology [373] but the TEM images confirms that the morphology of all *ZnO* samples are similar which indicates the variation in intensity is not due to the morphology but it may be due to the agglomeration.

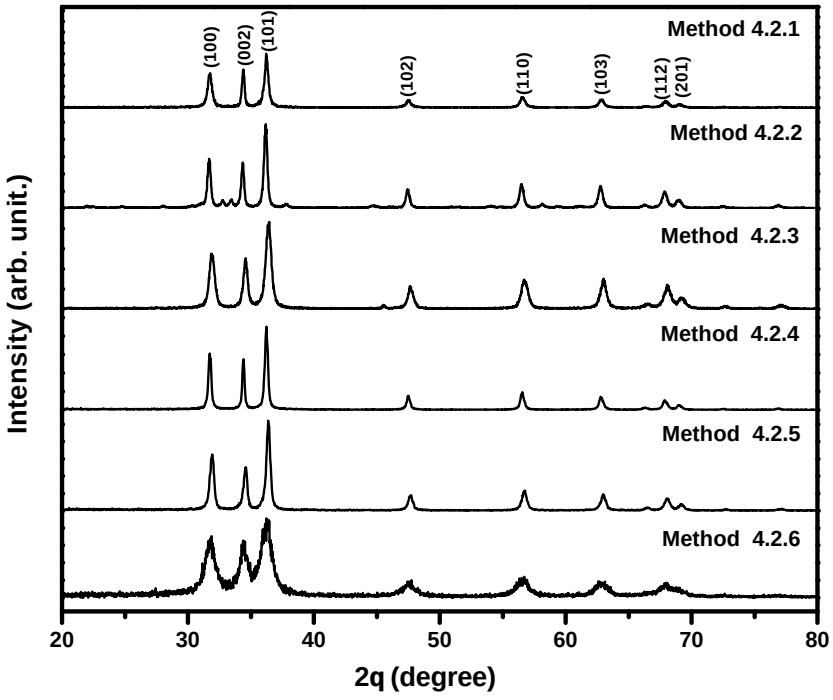

Figure 4.1: XRD spectra of all *ZnO* NP's.

In method 4.2.6 the capping agent DMSO was used to control agglomeration and the particle size was reduced indicated by the broadening of peaks. The lower intensity of

Table 4.1: Lattice parameters for all the samples and corresponding JCPDS card numbers

Method	Precursor	Solvent	Lattice parameter	JCPDS card No.
4.2.1	Zinc chloride	DI water	$a = b = 3.2490$Å, $c = 5.2060$Å	01-079-0206
4.2.2	Zinc chloride	Methanol	$a = b = 3.2170$Å, $c = 5.2130$Å	01-076-0704
4.2.3	Zinc chloride	Ethanol	$a = b = 3.2427$Å, $c = 5.1948$Å	01-075-0576
4.2.4	Zinc nitrate	DI water	$a = b = 3.2501$Å, $c = 5.2070$Å	01-079-2205
4.2.5	zinc acetate	DI water	$a = b = 3.2427$Å, $c = 5.1948$Å	01-079-0576
4.2.6	zinc acetate	DMSO	$a = b = 3.2417$Å, $c = 5.1876$Å	01-079-0205

peaks suggests the decreased crystalline quality of NP's using capping agent. The average crystalline size of these NP's was determined by equation 3.2 for each orientations The broadening of peaks indicates that synthesized NP's are in nanometer range. The calculated average crystalline size found from method 4.2.1 was 21 nm which is similar to previous result [367], from method 4.2.2 it was 26 nm which is higher then previous result (∼5.36 nm) and reduced to ∼16 nm when methanol was replaced by ethanol (method 4.2.3), from method 4.2.4 the average crystalline size was ∼17 nm which is nearly half from previous result [63], from method 4.2.5 it was 9 nm which is smaller then previous result [369] and from 4.2.6 it was found to be ∼7nm . The lattice parameters of *ZnO* NP's are as shown in table 4.1. It is clearly observed from figure 4.1 that broadening of peaks in method 4.2.6 is more as compared to other methods indicating that the particles synthesized by method 4.2.6 have smaller particle size. It is also clear that the average crystalline size of *ZnO* NP's synthesized using zinc acetate is smaller then zinc chloride precursor and it found smallest from above methods when ethylene glycol was used as capping agent (method 4.2.6).

4.3.2 Transmission Electron Microscopy (TEM)

figure 4.2(a), 4.2(d) and 4.3g show the TEM images of *ZnO* NP's synthesized using $ZnCl_2$ precursor with water, methanol and ethanol respectively (method 4.2.1-4.2.3). It can be observed that particles have almost spherical shape in ethanol (method 4.2.3) and methanol medium (method 4.2.2) (figure 4.3(g) and 4.2(d) and the selected area diffraction pattern (SADP) (figure 4.2b, 4.2(e) and 4.3 (h)) shows polycrystalline nature of NP's which is in good agreement with XRD results. Average particle size of *ZnO* in ethenol (4.2.3) was found to be 14 ± 2 nm which also agrees with XRD spectra. When ethanol was replaced by methanol keeping the same procedure, average size of particles

was increased to 18 ± 2 nm while the shape and size distribution was similar. In case of water solvent (4.2.1), well dispersed rod like structure was observed with average diameter of 18 ± 2 nm. figure 4.3(j) shows the TEM image of *ZnO* NP's prepared by zinc nitrate in DI water the NP's are almost spherical in shape with average size 16 ± 2 nm which is almost twice of the previous result [63]. The TEM image and selected area diffraction pattern of *ZnO* NP's prepared by 4.2.5 and 4.2.6 are shown in figure 4.3(p) & 4.3(q) and 4.3(m) & 4.3(n) respectively. Selected area diffraction pattern of both these samples show shows polycrystalline nature of NP's which also agrees with XRD result (figure 4.1(e), 4.1(f)). TEM images show that the shape of nanoparticle are almost spherical with small agglomeration. The particle size has been found to be 5 ± 2 nm and 13 ± 2 nm respectively which also agrees with XRD results. It is clear from the TEM study that the average diameter of *ZnO* NP's are almost same if we use zinc chloride as a precursor (method 4.2.1-4.2.3). It is also clear that average diameter of NP's are smaller if we use precursor zinc nitrate and zinc acetate as compare to zinc chloride. The average diameter of *ZnO* NP's found to be smallest among above methods when capping agent ethylene glycol was used (method 4.2.6). Figure 4.2 (c, f) and figure 4.3(i, l, o, r) shows the HRTEM images of *ZnO* NP's synthesized using method 4.2.1 to method 4.2.6 respectively. The calculated d spacing for specific plane are good agreements with XRD data.

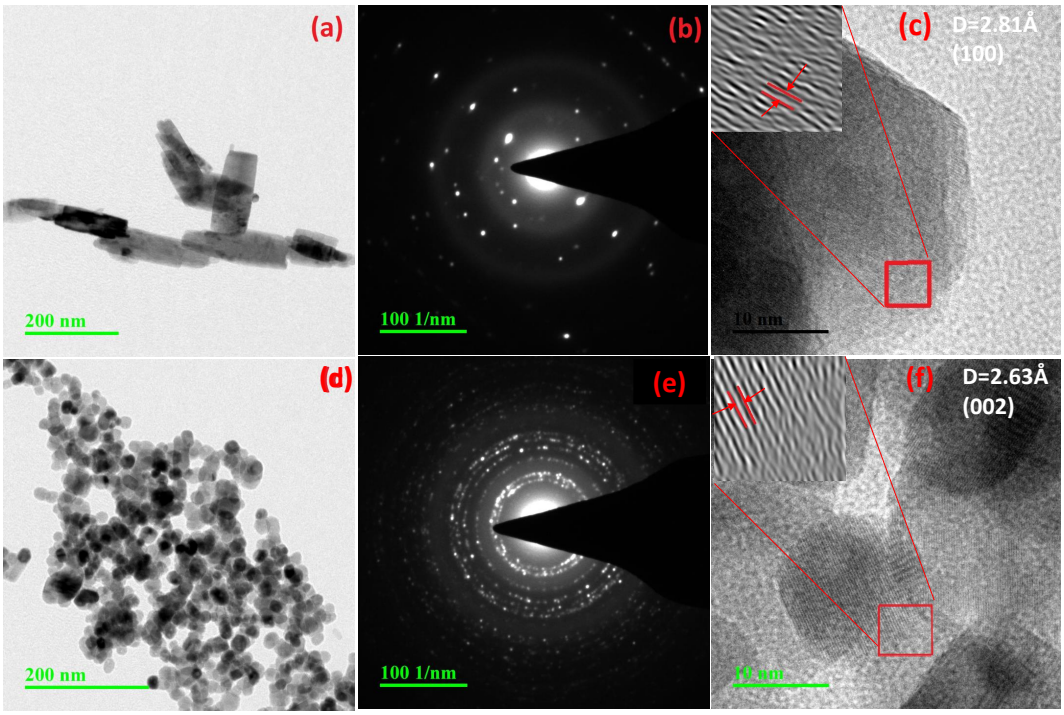

Figure 4.2: TEM image, diffraction pattern and HRTEM image of *ZnO* synthesized by method 4.2.1 (a, b & c) and 4.2.2 (d, e & f).

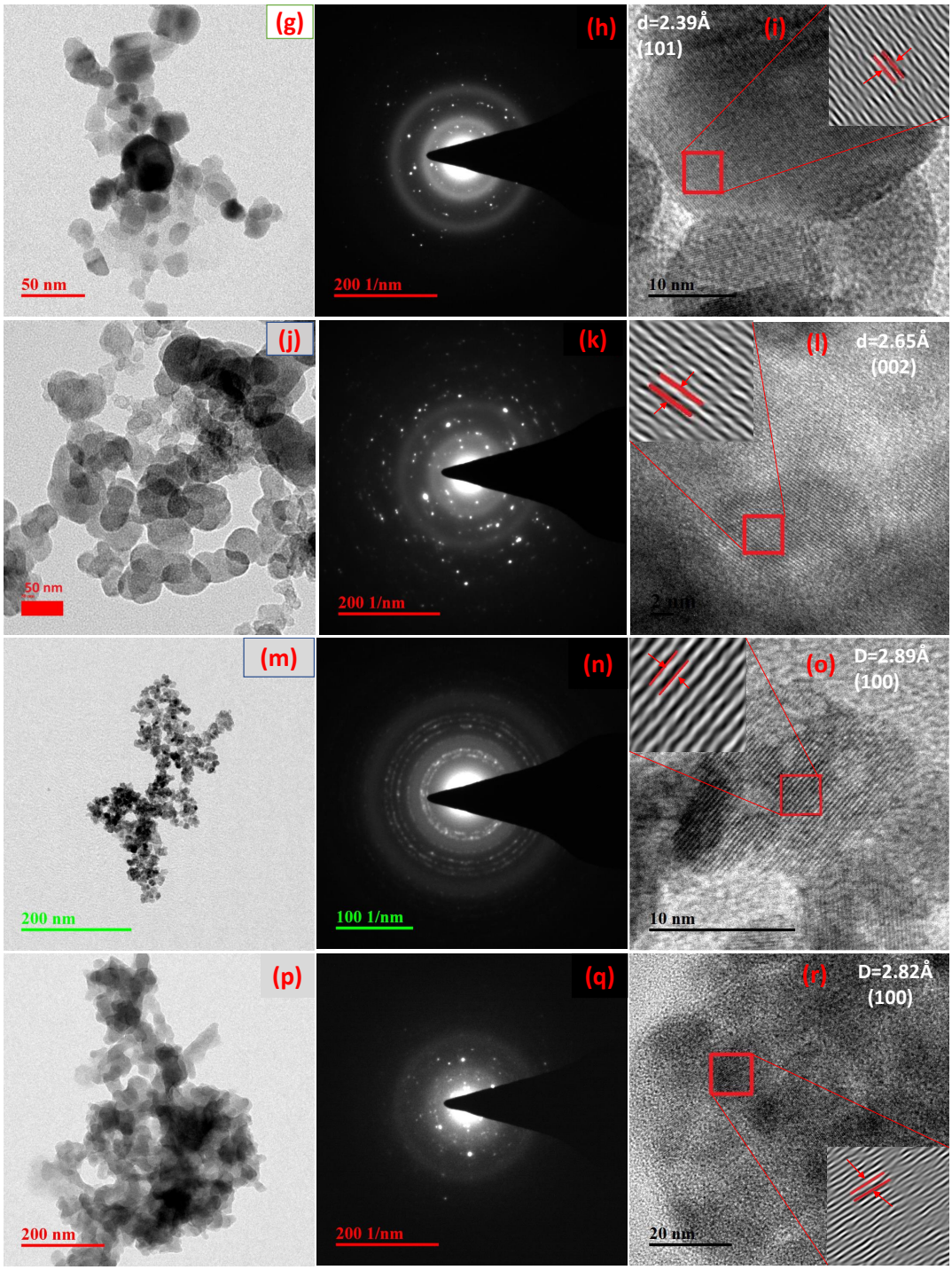

Figure 4.3: TEM image, diffraction pattern and HRTEM image of *ZnO* synthesized by method 4.2.3 (g, h & i), 4.2.4 (j, k & l), 4.2.6 (m, n & o) and 4.2.5 (p. q & r).

4.3.3 Diffuse Reflectance Spectroscopy (DRS)

The diffuse reflectance spectra of all the *ZnO* samples are shown in figure 4.4. Strong reflections was found above 400 nm for all samples. The absorbance has been calculated using equation 3.5 as describe in section 3.4.4. Corresponding absorption spectra for *ZnO* NP's are shown in figure 4.5. The absorption peaks were observed at 368 nm, 374 nm, 372 nm, 370 nm, 368 nm and 260 nm respectively indicating that the presence of blue shift is observed with decrease in particle size with respect to bulk *ZnO* (= 376 nm; 3.3 eV) the observed blue shift could be attributed to the confinement effects. The band gap energy of the samples are measured by the extrapolation of the linear portion of the graph between the modified Kubelka-Munk (K-M) function $[F(R)h\nu]^2$ versus photon energy ($h\nu$) using equation 3.7 in section 3.4.4, as shown in figure 4.6. The extrapolation of the straight lines in figure 4.6 gives the value of band gap energy. The optical band gap is found to be size dependent and there is an increase in the band gap of the semiconductor with a decrease in particle size. The optical band gap values obtained for *ZnO* NP's prepared by above methods are 3.25, 3.21, 3.23, 3.23, 3.2 and 3.32 eV respectively. There is no significant change in the optical band gap of the *ZnO* prepared by methods 4.2.1 to 4.2.5 because of the almost same particle size. There is a remarkable change 0.12 eV in the band gap was observed when the particle size decreases from 12 nm to 5 nm. The smaller band gap value in the as-synthesized *ZnO* NP's as compare to bulk materials ($\sim 3.3eV$) may attributed to planar defects, like stacking faults, twin boundaries and intrinsic defects like oxygen vacancies, zinc vacancies and Zn and O interstitials (as shown in energy level diagram figure 4.8)found in *ZnO* materials.

Table 4.2: Summary of present work

Method	Precursor	Solvent	d XRD (nm)	d TEM (nm)	Eg (eV)
4.2.1	Zinc chloride	DI water	21	18 ± 2	3.25
4.2.2	Zinc chloride	Methanol	26	17 ± 2	3.21
4.2.3	Zinc chloride	Ethanol	16	14 ± 2	3.23
4.2.4	Zinc nitrate	DI water	17	13 ± 2	3.23
4.2.5	Zinc acetate	DI water	9	12 ± 2	3.20
4.2.6	Zinc acetate	DMSO	7	5 ± 2	3.32

It is clear from UV-Vis spectra (figure 4.5) that there was no sharp change observed in the peak position in comparison to bulk *ZnO*. When zinc chloride was used as precursor, a large blue shift was observed when we use zinc acetate. The observed results are summarized in table 4.2. where d XRD is average crystallite size, d TEM is average diameter and *Eg* is optical band gap of *ZnO* NP's.

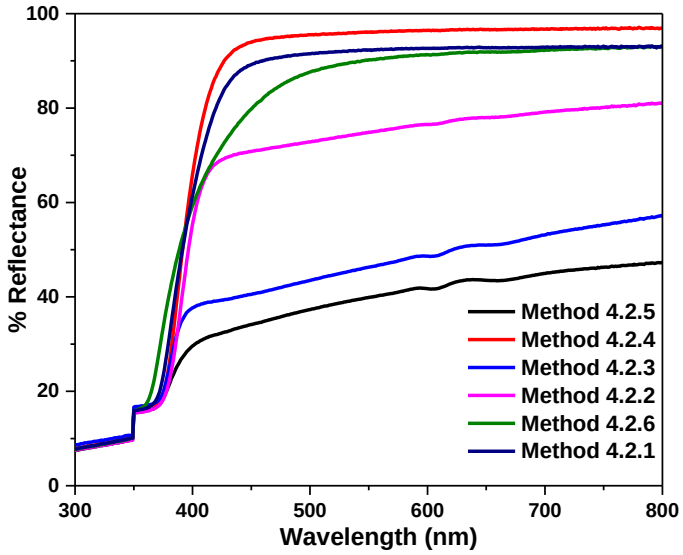

Figure 4.4: Room temperature diffuse reflectance spectra of *ZnO* NP's prepared by method 4.2.1 to 4.2.6

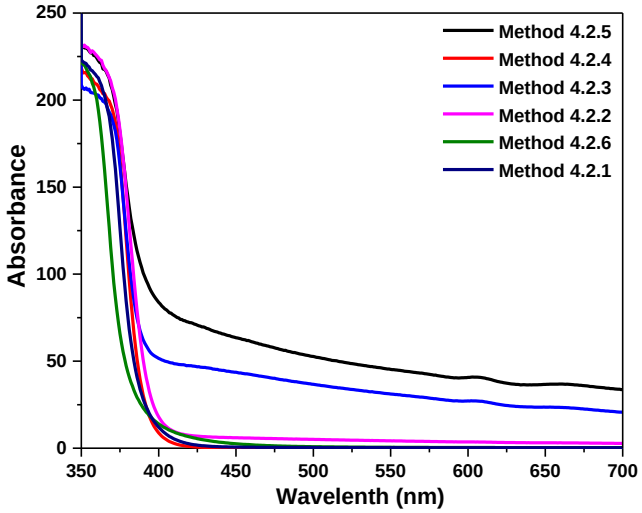

Figure 4.5: UV Vis absorption spectra of *ZnO* NP's prepared by method 4.2.1 to 4.2.6.

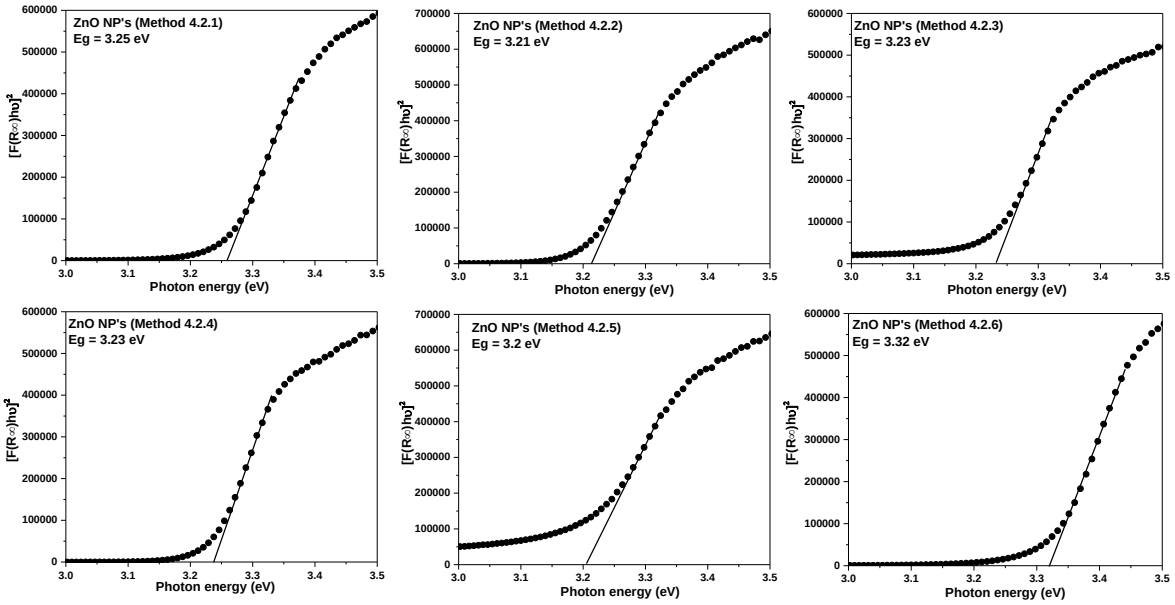

Figure 4.6: Kubelka-Munk function versus energy plots of all the *ZnO* samples.

It can observed from the table 4.2 that by using the solvent DI water and change the precursor zinc chloride, zinc nitrate and zinc acetate then both average crystalline size and average diameter decreases respectively. It can also seen from the 4.2, by keeping precursor same and changing solvent as ethanol, DI water and methanol the average dia and optical band gap founds almost same but average crystalline size increases respectively. In case of zinc acetate precursor when DI water and DMSO use as a solvent the average crystalline size remains almost same but average diameter changes. It is also clear that average crystalline size and average diameter of *ZnO* NP's synthesized using method 4.2.6 found to be smaller than all other used methods (method 4.2.1 to 4.2.5) but the optical band gap larger due quantum confinement effect. Because of capping agent (EG in this case) average particle size decreases and blue shift occurs in the absorption spectra [183].

4.3.4 Photo luminescence (PL) spectroscopy

In order to study the luminiscence properties and possible defects in the samples, Photo luminescence spectra was investigated at room temprature (figure 4.7) with excitation wavelength (λ_{exc}) 325 nm over a wavelength range from 350 nm to 650 nm for the *ZnO* nanopowder prepared by different methods. The PL spectra of the *ZnO* NP's exhibits two emission peaks, one in UV region (between 370-420 nm) corresponding to the near band gap excitonic emission (band to band transition) [225]. The second emission peak is located in the range 420-650 nm which attributes to the presence of singly ionized

oxygen vacancies (surface defects) [374]. The reason of second emission might be the radiative recombination of a photo generated hole with electron occupying the oxygen vacancy [375]. The emission bands of all ZnO samples were fitted by multiple Gaussian peak functions with optimal full width at half maxima (FWHM). The number of sub-peaks in all ZnO PL spectra reveals the pressance of defects and their influence on the optical properties. figure 4.8 shows the PL spectra along with the corresponding energy band diagrams of ZnO samples and the corresponding parameters from multi-peak fitting are tabulated in Table 4.3. The presence of multiple peaks in the visible region of the electromagnetic spectrum is typical for nanocrystalline ZnO [376]. The ZnO NP's prepared by method from 4.2.1 to 4.2.6 shows the band edge peaks at 432, 382, 407, 412, 408 and 374 nm, respectively. ZnO NP's prepared by method 4.2.2 and 4.2.3 shows the emission peaks in violet and green region while NP's prepared by method 4.2.4 shows an additional blue emission peak. NP's by method 4.2.5 and 4.2.6 shows the emission in violet, green and orange-red region and method 4.2.1 shows emission in green and orange region. The violet emission usually originates from the zinc interstitials (Zn_i) defects, where electronic transition occurs from Zn_i level to valence band [377]. The green emission in all the samples are due to transition from Zn_i to valance band of oxigen (V_o) [378]. The presence of more than one green emissions may be due to the different shallow energy levels in close vicinity inside the band gap (figure 4.8, method 4.2.2, 4.2.3) which is associated with interface trap in the grain boundaries and dislocations [379, 380]. The other reason may be the coexistence of interstitial sites with different energy configurations such as isolated or split interstitials.

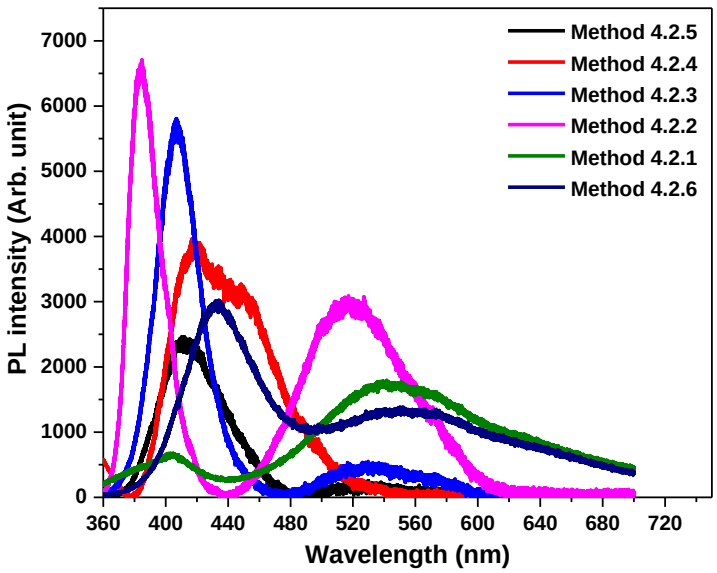

Figure 4.7: PL spectra of all the ZnO samples ($\lambda_{exc} = 325nm$)

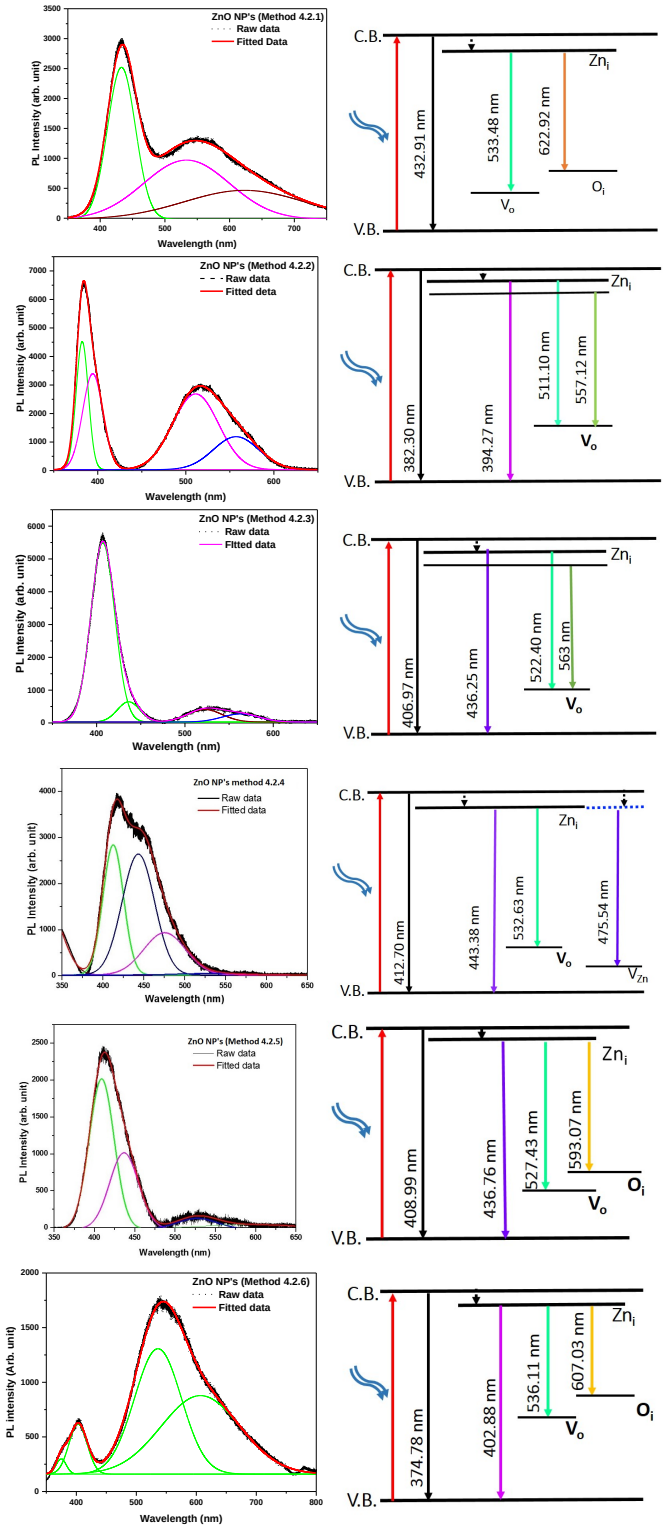

Figure 4.8: Gaussian fitted Photo luminescence spectra and corresponding possible energy level diagram for all the *ZnO* samples ($\lambda_{exc} = 325nm$)

The visible band observed in all *ZnO* samples is due to the existence of structural imperfection and IR emission from the n-type *ZnO*.

Table 4.3: Band position, relative intensities and bandwidth in individual band after Gaussian fitting of PL of ZnO NP's

Method	Peak position (nm)	Peak Intensity ($counts$)	Band width (nm)
	432.91	2538	50.78
4.2.1	533.48	988.58	156.35
	622.92	483.29	218.81
	382.30	67.6	16.30
4.2.2	394.27	50.6	27.10
	511.10	39.9	61.29
	557.12	17.4	60.96
	406.97	98.4	31.81
4.2.3	436.25	11.1	29.84
	522.40	6.8	46.11
	563.00	4.4	60.96
	412.70	73.9	29.61
4.2.4	443.38	68.7	46.78
	475.54	24.03	60.10
	532.63	0.8	92.42
	408.99	82.2	36.26
4.2.5	436.76	43.3	42.11
	527.43	6.02	57.23
	593.07	2.5	147.64
	374.78	139.73	19.85
4.2.6	402.88	457.2	35.64
	536.11	1143.50	92.02
	607.03	718	155.13

Blue emission oberved in *ZnO* NP's prepared with method 4.2.4 may be due to the transition from Zn_i level to V_{Zn}. However, it could also arise from the surface deep traps states [377]. The orange-red emission occurs in *ZnO* NP's prepared with method 4.2.5 and 4.2.6 is due to Zn_i to O_i transition [381]. In case of 4.2.2 and 3.7 method, the higher intensity showing the large population of low lying energy levels in range of 434-485 nm. Theoretically, the Zn_i, V_{Zn} and oxygen interstitial (O_i energy levels are located nearly 0.22, 3.06 and 2.28 eV below the conduction band, respectively whereas V_o level is 0.9 eV above the valence band [379]. The deep level emissions occur in the green (2.5 eV) and orange-red (1.95 eV) region, which are in good agreement with our experimental results. As observed from figure 4.8, the higher intensities of violet emission in method 4.2.2 and 4.2.3 as compared to other methods may due higher concentration of grain boundaries, dislocations and surface traps. The nanopowders shows an intense violet emission along with the emission in blue and green band. Position of the most intense peak lies in the range of 380-410 nm which corresponds to violet band. Blue and green emission band 435-593 nm like other reports [378, 382]. The relative intensity (method 4.2.2, 4.2.3, 4.2.4 and 4.2.5)in the visible region 530-593 nm are very low as compared to *ZnO* NP's prepared by method 4.2.1 and 4.2.6. This is because of the presence of the defects at the surface of the NP's. The defect density changes with the surface to volume ratio according to changes in morphology and sizes of NP's. Furthermore, variation in peak position of the emission spectra is attributes to change in the defect density on the surface of the NP's [383].

4.4 Conclusion

ZnO NP's were synthesized successfully by simple chemical routes using different precursors and solvents. The synthesized NP's were characterized by XRD, TEM, DRS and PL. The XRD and TEM results confirms the crystalline nature and single phase formation of *ZnO* NP's. The DRS results revealed that there is no drastic change in absorption edge and the optical band gap of *ZnO* NP's prepared by method 4.2.1 to 4.2.5 while the large blue shift observed in method 4.2.6 with an optical band gap of 3.32 eV. It can be concluded that method 4.2.6 can be used for smaller size and large band gap *ZnO* NP's. The zinc interstitial defects were present in all *ZnO* samples prepared with different precursors and solvents. Oxygen interstitial defects presents in *ZnO* NP's prepared by method 4.2.1, 4.2.5 and 4.2.6.

5

Synthesis of RE doped *ZnO* NP's and their Characterization

5.1 Introduction

Doped luminescent NP's are predicted to show improved optical properties, viz., luminescence efficiency, delay time and band edge emission according to the particle size variation. RE doped *ZnO* poses coexisting semiconducting, electromechanical and optical properties therefore it is a highly multifunctional material [384, 385]. 4f intra-shell transitions spectral lines stands these RE ions as one of the best luminescent material to dope in *ZnO*. The lanthanides have induced shielding effect due to presence of a partially filled 4f level and fully filled 5s and 5p orbitals. The photoluminescence (PL) spectra of these ions shows emission lines because of this shielding effect, which is relatively independent of host matrix [386]. Among the lanthanides, Er, Tb, and Eu has wide range of applications. Due to its better PL characteristics, RE^{3+} doped optical amplifiers are used in the telecommunications [387, 388]. The difficulties related to doping makes the structural and luminescence properties inaccurate in RE^{3+} doped bulk and nano-compounds. This makes it important to optimize the doping procedure [389–391]. Significantly low luminescence intensities even after successful incorporation of RE in *ZnO* matrix.which may be due to nonradiative transfer from RE^{3+} ion to *ZnO* host leading to the quenching of RE emission due to and/or may be due to rapid decay of excited *ZnO*, which facilitates direct energy transfer to RE ions [392–394]. In spite of that, the dynamics of transfer process and optimization of visible luminescence efficiency by manipulating defect-dopant interactions still not yet cleared.

The work presented in this chapter is an attempt in this direction. In this chapter, Suc-

cessful doping of Er, Tb and Eu ions in *ZnO* host using chemical precipitation technique is presented. This method has many advantages in terms of cost, minimal facilities, and low energy consumption. XRD and TEM were used to detail discussion of structural properties of synthesized NP's. DRS results shows decrease in band gap and PL data reveals enhanced visible luminescence intensity with increased RE^{3+} concentrations upon when host *ZnO* is excited into band gap, which indicates possible energy transfer from the host to dopant energy level. When excited to *ZnO* band, presence of characteristic intra-4f orbital transitions of RE^{3+} indicates energy transfer between host and guest, likely involving the *ZnO* defect states.

5.2 Experimental details

5.2.1 Synthesis of pure and RE doped *ZnO* NP's

1.0 gm of Zinc chloride was dissolved in 30 ml Ethylene glycol (EG) and stirred for 1 hour. Then, the reaction temperature was raised to $75°C$ and further stirred for 30 minutes. 0.3 gm NaOH was dissolved in 5 ml EG and NaOH solution was added dropwise to zinc chloride solution. The final solution was stirred for 2.5 hours at $75°C$ and then cooled at room temperature. The resultant solution was filtered with 0.2 micrometer filter and washed with DI water 4-5 times in order to remove the impurities. *ZnO* NP's was obtained in powder form.

5.2.2 Synthesis of RE doped *ZnO* NP's

The RE ion (Tb, Er, Eu) doped *ZnO* NP's were synthesized using the above method with a small change of adding the solution of RE precursor in 10 ml EG in zinc chloride solution before adding the NaOH solution.

5.3 Results and Discussion

Pure and RE doped *ZnO* NP's were characterized by XRD, TEM, SEM, UV-Vis. and PL. The discussion of obtained results are as follows:

5.3.1 X-ray Diffraction (XRD)

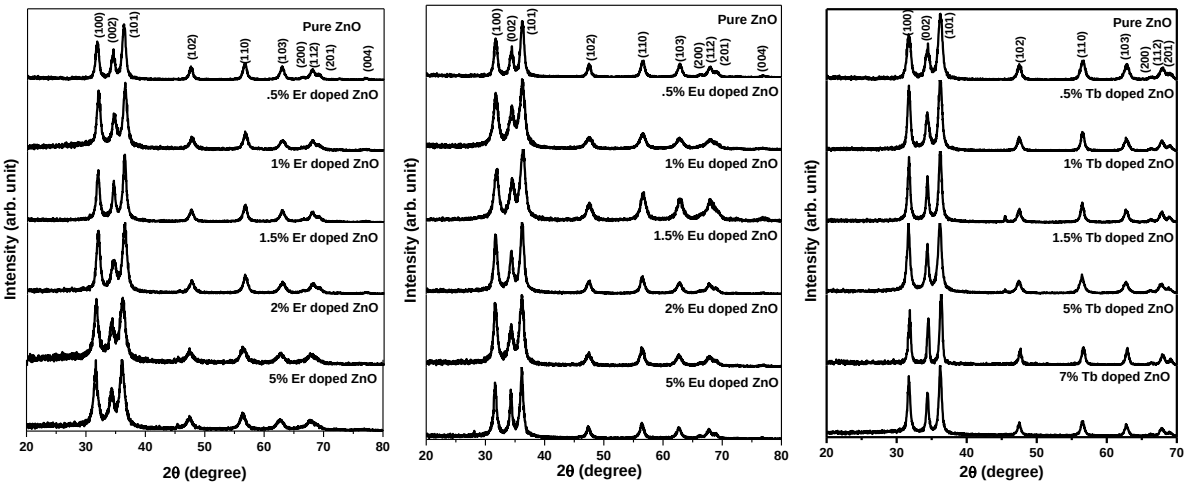

Figure 5.1: XRD patterns of undoped *ZnO* and Er, Eu and Tb doped *ZnO* NP's.

XRD spectra was used to investigate the crystallographic information of *ZnO* and RE-doped *ZnO*. Figure 5.1 shows XRD pattern of Er, Eu and Tb doped *ZnO* NP's.

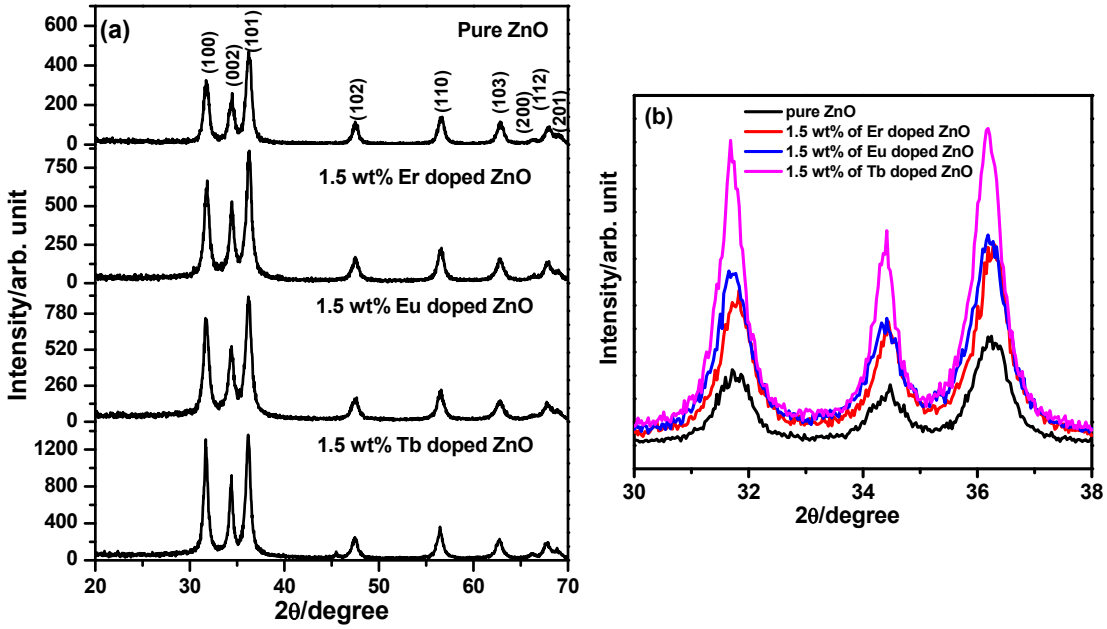

Figure 5.2: XRD patterns of undoped *ZnO* and 1.5 wt% RE doped (*Er, Eu, Tb*) *ZnO* NP's. (a) represents the enlarged peaks of the spectra , (b) indicates the shifting in most intense peaks towards lower angle.

The diffraction patterns confirm polycrystalline nature of pure and RE doped *ZnO* NP's. All the diffraction peaks were matched using the data available from the Joint

Committee for Powder Diffraction Studies (JCPDS), and the corresponding planes were indexed in figure 5.2. All the diffraction peaks in the XRD pattern indicate the typical hexagonal wurtzite structures of *ZnO* with space group P63mc. The characteristic peaks of XRD for all the samples are corresponding to *ZnO*, no peaks were observed for other impurities, which confirms that the RE-related compounds or other impurity were not formed during synthesis and the RE atoms were incorporated into the *ZnO* lattice. For comparative study figure 5.2 shows the XRD patterns of pure *ZnO*, Tb (1.5at%)/*ZnO*, Er(1.5at%)/*ZnO* and Eu(1.5at%)/*ZnO* which showed the shifting of diffraction peaks, slightly towards the lower angle for RE-doped samples in comparison with that of pure *ZnO* (figure 5.2(b)). Because the ionic radii of Tb^{3+}(0.092 nm), Er^{3+}(.088 nm) and Eu^{3+}(0.095 nm) is larger than that of Zn^{2+}(0.074 nm), doping of RE into the *ZnO* can cause the expansion of *ZnO* lattice and led to a shift of *ZnO* peaks to lower angles as also observed by other investigators [4, 184, 395–397]. It is confirm from figure 5.2(b) shifting towards lower angle is increases as the ionic radius of RE increases. Moreover, the average crystallite size of all the samples were calculated with the all peaks using Debye Scherer equation 3.2 describe in section 3.4.1. The results in table 5.1 showed that the average crystallite sizes of pure *ZnO* and RE doped *ZnO* were within the range of 12-14 nm. The FWHM values of RE-doped samples are slight larger as compared to pure *ZnO* that confirms the slight decrements in the crystallite size. This decrease in the crystal size of RE doped *ZnO* may be attributed to the RE-O-Zn formation on the surface of the doped products, which inhibits the growth of crystal grains [398, 399].

5.3.2 Scaning Electron Microscopy (SEM)

Figure 5.3 and 5.4 presents the SEM images and EDS spectra of Tb doped *ZnO* nanostructures. The obtained EDS results confirmed the presence of Tb, Zn and O in the final products. The EDS results also confirms that the intensity of Tb peaks increase with concentration of Tb in the sample. The surface morphology of synthesized NP's confirms that the particles are almost spherical in shape. Furthermore the agglomeration increases with doping concentration of Tb in *ZnO* NP's.

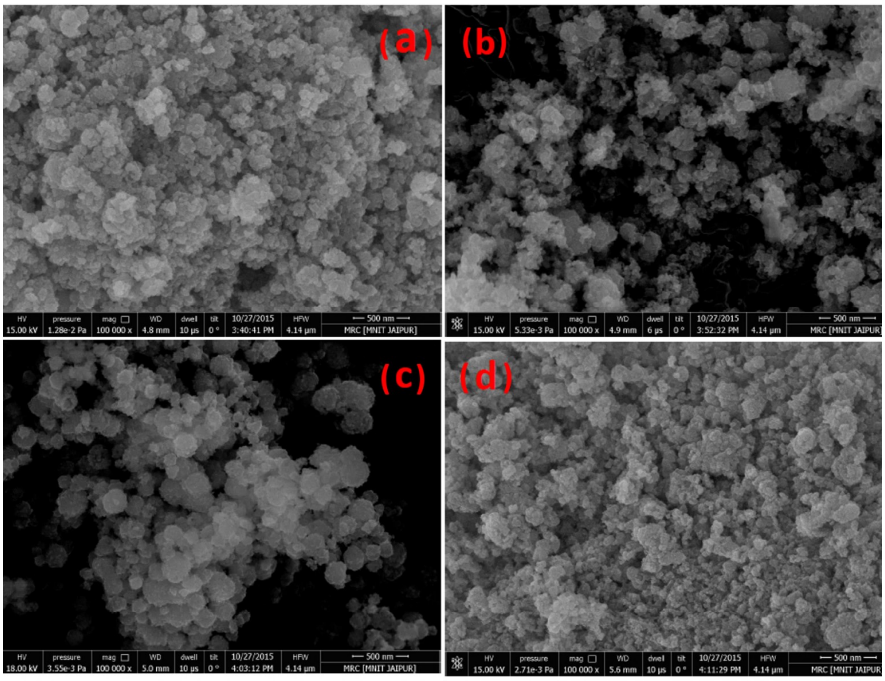

Figure 5.3: SEM image Tb doped (a .5 wt% Tb, b 1.5 wt% Tb, c 2 wt% Tb and d 5 wt% Tb) *ZnO* NP's.

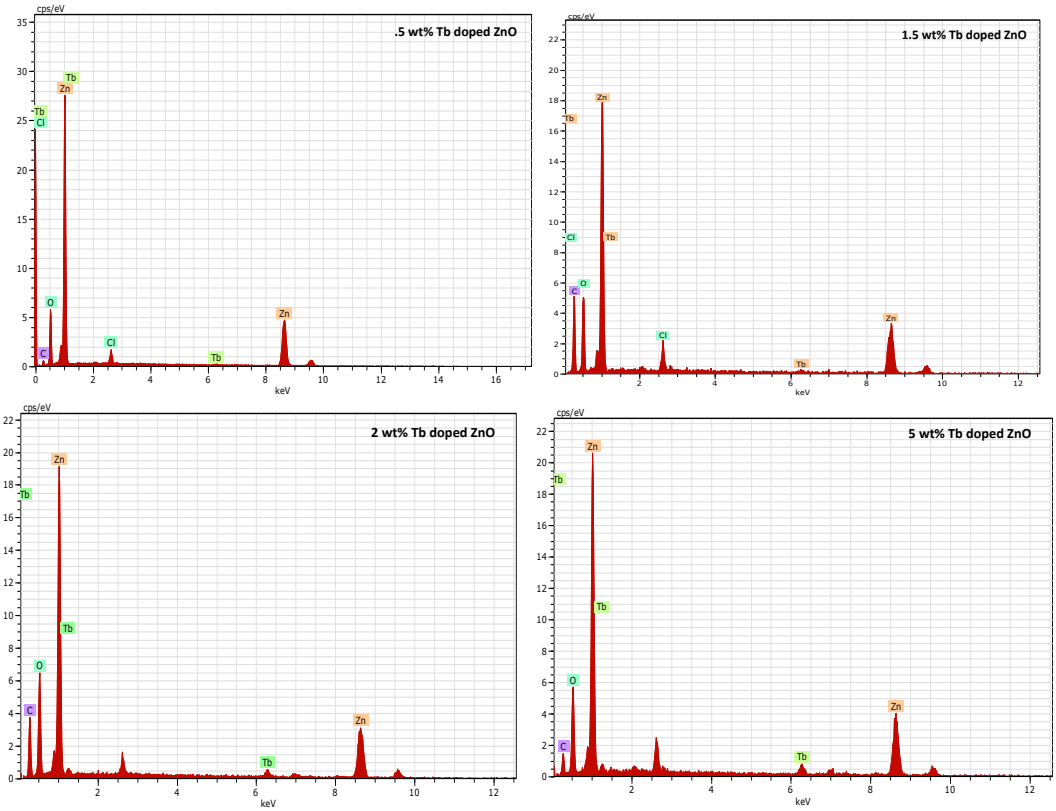

Figure 5.4: EDX spectra of different wt% Tb doped *ZnO* NP's.

5.3.3 Transmission Electron Microscopy (TEM)

TEM measurement were performed to explicate the morphologies of the pure and RE doped *ZnO* NP's. Figure 5.5a shows the TEM images of *ZnO* and 1.5 wt% RE-doped *ZnO* NP's. It can be observed that particles have almost spherical shape.

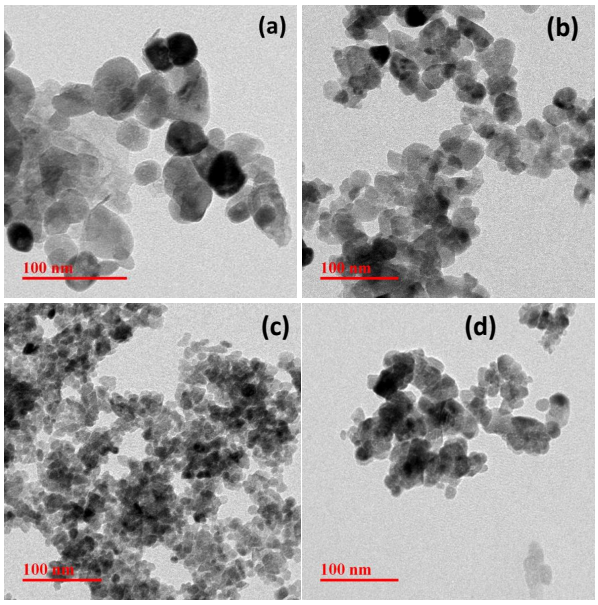

(a) TEM image

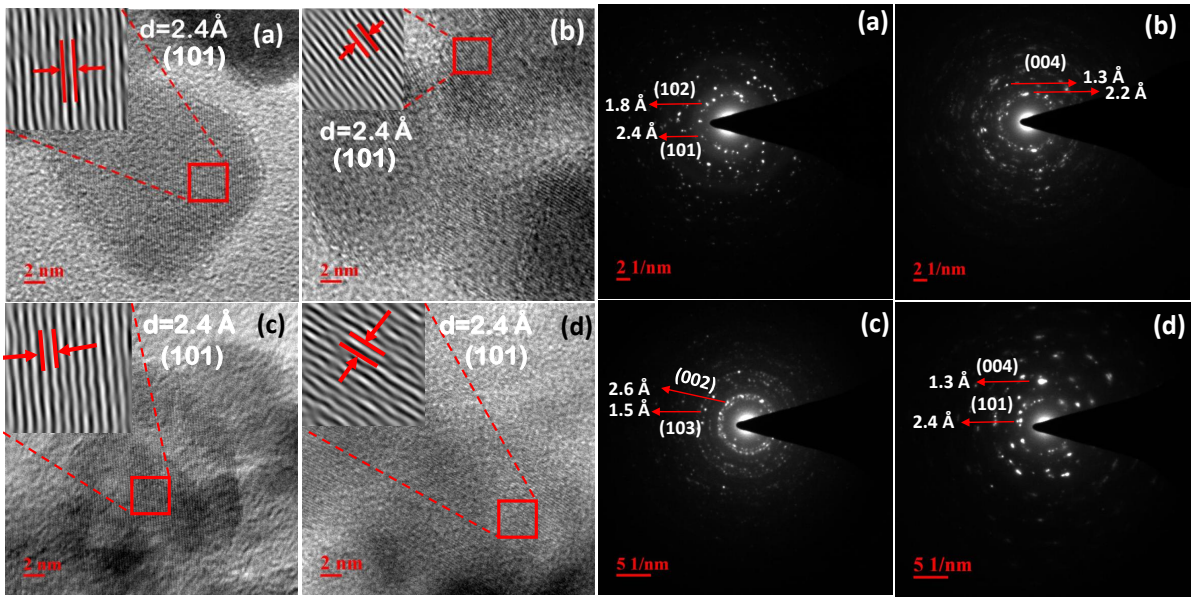

(b) HRTEM image **(c)** SAED pattern

Figure 5.5: TEM, HRTEM and SAED pattern of undoped(a) and 1.5 wt% RE (Tb (b), Er (c) and Eu (d)) doped *ZnO* NP's.

The selected area electron diffraction (SAED) pattern shows poly-crystalline nature of

NP's. The planes and their inter-planer spacing are calculated and indexed in SAED pattern, which are in good agreement with XRD results for all the NP's (figure 5.5c). Average diameter of the as-synthesized NP's as listed in table 5.1, was found in the range 10-14 nm which also a good agreement with XRD results. The average diameter of RE-doped *ZnO* NP's are less than pure *ZnO* which is again consistent with XRD results. HRTEM images (figure 5.5b) of pure and RE-doped *ZnO* shows clear lattice fringes with the distance between two parallel lattices planes were measured as 2.85 (100), 2.81 (100), 2.48 (101) and 2.83A (100) corresponding to *ZnO*, 1.5 wt% Tb: *ZnO*, 1.5 wt% Er: *ZnO* and 1.5 wt% Eu: *ZnO* respectively, which are consistent with XRD pattern. HRTEM images also shows defects are present at the grain boundaries.

5.3.4 UV-Vis. Diffuse Reflectance Spectroscopy (DRS)

The effect of RE doping on optical absorption by *ZnO* NP's was investigated using UV-Vis DRS. Figure 5.6 shows the DRS of different wt% Er, Eu and Tb doped *ZnO* NP's which represent strong absorption in UV and extended to visible region. The Er doped samples shows various absorption band in visible region. For comparative study DRS of undoped and 1.5 wt% Er, Eu and Tb doped samples are shown in figure 5.9a. The absorption threshold of undoped *ZnO* is 363 nm and shows a strong absorption band in UV region, which attributed to the band to band transition. While for RE/*ZnO* products, Er(1.5wt%)/*ZnO*, Eu(1.5wt%)/*ZnO* and Tb(1.5wt%)/*ZnO* exhibited extended absorption range to visible light region. Furthermore, the Er (1.5wt%)/*ZnO* (at 485, 520, 542 and 652nm) has much absorption bands in agreement with the visible-light absorbability. These peaks were ascribed to the Er characteristic of 4f electron transitions [184, 400]. The absorbance has been calculated using equation 3.5 as describe in section 3.4.4 in the limiting case of an infinitely thick sample at any wavelength [182, 401]. Corresponding absorption spectra for different wt% Er, Eu and Tb doped *ZnO* are shown figure 5.7 and for comparison *ZnO* and 1.5 wt% RE-doped *ZnO* NP's are shown in figure 5.9b. The absorption peaks are tabulated in table 5.1, indicating that all the has blue shift with respect to bulk *ZnO* ($\sim$376 nm; 3.3 eV) the observed blue shift could be attributed to the confinement effects.

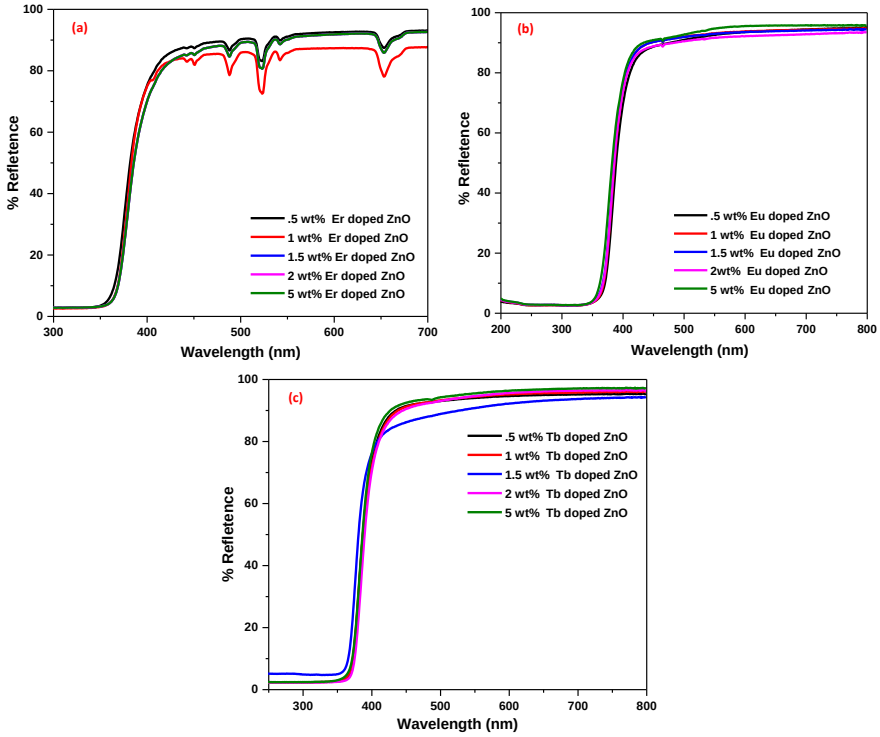

Figure 5.6: Room temperature DRS spectra of different wt% doped Er, Eu and Tb doped *ZnO* NP's.

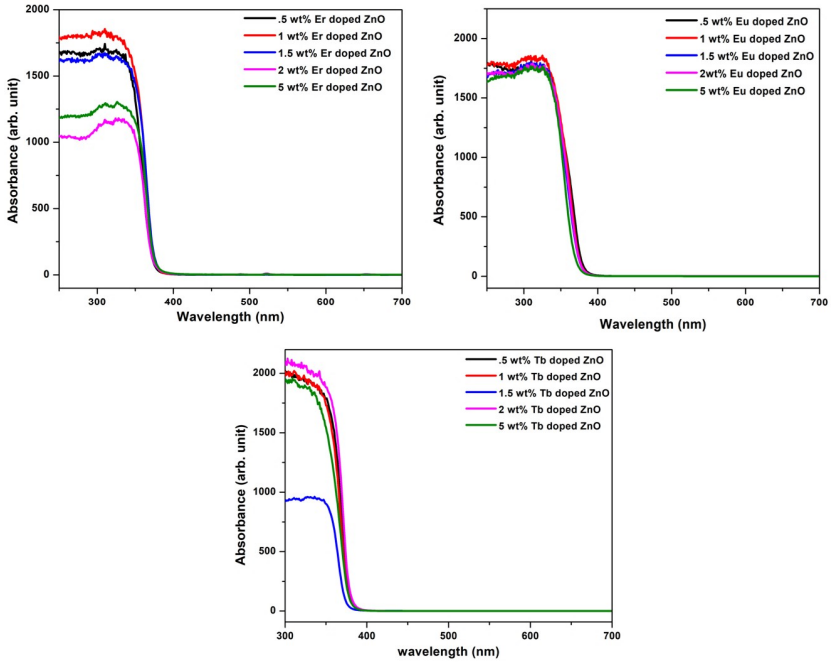

Figure 5.7: UV-Vis absorption spectra of different wt% doped Er, Eu and Tb doped *ZnO* NP's.

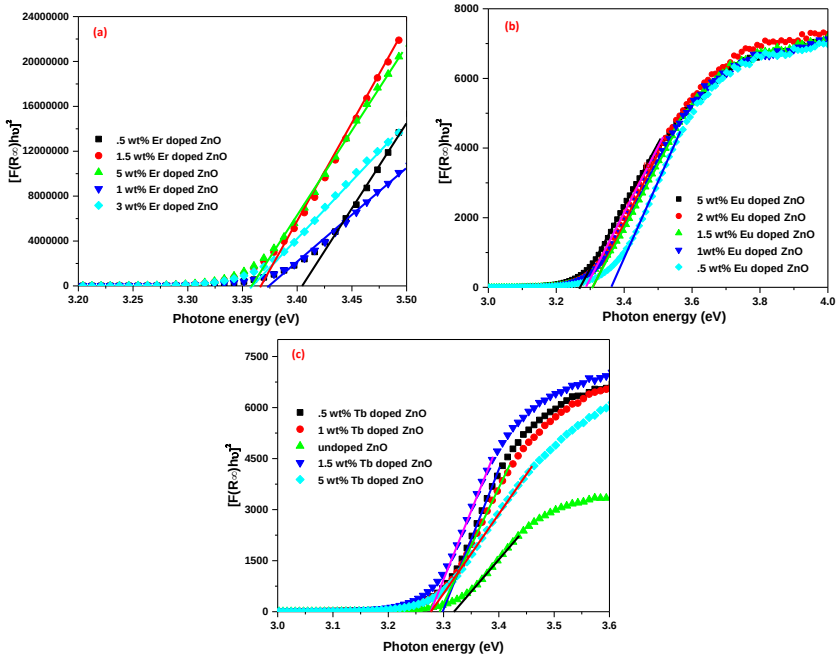

Figure 5.8: Kubelka-Munk function versus energy plots of different wt% doped Er, Eu and Tb doped *ZnO* NP's.

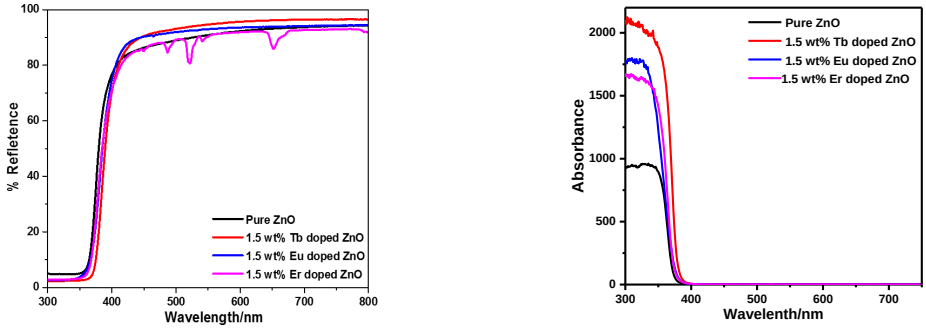

(a) Room temperature DRS spectra. **(b)** UV-Vis absorption spectra.

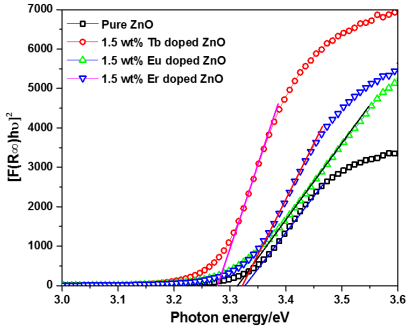

(c) Kubelka-Munk function vs energy plots.

Figure 5.9: DRS, UV-Vis absorption spectra and Kubelka-Munk function versus energy plots of undoped and 1.5 wt% RE (Er, Tb and Eu) doped *ZnO* NP's.

The band gap energy of the samples is measured by the extrapolation of the linear portion of the graph between the modified Kubelka-Munk (K-M) function $[F(R)h\nu]^2$ versus photon energy ($h\nu$) using 3.7 in section 3.4.4 as shown in figure 5.8 and 5.9c. The extrapolation of the straight lines gives the value of band gap energy. From figure 5.8 it is conclude that optical band gap of RE doped samples decreases with increasing concentration of RE ions. The measured band gap energies of pure and 1.5 wt% RE (Er, Eu and Tb) doped products are shown in table 5.1. Above results revealed that the RE-doped *ZnO* can absorb in UV as well as in visible region of the solar light. Hence, the absorption property deduced that the RE doped *ZnO* could be promising in visible light photo catalysis. The observed results are summarized in table 5.1. where d XRD

Table 5.1: Calculated Lattice parameter, crystalline size and optical band-gap of NP's

NP's	Lattice Parameter(Å)	d XRD (nm)	d TEM (nm)	E_g (eV)
ZnO	$a = 3.249; c = 5.204$	14	18 ± 2	3.325
Tb doped *ZnO*	$a = 3.251; c = 5.201$	11	14 ± 2	3.321
Er doped *ZnO*	$a = 3.250; c = 5.202$	12	13 ± 2	3.311
Eu doped *ZnO*	$a = 3.257; c = 5.216$	12	12 ± 2	3.276

is average crystallite size, d TEM is average diameter and E_g is optical band gap of *ZnO* and RE doped *ZnO* NP's.

5.3.5 Photo luminescence (PL) spectroscopy

PL spectrum is a useful tool to track the possible defects in the sample and to investigate the efficiency of charge carrier trapping, immigration and luminescence properties. The emission intensity depends on nature of RE ions, concentration amount of RE ions and excited wavelength. In general, a higher PL intensity implies larger rate of electron hole recombination hence reducing the reaction rate of photo generated charge carriers. Such systems are useful in device application. Whereas, a lower PL intensity indicates a low rate of photo generated electron-hole recombination, which makes more photo generated electrons and holes available for the oxidation and reduction reaction, consequently improving the photocatalytic performance [402]. Figure 5.10 represents the room temperature PL spectra of different wt% of Er, Eu and Tb doped *ZnO* NP's. The excitation wave length of laser light was 325 nm. As the concentration of RE in

ZnO is increased, the visible emission is enhanced (up to 1.5 wt% doped *ZnO*) because as the RE material concentration is increased the particle size is slightly decreasing, which might enhance the content of oxygen vacancies on the surface of the material but excessive doping of RE consumes the *ZnO* NP's (concentration quenching), decreasing the PL intensity.

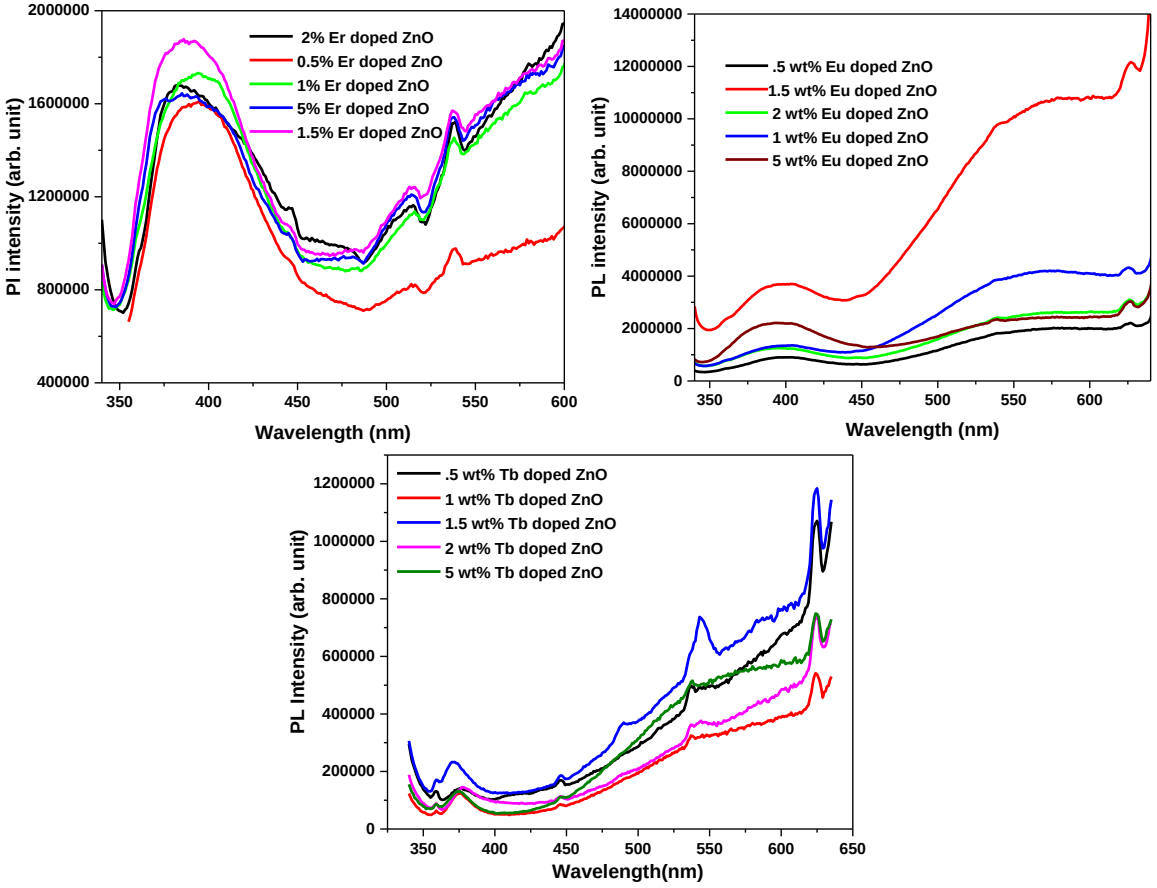

Figure 5.10: Room temperature PL spectra of different wt% doped Er, Eu and Tb doped *ZnO* NP's. ($\lambda_{exc} = 325nm$)

To complete the valence site of one Zn^{2+}, one O^{2+} will attach to form a *ZnO* compound while in the case of RE^{3+}, two RE^{3+} will be made bonded to three O^{2-} to form Er_2O_3 compound. In this process, two RE^{3+} ions replace the three Zn^{2+} ions and oxygen concentration remains constant. Thus, the reason behind the change in oxygen vacancies is not the exchange of Zn^{2+} by RE^{3+} but increase in the surface to volume ratio due to reduced particle size. Further increasing the doping percentage of RE^{3+} the broad visible emission peak of pure *ZnO* overlap the RE^{3+} doped *ZnO* peaks. These results conclude that energy is transferring from *ZnO* to RE^{3+} and it emits light. From the above study for optoelectronic application 1.5 wt% of RE doping is optimised concentration.

Room temperature PL spectra of undoped *ZnO* NP's (figure 5.11(a)) and 1.5 wt% RE doped *ZnO* (figure 5.11(b)) was studied with excitation of wavelength 325nm. Two emission peaks were observed in PL of undoped *ZnO* NP's, one in the UV region 370-420nm, agreeing to near band edge transition, and the secondary broad emission peak is in the range 425-650 nm which attributes to the presence of singly ionized oxygen vacancies (surface defects) [182]. A photo generated hole with electron occupying the oxygen vacancy can be the reason behind the secondary emission [375]. The higher PL intensities of RE- doped *ZnO* showed that the radiative recombination was increased by doping with RE, leading to strong recombination of photo generated charge carriers, which will be benefited in the optoelectronic applications. Compared with the other RE-doped *ZnO* products, the Eu^{3+} (1.5 wt%) doped *ZnO* had the highest PL intensity in visible range, which indicated that the Eu doping should have the highest defect density whereas Er doping have best recombination rate of electrons and holes in UV region. Furthermore, the PL intensity of RE-doped *ZnO* changed with the doping content. Reports show that the PL intensity of RE-doped *ZnO* increased gradually with the increase of doping, reaches a maximum at some critical concentration and then decreases [403]. Tb^{3+} and Eu^{3+} doped *ZnO* NP's shows the characteristic PL emissions due to intra 4f (^5D to ^7F) transitions of Tb^{3+} and Eu^{3+} whereas Er^{3+} doped *ZnO* shows characteristic peaks corresponding to ^4F to ^4I and ^4S to ^4I transitions. 446, 490, 543 and 624 nm are leading four lines found in the emission spectra for Tb^{3+} doped *ZnO* under 325 nm excitation. The sharp peaks of intra-4f transitions act along with wide defect luminescence of *ZnO*.Also notable think is that the excitation wavelength of 325nm for does not match to any actual intra-4f excitation of Tb^{3+} or Eu^{3+}.In the Eu-doped *ZnO* also show three PL signatures centered at 538, 579 and 625 nm which are attributed to ^5D to ^7F transitions [404, 405]. The electric dipole transition accounts for the high intensity peak at 625 nm (red) for all RE doped samples. Which is an attributed signature indicating the larger degree of disorder and non- centrosymmetric without inversion center [179, 406]. The relatively larger covalent radius of the RE^{3+} ions induces local distortion in the *ZnO* lattice as RE^{3+} substitutes the Zn^{2+} ions which are confirmed in the XRD patterns. The shifting of (100), (101) and (002) diffraction planes toward lower Bragg angles in XRD spectra confirms the substitution of Zn^{2+} by RE^{3+}. Furthermore the characteristic red emissions at 625nm in RE doped samples, due to sensitivity of local symmetry like subsurfaces and/or nanoparticle surface [407, 408], specifies that the energy transmission from host *ZnO* to RE^{3+} ions. It is recognized that the peak resembles to $^5D_0 -^7 F_1$ at 590nm (orange) in case of Eu doped samples, because of the magnetic dipole transition, which is permitted if Eu^{3+} ions are in a non-centrosymmetric site. And also unaffected to the nearby environment of the Eu^{3+} ions.

In the condition when all Eu^{3+} ions were occupied the Zn^{2+} sites in the stoichiometric *ZnO* then the Eu^{3+} ions must have the matching point of symmetry as of Zn^{2+} ions(C6v) and no transition were observed rather then $^5D_0 - ^7F_1$.

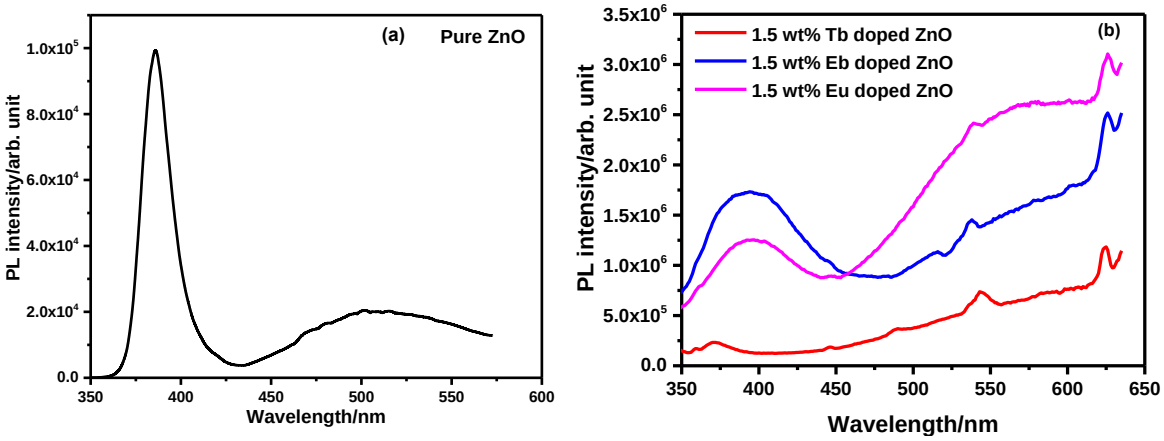

Figure 5.11: PL spectra of undoped and 1.5 wt% RE (Er, Tb and Eu) doped *ZnO* NP's. ($\lambda_{exc} = 325nm$)

The presence of peak corrosponding to $^5D_0 - ^7F_0$ transition is a clear indication that some of Eu^{3+} occupying any other sites such like interstitial sites, in addition to substituting the Zn^{2+} sites because J=0 to J=0 transition is strictly forbidden. The comparative intensities of the magnetic dipole and electric dipole transition are also sensitive to the local symmetry of Eu^{3+} ions. Exited state energy transfer mechanism was proposed for the intra-4f transition by Wang *et al.*, which consist of the band gap excitation of carriers tracked by their relaxation to the band edge. Later in this transitions the carriers are either undergo radiative transition or stuck in the defects [88]. These trapped excitons are responsible for the intra-4f emission. Er doped *ZnO* NP's shows characteristic emission peaks centered at 515, 537 and 628 nm. These transitions are corresponding to $^4S_{3/2} \rightarrow ^4 I_{15/2}$, $^H S_{11/2} \rightarrow ^4 I_{15/2}$ and $^4F_{9/2} \rightarrow ^4 I_{15/2}$ as shown in energy level diagram. In the Er doped samples, intensity of the excitonic emission band increased compared with that for the undoped *ZnO* and Eu^{3+} and Tb^{3+} doped *ZnO*. This can be explained by the formation mechanism and structure of the Er-doped *ZnO* NP's as proposed by Kai-sheng Yu *et al* that Er^{3+} would have caused an increase local concentration of excitons more as compare to Tb and Eu during photoexcitation, because of more accumulation of *ZnO* nano particles in presence of Er thus resulting in an increased excitonic emission intensity compared with the undoped *ZnO* [187]. This accumulation of *ZnO* particles in the presence of The fluorescent light intensity was therefore enhanced with increasing Er contents. The Er doped *ZnO* sample is excited at 340 nm then the intensity of

band edge emission is decrease and visible range intensity increases with high intense characteristic peak at 650nm.

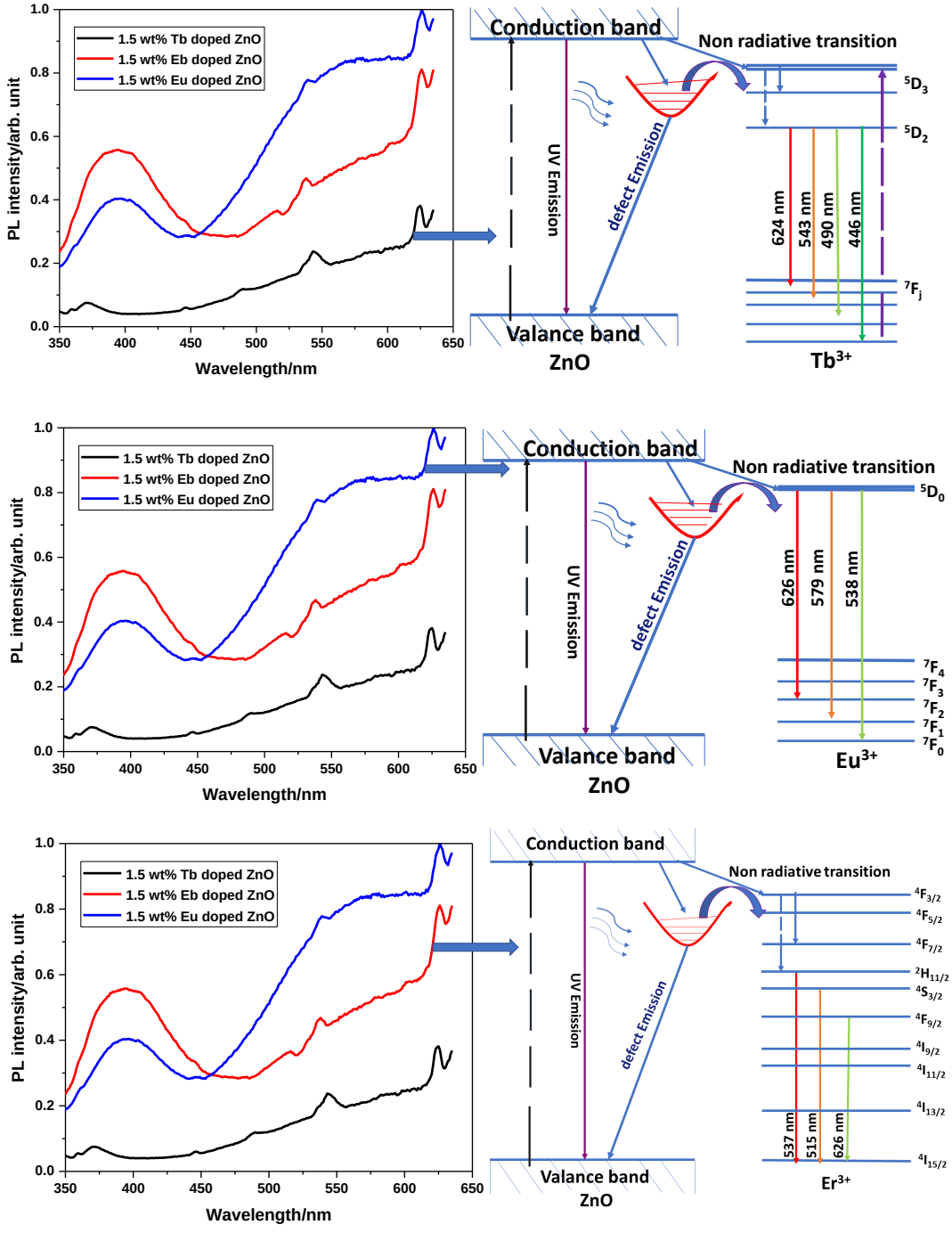

Figure 5.12: Schematic of energy level diagram and possible transitions for RE (Tb, Er and Eu) doped *ZnO* NPs.

Overall, Doping of RE enhances the luminescence properties of *ZnO* NP's the possible transition and energy level diagram for RE doped *ZnO* NP's are shown in figure 5.12.

In Eu doped *ZnO* NP's PL shows very less intense characteristics peaks as compare to Tb and Er doped *ZnO* NP's.

5.4 Conclusion

In this chapter, we have synthesized *ZnO* and different wt% Er, Tb, and Eu doped *ZnO* NP's with diameter 10-14 nm by simple wet chemical route. The incorporation of RE^{3+} ions into the *ZnO* host and formation of single phase spherical RE^{3+} doped *ZnO* NP's without any RE compound with the help of XRD and TEM measurements was presented. DRS analysis reveals that incorporation of RE^{3+} ions causes a shift in the excited absorption band toward higher energy due to induced lattice strain . 300 kelvin solid phase PL with 325 nm Xe light excitation shows narrow (FWHM $<$ 35 nm) and strong UV luminescence and also musltiple deep level defects leading to broad visible emissions. It has been established that by increasing RE^{3+} dopant concentrations, visible luminescence intensity increases up to 1.5 wt% of RE. This may be due to presence of more strain induced defects created by size disparity between Zn^{2+}/RE^{3+} ions and energy transfer carried by deffects from host *ZnO* to guest dopant ions. we visualized characteristic intra-4f transition lines of RE^{3+} ions using solid state PL, measurements with 325 laser excitations. Present research establishes that RE-doped *ZnO* NP's may indeed find a varity of applications in optoelectronic and multicolor emission display devices through defect engineering.

6

Block copolymer directed nanostructures

6.1 Introduction

Fabrication of highly ordered organic/inorganic nanostructures are made easy by the ordered nanotemplates which makes them interesting in the field of nano fabrications. Different morphologies of diblock copolymer thin films can be achieved with a narrow distribution of molecular weights. Tuning of size and periodicity of blocks can be achieved by changing the molecular weight of copolymer, which are the key parameters for various applications in energy, membranes, fluidics and information technology [409–412]. Polymer-substrate and polymer-air interaction plays an important role in controlling the morphology of block copolymer thin films. The position of the copolymer depends on these interaction. For example, the copolymer which occupy the interface of the substrate have a better interaction with surface. Nanotemplate application of block copolymer makes it imperative to have well ordered structure which provides high density and equal separation of domains. These domains have preferred orientations. The perpendicularly oriented domains have a tendency to align parallel to the surface due to the preferential interaction. [413, 414]. Various approaches like external stimuli, surface modification and non-equilibrium methods are employed to achieve desired orientation [415–417]. Supramolecular assembly has also been used as an efficient approach to obtain well-ordered perpendicular nanoporous templates [26, 418–421]. These nanotemplates can be used for fabrication of highly ordered inorganic nanostructures for various applications like solar cells, light-emitting diode (LED), gas sensing, gas separation, field effect transistor (FET) and to study antibacterial activity [232, 422–426]. Ordered assemblies

of nanomaterials in 1D, 2D, and 3D, can be produced by bottom-up technique which has been recognized as a well-designed and efficient approach [427–430]. The flexibility in the selection of inorganic material and the arrangement of molecules make these approaches versatile over the well-known top-down lithographic techniques. Particularly, block copolymers pattering represents a most promising technique for the fabrication of ordered inorganic nanostructures (metal/metal oxide nanoparticles, nanorods, quantum dots) due to their self-assembly into a variety of well-ordered and periodic nanoscale patterns with a typical dimension of $5 - 100\ nm$ [13, 413, 431, 432].
Nanostructures can be fabricated by either *in-situ* or *ex-situ* approach. However the *ex-situ* approach is more controllable and efficient because the properties of the pre-synthesized nanoparticles can be tailored easily. In the *in-situ* approach, selective incorporation of nanoparticles in one of the blocks of block copolymer is an easy process, but it is less attractive because it enhances the tendency of agglomeration of nanoparticles and form the clusters [433] and the morphology will also be altered at a particular concentration of nanoparticles [434]. To retain the same structure as that of block copolymer domains and to avoid the cluster formation, direct deposition of nanoparticles (*ex-situ*) into the templates is an effective approach to fabricate the well-ordered nanoparticles array with high fidelity. In this chapter, we have investigated the supramolecular assembly from PS-*b*-P4VP and additive HABA in 1-4 dioxane solvent with the different molecular weight of PS-*b*-P4VP (M_n =39.9 kg/mol, M_n = 41 kg/mol, and M_n = 205 kg/mol) and different relative volume fraction of P4VP. Cylindrical (with different size) and lamellar nanodomains with an orientation perpendicular to the surface have been observed. Furthermore we herein made an effort to subdue the agglomeration by sonication during deposition and a well-ordered array of ZnO and RE doped ZnO nanodots has been obtained by incorporating the pre-synthesized nanoparticles into the templates. This approach is versatile and can be applied to the other metal oxides nanostructures also.

6.2 Experimental details

In this section we describe the fabrication of well ordered nanotemplates. Prepared nanotemplates were then backfilled by direct deposition of nanoparticles. Subsequently, the templates were characterized by AFM to observe the morphological behavior.

6.2.1 Deposition of thin films of supramolecular assembly

Diblock copolymer PS-*b*-P4VP and HABA were used to prepare supramolecular assembly of thin films. For this, solution of PS-*b*-P4VP with HABA was prepared using the following steps:

- An appropriate amount of PS-*b*-P4VP and HABA (P4VP/HABA molar ratio 1:1, 1wt%) was dissolved separately in 1-4 dioxane under sonication.
- The polymer solution was added dropwise into the HABA solution, and the resultant solution was stirred in a closed volumetric flask for 3 hrs at 75°C.
- The resulted solution was allowed to cool at room temperature and left for overnight to complete the hydrogen bonding between HABA and P4VP.
- The solution was filtered with 0.2μ PVDF syringe filter.

Separate solutions were prepared for PS-*b*-P4VP of different molecular weight following the same procedure. Thin films of block copolymer were deposited onto the cleaned silicon substrates by dip coating technique. Substrates were immersed into the filtered PS-*b*-P4VP/HABA solution for one minute and withdrawn at a speed of 100 mm/min.

6.2.2 Ordering in thin films and surface reconstruction

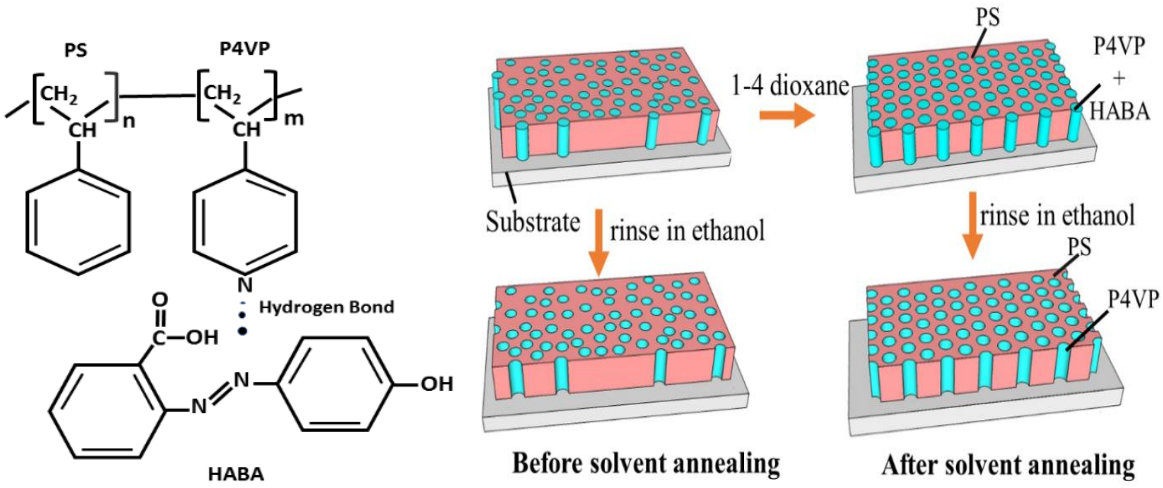

Figure 6.1: Chemical structure of PS-*b*-P4VP/HABA supramolecular assembly (left) and schematic for the fabrication of nanotemplates (right).

Block copolymer thin films were dried and further annealed for 5 days in the vapours of 1-4 dioxane in an air sealed glass chamber in order to improve the ordering of nanodomains.

Glass chamber was opened and allowed the solvent to evaporate freely. The ordered thin films were rinsed with ethanol for fabrication of nanotemplates. Ethanol is good solvent for P4VP/HABA and poor solvent for PS so it extract P4VP/HABA selectively. Chemical structure of PS, P4VP/HABA (left) and schematic for the fabrication of block copolymer nanotemplates (right) is depicted in figure 6.1. Block copolymer thin films were dried and further annealed for 5 days in the vapours of 1-4 dioxane in an air sealed glass chamber in order to improve the ordering of nanodomains. Glass chamber was opened and allowed the solvent to evaporate freely. The ordered thin films were rinsed with ethanol for fabrication of nanotemplates. Ethanol is good solvent for P4VP/HABA and poor solvent for PS so it extract P4VP/HABA selectively. Chemical structure of PS, P4VP/HABA (left) and schematic for the fabrication of block copolymer nanotemplates (right) is depicted in figure 6.1.

6.2.3 Deposition of NP's into the templates

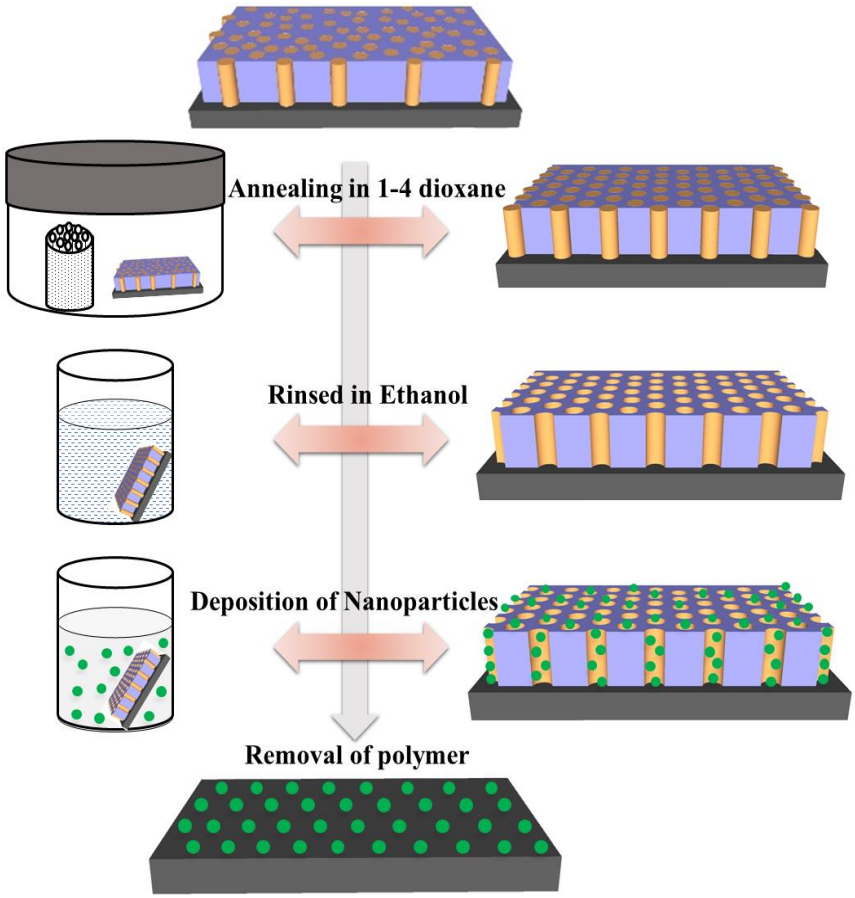

Figure 6.2: Scheme for the fabrication of ordered ZnO and RE doped ZnO nanostructures.

Cylindrical porous nanotemplates were used for the fabrication of ordered nanodots. Templates were immersed into the aqueous solution of ZnO NP's. Synthesis of ZnO and RE doped ZnO NP's has been described in detail in section 3.3.1. For the deposition of nanoparticles, 0.05 gm powder of pre-synthesized ZnO and RE doped ZnO NP's was dispersed in 20 ml of deionized (DI) water by sonication and then filtered through $0.2\mu m$ PVDF filter. The filtered solution becomes almost transparent which indicates the of dispersion of NP's and reduction of agglomeration. The ordered vertically aligned cylindrical nanoporus templates were dipped into the filtered solution for 6-12 hours under the sonication. Continuous sonication reduces the problem of agglomeration of metal oxide NP's. Schematic of the process for *ex-situ* deposition, followed in the present study is depicted in figure 6.2.

6.3 Results and discussion

PS-*b*-P4VP is most popular diblock copolymer and easily available in a large variety of molecular weight. Mostly, carboxylic or hydroxyl functional group of small molecules have been hydrogen bonded with P4VP block. Supramolecular assembled thin films of diblock copolymers were deposited on cleaned Si substrate by dip coating from 1 wt% composite solution of PS-*b*-P4VP and HABA. HABA molecules are expected to associate with P4VP blocks via hydrogen bond. Thin films were annealed in the vapours of 1-4 dioxane for 5 days in a sealed glass chamber. Surface morphology of thin films was observed by AFM in both the cases, before annealing and after annealing.

6.3.1 Vertically aligned cylindrical porous templates

Dip coating method were used to prepare supramolecular assembly of di-block copolymer PS-*b*-P4VP/HABA as described in section 6.2.1. In order to achieve the ordering of these thin film templates, solvent annealing were done as describe in section 6.2.2 Figure 6.3 (left) represents the height image of surface morphology of as deposited thin films of PS-*b*-P4VP/HABA ($M_n^{PS} = 35.5\ kg/mol$, $M_n^{P4VP} = 4.4\ kg/mol$). It can be observed from the images that blocks are not well ordered while the both phases are separated within nanoscale which were attributed to the fast evaporation of solvent due to which polymer chains have not sufficient time to rearrange themselves to attain the equilibrium morphology. Root mean squre (RMS) roughness of the image was found as $\sim$1.2 nm.Thermal and solvant annealing are the responsible factors for ordering of thin films. Solvant annealing has been adopted in order to achieve supramolecular assembly to avoid the evaporation of small molecules at high temperatures because a little loss of

small molecules can greatly affect the structures in thin films [418]. Further deposited thin film were chemically annealed by using 1-4 dioxane in glass chamber which were further examined by AFM, appearance of nanodot like structure were observed (shown in figure 6.3 (right)).

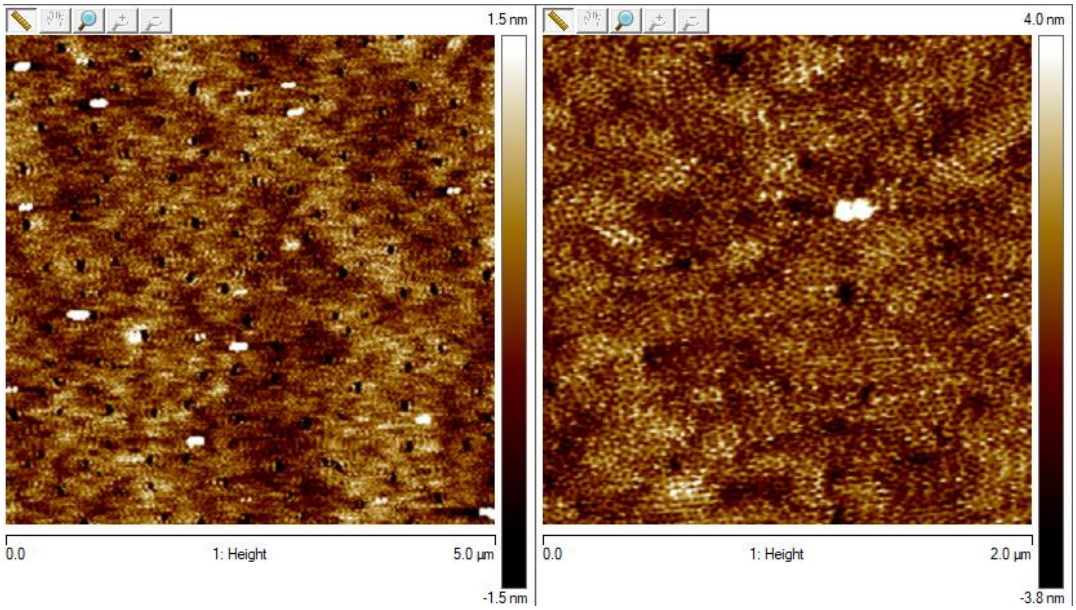

Figure 6.3: AFM height and phase images of PS-*b*-P4VP/HABA ($M_n^{PS} = 35.5\ kg/mol$, $M_n^{P4VP} = 4.4\ kg/mol$) thin films (left) without annealing and (right) annealed in 1-4 dioxane vapours.

Dispersion of domains of P4VP/HABA in PS matrix resulting dot like stucture. annealed thin films having reduced RMS roughness from $\sim$1 nm for an area $2 \times 2\ \mu m^2$ (lateral scale). The relative volume fraction of P4VP/HABA in supramolecular assembly of PS-*b*-P4VP/HABA is 0.3. Arrangement of cylindrical domains (phase diagram demonstrated by Matsen and Bates [20]) is acceptable for this fraction. It could be hypothesized that these dots like features are the apex of cylindrical domains formed by P4VP/HABA. The orientation of cylindrical domains in supramolecular assembled thin films are strongly depends on two factors one is selection of solvents to each block and the second one is preferential interaction of the blocks to the surface of substrate, which is already reported by Tung *et al.* [280]. In annealing, the solvent molecules provide the mobility to supramolecules which causes the rearrangement of supramolecules into more ordered structures. Though mobility of each phase may be different in different solvent. In order to prepare ordered nano templates, the films were removed from the annealing chamber and rinsed in ethanol for 20 minutes for surface reconstruction and selectively extraction of HABA. The role of ethanol is to create the disturbance of hydrogen bonds

between HABA and P4VP and removal HABA molecules from P4VP/HABA domains in thin films.

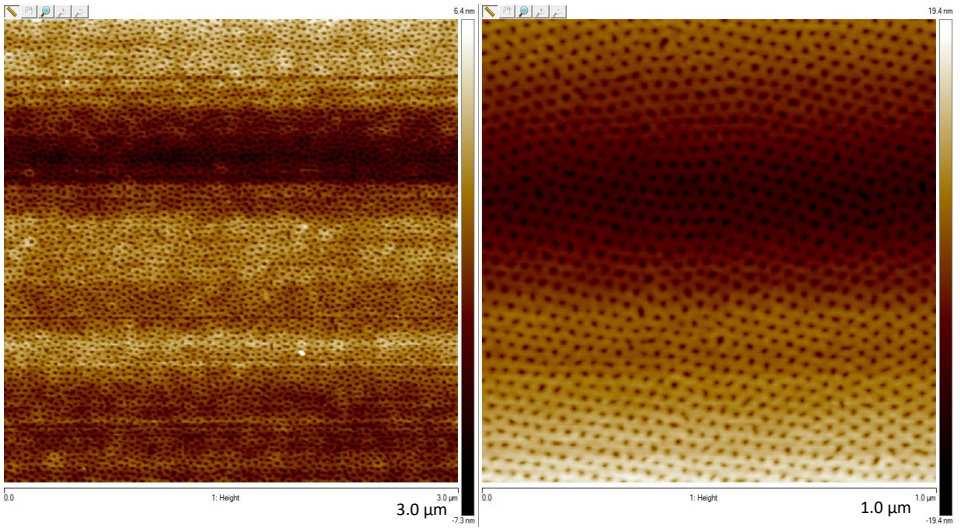

Figure 6.4: AFM height image of PS-*b*-P4VP/HABA ($M_n^{PS} = 35.5\ kg/mol$, $M_n^{P4VP} = 4.4\ kg/mol$) thin films after immersing in ethanol.

So, the removal of HABA responsible for leaving the nanochannels/nanopores lined with functional group. Ethanol enhances the mobility of P4VP/HABA chains but the movement is hindered by frozen PS chains as it is good solvent for P4VP/HABA and bad solvent for PS. This helps to retain the morphology after dipping into ethanol. PS-*b*-P4VP/HABA thin films after annealing as shown in (after washing in ethanol) figure 6.4. Ethanol washed images are clear to observe that the solvent annealed thin films shows hexagonally arranged cynlindrical pores normal to the surface of the substrate after surface reconstruction as well as removal of HABA by dipping the film into ethanol. As stated by the self-consistent field theory, the morphological parameters depends on the molecular weight, Flory Huggins interaction χ, volume fraction and the degree of polymerization [435]. Figure 6.5 morphology of the supramolecular assembled as spun (left) and further after solvent annealing (right) thin films of PS-*b*-P4VP with the high molecular weight of polymer $M_n^{PS} = 130\ kg/mol$, $M_n^{P4VP} = 75\ kg/mol$. Relative volume fraction of P4VP is also much higher. P4VP has weight fraction of ~ 0.36 and it increases to ~ 0.65 after addition of HABA in equimolar ratio which is nearly at the boundary of lamellar/cylindrical in bulk. Deposition and annealing parameters are kept same as for the lower molecular weight ($M_n^{PS} = 35.5\ kg/mol$, $M_n^{P4VP} = 4.4\ kg/mol$). P4VP/HABA dots in PS matrix are observed in figure 6.5.When HABA and P4VP are bind together then the P4VP-HABA constitutes the majority phase. In spite of P4VP-HABA constituting the majority phase, P4VP-HABA core surrounded with PS corona

was observed. This is referred as "inverted phase" which is dependent on either nature of the solvent or the interaction between the block and solvent and concentration of the solution.

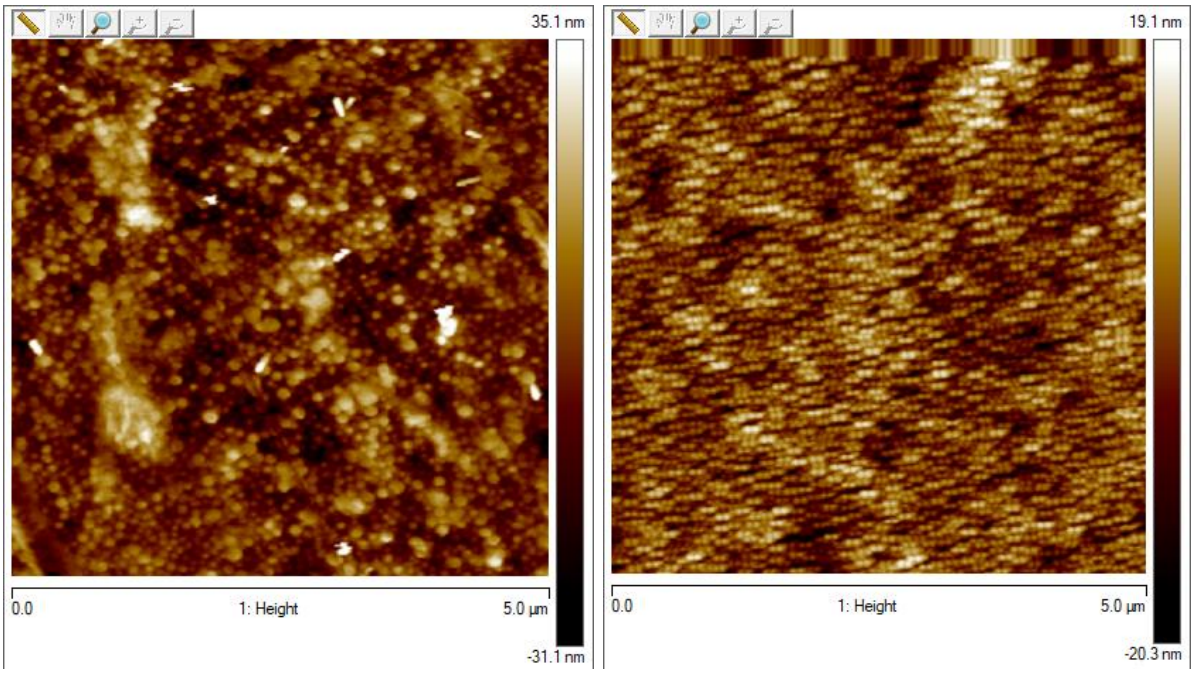

Figure 6.5: AFM height images of PS-*b*-P4VP/HABA ($M_n^{PS} = 130\ kg/mol$, $M_n^{P4VP} = 75\ kg/mol$) thin films, (left) without annealing and (right) annealed in 1-4 dioxane

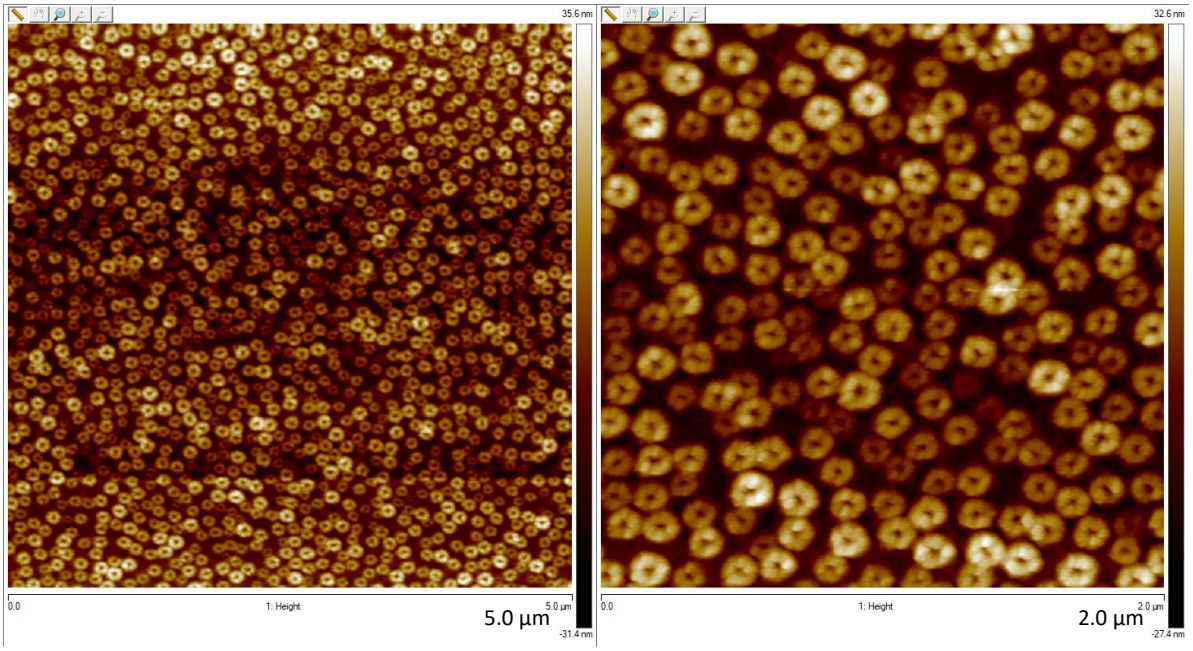

Figure 6.6: AFM height images of PS-*b*-P4VP/HABA ($M_n^{PS} = 130\ kg/mol$, $M_n^{P4VP} = 75\ kg/mol$) thin films after immersing in ethanol

If the solvent possesses a preferential affinity to the minority block then rate of swollen will be more than the majority block and effectively it become the majority block. In present case the the affiity of the 1-4 dioxane is greater towards the PS than P4VP. Evaporation rate of solvent and interfacial interactions during the deposition are also important factors [436, 437]. Rinsing in ethanol results the nanoporous film with higher pore size as compared to lower molecular weight ($M_n^{PS} = 35.5\ kg/mol$, $M_n^{P4VP} = 4.4\ kg/mol$) (figure 6.6). Similar results for high molecular weight have also been obtained by Laforgue *et al.* using DHN as an additive [27].

6.3.2 Vertically aligned lamellar templates

Different morphology other than cylindrical behavior were also obtained by changing the molecular weight of the block-copolymer and the variation in the sharing ratio of copolymer. For the lamellar microdomains we used the HABA and P4VP in the 1:1 fraction. Because the ratio 0.5 of P4VP/HABA is correspond the lamellar microdomains. Annealing is key parameter for the morphology of the block-copolymer, without the annealing we can't suppose the characteristic features. And the expected morphology is far from equilibrium (figure 6.7(left)), similar to case of lower relative fraction of P4VP/HABA (figure 6.3 (left)).

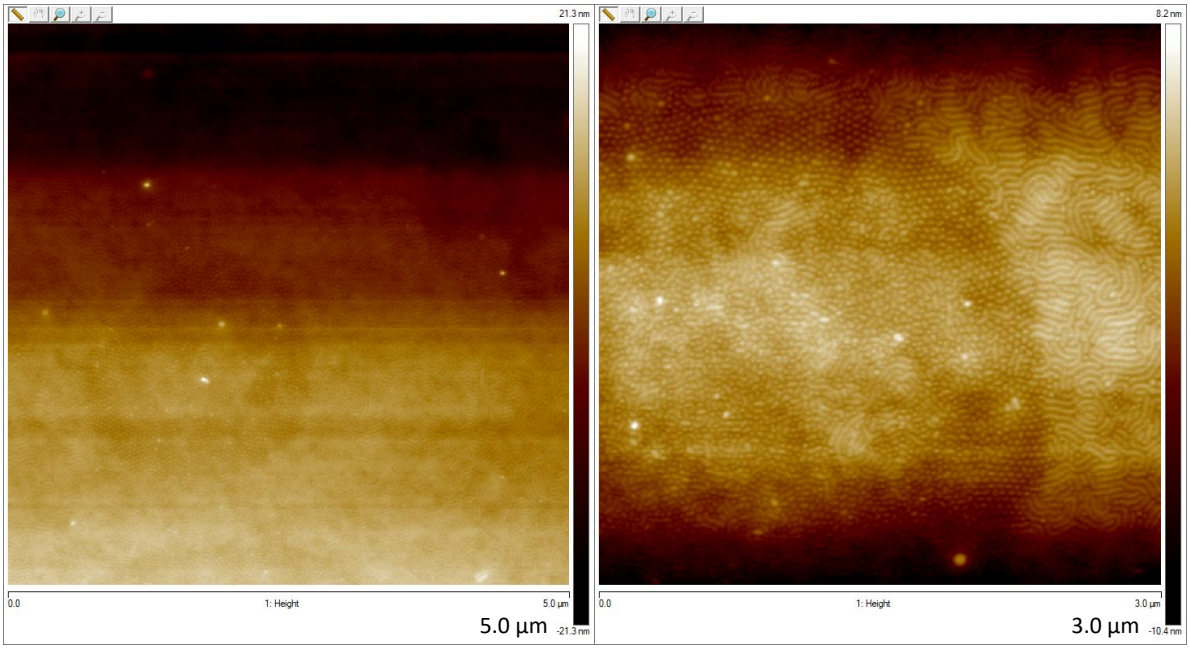

Figure 6.7: AFM height and phase images of PS-*b*-P4VP/HABA ($M_n^{PS} = 33\ kg/mol$, $M_n^{P4VP} = 8\ kg/mol$) thin films (left) without annealing and (right) annealed in the vapours of 1-4 dioxane.

By more time of annealing in the vapours of 1-4 dioxane, lamellar structure take place for the cause of the structural reorganization property as shown in the figure 6.7 (right) with the help of the mobility imparted. Also after the annealing, the surface roughness reduced significantly. In our case roughness become 0.5 nm from 3.9nm after annealing. Above study confirms that by varying the volume fraction, molecular weight with compatible solvent annealing in 1-4 dioxane can control nanodomains from cylinder to lamellar. Selective extraction of HABA from the annealed thin films of PS-*b*-P4VP/HABA by dipping in ethanol left the films with periodically arranged channels perpendicular to surface of substrate (figure 6.8). Figure 6.8 (left) and (right) are taken at different magnification for the clear view of lamellar channels created in the film.

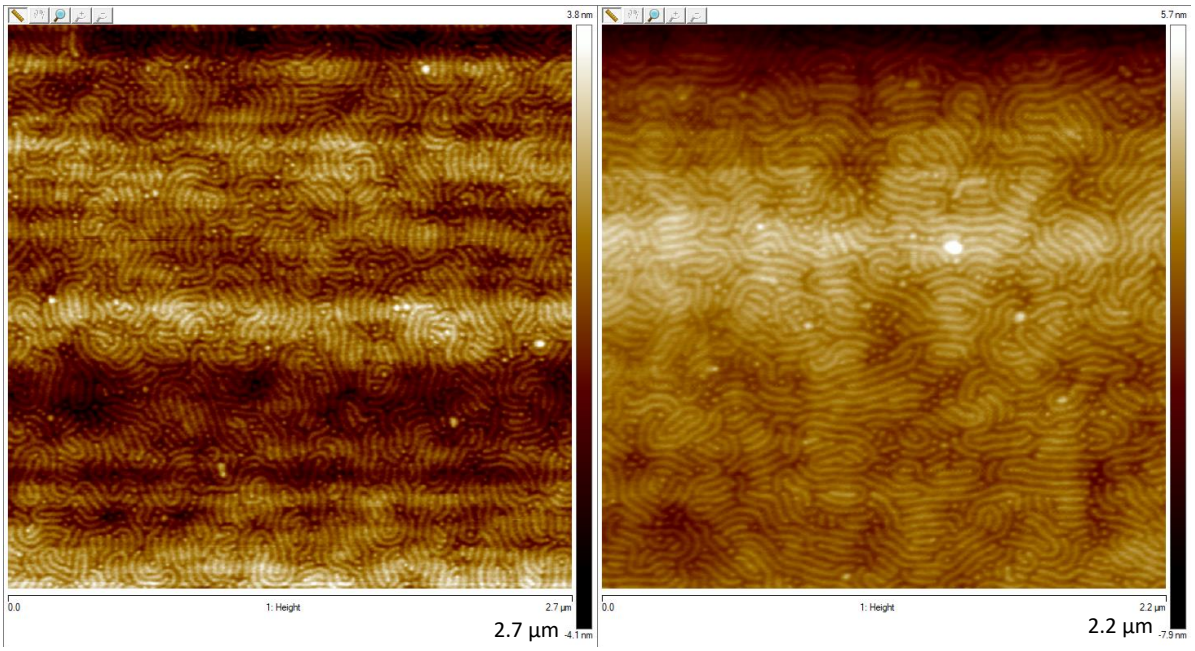

Figure 6.8: (a, b) AFM images of PS-*b*-P4VP/HABA ($M_n^{PS} = 33\ kg/mol$, $M_n^{P4VP} = 8\ kg/mol$) thin films annealed in 1-4 dioxane and after immersing in ethanol.

6.3.3 Switching behavior of thin film

Annealing the solvent plays important behavior in controlling the morphology of block copolymer thin films [285]. Switching behavior was observed in thin films after annealing in two solvents for different duration. Annealing in oxygen-bearing (benzene, chloroform etc...) and non-oxygen-bearing (THF, 1,4-dioxane etc...) solvents has shown completely different surface patterns. After fabrication of films, it was initially annealed in chloroform for 5 days to get perpendicularly arranged cylindrical structures 6.9(leftt). Further the hence obtained structures were annealed in 1,4-dioxane for 3 days to obtain mixed

morphology (6.9 (middle)) where some of the nanostructures were arranged parallel and some perpendicular to the substrate. Increasing the annealing time to 5 days, we could observe a complete transformation from perpendicular arrangement to parallel arrangement as shown in figure 6.9 (right). Similar kind of results were obtained by Stamm *et al.* [22, 285]. It was due to the different selectivity of solvents to each copolymer. Correlation between the orientation of microdomains in thin films and the content of associated small molecules is well reported and observed that the adequately high molar ratio of small molecules drives/directs the perpendicular orientation of microdomains [24, 438].

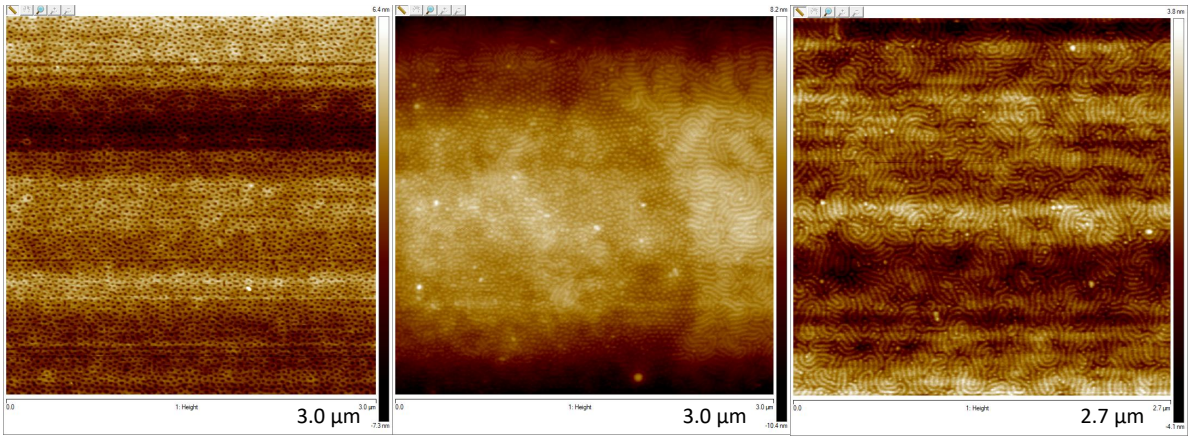

Figure 6.9: AFM images of PS-*b*-P4VP/HABA ($M_n^{PS} = 33\ kg/mol$, $M_n^{P4VP} = 8\ kg/mol$) thin films annealed in chloroform and after immersing in ethanol.

6.3.4 ZnO and RE doped ZnO NP's deposition in nanotemplates

These nanotemplates were dipped into the aqueous solution of pre-synthesized nanoparticles, and the nanoparticles were allowed to enter into the hexagonally arranged cylindrical pores by the diffusion and the capillary forces. This step was performed in the ultrasonic bath to avoid the agglomeration of nanoparticles and blocking of the pores. Morphology of as-deposited and solvent annealed thin film of Supramolecular assembly on surface reconstruction by immersing in ethanol has been discussed in section 4.3.1. Unlike to the metal nanoparticles, metal oxide nanoparticles agglomerate and settle down very fast which is unfavorable for the successful deposition of nanoparticles into the pores. Nanoparticles were mixed with deionized water under sonication and subsequently filtered twice with $0.2\mu m$ PVDF filter. Obtained aqueous solution of nanoparticles turns transparent from milky white, which indicates the dispersion of nanoparticles in the solution, while bigger sized particle are filtered out.

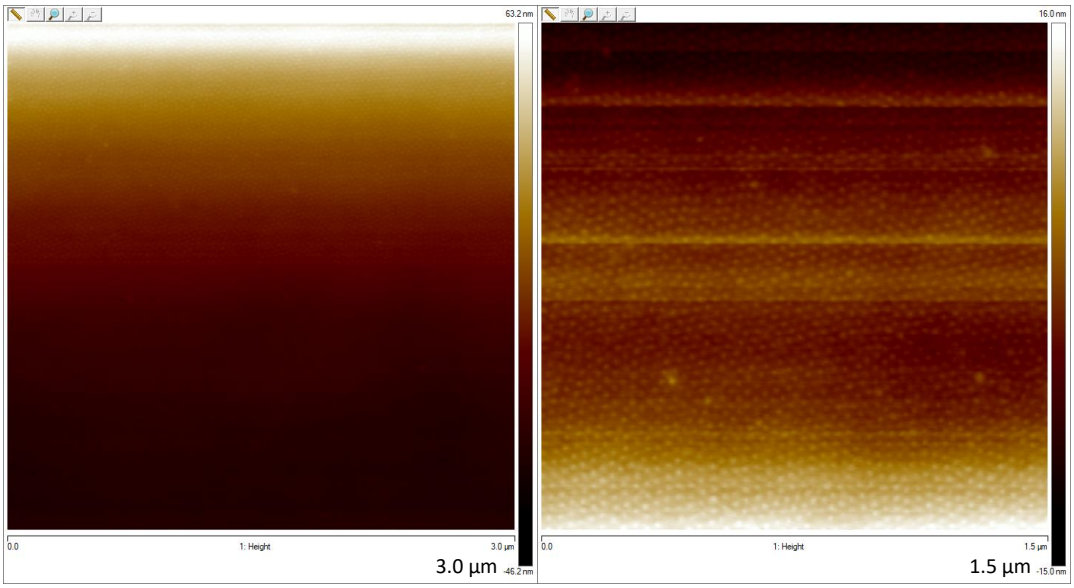

Figure 6.10: AFM images of an array of ZnO nanostructures in nanotemplate.

In addition to above method, the nanoparticles solution was continuously sonicated during the deposition, to reduce the agglomeration and cluster formation. The Supramolecular assembly nanotemplates were immersed into the sonicated and filtered aqueous solution of pre-synthesized ZnO and RE doped ZnO NP's for 9 to 10 hours. The templates were removed from the nanoparticles solution and then washed with deionized water to remove the weakly attached nanoparticles.

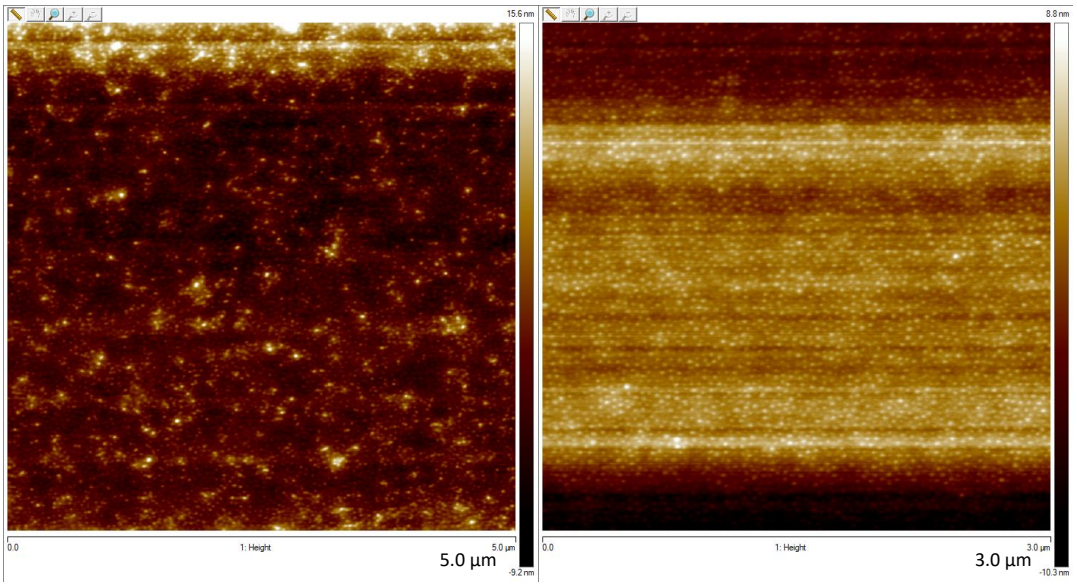

Figure 6.11: AFM images of an array of RE doped ZnO nanostructures in nanotemplate.

Figure 6.10 and 6.11 represents the AFM images of templates after deposition. AFM

image confirms the deposition of ZnO NP's into the templates. The mechanism for the deposition of ZnO and RE doped ZnO NP's into the cylindrical pores of templates can be proposed as follows. The first and foremost condition for the direct deposition of pre-synthesized nanoparticles is its size, which should be much smaller than the pore size which is satisfied in the present study. However, in case of transition metal oxides, especially ZnO and RE doped ZnO NP's, the agglomeration of NP's is a hurdle which has been subdued here by filtration and sonication during the deposition. So, in the present case, the diffusion of nanoparticles into the pores is tuned. Second, the selection of the solvent for the dispersion of nanoparticles is also important. It should not perturb the structure of templates, and it is required to allow the wetting of pores exclusively. In this regard, the aqueous solution of nanoparticles is advantageous in the present study. Since P4VP is hydrophilic and PS is hydrophobic, so the solution of nanoparticles readily wet the pore walls since the pores are lined with the P4VP functional group. The structure remains intact after deposition of nanoparticles into the pores since the PS matrix won't expand by imbibing the solution. Once the pore walls get wet by the solution, the capillary force assist entering the nanoparticles into the pores. Additionally, coordination of the nanoparticles with pyridine group lined in the pore walls plays a crucial role which further promotes the deposition of nanoparticles into the pores.

6.4 Applications

Ordered ZnO and RE doped ZnO nanostructures can be obtained after the removal of PS matrix from the silicon substrate. Ordered nanostructures are of particular interest since it has potential applications in optoelectronic devices such as LED's, laser diodes, field emitters etc...

6.5 Conclusions

In this chapter, different molecular weight were used to prepare supramoleculer assembly of PS-*b*-P4VP/HABA. It can be concluded that, to prepare ordered and dense nanostructure, use of supramolecular assembly is a functional and reliable approach. In the beginning of the process ordered structure of the thin film is not obtained because the fast evaporation of solvent. But the solvent annealing with 1-4 dioxane starts the ordering of the supermolecular assembly. In the process of solvent annealing the mobility of copolymer molecules imparted by the evaporated solvent molecules, which guides

the copolymer molecules for rearrangement. Based on the selectivity of solvent decide the structure of block-copolymer. In our case, the Minority block (P4VP/HABA) forms cylinders surround by majority block (PS) with 1-4 dioxane solvent. By the molecular rearrangement, nanotemplates of cylindrical pores obtained with hexagonal arrangement. To control the size of porous structure we can change the molecular weight keeping the volume fraction of copolymers as same. Lamellar microdomains have been also obtained by fluctuating the molecular weight as well as the changing the fraction of each phase. By using these porous nanotemplates ZnO and RE doped ZnO nanostructures were obtained. For the both type of nanostructures aqueous solution of nanoparticles and immersion process was used. In the immersion, wetting of walls helps the selective assembly of NP's. Sonication is used during the deposition, because sonication delivers a pathway to nanoparticles to go inside the pores. At the last by removing the copolymer, ordered Zno and RE doped ZnO has been achieved. This type of procedure can be applied to other shape and size of ZnO and ZnO composites, because these structure have various valuable optoelectronics applications.

7

Antibacterial activities of *ZnO* NP's

7.1 Introduction

Inorganic Metal oxides like MgO, TiO_2, SiO_2 and *ZnO* are being used for antimicrobial applications [439–442] because of their stability and long shelf life as compared with organic antimicrobial agent. The antibacterial activity of these NP's have been tested with different bacteria such as *Staphylococcus aureus*, *Escherichia coli* and *Bacillus subtilis*. Due to antibacterial, low toxic and biocompatible property of *ZnO* NP's it is used as filling in medical materials and drug packaging. Krishna *et al.* reported that antibacterial activity of *ZnO* NP's is inversely proportional to the size of NP's in S. aureus [443], size-dependent antimicrobial response of zinc oxide NP's is also reported by Palanikumar L. *et al.* [444]. There are several individual reports on antibacterial properties of *ZnO* NP's prepared by various route and morphology dependent antibacterial properties against some bacteria. Microorganisms attached to surfaces form biofilms. This biofilm is a slimy protective layer of exopolysaccharides (EPS) which protects the microbial cells from direct contact and effect of antibiotics and xenobiotics [445, 446]. These structures cause hygienic problems in food industry [447], septic conditions in medical dominion [448, 449] and membrane fouling in water treatment plants [450]. Biofilm formation is significant for both medical and industrial operations. It causes biofouling which reduces permeability of membrane thereby increasing energy costs, limits lifetime of membrane and hence its cost effectiveness. To overcome the evolving problem of biofilms two strategies have been proposed, the inhibition of biofilm formation or treatment and eradication of biofilms already formed. Microorganisms within biofilms are more resistant to antimicrobial compounds than planktonic cells [451, 452]. Several treatment methods are adopted which includes use of enzymes, surfactants, biocide treatment etc... Enzymes can be used to disrupt the outer biofilm

matrix as they cause cells dispersion leading to exposure of antibiotics. However, their large cost is a major limitation in their use [453]. Surfactants when applied to surfaces inhibit adhesion and attachment of bacteria but their activity depends on the type of surface, microorganism and temperature [454]. The major challenge in the food and water treatment industry is to prevent the conditioning biofilm formation on the surfaces of equipment and membranes. Second messenger cyclic di-GMP (c-di-GMP) has emerged as a novel signal which can control formation of biofilm [455, 456]. c-di-GMP synthesis takes place via DGC which inhibit the activity of the enzyme that produces cyclic di-GMP. These molecules prevent biofilm formation via targeting of c-di-GMP signaling [457, 458]. Winkelstroter *et al.* [459] used bacteriocins to evaluate Listeria monocytogenes biofilm formation. Lequete *et al.* [460] reported the cleaning efficiency of polysaccharides and proteolytic enzymes against biofilms of food industry bacteria. Another antibiofilm strategy these days embraces nanotechnology which has emerged as one of the most promising approach [461, 462]. NP's are recently being exploited as antibiofilm agents for the treatment of infection involving biofilms. The nanomaterials have attracted many researchers as they possess superior features like extremely small size, enormous surface area, high reactivity and easy penetration into biofilm matrix. Martinez-Gutierreza *et al.* [463] studied the effect of Ag NP's on biofilm under static and high fluid shear conditions. Lungu *et al.* [464] revealed that Ag-TiO_2 nanocomposites possess strong activity against biofilm formation. The effect of Ag NP's decorated with graphene towards biofilm formation was assessed against S. typhimurium present on stainless steel surfaces [465]. Similarly, it was observed that graphene nanocomposites with *ZnO* NP's inhibited S. mutans biofilms formed on artificial tooth model [466]. Chitosan-Ag NP's exhibited excellent antibiofilm activity against P. aeruginosa, while same amount of chitosan did not show any significant inhibition in biofilm activity of S. aureus [467]. Sambhy *et al.* [468] showed that silver bromide nanocomposites possess good antibiofilm activity. Polyvinyl chloride *ZnO* nanocomposite was reported to have high antibiofilm activity against S. aureus as compared to pure polymer [469]. Eshed *et al.* [470] reported that *ZnO* and CuO NP's coated teeth have significantly reduced biofilm formation when compared with untreated teeth. Shrestha *et al.* [471] showed that chitosan-NP's and *ZnO*-NP's disrupted biofilm structure of E. faecalis when exposed to 90 days. Hsueh *et al.* [472], demonstrated the effect of *ZnO* NP's on biofilm formation of *Bacillus subtilis*. Se NP's were used to nano-functionalize polycarbonate medical devices and antibiofilm activity was studied [473]. Hernandez-Delgadillo *et al.* [474] reported that colloidal aqueous solution of bismuth oxide NP's completely inhibited biofilm formation. *ZnO* NP's are one of the most popular choices among metal oxides of commercial importance and has been widely used as a potent antimicrobial

agent and as a UV protector in cosmetics [122, 182, 232, 475]. Their high catalytic activity make them important industrial additive for many products, including plastics, cement, lubricants, rubber, glass, and food [476, 477]. In the present study, *ZnO* NP's have been synthesized by via chemical method and their effect on bacterial growth and biofilm formation of model non-pathogenic gram positive bacteria, *Bacillus subtilis*, was evaluated. To assess the variation in biofilm mass, crystal violet staining was done in which the proportion of dye bound to the adhered cells is related to the overall biofilm biomass. Morphological changes were analysed via phase contrast and scanning electron microscopy that provides the information regarding biofilm surface architecture and modifications. The impact of NP's on bacterial adhesion property was correlated to the bacterial cell viability which has been assessed in term of ROS generation and subsequent catalase activity changes.

7.2 Results and discussion

7.2.1 Antibacterial activity

The antimicrobial activity of these *ZnO* NP's synthesized by method 4.2.2 was evaluated using *Bacillus subtilis* bacteria. The NP's were taken at concentration of 2, 5 and 10 mg/ml. The growth of bacteria was found to be inhibited near and around the areas where the NP's were placed on the media (figure 7.1).

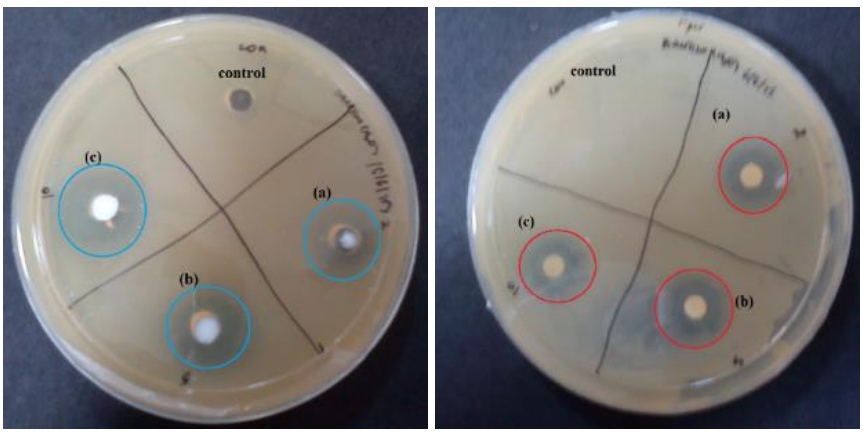

Figure 7.1: Antibacterial activity of *ZnO* NP's on *Bacillus subtilis* at concentration of (a) 2mg/ml (b) 5mg/ml (c) 10mg/ml.

The diameter of zone of inhibition for these *ZnO* NP's were found to increase with increase in the concentration of NP's. The antimicrobial activity of *ZnO* NP's can be attributed to the fact that the NP's can easily impregnate into the cell wall of the

bacteria [478]. As shown in figure 7.2(a), untreated *Bacillus subtilis* cells exhibited green fluorescence indicating presence of 100% viable bacterial cells, whereas the *ZnO* NP's treated bacterial samples show a mixture of red and green fluorescence confirming a mixture of viable and non-viable cells (figure 7.2 (b)- 7.2(e)). The viable bacterial cells having intact cell membrane are stained green by the FITC fluorescence dye, whereas non-viable bacterial cells with deformed cell membrane upon NP's treatment are stained red by propidium iodide fluorescence dye.

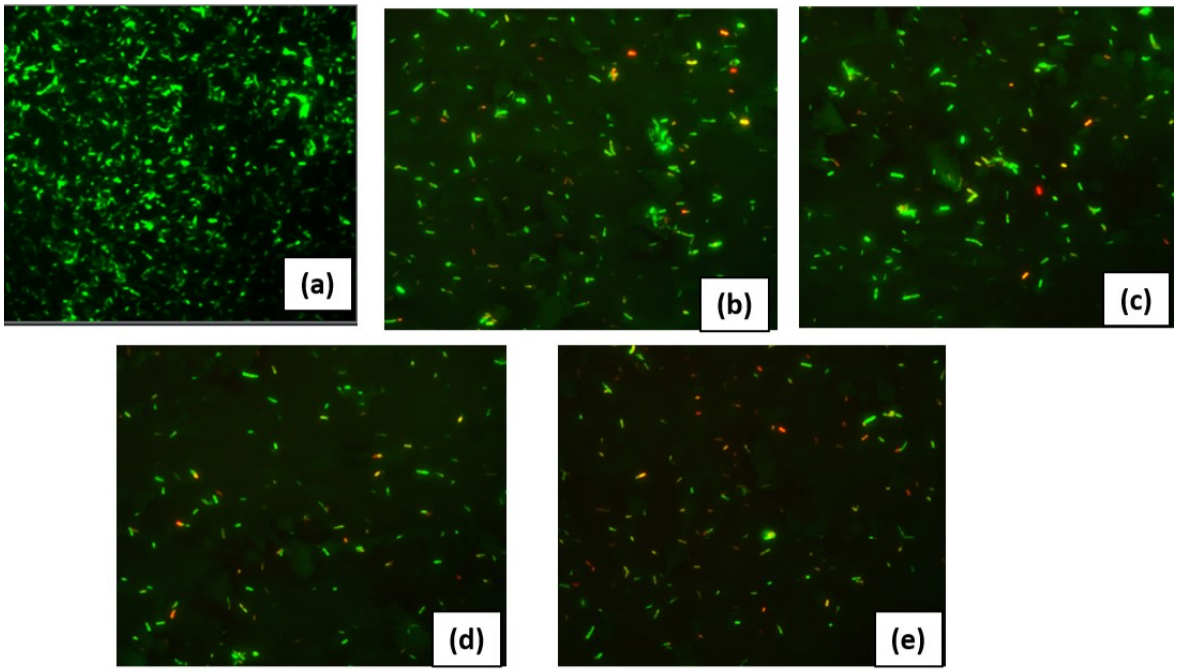

Figure 7.2: Fluorescence micrographs (a) Control (witout *ZnO* NP's) (b) at *ZnO* concentration of 1mg/ml (c) 2mg/ml (d) 5 mg/ml (e) 10 mg/ml.

7.2.2 Effect of *ZnO* NP's on *Bacillus subtilis* biofilm formation

After an incubation of 24 hrs, the bacterial cells were found to adhere at air-media interface in the form of biofilm (figure 7.3). This confirms that *Bacillus subtilis* is motile organisms and forms a biofilm at the air-liquid interface. The density and area of the biofilm present on the surface was observed as seen in figure 7.3(b). In case of negative control (where the coverslip was kept in blank solution i.e., no bacterial inoculation or NP's treatment) there was no signs of bacterial adhesion (figure 7.3(a)) while in case of positive control and *ZnO* NP's treated tubes (figure 7.3(b) bacterial biofilm was observed. However, it was more prominent in case of control and showed a reduction in density with increase in NP's concentration. Also the turbidity of the culture showed the same decline.

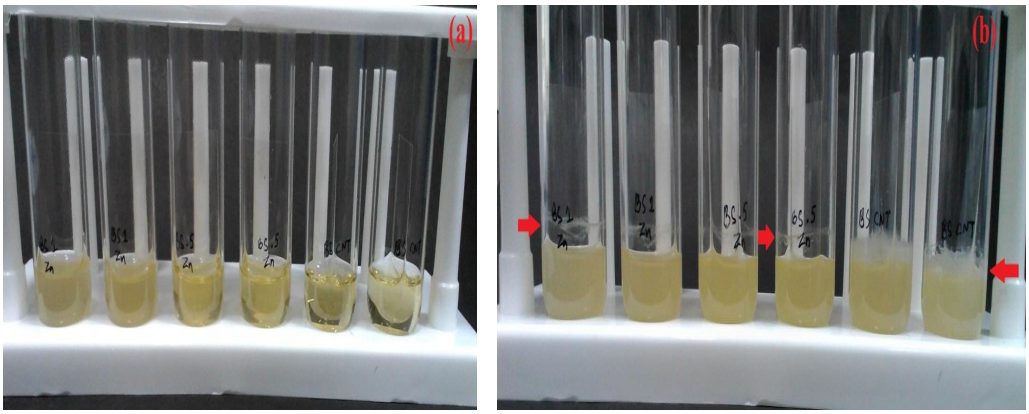

Figure 7.3: Biofilm formation setup (a) before incubation and (b) after incubation with *ZnO* NP's. The concentration *ZnO* NP's in tubes: control (first 2 tubes from left), 0.5 mg ml^{-1} (2 tubes in mid) and 1 mg ml^{-1}(first 2 tubes from right).

This indicated the biofilm formation was affected in the presence of *ZnO* NP's. It was observed that the increase in dose of the NP's in medium reduces the adhesion of bacterium and hence delays the formation of biofilm [479].

7.2.3 Crystal Violet Assay

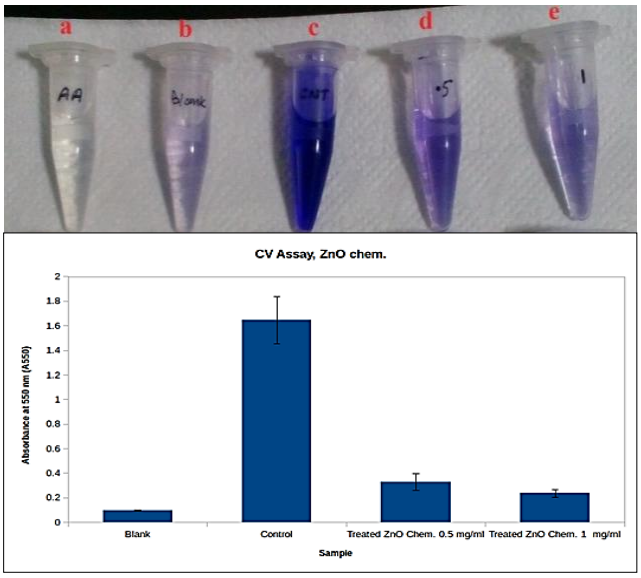

Figure 7.4: (1) Dissolution of Crystal Violet Dye: (a) Acetic acid (b) Blank (c) Control (d, e), treated with *ZnO* NP's with concentrations 0.2 and 0.5 mg ml^{-1} respectively. (2) Graph showing crystal violet absorbance at 550 nm by blank, control and *ZnO* NP's treated samples.

The coverslips after incubation were stained with the dye and the biofilm region was detected as violet. The control coverslip had more prominent stained region as compared to the *ZnO* NP's treated ones. The dissolved stain showed a gradual decline in concentration dependent manner (figure 7.4(up)). This surface-associated dye can also be solubilized and measured in optical density (OD) for semi quantitative assessment of the biofilm formed [480, 481]. The mean absorbance values at 550 nm after 24 hrs showed that control culture formed more biofilm as compared to those treated with NP's, while the mean absorbance values reduced with increase in NP's dose (figure 7.4(down)). There was nearly 86% reduction in biofilm formation after NP's treatment. Crystal Violet dye binds to negatively charged surface molecules like polysaccharides and eDNA of extracellular matrix [482]. Since it binds cells as well as matrix components it is generally used to evaluate biofilm biomass in toto [483].

7.2.4 Scanning Electron Micrographs

Micromorphology of the biofilm was observed by SEM. The formation of exopolyssacharide (EPS) assisted bacterial surface adhesion was observed in the scanning electron micrographs (figure 7.5(a)). The biofilms were composed of aggregated rod, and extracellular matrix-like structures were visible (figure 7.5(b)). In control macrocolony was observed having a mesh-like structure (figure 7.5(c)), while most of the region in treated sample showed initial phases of biofilm formation, i.e., adherence of cells and linear chain formations (figure 7.5(d)). In control, biofilms exhibited a smooth surface, cells well embedded in the EPS matrix and proper network of channels (figure 7.5(e)) while in *ZnO* treated samples, biofilm exhibited rough surface, NP's were embedded along with very few cells, and empty EPS matrix was observed (figure 7.5(b, d & f)). Since the particles cause decrease in density of biofilm (which is clear from crystal violet assay) the adhered cells are prone to detach more during the sample preparation, hence empty EPS matrix are prevalent in treated sample. As reported *ZnO* NP's cause collapse of the bacterium by metal ions uptake into cells, intracellular depletion, and disruption of DNA replication, releasing metallic ions and ROS generation and accumulation and dissolution of NP's in the bacterial membrane [484, 485]. Similar results were observed in treated sample where rod shaped normal cells (in control) and circular shaped collapsed and deformed cells (in treated sample) were visualised (figure 7.5(f & h)). The micrographs not only concluded the concentration dependent decrease in bacterial adhesion but also showed the change in the morphology of the bacterial cells on treatment with NP's.

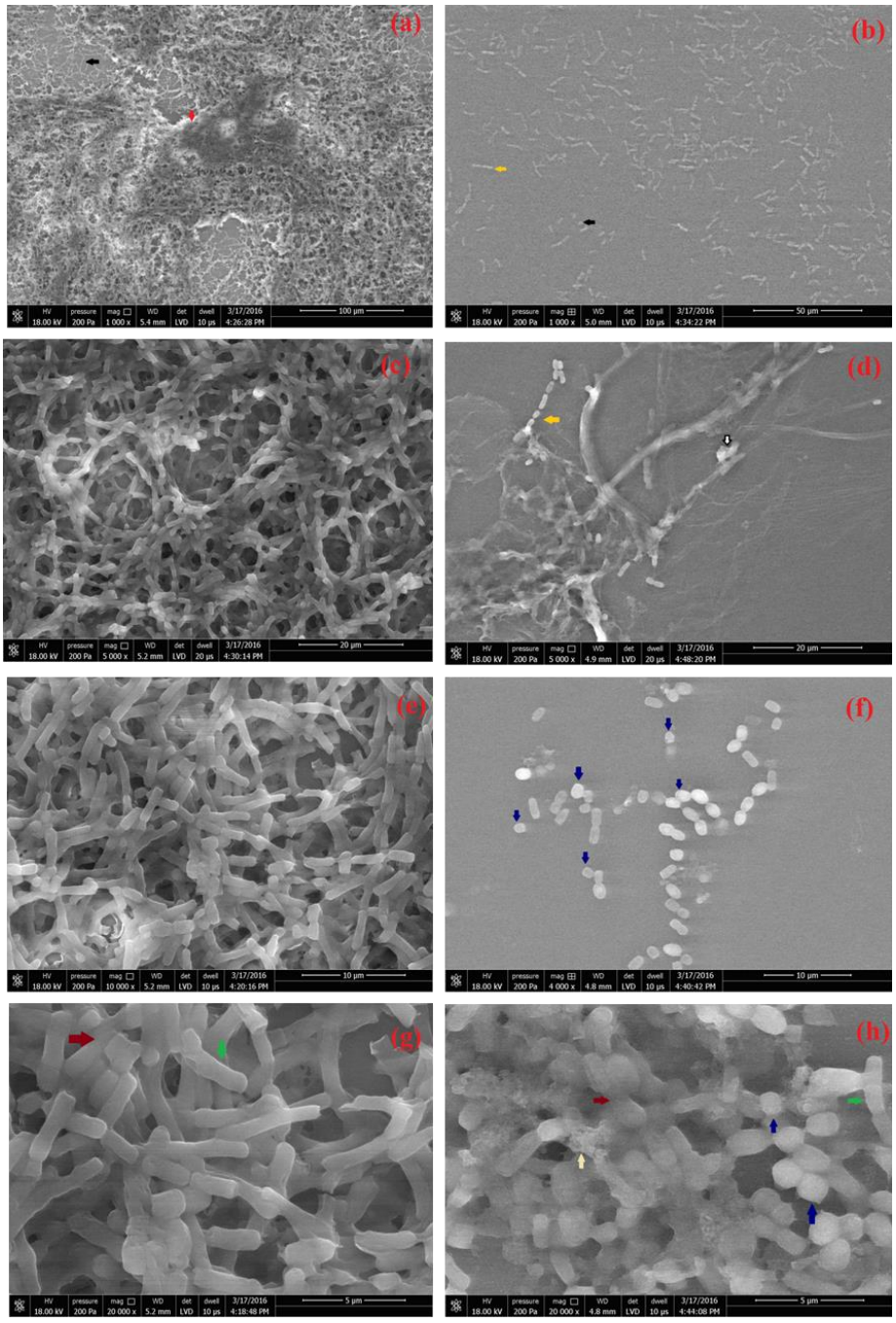

Figure 7.5: Scanning Electron Micrographs of biofilm: (a, c, e, g) Control; (b, d, f, h) treated with *ZnO* with concentration 0.2 mg ml-1. The arrows indicate: Red: biofilm (a) Black: adhered cells (a, b) Gold: linear chain formation, initial stage (b, d) Blue: deformed cells (h, f) Green: viable cell (g, h) Dark Red: EPS (g, h, i) White: embedded NP's (d, h)

7.3 Conclusion

In summary, we have studied the effect of Zinc oxide NP's on bacterial growth and biofilm formation. The *ZnO* NP's were found to have antibacterial activity and the bacterial growth was reduced in a dose dependent manner. *ZnO* also affected biofilm formation in *Bacillus subtilis*. The dose dependent reduction in biofilm biomass and density was observed as a result of NP's exposure. From the results it can be concluded that *ZnO* NP's can be exploited in prevention of biofilm formation. The exact mechanism of action of *ZnO* NP's in biofilm related studies is yet to be demonstrated. In the near future, *ZnO* NP's may play a major role in water purification membranes to reduce biofouling.

8

Conclusion and future aspects

8.1 Introduction

The present thesis reports the successful deposition of highly ordered *ZnO* and RE doped *ZnO* NP's into the nanotemplates on silicon substrate which could be used in optoelectronic applications. The following conclusions are made on the basis of the studies carried out:

- √ *ZnO* and RE doped *ZnO* NP's were synthesized successfully by simple chemical routes. The incorporation of RE^{3+} ions into the *ZnO* host and formation of single phase spherical RE^{3+} doped *ZnO* NP's without any RE compound was confirmed with the help of XRD and TEM measurements.

- √ The DRS results revealed that there are no drastic changes in absorption edges and the optical band gaps of the *ZnO* NP's prepared by methods 3.1 to 3.5, while a large blue shift was observed for the NP's synthesized by method 3.6 with an optical band gap of 3.32 eV. Method 3.6 can be used for smaller size and large band gap *ZnO* NP's. DRS measurements also indicates that incorporation of RE^{3+} ions induce lattice strain which causes a shift in the excitonic absorption band toward higher energy.

- √ The zinc interstitial defects were present in all of the *ZnO* samples prepared with different precursors and solvents where as oxygen interstitial defects were present in the *ZnO* NP's prepared by methods 3.1, 3.5 and 3.6 only.

- √ With increasing RE^{3+} dopant concentrations visible luminescence intensity increased up to a concentration of 1.5 wt%. Further increase in concentration of

dopant, intensity decreases due to concentration quenching effect. Solid state PL, measurements clearly show characteristic intra-4f transition lines of RE^{3+} ions.

√ The present study indicates that via defect engineering, RE-doped *ZnO* NP's may find avenues for potential applications in optoelectronic and multicolor emission display devices.

√ Synthesis of the SMA thin films using diblock copolymer PS-b-P4VP and additive HABA have been done using dip coating technique. It was observed that each domain is microphase separated, but they are not arranged in a regular way. This could be due to the fast evaporation of the solvent.

√ SMA thin films were exposed to the vapors of 1-4 dioxane for the ordering in the thin films (solvent annealing). 1-4 dioxane is a selective solvent, and it offers the different mobility to each copolymer PS and P4VP/HABA. It led to the ordered cylindrical domains normal to the substrate.

√ For the template formation, the additive was removed chemically. Additive HABA is soluble in ethanol while PS is non-soluble, Hence ordered porous nanotemplates were obtained just by immersing the ordered SMA thin films in ethanol.

√ Effect of molecular weight and relative volume fraction of minority block have also been studied. Increasing the molecular weight and keeping the relative volume fraction almost same, the morphology remains the same but the domain size (or pore size) and periodicity increases. And changing the relative volume fraction of P4VP/HABA from 0.3 to 0.45, the morphological transition from cylindrical domains to lamellar domains were observed.

√ Sweating in the morphology of PS-b-P4VP diblock copolymer from perpendicular oriented cylinder to parallel oriented cylinder have been observed oxygen baring nonoxygen baring solvent.

√ Ordered *ZnO* and RE doped *ZnO* nanostructures in PS matrix were obtained when nanotemplates were imersed in aqueous solution of pre synthesized *ZnO* and RE doped *ZnO* nanostructures for 9-10 hours.

√ These ordered arrays of *ZnO* and RE doped *ZnO* could be suggested for optoelectronic applications like LED's, display devices, UV sensor etc...

√ *ZnO* NP's affected the biofilm formation in *Bacillus subtilis*. There was ∼86% reduction in biofilm formation after treatment with *ZnO* NP's.

√ Change in surface morphology of the *Bacillus subtilis* cells was observed which could be due to oxidative stress induced by *ZnO* NP's.

√ Based on these results, we can fabricate membranes with *ZnO* NP's and check their biofouling activity.

8.2 Future scope of the work

Based on the findings in the present work, future outlook of the work can be proposed as follows:

√ Removal of polymer matrix from the substrate to obtain ordered nanostructures.

√ Fabrication of highly ordered other metal oxide nanostructures by ex-situ approach has been discussed here. So, the same method can be applied for other metal oxides also.

√ *ZnO* and RE doped *ZnO* have shown their extensive use in optoelectronics. So, the use of these ordered nanostructures can be extended to the device fabrication. Here, we are proposing the plan for the fabrication of LED device. The schematic of the device is shown in figure 8.1

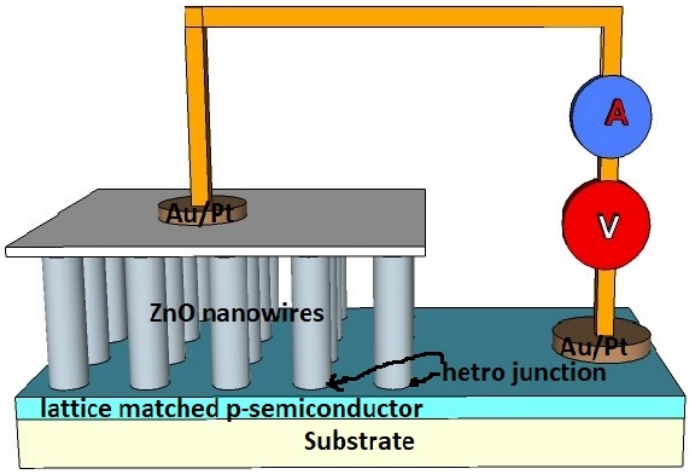

Figure 8.1: Schematic for the proposed LED device.

Bibliography

[1] MG Buonomenna, W Yave, and G Golemme. **Some approaches for high performance polymer based membranes for gas separation: block copolymers, carbon molecular sieves and mixed matrix membranes**. *RSC Advances*, **2**(29):10745–10773, 2012. xix, 2

[2] Yiyong Mai and Adi Eisenberg. **Self-Assembly of Block Copolymers**. **41**:5969–85, 07 2012. xix, 4

[3] Padmini Pandey, Rajnish Kurchania, and Fozia Z Haque. **Optical Studies of Europium-Doped ZnO Nanoparticles Prepared by Sol–Gel Technique**. *Journal of Advanced Physics*, **3**(2):104–110, 2014. xix, 18

[4] A Layek, S Banerjee, B Manna, and A Chowdhury. **Synthesis of rare-earth doped ZnO nanorods and their defect–dopant correlated enhanced visible-orange luminescence**. *RSC Advances*, **6**(42):35892–35900, 2016. xix, 20, 22, 72

[5] Jing-Jing Dong, Chun-Yang Zhen, Hui-Ying Hao, Jie Xing, Zhen-Jun Fan, and Zi-Li Zhang. **Highly ordered ZnO nanostructure arrays: preparation and light-emitting diode application**. *Japanese Journal of Applied Physics*, **53**(5):055201, 2014. xx, 36, 37

[6] O Lupan, VV Ursaki, G Chai, L Chow, GA Emelchenko, IM Tiginyanu, AN Gruzintsev, and AN Redkin. **Selective hydrogen gas nanosensor using individual ZnO nanowire with fast response at room temperature**. *Sensors and Actuators B: Chemical*, **144**(1):56–66, 2010. xx, 37, 38

[7] Daniel Bratton, Da Yang, Junyan Dai, and Christopher K Ober. **Recent progress in high resolution lithography**. *Polymers for Advanced Technologies*, **17**(2):94–103, 2006. 1

[8] Byron D Gates, Qiaobing Xu, Michael Stewart, Declan Ryan, C Grant Willson, and George M Whitesides. **New approaches to nanofabrication: molding, printing, and other techniques**. *Chemical reviews*, **105**(4):1171–1196, 2005.

[9] Takashi Ito and Shinji Okazaki. **Pushing the limits of lithography**. *Nature*, **406**(6799):1027–1031, 2000. 1

[10] IW Hamley. **Nanotechnology with soft materials**. *Angewandte Chemie International Edition*, **42**(15):1692–1712, 2003. 1

[11] M Reza Ghadiri, Juan R Granja, Ronald A Milligan, Duncan E McRee, and Nina Khazanovich. **Self-assembling organic nanotubes based on a cyclic peptide architecture**. *Nature*, **366**(6453):324–327, 1993. 1

[12] Seeram Ramakrishna, Kazutoshi Fujihara, Wee-Eong Teo, Thomas Yong, Zuwei Ma, and Ramakrishna Ramaseshan. **Electrospun nanofibers: solving global issues**. *Materials today*, **9**(3):40–50, 2006. 1

[13] Soojin Park, Jia-Yu Wang, Bokyung Kim, Ji Xu, and Thomas P Russell. **A simple route to highly oriented and ordered nanoporous block copolymer templates**. *Acs Nano*, **2**(4):766–772, 2008. 1, 35, 86

[14] Russell B Thompson, Valeriy V Ginzburg, Mark W Matsen, and Anna C Balazs. **Predicting the mesophases of copolymer-nanoparticle composites**. *Science*, **292**(5526):2469–2472, 2001. 2

[15] Russell B Thompson, Valeriy V Ginzburg, Mark W Matsen, and Anna C Balazs. **Block copolymer-directed assembly of nanoparticles: Forming mesoscopically ordered hybrid materials**. *Macromolecules*, **35**(3):1060–1071, 2002. 2

[16] E Bhoje Gowd, Bhanu Nandan, Nadja C Bigall, Alexander Eychmüller, Petr Formanek, and Manfred Stamm. **Hexagonally ordered arrays of metallic nanodots from thin films of functional block copolymers**. *Polymer*, **51**(12):2661–2667, 2010. 2, 33, 34, 35

[17] Wei Zheng and Zhen-Gang Wang. **Morphology of ABC triblock copolymers**. *Macromolecules*, **28**(21):7215–7223, 1995. 3

[18] Eugene Helfand and ZR Wasserman. **Block copolymer theory. 4. Narrow interphase approximation**. *Macromolecules*, **9**(6):879–888, 1976. 3

[19] Ludwik Leibler. **Theory of microphase separation in block copolymers**. *Macromolecules*, **13**(6):1602–1617, 1980. 3

[20] MW Matsen and Frank S Bates. **Unifying weak-and strong-segregation block copolymer theories**. *Macromolecules*, **29**(4):1091–1098, 1996. 3, 90

[21] Frank S Bates and Glenn H Fredrickson. **Block copolymers-designer soft materials**. *Physics today*, 2000. 4

[22] Biplab K Kuila, E Bhoje Gowd, and Manfred Stamm. **Supramolecular assembly of poly (styrene)-b-poly (4-vinylpyridine) and 1-pyrenebutyric acid in thin film and their use for nanofabrication**. *Macromolecules*, **43**(18):7713–7721, 2010. 5, 95

[23] Igor Tokarev, Radim Krenek, Yevgen Burkov, Dieter Schmeisser, Alexander Sidorenko, Sergiy Minko, and Manfred Stamm. **Microphase separation in thin films of poly (styrene-block-4-vinylpyridine) copolymer- 2-(4 -hydroxybenzeneazo) benzoic acid assembly**. *Macromolecules*, **38**(2):507–516, 2005. 5

[24] Valeriy Luchnikov, Alexey Kondyurin, Petr Formanek, Hannes Lichte, and Manfred Stamm. **Moiré patterns in superimposed nanoporous thin films derived from block-copolymer assemblies**. *Nano Letters*, **7**(12):3628–3632, 2007. 5, 95

[25] Krystyna Albrecht, Ahmed Mourran, Xiaomin Zhu, Tommi Markkula, Juergen Groll, Uwe Beginn, Wim H de Jeu, and Martin Moeller. **Thin film morphologies of block copolymers complexed with wedge-shaped liquid crystalline amphiphilic molecules**. *Macromolecules*, **41**(5):1728–1738, 2008. 5

[26] Joseph Kao, Joseph Tingsanchali, and Ting Xu. **Effects of interfacial interactions and film thickness on nonequilibrium hierarchical assemblies of block copolymer-based supramolecules in thin films**. *Macromolecules*, **44**(11):4392–4400, 2011. 5, 29, 85

[27] Alexis Laforgue, C Geraldine Bazuin, and Robert E Prud'Homme. **A study of the supramolecular approach in controlling diblock copolymer nanopatterning and nanoporosity on surfaces**. *Macromolecules*, **39**(19):6473–6482, 2006. 5, 93

[28] Haiying Huang, Zhijun Hu, Yongzhong Chen, Fajun Zhang, Yumei Gong, Tianbai He, and Chi Wu. **Effects of casting solvents on the formation of inverted phase in block copolymer thin films**. *Macromolecules*, **37**(17):6523–6530, 2004.

[29] Christophe Sinturel, Marylène Vayer, Michael Morris, and Marc A Hillmyer. **Solvent vapor annealing of block polymer thin films**. *Macromolecules*, **46**(14):5399–5415, 2013. 5, 26, 29

[30] Ian P Campbell, Chunlin He, and Mark P Stoykovich. **Topologically distinct lamellar block copolymer morphologies formed by solvent and thermal annealing**. *ACS Macro Letters*, **2**(10):918–923, 2013. 5, 26

[31] Olli Ikkala and Gerrit ten Brinke. **Functional materials based on self-assembly of polymeric supramolecules**. *science*, **295**(5564):2407–2409, 2002. 6

[32] Gyu-Chul Yi, Chunrui Wang, and Won Il Park. **ZnO nanorods: synthesis, characterization and applications**. *Semiconductor Science and Technology*, **20**(4):S22, 2005. 6

[33] Waseem Raza, Syed Mohammad Faisal, Mohammad Owais, D Bahnemann, and M Muneer. **Facile fabrication of highly efficient modified ZnO photocatalyst with enhanced photocatalytic, antibacterial and anticancer activity**. *RSC Advances*, **6**(82):78335–78350, 2016.

[34] Yangyang Zhang, Manoj K Ram, Elias K Stefanakos, and D Yogi Goswami. **Synthesis, characterization, and applications of ZnO nanowires**. *Journal of Nanomaterials*, **2012**:20, 2012.

[35] JOHN Rita, Sasi Florence Shanmugaraj, and Rajakumari Rajaram. **Synthesis and characterization of nano ZnO and CdO**. *Journal of the Ceramic Society of Japan*, **118**(1377):329–332, 2010.

[36] Dawit Gedamu, Ingo Paulowicz, Sören Kaps, Oleg Lupan, Sebastian Wille, Galina Haidarschin, Yogendra Kumar Mishra, and Rainer Adelung. **Rapid fabrication technique for interpenetrated ZnO nanotetrapod networks for fast UV sensors**. *Advanced materials*, **26**(10):1541–1550, 2014.

[37] O Lupan, V Postica, J GroÌĹttrup, AK Mishra, NH De Leeuw, JFC Carreira, J Rodrigues, N Ben Sedrine, MR Correia, T Monteiro, et al. **Hybridization of zinc oxide tetrapods for selective gas sensing applications**. *ACS applied materials & interfaces*, **9**(4):4084–4099, 2017. 6

[38] Jia-Xing Zhao, Xin-Hong Lu, Yan-Zhen Zheng, Shi-Qing Bi, Xia Tao, Jian-Feng Chen, and Weilie Zhou. **Eu doping for hierarchical ZnO nanocrystalline aggregates based dye-sensitized solar cell**. *Electrochemistry communications*, **32**:14–17, 2013. 6

[39] Hayoung Yoon, Jun Hua Wu, Ji Hyun Min, Ji Sung Lee, Jae-Seon Ju, and Young Keun Kim. **Magnetic and optical properties of monosized Eu-doped ZnO nanocrystals from nanoemulsion**. *Journal of Applied Physics*, **111**(7):07B523, 2012.

[40] Mohammad Hussein Naseef Assadi, Yuebin Zhang, Rong-Kun Zheng, Simon Peter Ringer, and Sean Li. **Structural and electronic properties of Eu-and Pd-doped ZnO**. *Nanoscale research letters*, **6**(1):357, 2011. 6, 10, 24, 41

[41] Wei Chen, Jin Z Zhang, and Alan G Joly. **Optical properties and potential applications of doped semiconductor nanoparticles**. *Journal of nanoscience and nanotechnology*, **4**(8):919–947, 2004. 6

[42] Rui Cheng, Yanrui Chen, Zhiqiang Li, Xiaohong Chen, Pingxiong Yang, Hongbing Zhu, Yuelong Huang, Zhuo Sun, and Sumei Huang. **Citric acid-assisted growth of lanthanide ions co-doped one-dimensional upconversion microcrystals and their photovoltaic applications**. *Journal of Materials Science: Materials in Electronics*, **25**(9):4066–4073, 2014.

[43] Yanfeng Miao, Peng Wang, Huiyuan Guan, and Yulong Chen. **Synthesis and up-conversion luminescence of NaGdF4: Yb3+, Tm3+**. *Journal of Materials Science: Materials in Electronics*, **26**(8):5748–5752, 2015. 6

[44] Atsushi Ishizumi and Yoshihiko Kanemitsu. **Structural and luminescence properties of Eu-doped ZnO nanorods fabricated by a microemulsion method**. *Applied Physics Letters*, **86**(25):253106, 2005. 7

[45] AleksandraâĂĔB. DjuriÅąiÄĞ and Yu Hang Leung. **Optical Properties of ZnO Nanostructures**. *Small*, **2**(8-9):944–961, 2006. 7

[46] J.C. Fan, K.M. Sreekanth, Z. Xie, S.L. Chang, and K.V. Rao. **p-Type ZnO materials: Theory, growth, properties and devices**. *Progress in Materials Science*, **58**(6):874 – 985, 2013. 7

[47] M Hadis and Ö Ümit. **Zinc Oxide: Fundamentals, Materials and Device Technology**, 2009. 7

[48] Chennupati Jagadish and Stephen J Pearton. *Zinc oxide bulk, thin films and nanostructures: processing, properties, and applications*. Elsevier, 2011. 7

[49] K Zakrzewska. **Gas sensing mechanism of TiO 2-based thin films**. *Vacuum*, **74**(2):335–338, 2004. 8

[50] Anil A Kashale, Ketan P Gattu, Kalyani Ghule, Vijay H Ingole, Swapnali Dhanayat, Ramphal Sharma, Jia-Yaw Chang, and Anil Vithal Ghule. **Biomediated green synthesis of TiO 2 nanoparticles for lithium ion battery application**. *Composites Part B: Engineering*, **99**:297–304, 2016.

[51] A Bharathi, Selvaraj Mohana Roopan, Amir Kajbafvala, RD Padmaja, MS Darsana, and G Nandhini Kumari. **Catalytic activity of TiO 2 nanoparticles in the synthesis of some 2, 3-disubstituted dihydroquinazolin-4 (1H)-ones**. *Chinese Chemical Letters*, **25**(2):324–326, 2014. 8

[52] Chuanmin Ruan, Maggie Paulose, Oomman K Varghese, Gopal K Mor, and Craig A Grimes. **Fabrication of highly ordered TiO2 nanotube arrays using an organic electrolyte**. *The Journal of Physical Chemistry B*, **109**(33):15754–15759, 2005.

[53] Sasipriya Kathirvel, Chaochin Su, Yung-Jen Shiao, Ya-Fen Lin, Bo-Ren Chen, and Wen-Ren Li. **Solvothermal synthesis of TiO 2 nanorods to enhance photovoltaic performance of dye-sensitized solar cells**. *Solar Energy*, **132**:310–320, 2016. 8

[54] SM Reda. **Synthesis of ZnO and Fe 2 O 3 nanoparticles by sol–gel method and their application in dye-sensitized solar cells**. *Materials Science in Semiconductor Processing*, **13**(5):417–425, 2010. 8

[55] BP Zhang, NT Binh, Y Segawa, K Wakatsuki, and N Usami. **Optical properties of ZnO rods formed by metalorganic chemical vapor deposition**. *Applied Physics Letters*, **83**(8):1635–1637, 2003. 8

[56] LC Nehru, V Swaminathan, and C Sanjeeviraja. **Rapid synthesis of nanocrystalline ZnO by a microwave-assisted combustion method**. *Powder technology*, **226**:29–33, 2012. 8

[57] Hongqiang Wang, Caihong Li, Haigang Zhao, and Jinrong Liu. **Preparation of nano-sized flower-like ZnO bunches by a direct precipitation method**. *Advanced Powder Technology*, **24**(3):599–604, 2013. 8

[58] Ravi Kant Sharma and Ranjana Ghose. **Synthesis of zinc oxide nanoparticles by homogeneous precipitation method and its application in antifungal activity against Candida albicans**. *Ceramics International*, **41**(1):967–975, 2015. 8

[59] Sang Kyoo Lim, Sung-Ho Hwang, Soonhyun Kim, and Hyunwoong Park. **Preparation of ZnO nanorods by microemulsion synthesis and their application as a CO gas sensor**. *Sensors and Actuators B: Chemical*, **160**(1):94–98, 2011. 8

[60] T Tharsika, ASMA Haseeb, SA Akbar, and M Thanihaichelvan. **Tailoring ZnO nanostructures by spray pyrolysis and thermal annealing**. *Ceramics International*, **41**(3):5205–5211, 2015. 8

[61] Hsiu-Fen Lin, Shih-Chieh Liao, and Sung-Wei Hung. **The dc thermal plasma synthesis of ZnO nanoparticles for visible-light photocatalyst**. *Journal of photochemistry and photobiology A: Chemistry*, **174**(1):82–87, 2005. 8

[62] MV Zdujić, OB Milošević, and Lj Č Karanović. **Mechanochemical treatment of ZnO and Al 2 O 3 powders by ball milling**. *Materials Letters*, **13**(2):125–129, 1992. 8

[63] MK Debanath and S Karmakar. **Study of blueshift of optical band gap in zinc oxide (ZnO) nanoparticles prepared by low-temperature wet chemical method**. *Materials Letters*, **111**:116–119, 2013. 8, 57, 59, 60

[64] Yan-Xiang Wang, Jian Sun, XueYun Fan, and Xi Yu. **A CTAB-assisted hydrothermal and solvothermal synthesis of ZnO nanopowders**. *Ceramics International*, **37**(8):3431–3436, 2011. 8

[65] E Fazio, AM Mezzasalma, G Mondio, F Neri, and R Saija. **ZnO nanostructures produced by laser ablation in water: Optical and structural properties**. *Applied Surface Science*, **272**:30–35, 2013. 8

[66] Joakim Reimer Jensen, Tue Johannessen, Stig Wedel, and Hans Livbjerg. **A study of Cu/ZnO/Al 2 O 3 methanol catalysts prepared by flame combustion synthesis**. *Journal of catalysis*, **218**(1):67–77, 2003. 8

[67] A Salvador, MC Pascual-Marti, JR Adell, A Requeni, and JG March. **Analytical methodologies for atomic spectrometric determination of metallic oxides in UV sunscreen creams**. *Journal of pharmaceutical and biomedical analysis*, **22**(2):301–306, 2000. 8

[68] R Zallen and MP Moret. **The optical absorption edge of brookite TiO 2**. *Solid State Communications*, **137**(3):154–157, 2006.

[69] L Kavan, M Grätzel, SE Gilbert, C Klemenz, and HJ Scheel. **Electrochemical and photoelectrochemical investigation of single-crystal anatase**. *Journal of the American Chemical Society*, **118**(28):6716–6723, 1996. 8

[70] Soojin Park, Bokyung Kim, Ji Xu, Tommy Hofmann, Benjamin M Ocko, and Thomas P Russell. **Lateral ordering of cylindrical microdomains under solvent vapor**. *Macromolecules*, **42**(4):1278–1284, 2009. 9, 28

[71] Kevin W Gotrik and CA Ross. **Solvothermal annealing of block copolymer thin films**. *Nano letters*, **13**(11):5117–5122, 2013. 9, 28

[72] Woon Ik Park, Kyungho Kim, Hyun-Ik Jang, Jae Won Jeong, Jong Min Kim, Jaesuk Choi, Jae Hong Park, and Yeon Sik Jung. **Directed Self-Assembly with Sub-100 Degrees Celsius Processing Temperature, Sub-10 Nanometer Resolution, and Sub-1 Minute Assembly Time**. *Small*, **8**(24):3762–3768, 2012. 9

[73] Jonathan E Seppala, Ronald L Lewis III, and Thomas H Epps III. **Spatial and orientation control of cylindrical nanostructures in ABA triblock copolymer thin films by raster solvent vapor annealing**. *ACS nano*, **6**(11):9855–9862, 2012. 9, 28

[74] Yanfa Yan and Su-Huai Wei. **Doping asymmetry in wide-bandgap semiconductors: Origins and solutions**. *physica status solidi (b)*, **245**(4):641–652, 2008. 9

[75] Stephen J Pearton, David P Norton, Matt P Ivill, Art F Hebard, John M Zavada, Weimin M Chen, and Irina A Buyanova. **ZnO doped with transition metal ions**. *IEEE Transactions on Electron Devices*, **54**(5):1040–1048, 2007. 9

[76] Tadatsugu Minami, Hirotoshi Sato, Hidehito Nanto, and Shinzo Takata. **Group III impurity doped zinc oxide thin films prepared by RF magnetron sputtering**. *Japanese Journal of Applied Physics*, **24**(10A):L781, 1985.

[77] Benjamin D Yuhas, David O Zitoun, Peter J Pauzauskie, Rongrui He, and Peidong Yang. **Transition-Metal Doped Zinc Oxide Nanowires**. *Angewandte Chemie*, **118**(3):434–437, 2006. 9

[78] Raghvendra S Yadav, Avinash C Pandey, and Sharda S Sanjay. **OPTICAL PROPERTIES OF EUROPIUM DOPED BUNCHES OF ZnO NANOWIRES SYNTHESIZED BY CO-PRECIPITATION METHOD.** *Chalcogenide Letters*, **6**(5), 2009. 10

[79] Jin-Chung Sin, Sze-Mun Lam, Keat-Teong Lee, and Abdul Rahman Mohamed. **Fabrication of erbium-doped spherical-like ZnO hierarchical nanostructures with enhanced visible light-driven photocatalytic activity**. *Materials Letters*, **91**:1–4, 2013. 9, 17, 24, 41

[80] Xian-Hua Zhang, Jie Chen, Yaping Wu, Zhaoxiong Xie, Junyong Kang, and Lansun Zheng. **A simple route to fabricate high sensibility gas sensors based on erbium doped ZnO nanocrystals**. *Colloids and Surfaces A: Physicochemical and Engineering Aspects*, **384**(1):580–584, 2011. 9, 17, 24

[81] SB Zhang, S-H Wei, and Alex Zunger. **Microscopic origin of the phenomenological equilibrium âĂIJdoping limit ruleâĂİ in n-type III-V semiconductors**. *Physical review letters*, **84**(6):1232, 2000. 9

[82] R Vettumperumal, S Kalyanaraman, and R Thangavel. **Optical constants and near infrared emission of Er doped ZnO sol–gel thin films**. *Journal of Luminescence*, **158**:493–500, 2015. 10, 17

[83] Chien-Yie Tsay and Min-Chi Wang. **Structural and optical studies on sol–gel derived ZnO thin films by excimer laser annealing**. *Ceramics International*, **39**(1):469–474, 2013. 10, 17, 24

[84] Zhe Liu, Fabian Kiessling, and Jessica Gätjens. **Advanced nanomaterials in multimodal imaging: design, functionalization, and biomedical applications**. *Journal of Nanomaterials*, **2010**:51, 2010. 10

[85] Catherine C Berry and Adam SG Curtis. **Functionalisation of magnetic nanoparticles for applications in biomedicine**. *Journal of physics D: Applied physics*, **36**(13):R198, 2003. 10, 25

[86] Younan Xia, Peidong Yang, Yugang Sun, Yiying Wu, Brian Mayers, Byron Gates, Yadong Yin, Franklin Kim, and Haoquan Yan. **One-dimensional nanostructures: synthesis, characterization, and applications**. *Advanced materials*, **15**(5):353–389, 2003. 10

[87] Anderson Janotti and Chris G Van de Walle. **Fundamentals of zinc oxide as a semiconductor**. *Reports on progress in physics*, **72**(12):126501, 2009.

[88] Meili Wang, Changgang Huang, Zhi Huang, Wang Guo, Jiquan Huang, Hong He, Hai Wang, Yongge Cao, Quanlin Liu, and Jingkui Liang. **Synthesis and photoluminescence of Eu-doped ZnO microrods prepared by hydrothermal method**. *Optical Materials*, **31**(10):1502–1505, 2009. 24, 41, 81

[89] SK Lathika Devi, K Sudarsana Kumar, and A Balakrishnan. **Rapid synthesis of pure and narrowly distributed Eu doped ZnO nanoparticles by solution combustion method**. *Materials Letters*, **65**(1):35–37, 2011. 24

[90] Atsushi Ishizumi, Satoshi Fujita, and Hisao Yanagi. **Influence of atmosphere on photoluminescence properties of Eu-doped ZnO nanocrystals**. *Optical Materials*, **33**(7):1116–1119, 2011. 17

[91] Mehrdad Najafi and Hamid Haratizadeh. **The effect of growth conditions and morphology on photoluminescence properties of Eu-doped ZnO nanostructures**. *Solid State Sciences*, **41**:48–51, 2015. 17

[92] Daksh Daksh and Yadvendra Kumar Agrawal. **Rare earth-doped zinc oxide nanostructures: a review**. *Reviews in Nanoscience and Nanotechnology*, **5**(1):1–27, 2016. 14, 24

[93] Yongjin Luo, Kuncan Wang, Qingrong Qian, Weiwei Zheng, Hun Xue, Baoquan Huang, Liren Xiao, and Qinghua Chen. **Fabrication and photocatalytic properties of Gd-doped ZnO nanoparticle-assembled nanorods**. *Materials Letters*, **149**:70–73, 2015.

[94] Surender Kumar and PD Sahare. **Gd 3+ incorporated ZnO nanoparticles: a versatile material**. *Materials research bulletin*, **51**:217–223, 2014. 24

[95] S Bhushan, AN Pandey, and Balakrishna Rao Kaza. **Photo-and electroluminescence of undoped and rare earth doped ZnO electroluminors**. *Journal of Luminescence*, **20**(1):29–38, 1979.

[96] Alireza Khataee, Reza Darvishi Cheshmeh Soltani, Atefeh Karimi, and Sang Woo Joo. **Sonocatalytic degradation of a textile dye over Gd-doped ZnO nanoparticles synthesized through sonochemical process**. *Ultrasonics sonochemistry*, **23**:219–230, 2015. 24

[97] JH Zheng, JL Song, Zhen Zhao, Qing Jiang, and JS Lian. **Optical and magnetic properties of Nd-doped ZnO nanoparticles**. *Crystal Research and Technology*, **47**(7):713–718, 2012.

[98] O Oprea, OR Vasile, G Voicu, L Craciun, and E Andronescu. **PHOTOLUMINESCENCE, MAGNETIC PROPERTIES AND PHOTOCATALYTIC ACTIVITY OF Gd 3+ DOPED ZnO NANOPARTICLES.** *Digest Journal of Nanomaterials & Biostructures (DJNB)*, **7**(4), 2012.

[99] M Faisal, Adel A Ismail, Ahmed A Ibrahim, Houcine Bouzid, and Saleh A Al-Sayari. **Highly efficient photocatalyst based on Ce doped ZnO nanorods: Controllable synthesis and enhanced photocatalytic activity**. *Chemical engineering journal*, **229**:225–233, 2013.

[100] Chockalingam Karunakaran, Paramasivan Gomathisankar, and Govindasamy Manikandan. **Preparation and characterization of antimicrobial Ce-doped ZnO nanoparticles for photocatalytic detoxification of cyanide**. *Materials Chemistry and Physics*, **123**(2):585–594, 2010.

[101] Waleed E Mahmoud. **Synthesis and optical properties of Ce-doped ZnO hexagonal nanoplatelets**. *Journal of Crystal Growth*, **312**(21):3075–3079, 2010.

[102] GX Wan, SY Ma, XB Li, FM Li, HQ Bian, LP Zhang, and WQ Li. **Synthesis and acetone sensing properties of Ce-doped ZnO nanofibers**. *Materials Letters*, **114**:103–106, 2014.

[103] Jing-hai YANG, Gao Ming, Yong-jun ZHANG, Li-li YANG, Ji-hui LANG, Dan-dan WANG, Ya-xin WANG, Hui-lian LIU, Hou-gang FAN, Mao-bin WEI, et al. **Synthesis and optical properties of Ce-doped ZnO**. *Chemical Research in Chinese Universities*, **24**(3):266–269, 2008. 15

[104] P Ilanchezhiyan, G Mohan Kumar, M Subramanian, and R Jayavel. **Effect of Pr doping on the structural and optical properties of ZnO nanorods**. *Materials Science and Engineering: B*, **175**(3):238–242, 2010.

[105] Mao-Hua Wang, Zhong-Yin Zhao, and Ting-Ting Liu. **Synthesis of Pr-doped ZnO nanoparticles by sol–gel method and varistor properties study**. *Journal of Alloys and Compounds*, **621**:220–224, 2015.

[106] Ahmed Ziani, Christian Davesnne, Christophe Labbé, Julien Cardin, Philippe Marie, C Frilay, S Boudin, and X Portier. **Annealing effects on the photoluminescence of terbium doped zinc oxide films**. *Thin Solid Films*, **553**:52–57, 2014.

[107] Anita Hastir, Nipin Kohli, and Ravi Chand Singh. **Temperature dependent selective and sensitive terbium doped ZnO nanostructures**. *Sensors and Actuators B: Chemical*, **231**:110–119, 2016. 10, 18

[108] ZHAO Zhen, Ji-ling Song, Jia-hong Zheng, and Jian-she Lian. **Optical properties and photocatalytic activity of Nd-doped ZnO powders**. *Transactions of Nonferrous Metals Society of China*, **24**(5):1434–1439, 2014. 10, 24

[109] Sunil Chauhan, Manoj Kumar, Sandeep Chhoker, SC Katyal, and VPS Awana. **Structural, vibrational, optical and magnetic properties of sol–gel derived Nd doped ZnO nanoparticles**. *Journal of Materials Science: Materials in Electronics*, **24**(12):5102–5110, 2013. 17

[110] B Roy, S Chakrabarty, O Mondal, M Pal, and A Dutta. **Effect of neodymium doping on structure, electrical and optical properties of nanocrystalline ZnO**. *Materials Characterization*, **70**:1–7, 2012.

[111] Surender Kumar and PD Sahare. **Nd-doped ZnO as a multifunctional nanomaterial**. *Journal of rare earths*, **30**(8):761–768, 2012. 10

[112] A Urbieta, R del Campo, R Pérez, P Fernández, and J Piqueras. **Luminescence and waveguiding behavior in Tb doped ZnO micro and nanostructures**. *Journal of Alloys and Compounds*, **610**:416–421, 2014. 10

[113] Myung-Seok Seo, Inyoung Jeong, Joon-Suh Park, Jinwoo Lee, Il Ki Han, Wan In Lee, Hae Jung Son, Byeong-Hyeok Sohn, and Min Jae Ko. **Vertically aligned nanostructured TiO 2 photoelectrodes for high efficiency perovskite solar cells via a block copolymer template approach**. *Nanoscale*, **8**(22):11472–11479, 2016. 10

[114] Jonathan E Allen, Biswajit Ray, M Ryyan Khan, Kevin G Yager, Muhammad A Alam, and Charles T Black. **Self-assembly of single dielectric nanoparticle layers and integration in polymer-based solar cells**. *Applied Physics Letters*, **101**(6):063105, 2012.

[115] Guoqiang Ren, Pei-Tzu Wu, and Samson A Jenekhe. **Solar cells based on block copolymer semiconductor nanowires: effects of nanowire aspect ratio**. *ACS nano*, **5**(1):376–384, 2010. 10

[116] Wendy van Zoelen and Gerrit ten Brinke. **Thin films of complexed block copolymers**. *Soft Matter*, **5**(8):1568–1582, 2009. 13

[117] Volker Abetz and Peter Simon. **Phase behaviour and morphologies of block copolymers**. *Block copolymers I*, pages 125–212, 2005. 13

[118] P Mansky, P Haikin, and EL Thomas. **Monolayer films of diblock copolymer microdomains for nanolithographic applications**. *Journal of Materials Science*, **30**(8):1987–1992, 1995. 13

[119] P Mansky, CK Harrison, PM Chaikin, RA Register, and N Yao. **Nanolithographic templates from diblock copolymer thin films**. *Applied physics letters*, **68**(18):2586–2588, 1996. 13

[120] Rupesh S Devan, Ranjit A Patil, Jin-Han Lin, and Yuan-Ron Ma. **One-Dimensional Metal-Oxide Nanostructures: Recent Developments in Synthesis, Characterization, and Applications**. *Advanced Functional Materials*, **22**(16):3326–3370, 2012. 14

[121] Jinping Liu, Xintang Huang, Yuanyuan Li, KM Sulieman, Fenglou Sun, and Xiang He. **Selective growth and properties of zinc oxide nanostructures**. *Scripta materialia*, **55**(9):795–798, 2006. 15, 16

[122] Agnieszka Kołodziejczak-Radzimska and Teofil Jesionowski. **Zinc oxideâĂŤfrom synthesis to application: a review**. *Materials*, **7**(4):2833–2881, 2014. 16, 24, 55, 101

[123] Wei Jia, Suihu Dang, Hairui Liu, Zhuxia Zhang, Chunyan Yu, Xuguang Liu, and Bingshe Xu. **Evidence of the formation mechanism of ZnO in aqueous solution**. *Materials Letters*, **82**:99–101, 2012. 16

[124] Ruoyu Hong, Tingting Pan, Jianzhong Qian, and Hongzhong Li. **Synthesis and surface modification of ZnO nanoparticles**. *Chemical Engineering Journal*, **119**(2):71–81, 2006. 15

[125] A Moballegh, HR Shahverdi, R Aghababazadeh, and AR Mirhabibi. **ZnO nanoparticles obtained by mechanochemical technique and the optical properties**. *Surface Science*, **601**(13):2850–2854, 2007. 15

[126] A Stanković, Lj Veselinović, SD Škapin, S Marković, and D Uskoković. **Controlled mechanochemically assisted synthesis of ZnO nanopowders in the presence of oxalic acid**. *Journal of materials science*, **46**(11):3716–3724, 2011. 15

[127] Amrut S Lanje, Satish J Sharma, Raghumani S Ningthoujam, J-S Ahn, and Ramchandra B Pode. **Low temperature dielectric studies of zinc oxide (ZnO) nanoparticles prepared by precipitation method**. *Advanced Powder Technology*, **24**(1):331–335, 2013. 15

[128] Jiaqiang Xu, Qingyi Pan, Zhizhuang Tian, et al. **Grain size control and gas sensing properties of ZnO gas sensor**. *Sensors and Actuators B: Chemical*, **66**(1):277–279, 2000. 15

[129] Xinyu Zhao, Baicun Zheng, Chunzhong Li, and Hongchen Gu. **Acetate-derived ZnO ultrafine particles synthesized by spray pyrolysis**. *Powder Technology*, **100**(1):20–23, 1998. 16

[130] Guvenc Akgul, Funda Aksoy Akgul, Klaus Attenkofer, and Markus Winterer. **Structural properties of zinc oxide and titanium dioxide nanoparticles prepared by chemical vapor synthesis**. *Journal of Alloys and compounds*, **554**:177–181, 2013. 16

[131] LN Dem'Yanets, LE Li, and TG Uvarova. **Zinc oxide: hydrothermal growth of nano-and bulk crystals and their luminescent properties**. *Journal of materials science*, **41**(5):1439–1444, 2006. 16

[132] Mira Ristić, Svetozar Musić, Mile Ivanda, and Stanko Popović. **Sol–gel synthesis and characterization of nanocrystalline ZnO powders**. *Journal of Alloys and Compounds*, **397**(1):L1–L4, 2005. 16

[133] Svetozar Musić, Đurđica Dragčević, Stanko Popović, and Mile Ivanda. **Precipitation of ZnO particles and their properties**. *Materials letters*, **59**(19):2388–2393, 2005. 16

[134] Jianda Zhang, Jianxin Wang, Shaobing Zhou, Ke Duan, Bo Feng, Jie Weng, Hongmei Tang, and Peizuo Wu. **Ionic liquid-controlled synthesis of ZnO microspheres**. *Journal of Materials Chemistry*, **20**(43):9798–9804, 2010. 16

[135] Zeshan Hu, Gerko Oskam, and Peter C Searson. **Influence of solvent on the growth of ZnO nanoparticles**. *Journal of Colloid and Interface Science*, **263**(2):454–460, 2003. 16, 24

[136] Ana Stanković, S Dimitrijević, and Dragan Uskoković. **Influence of size scale and morphology on antibacterial properties of ZnO powders hydrothemally synthesized using different surface stabilizing agents**. *Colloids and Surfaces B: Biointerfaces*, **102**:21–28, 2013. 16, 17

[137] Franz G Petzold, Jacek Jasinski, Ezra L Clark, Jeong H Kim, Jason Absher, Helge Toufar, and Mahendra K Sunkara. **Nickel supported on zinc oxide nanowires as advanced hydrodesulfurization catalysts**. *Catalysis today*, **198**(1):219–227, 2012. 16

[138] Chung-Hsin Lu and Chi-Hsien Yeh. **Emulsion precipitation of submicron zinc oxide powder**. *Materials Letters*, **33**(3-4):129–132, 1997. 16

[139] Agnieszka Kołodziejczak-Radzimska, Ewa Markiewicz, and Teofil Jesionowski. **Structural characterisation of ZnO particles obtained by the emulsion precipitation method**. *Journal of Nanomaterials*, **2012**:15, 2012. 16

[140] Meghana Ramani, S Ponnusamy, and C Muthamizhchelvan. **From zinc oxide nanoparticles to microflowers: a study of growth kinetics and biocidal activity**. *Materials Science and Engineering: C*, **32**(8):2381–2389, 2012. 16

[141] Xiangcun Li, Gaohong He, Gongkui Xiao, Hongjing Liu, and Mei Wang. **Synthesis and morphology control of ZnO nanostructures in microemulsions**. *Journal of Colloid and Interface Science*, **333**(2):465–473, 2009. 16

[142] Zhi Cao, Zhijun Zhang, Fenxia Wang, and Guangzhong Wang. **Synthesis and UV shielding properties of zinc oxide ultrafine particles modified with silica and trimethyl siloxane**. *Colloids and Surfaces A: Physicochemical and Engineering Aspects*, **340**(1):161–167, 2009. 16

[143] Huihu Wang and Changsheng Xie. **Effect of annealing temperature on the microstructures and photocatalytic property of colloidal ZnO nanoparticles**. *Journal of Physics and Chemistry of Solids*, **69**(10):2440–2444, 2008. 16

[144] Marko Bitenc and Zorica Crnjak Orel. **Synthesis and characterization of crystalline hexagonal bipods of zinc oxide**. *Materials Research Bulletin*, **44**(2):381–387, 2009. 16

[145] Razieh Jalal, Elaheh K Goharshadi, Maryam Abareshi, Majid Moosavi, Abbas Yousefi, and Paul Nancarrow. **ZnO nanofluids: green synthesis, characterization, and antibacterial activity**. *Materials Chemistry and Physics*, **121**(1):198–201, 2010. 16

[146] Tengfei Xu, Pengfei Ji, Meng He, and Jianye Li. **Growth and structure of pure ZnO micro/nanocombs**. *Journal of Nanomaterials*, **2012**:12, 2012. 16

[147] Lamia Znaidi. **Sol–gel-deposited ZnO thin films: A review**. *Materials Science and Engineering: B*, **174**(1):18–30, 2010. 16, 24

[148] Qin Xie, Zhou Dai, Jianbo Liang, Liqiang Xu, Weichao Yu, and Yitai Qian. **Synthesis of ZnO three-dimensional architectures and their optical properties**. *Solid state communications*, **136**(5):304–307, 2005. 16

[149] JT Chen, Jun Wang, RF Zhuo, D Yan, JJ Feng, F Zhang, and PX Yan. **The effect of Al doping on the morphology and optical property of ZnO nanostructures prepared by hydrothermal process**. *Applied Surface Science*, **255**(7):3959–3964, 2009. 15

[150] Seu Yi Li, Pang Lin, Chia Ying Lee, Tseung Yuen Tseng, and Chorng Jye Huang. **Effect of Sn dopant on the properties of ZnO nanowires**. *Journal of Physics D: Applied Physics*, **37**(16):2274, 2004.

[151] Edit Pál, Viktória Hornok, Albert Oszkó, and Imre Dékány. **Hydrothermal synthesis of prism-like and flower-like ZnO and indium-doped ZnO structures**. *Colloids and Surfaces A: Physicochemical and Engineering Aspects*, **340**(1):1–9, 2009.

[152] Chao Liu, Haiping He, Luwei Sun, Qian Yang, Zhizhen Ye, and Lanlan Chen. **Acceptor-related emissions in indium-doped ZnO nanorods**. *Journal of Applied Physics*, **109**(5):053507, 2011.

[153] Seonghoon Baek, Jaejin Song, and Sangwoo Lim. **Improvement of the optical properties of ZnO nanorods by Fe doping**. *Physica B: Condensed Matter*, **399**(2):101–104, 2007.

[154] Akiko Kobayashi, Otto F Sankey, and John D Dow. **Deep energy levels of defects in the wurtzite semiconductors AIN, CdS, CdSe, ZnS, and ZnO**. *Physical Review B*, **28**(2):946, 1983.

[155] GD Yuan, WJ Zhang, JS Jie, Xia Fan, Juan Antonio Zapien, Yu Hang Leung, LB Luo, PF Wang, Chun Sing Lee, and Shuit Tong Lee. **p-type ZnO nanowire arrays**. *Nano letters*, **8**(8):2591–2597, 2008.

[156] Mingya Zhong, Guiye Shan, Yajun Li, Guorui Wang, and Yichun Liu. **Synthesis and luminescence properties of Eu 3+-doped ZnO nanocrystals by a hydrothermal process**. *Materials Chemistry and Physics*, **106**(2):305–309, 2007.

[157] Natalie OV Plank, Henry J Snaith, Caterina Ducati, James S Bendall, Lukas Schmidt-Mende, and Mark E Welland. **A simple low temperature synthesis route for ZnO–MgO core–shell nanowires**. *Nanotechnology*, **19**(46):465603, 2008.

[158] Guozhen Shen, Jung Hee Cho, Jin Kyoung Yoo, Gyu-Chul Yi, and Cheol Jin Lee. **Synthesis and optical properties of S-doped ZnO nanostructures: nanonails and nanowires**. *The Journal of Physical Chemistry B*, **109**(12):5491–5496, 2005.

[159] S Anandan, S Muthukumaran, and M Ashokkumar. **Structural and optical properties of Y, Cu co-doped ZnO nanoparticles by sol–gel method**. *Superlattices and Microstructures*, **74**:247–260, 2014.

[160] Ruey-Chi Wang and Hsin-Ying Lin. **ZnO–CuO core–shell nanorods and CuO-nanoparticle–ZnO-nanorod integrated structures**. *Applied Physics A*, **95**(3):813–818, 2009.

[161] Shulin Ji, Liangliang Yin, Guodong Liu, Lide Zhang, and Changhui Ye. **A facile method for effective doping of Tb 3+ into ZnO nanocrystals**. *Chemical Communications*, (17):2344–2346, 2009.

[162] Guy L Kabongo, Gugu H Mhlongo, Thomas Malwela, Bakang M Mothudi, Kenneth T Hillie, and Mokhotjwa S Dhlamini. **Microstructural and photoluminescence properties of sol–gel derived Tb 3+ doped ZnO nanocrystals**. *Journal of Alloys and Compounds*, **591**:156–163, 2014.

[163] Debasis Bera, Lei Qian, and Paul H Holloway. **Time-evolution of photoluminescence properties of ZnO/MgO core/shell quantum dots**. *Journal of Physics D: Applied Physics*, **41**(18):182002, 2008.

[164] BY Geng, GZ Wang, Z Jiang, T Xie, SH Sun, GW Meng, and LD Zhang. **Synthesis and optical properties of S-doped ZnO nanowires**. *Applied Physics Letters*, **82**(26):4791–4793, 2003.

[165] S Mridha and D Basak. **The fabrication of a ZnO nanowire/La0. 65Sr0. 35MnO3 heterojunction and characterization of its rectifying behavior**. *Nanotechnology*, **20**(7):075203, 2009.

[166] Jen-Hau Cheng. **Atomic Layer Deposition Enabled Interconnect and Packaging Technologies for As-Grown Nanowire Devices**. 2010.

[167] Mariano A Zimmler, Daniel Stichtenoth, Carsten Ronning, Wei Yi, Venkatesh Narayanamurti, Tobias Voss, and Federico Capasso. **Scalable fabrication of nanowire photonic and electronic circuits using spin-on glass**. *Nano letters*, **8**(6):1695–1699, 2008.

[168] HK Liang, SF Yu, and HY Yang. **Edge-emitting ultraviolet n-ZnO: Al/i-ZnO/p-GaN heterojunction light-emitting diode with a rib waveguide**. *Optics express*, **18**(4):3687–3692, 2010.

[169] Soumen Dhara and PK Giri. **Stable p-type conductivity and enhanced photoconductivity from nitrogen-doped annealed ZnO thin film**. *Thin Solid Films*, **520**(15):5000–5006, 2012. 15

[170] PP Murmu, J Kennedy, BJ Ruck, A Markwitz, GVM Williams, and S Rubanov. **Structural and magnetic properties of low-energy Gd implanted ZnO single crystals**. *Nuclear Instruments and Methods in Physics Research Section B: Beam Interactions with Materials and Atoms*, **272**:100–103, 2012. 17

[171] A Douayar, P Prieto, G Schmerber, K Nouneh, R Diaz, I Chaki, S Colis, A El Fakir, N Hassanain, A Belayachi, et al. **Investigation of the structural, optical and electrical properties of Nd-doped ZnO thin films deposited by spray pyrolysis**. *The European Physical Journal-Applied Physics*, **61**(1), 2013. 17, 24

[172] Hashem Shahroosvand and Mahsa Ghorbani-asl. **Solution-based synthetic strategies for Eu doped ZnO nanoparticle with enhanced red photoluminescence**. *Journal of Luminescence*, **144**:223–229, 2013. 17, 24

[173] A Jagannatha Reddy, MK Kokila, H Nagabhushana, C Shivakumara, RPS Chakradhar, BM Nagabhushana, and R Hari Krishna. **Luminescence studies and EPR investigation of solution combustion derived Eu doped ZnO**. *Spectrochimica Acta Part A: Molecular and Biomolecular Spectroscopy*, **132**:305–312, 2014. 17, 24

[174] PV Korake, AN Kadam, and KM Garadkar. **Photocatalytic activity of Eu 3+-doped ZnO nanorods synthesized via microwave assisted technique**. *Journal of Rare Earths*, **32**(4):306–313, 2014. 17

[175] CJ Pan, CW Chen, JY Chen, PJ Huang, GC Chi, CY Chang, F Ren, and SJ Pearton. **Optical and structural properties of Eu-diffused and doped ZnO nanowires**. *Applied Surface Science*, **256**(1):187–190, 2009. 17

[176] Yanlan Liu, Kelong Ai, Qinghai Yuan, and Lehui Lu. **Fluorescence-enhanced gadolinium-doped zinc oxide quantum dots for magnetic resonance and fluorescence imaging**. *Biomaterials*, **32**(4):1185–1192, 2011. 17

[177] MI Gouri, E Ahmed, NR Khalid, M Ahmad, M Ramzan, A Shakoor, and NA Niaz. **Gadolinium doped zno nanocrystalline powders and its photocatalytic performance for degradation of methyl blue under sunlight**. *Journal of Ovonic Research*, **10**:89–100, 2014. 17

[178] PM Aneesh and MK Jayaraj. **Red luminescence from hydrothermally synthesized Eu-doped ZnO nanoparticles under visible excitation**. *Bulletin of Materials Science*, **33**(3):227–231, 2010. 17, 22

[179] HVS Pessoni, LJQ Maia, and A Franco. **Eu-doped ZnO nanoparticles prepared by the combustion reaction method: Structural, photoluminescence and dielectric characterization**. *Materials Science in Semiconductor Processing*, **30**:135–141, 2015. 17, 80

[180] Xiying Ma and Zui Wang. **The optical properties of rare earth Gd doped ZnO nanocrystals**. *Materials Science in Semiconductor Processing*, **15**(3):227–231, 2012. 17, 24

[181] Haq Nawaz Sheikh, Heena Khajuria, Jigmet Ladol, Rajinder Singh, et al. **Surfactant assisted sono-chemical synthesis and characterization of gadolinium doped zinc oxide nanoparticles**. *Acta Chimica Slovenica*, **62**(4):849–858, 2015. 17

[182] Lokesh Kumar Jangir, Yogita Kumari, Anil Kumar, Manoj Kumar, and Kamlendra Awasthi. **Investigation of luminescence and structural properties of ZnO nanoparticles, synthesized with different precursors**. *Materials Chemistry Frontiers*, **1**:1413–1421, 2017. 15, 75, 80, 101

[183] AK Singh, V Viswanath, and VC Janu. **Synthesis, effect of capping agents, structural, optical and photoluminescence properties of ZnO nanoparticles**. *Journal of Luminescence*, **129**(8):874–878, 2009. 15, 64

[184] Jin-Chung Sin, Sze-Mun Lam, Keat-Teong Lee, and Abdul Rahman Mohamed. **Preparation of rare earth-doped ZnO hierarchical micro/nanospheres and their enhanced photocatalytic activity under visible light irradiation**. *Ceramics International*, **40**(4):5431–5440, 2014. 18, 72, 75

[185] Keigo Suzuki, Koji Murayama, and Nobuhiko Tanaka. **Enhanced luminescence in Eu-doped ZnO nanocrystalline films**. *Applied Physics Letters*, **107**(3):031902, 2015. 18

[186] C Jayachandraiah and G Krishnaiah. **Erbium induced raman studies and dielectric properties of Er-doped ZnO nanoparticles**. *Adv. Mater. Lett. Adv. Mater. Lett*, **6**:743–748, 2015. 18

[187] Kai-sheng Yu, Jian-ying Shi, Zai-li Zhang, Yong-mei Liang, and Wei Liu. **Synthesis, characterization, and photocatalysis of ZnO and Er-Doped ZnO**. *Journal of Nanomaterials*, **2013**:75, 2013. 18, 81

[188] D Sridevi and KV Rajendran. **Enhanced optical properties La doped ZnO nanoparticles**. *Optoelectron. Adv. Mater. Rapid Commun*, **4**:1591–1593, 2010. 18

[189] Z Pan, SH Morgan, A Ueda, R Aga Jr, A Steigerwald, AB Hmelo, and R Mu. **Er-doped ZnO films grown by pulsed e-beam deposition**. *Journal of Physics: Condensed Matter*, **19**(26):266216, 2007. 18

[190] KH Tam, CK Cheung, YH Leung, AB Djurišić, CC Ling, CD Beling, S Fung, WM Kwok, WK Chan, DL Phillips, et al. **Defects in ZnO nanorods prepared by a hydrothermal method**. *The Journal of Physical Chemistry B*, **110**(42):20865–20871, 2006. 18, 20, 21

[191] WI Park, YH Jun, SW Jung, and Gyu-Chul Yi. **Excitonic emissions observed in ZnO single crystal nanorods**. *Applied Physics Letters*, **82**(6):964–966, 2003. 19

[192] C Bekeny, T Voss, B Hilker, J Gutowski, R Hauschild, H Kalt, B Postels, A Bakin, and A Waag. **Influence of ZnO seed crystals and annealing on the optical quality of low-temperature grown ZnO nanorods**. *Journal of Applied Physics*, **102**(4):044908, 2007. 19

[193] Johannes Fallert, Robert Hauschild, Felix Stelzl, Alex Urban, Markus Wissinger, Huijuan Zhou, Claus Klingshirn, and Heinz Kalt. **Surface-state related luminescence in ZnO nanocrystals**. *Journal of Applied Physics*, **101**(7):073506, 2007. 19

[194] David C Look, Cevdet Coşkun, Bruce Claflin, and Gary C Farlow. **Electrical and optical properties of defects and impurities in ZnO**. *Physica B: Condensed Matter*, **340**:32–38, 2003. 19

[195] BK Meyer, H Alves, DM Hofmann, W Kriegseis, D Forster, F Bertram, J Christen, A Hoffmann, M Strassburg, M Dworzak, et al. **Bound exciton and donor–acceptor pair recombinations in ZnO**. *physica status solidi (b)*, **241**(2):231–260, 2004. 19

[196] E Tomzig and R Helbig. **Band-edge emission in ZnO**. *Journal of Luminescence*, **14**(3):403–415, 1976. 19

[197] U Ozgur, Ya I Alivov, C Liu, and A Teke. **M. a. Reshchikov, S. DogÌĘan, V. Avrutin, S**. *JJ Cho, H. MorkocÌğ, Ü. OÌĹzguÌĹr, YI Alivov, C. Liu, A. Teke, M. a. Reshchikov, S. DoÇğan, V. Avrutin, S.-JJ Cho, and H. MorkoÌğ, J. Appl. Phys*, **98**:041301, 2005. 19

[198] A Teke, Ü Özgür, S Doğan, X Gu, Hadis Morkoç, B Nemeth, J Nause, and HO Everitt. **Excitonic fine structure and recombination dynamics in single-crystalline ZnO**. *Physical Review B*, **70**(19):195207, 2004. 19

[199] J Gutowski, N Presser, and I Broser. **Acceptor-exciton complexes in ZnO: A comprehensive analysis of their electronic states by high-resolution magnetooptics and excitation spectroscopy**. *Physical Review B*, **38**(14):9746, 1988. 19

[200] DC Reynolds, David C Look, B Jogai, CW Litton, TC Collins, W Harsch, and G Cantwell. **Neutral-donor–bound-exciton complexes in ZnO crystals**. *Physical Review B*, **57**(19):12151, 1998. 19

[201] K Thonke, Th Gruber, N Teofilov, R Schönfelder, A Waag, and R Sauer. **Donor–acceptor pair transitions in ZnO substrate material**. *Physica B: Condensed Matter*, **308**:945–948, 2001. 19

[202] T Monteiro, C Boemare, MJ Soares, E Rita, and E Alves. **Photoluminescence and damage recovery studies in Fe-implanted ZnO single crystals**. *Journal of Applied Physics*, **93**(11):8995–9000, 2003. 19

[203] BP Zhang, NT Binh, Y Segawa, Y Kashiwaba, and K Haga. **Photoluminescence study of ZnO nanorods epitaxially grown on sapphire (1120) substrates**. *Applied physics letters*, **84**(4):586–588, 2004. 19

[204] S Ozaki, T Tsuchiya, Y Inokuchi, and S Adachi. **Photoluminescence and photomodulated transmittance spectroscopy of ZnO nanowires**. *physica status solidi (a)*, **202**(7):1325–1335, 2005. 19

[205] M Strassburg, A Rodina, M Dworzak, U Haboeck, IL Krestnikov, A Hoffmann, O Gelhausen, MR Phillips, HR Alves, A Zeuner, et al. **Identification of bound exciton complexes in ZnO**. *physica status solidi (b)*, **241**(3):607–611, 2004. 19

[206] Cheng-Ying Chen, Ming-Wei Chen, Jian Ke Jr, Chin-An Lin, José RD Retamal, and Hau He Jr. **Surface effects on optical and electrical properties of ZnO nanostructures**. *Pure and Applied Chemistry*, **82**(11):2055–2073, 2010. 20

[207] Davood Raoufi. **Synthesis and microstructural properties of ZnO nanoparticles prepared by precipitation method**. *Renewable Energy*, **50**:932–937, 2013. 20

[208] Lin Guo, Yun Liang Ji, Huibin Xu, Paul Simon, and Ziyu Wu. **Regularly shaped, single-crystalline ZnO nanorods with wurtzite structure**. *Journal of the American Chemical Society*, **124**(50):14864–14865, 2002.

[209] Arunasish Layek, Suman De, Ruhi Thorat, and Arindam Chowdhury. **Spectrally resolved photoluminescence imaging of ZnO nanocrystals at single-particle levels**. *The journal of physical chemistry letters*, **2**(11):1241–1247, 2011. 20

[210] S Venkataprasad Bhat, SRC Vivekchand, A Govindaraj, and CNR Rao. **Photoluminescence and photoconducting properties of ZnO nanoparticles**. *Solid State Communications*, **149**(13):510–514, 2009. 20, 21

[211] AB Djurišić, Wallace CH Choy, Vellaisamy Arul Lenus Roy, Yu Hang Leung, Chung Yin Kwong, Kok Wai Cheah, TK Gundu Rao, Wai Kin Chan, H Fei Lui, and Charles Surya. **Photoluminescence and electron paramagnetic resonance of ZnO tetrapod structures**. *Advanced Functional Materials*, **14**(9):856–864, 2004. 20, 21

[212] NY Garces, L Wang, L Bai, NC Giles, LE Halliburton, and G Cantwell. **Role of copper in the green luminescence from ZnO crystals**. *Applied Physics Letters*, **81**(4):622–624, 2002. 21

[213] Peter Klason, Thomas Moe Børseth, Qing X Zhao, Bengt G Svensson, Andrej Yu Kuznetsov, Peder J Bergman, and Magnus Willander. **Temperature dependence and decay times of zinc and oxygen vacancy related photoluminescence bands in zinc oxide**. *Solid State Communications*, **145**(5):321–326, 2008. 21

[214] Bixia Lin, Zhuxi Fu, and Yunbo Jia. **Green luminescent center in undoped zinc oxide films deposited on silicon substrates**. *Applied Physics Letters*, **79**(7):943–945, 2001. 21

[215] K Vanheusden, WL Warren, CH Seager, DR Tallant, JA Voigt, and BE Gnade. **Mechanisms behind green photoluminescence in ZnO phosphor powders**. *Journal of Applied Physics*, **79**(10):7983–7990, 1996. 21

[216] Aleksandra B Djurišić and Yu Hang Leung. **Optical properties of ZnO nanostructures**. *small*, **2**(8-9):944–961, 2006. 21

[217] DH Zhang, ZY Xue, and QP Wang. **The mechanisms of blue emission from ZnO films deposited on glass substrate by rf magnetron sputtering**. *Journal of Physics D: Applied Physics*, **35**(21):2837, 2002. 21

[218] MK Patra, K Manzoor, M Manoth, SR Vadera, and N Kumar. **Studies of luminescence properties of ZnO and ZnO: Zn nanorods prepared by solution growth technique**. *Journal of Luminescence*, **128**(2):267–272, 2008. 21

[219] Xiang Liu, Xiaohua Wu, Hui Cao, and RPH Chang. **Growth mechanism and properties of ZnO nanorods synthesized by plasma-enhanced chemical vapor deposition**. *Journal of Applied Physics*, **95**(6):3141–3147, 2004. 21

[220] Addy van Dijken, Eric A Meulenkamp, Daniël Vanmaekelbergh, and Andries Meijerink. **The kinetics of the radiative and nonradiative processes in nanocrystalline ZnO particles upon photoexcitation**. *The Journal of Physical Chemistry B*, **104**(8):1715–1723, 2000. 21

[221] Wen-Feng Hsieh, Hsu-Cheng Hsu, Wan-Jiun Liao, Hsin-Ming Cheng, Kuo-Feng Lin, WEITZE HSU, and Chin-Jiu Pan. **Optical Properties of Zinc Oxide Quantum Dots**. In *Optical Processes in Microparticles and Nanostructures: A Festschrift Dedicated to Richard Kounai Chang on his Retirement from Yale University. Edited by SERPENGUZEL ALI ET AL. Published by World Scientific Publishing Co. Pte. Ltd., 2011. ISBN# 9789814295789, pp. 253-267*, pages 253–267, 2011. 21

[222] NR Panda, BS Acharya, and P Nayak. **Growth and enhanced optical properties of ZnO: S nanorods and multipodes**. *Materials Letters*, **100**:257–260, 2013. 21

[223] D Li, YH Leung, AB Djurišić, ZT Liu, MH Xie, SL Shi, SJ Xu, and WK Chan. **Different origins of visible luminescence in ZnO nanostructures fabricated by the chemical and evaporation methods**. *Applied Physics Letters*, **85**(9):1601–1603, 2004. 21

[224] Jijun Qiu, Xiaomin Li, Weizhen He, Se-Jeong Park, Hyung-Kook Kim, Yoon-Hwae Hwang, Jae-Ho Lee, and Yang-Do Kim. **The growth mechanism and optical properties of ultralong ZnO nanorod arrays with a high aspect ratio by a preheating hydrothermal method**. *Nanotechnology*, **20**(15):155603, 2009. 21

[225] RBM Cross, MM De Souza, and EM Sankara Narayanan. **A low temperature combination method for the production of ZnO nanowires**. *Nanotechnology*, **16**(10):2188, 2005. 21, 64

[226] JP Kar, MH Ham, SW Lee, and JM Myoung. **Fabrication of ZnO nanostructures of various dimensions using patterned substrates**. *Applied Surface Science*, **255**(7):4087–4092, 2009. 21

[227] Lori E Greene, Matt Law, Joshua Goldberger, Franklin Kim, Justin C Johnson, Yanfeng Zhang, Richard J Saykally, and Peidong Yang. **Low-temperature wafer-scale production of ZnO nanowire arrays**. *Angewandte Chemie International Edition*, **42**(26):3031–3034, 2003. 21

[228] Gang Xiong, U Pal, JG Serrano, KB Ucer, and RT Williams. **Photoluminesence and FTIR study of ZnO nanoparticles: the impurity and defect perspective**. *physica status solidi (c)*, **3**(10):3577–3581, 2006. 21

[229] Partha P Pal and J Manam. **Structural and photoluminescence studies of Eu3+ doped zinc oxide nanorods prepared by precipitation method**. *Journal of Rare Earths*, **31**(1):37–43, 2013. 21

[230] G Krishna Reddy, A Jagannatha Reddy, R Hari Krishna, BM Nagabhushana, and G Ram Gopal. **Luminescence and spectroscopic investigations on Gd^{3+} doped ZnO nanophosphor**. *Journal of Asian Ceramic Societies*, 2017. 22

[231] Shulin Ji, Liangliang Yin, Guodong Liu, Lide Zhang, and Changhui Ye. **Synthesis of Rare Earth Ions-Doped ZnO Nanostructures with Efficient Host- Guest Energy Transfer**. *The Journal of Physical Chemistry C*, **113**(37):16439–16444, 2009. 22

[232] Amna Sirelkhatim, Shahrom Mahmud, Azman Seeni, Noor Haida Mohamad Kaus, Ling Chuo Ann, Siti Khadijah Mohd Bakhori, Habsah Hasan, and Dasmawati Mohamad. **Review on zinc oxide nanoparticles: antibacterial activity and toxicity mechanism**. *Nano-Micro Letters*, **7**(3):219–242, 2015. 23, 85, 101

[233] Jin-Hyung Lee, Yong-Guy Kim, Moo Hwan Cho, and Jintae Lee. **ZnO nanoparticles inhibit Pseudomonas aeruginosa biofilm formation and virulence factor production**. *Microbiological research*, **169**(12):888–896, 2014. 23

[234] P Gopinath, Sonit Kumar Gogoi, Pallab Sanpui, Anumita Paul, Arun Chattopadhyay, and Siddhartha Sankar Ghosh. **Signaling gene cascade in silver nanoparticle induced apoptosis**. *Colloids and Surfaces B: Biointerfaces*, **77**(2):240–245, 2010. 23

[235] Rob J Vandebriel and Wim H De Jong. **A review of mammalian toxicity of ZnO nanoparticles**. *Nanotechnology, science and applications*, **5**:61, 2012. 23

[236] Rizwan Wahab, Maqsood A Siddiqui, Quaiser Saquib, Sourabh Dwivedi, Javed Ahmad, Javed Musarrat, Abdulaziz A Al-Khedhairy, and Hyung-Shik Shin. **ZnO nanoparticles induced oxidative stress and apoptosis in HepG2 and MCF-7 cancer cells and their antibacterial activity**. *Colloids and Surfaces B: Biointerfaces*, **117**:267–276, 2014. 23

[237] Kumud Kant Awasthi, Anjali Awasthi, Rajbala Verma, Narender Kumar, Partha Roy, Kamlendra Awasthi, and PJ John. **Cytotoxicity, genotoxicity and alteration of cellular antioxidant enzymes in silver nanoparticles exposed CHO cells**. *RSC Advances*, **5**(44):34927–34935, 2015. 23

[238] Nagaprasad Puvvada, Shashi Rajput, BN Prashanth Kumar, Siddik Sarkar, Suraj Konar, Keith R Brunt, Raj R Rao, Abhijit Mazumdar, Swadesh K Das, Ranadhir Basu, et al. **Novel ZnO hollow-nanocarriers containing paclitaxel targeting folate-receptors in a malignant pH-microenvironment for effective monitoring and promoting breast tumor regression**. *Scientific reports*, **5**:11760, 2015. 23

[239] Mohd Javed Akhtar, Hisham A Alhadlaq, Aws Alshamsan, MA Majeed Khan, and Maqusood Ahamed. **Aluminum doping tunes band gap energy level as well as oxidative stress-mediated cytotoxicity of ZnO nanoparticles in MCF-7 cells**. *Scientific reports*, **5**:13876, 2015. 24

[240] Karuppaiya Vimala, Shenbagamoorthy Sundarraj, Manickam Paulpandi, Srinivasan Vengatesan, and Soundarapandian Kannan. **Green synthesized doxorubicin loaded zinc oxide nanoparticles regulates the Bax and Bcl-2 expression in breast and colon carcinoma**. *Process Biochemistry*, **49**(1):160–172, 2014. 24

[241] VP Makhniy and VV Melnik. **Surface barrier diode based on zinc selenide with a passivating zinc oxide film**. *Technical Physics Letters*, **29**(9):712–713, 2003. 24

[242] Rajeev Jain, Ankita Sinha, et al. **Graphene-zinc oxide nanorods nanocomposite based sensor for voltammetric quantification of tizanidine in solubilized system**. *Applied Surface Science*, **369**:151–158, 2016.

[243] Jamal Al-Sabahi, Tanujjal Bora, Mohammed Al-Abri, and Joydeep Dutta. **Controlled defects of zinc oxide nanorods for efficient visible light photocatalytic degradation of phenol**. *Materials*, **9**(4):238, 2016.

[244] Mohammed Marie, Sanghamitra Mandal, and Omar Manasreh. **An electrochemical glucose sensor based on zinc oxide nanorods**. *Sensors*, **15**(8):18714–18723, 2015. 24

[245] G Vijayaprasath, R Murugan, T Mahalingam, Y Hayakawa, and G Ravi. **Enhancement of ferromagnetic property in rare earth neodymium doped ZnO nanoparticles**. *Ceramics International*, **41**(9):10607–10615, 2015. 24

[246] Reza Zamiri, Ajay Kaushal, Avito Rebelo, and JMF Ferreira. **Er doped ZnO nanoplates: Synthesis, optical and dielectric properties**. *Ceramics International*, **40**(1):1635–1639, 2014. 24

[247] Yanqing Zong, Zhe Li, Xingmin Wang, Jiantao Ma, and Yi Men. **Synthesis and high photocatalytic activity of Eu-doped ZnO nanoparticles**. *Ceramics International*, **40**(7):10375–10382, 2014.

[248] Silan Baturay, Yusuf Selim Ocak, and Derya Kaya. **The effect of Gd doping on the electrical and photoelectrical properties of Gd: ZnO/p-Si heterojunctions**. *Journal of Alloys and Compounds*, **645**:29–33, 2015. 24

[249] Mariana Ungureanu, Heidemarie Schmidt, Qingyu Xu, Holger von Wenckstern, Daniel Spemann, Holger Hochmuth, Michael Lorenz, and Marius Grundmann. **Electrical and magnetic properties of RE-doped ZnO thin films (RE= Gd, Nd)**. *Superlattices and Microstructures*, **42**(1):231–235, 2007. 24

[250] Govindan Poongodi, Rangasamy Mohan Kumar, and Ramasamy Jayavel. **Structural, optical and visible light photocatalytic properties of nanocrystalline Nd doped ZnO thin films prepared by spin coating method**. *Ceramics International*, **41**(3):4169–4175, 2015. 24

[251] M Singhai, V Chhabra, P Kang, and DO Shah. **Synthesis of ZnO nanoparticles for varistor application using Zn-substituted aerosol OT microemulsion**. *Materials Research Bulletin*, **32**(2):239–247, 1997. 24

[252] Rodoula Moleski, Epameinondas Leontidis, and Frank Krumeich. **Controlled production of ZnO nanoparticles from zinc glycerolate in a sol–gel silica matrix**. *Journal of colloid and interface science*, **302**(1):246–253, 2006.

[253] Chung-Chi Liau and Liang-Chiun Chao. **Growth and characterization of Er doped ZnO prepared by reactive ion beam sputtering**. In *Nanoelectronics Conference (INEC), 2010 3rd International*, pages 976–977. IEEE, 2010.

[254] JL Noel, R Udayabhaskar, B Renganathan, S Muthu Mariappan, D Sastikumar, and B Karthikeyan. **Spectroscopic and fiber optic ethanol sensing properties Gd doped ZnO nanoparticles**. *Spectrochimica Acta Part A: Molecular and Biomolecular Spectroscopy*, **132**:634–638, 2014. 24

[255] Dan-dan Wang, Jing-hai Yang, Jian Cao, Ji-hui Lang, Ming Gao, and Xiao-yan LIU. **Synthesis and photoluminescence of Eu-doped ZnO nanosheets**. *Chem. Res. Chinese. U.*, **27**:174–176, 2011. 24

[256] Jianzhong Ma, Junli Liu, Yan Bao, Zhenfeng Zhu, Xiaofeng Wang, and Jing Zhang. **Synthesis of large-scale uniform mulberry-like ZnO particles with microwave hydrothermal method and its antibacterial property**. *Ceramics International*, **39**(3):2803–2810, 2013. 24

[257] Magnus Willander, Omer Nur, Jamil Rana Sadaf, Muhammad Israr Qadir, Saima Zaman, Ahmed Zainelabdin, Nargis Bano, and Ijaz Hussain. **Luminescence from zinc oxide nanostructures and polymers and their hybrid devices**. *Materials*, **3**(4):2643–2667, 2010. 25

[258] Hadis Morkoc, Jen-Inn Chyi, Alois Krost, Yasushi Nanishi, and Donald J Silversmith. **Challenges and Opportunities in GaN and ZnO Devices and Materials [Scanning the Issue]**. *Proceedings of the IEEE*, **98**(7):1113–1117, 2010. 25

[259] IW Hamley. **Ordering in thin films of block copolymers: Fundamentals to potential applications**. *Progress in Polymer Science*, **34**(11):1161–1210, 2009. 26

[260] Xiaodan Gu, Ilja Gunkel, Alexander Hexemer, Weiyin Gu, and Thomas P Russell. **An In Situ Grazing Incidence X-Ray Scattering Study of Block Copolymer Thin Films During Solvent Vapor Annealing**. *Advanced Materials*, **26**(2):273–281, 2014. 26

[261] Zhe Qiang, Yuanzhong Zhang, Jesse A Groff, Kevin A Cavicchi, and Bryan D Vogt. **A generalized method for alignment of block copolymer films: solvent vapor annealing with soft shear**. *Soft Matter*, **10**(32):6068–6076, 2014. 26

[262] Souheng Wu. **Surface and interfacial tensions of polymer melts. II. Poly (methyl methacrylate), poly (n-butyl methacrylate), and polystyrene**. *The Journal of Physical Chemistry*, **74**(3):632–638, 1970. 26

[263] Adam M Welander, Huiman Kang, Karl O Stuen, Harun H Solak, Marcus Müller, Juan J de Pablo, and Paul F Nealey. **Rapid directed assembly of block copolymer films at elevated temperatures**. *Macromolecules*, **41**(8):2759–2761, 2008. 26, 27

[264] F Ferrarese Lupi, TJ Giammaria, M Ceresoli, G Seguini, K Sparnacci, D Antonioli, V Gianotti, M Laus, and M Perego. **Rapid thermal processing of self-assembling block copolymer thin films**. *Nanotechnology*, **24**(31):315601, 2013. 26

[265] Gabriele Seguini, Tommaso J Giammaria, Federico Ferrarese Lupi, Katia Sparnacci, Diego Antonioli, Valentina Gianotti, Francesco Vita, Immacolata F Placentino, Jan Hilhorst, Claudio Ferrero, et al. **Thermally induced self-assembly of cylindrical nanodomains in low molecular weight PS-b-PMMA thin films**. *Nanotechnology*, **25**(4):045301, 2014. 26, 27

[266] Takehiro Seshimo, Rina Maeda, Rin Odashima, Yutaka Takenaka, Daisuke Kawana, Katsumi Ohmori, and Teruaki Hayakawa. **Perpendicularly oriented sub-10-nm block copolymer lamellae by atmospheric thermal annealing for one minute**. *Scientific reports*, **6**, 2016. 26

[267] F Ferrarese Lupi, TJ Giammaria, FG Volpe, F Lotto, G Seguini, Branko Pivac, M Laus, and M Perego. **High aspect ratio PS-b-PMMA block copolymer masks for lithographic applications**. *ACS applied materials & interfaces*, **6**(23):21389–21396, 2014. 26, 27

[268] Shengxiang Ji, Chi-Chun Liu, Wen Liao, Alyssa L Fenske, Gordon SW Craig, and Paul F Nealey. **Domain orientation and grain coarsening in cylinder-forming poly (styrene-b-methyl methacrylate) films**. *Macromolecules*, **44**(11):4291–4300, 2011. 27

[269] Seung Hyun Kim, Matthew J Misner, and Thomas P Russell. **Solvent-Induced Ordering in Thin Film Diblock Copolymer/Homopolymer Mixtures**. *Advanced Materials*, **16**(23-24):2119–2123, 2004. 28

[270] Seung Hyun Kim, Matthew J Misner, Ting Xu, Masahiro Kimura, and Thomas P Russell. **Highly oriented and ordered arrays from block copolymers via solvent evaporation**. *Advanced Materials*, **16**(3):226–231, 2004. 28

[271] Dipu Borah, Matthew T Shaw, Justin D Holmes, and Michael A Morris. **Sub-10 nm feature size PS-b-PDMS block copolymer structures fabricated by a microwave-assisted solvothermal process**. *ACS applied materials & interfaces*, **5**(6):2004–2012, 2013. 28

[272] Xiaojiang Zhang, Kenneth D Harris, Nathanael LY Wu, Jeffrey N Murphy, and Jillian M Buriak. **Fast assembly of ordered block copolymer nanostructures through microwave annealing**. *ACS nano*, **4**(11):7021–7029, 2010.

[273] Jae Won Jeong, Yoon Hyung Hur, Hyeong-jun Kim, Jong Min Kim, Woon Ik Park, Mi Jeong Kim, Bumjoon J Kim, and Yeon Sik Jung. **Proximity injection of plasticizing molecules to self-assembling polymers for large-area, ultrafast nanopatterning in the sub-10-nm regime**. *ACS nano*, **7**(8):6747–6757, 2013. 28

[274] Erik M Freer, Leslie E Krupp, William D Hinsberg, Philip M Rice, James L Hedrick, Jennifer N Cha, Robert D Miller, and Ho-Cheol Kim. **Oriented mesoporous organosilicate thin films**. *Nano letters*, **5**(10):2014–2018, 2005. 28

[275] William A Phillip, Brandon OâĂŹNeill, Marc Rodwogin, Marc A Hillmyer, and EL Cussler. **Self-assembled block copolymer thin films as water filtration membranes**. *ACS applied materials & interfaces*, **2**(3):847–853, 2010.

[276] Jun Yin, Xueping Yao, Jiun-You Liou, Wei Sun, Ya-Sen Sun, and Yong Wang. **Membranes with highly ordered straight nanopores by selective swelling of fast perpendicularly aligned block copolymers**. *ACS nano*, **7**(11):9961–9974, 2013. 28

[277] Tomoyasu Hirai, Melvina Leolukman, Chi Chun Liu, Eungnak Han, Yun Jun Kim, Yoshihito Ishida, Teruaki Hayakawa, Masa-aki Kakimoto, Paul F Nealey, and Padma Gopalan. **One-Step Direct-Patterning Template Utilizing Self-Assembly of POSS-Containing Block Copolymers**. *Advanced Materials*, **21**(43):4334–4338, 2009. 28

[278] Eunhye Kim, Hyungju Ahn, Sungmin Park, Hoyeon Lee, Moongyu Lee, Sumi Lee, Taewoo Kim, Eun-Ae Kwak, Jun Han Lee, Xie Lei, et al. **Directed assembly of high molecular weight block copolymers: highly ordered line patterns of perpendicularly oriented lamellae with large periods**. *ACS nano*, **7**(3):1952–1960, 2013. 28

[279] G Kim and M Libera. **Morphological Development in Solvent-Cast Polystyrene- Polybutadiene-Polystyrene (SBS) Triblock Copolymer Thin Films**. *Macromolecules*, **31**(8):2569–2577, 1998. 28

[280] Wei-Han Huang, Po-Yu Chen, and Shih-Huang Tung. **Effects of annealing solvents on the morphology of block copolymer-based supramolecular thin films**. *Macromolecules*, **45**(3):1562–1569, 2012. 28, 30, 90

[281] Yu Xuan, Juan Peng, Liang Cui, Hanfu Wang, Binyao Li, and Yanchun Han. **Morphology development of ultrathin symmetric diblock copolymer film via solvent vapor treatment**. *Macromolecules*, **37**(19):7301–7307, 2004.

[282] You Wang, Xiaodong Hong, Baoquan Liu, Changyou Ma, and Chunfang Zhang. **Two-dimensional ordering in block copolymer monolayer thin films upon selective solvent annealing**. *Macromolecules*, **41**(15):5799–5808, 2008.

[283] Haiying Huang, Fajun Zhang, Zhijun Hu, Binyang Du, Tianbai He, Fuk Kay Lee, Yongjian Wang, and Ophelia KC Tsui. **Study on the origin of inverted phase in drying solution-cast block copolymer films**. *Macromolecules*, **36**(11):4084–4092, 2003. 28

[284] W Bai, KG Yager, and CA Ross. **In situ characterization of the self-assembly of a polystyrene–polydimethylsiloxane block copolymer during solvent vapor annealing**. *Macromolecules*, **48**(23):8574–8584, 2015. 30

[285] Alexander Sidorenko, Igor Tokarev, Sergiy Minko, and Manfred Stamm. **Ordered reactive nanomembranes/nanotemplates from thin films of block copolymer supramolecular assembly**. *Journal of the American Chemical Society*, **125**(40):12211–12216, 2003. 30, 31, 94, 95

[286] E Bhoje Gowd, Bhanu Nandan, Mukesh Kumar Vyas, Nadja C Bigall, Alexander Eychmüller, Heike Schlörb, and Manfred Stamm. **Highly ordered palladium nanodots and nanowires from switchable block copolymer thin films**. *Nanotechnology*, **20**(41):415302, 2009. 30

[287] T Thurn-Albrecht, J Schotter, GA Kästle, N Emley, T Shibauchi, L Krusin-Elbaum, K Guarini, CT Black, MT Tuominen, and TP Russell. **Ultrahigh-density nanowire arrays grown in self-assembled diblock copolymer templates**. *Science*, **290**(5499):2126–2129, 2000. 31

[288] Miri Park, Christopher Harrison, Paul M Chaikin, Richard A Register, and Douglas H Adamson. **Block copolymer lithography: periodic arrays of˜ 1011 holes in 1 square centimeter**. *Science*, **276**(5317):1401–1404, 1997. 31

[289] Sokol Ndoni, Martin E Vigild, and Rolf H Berg. **Nanoporous materials with spherical and gyroid cavities created by quantitative etching of polydimethylsiloxane in polystyrene- polydimethylsiloxane block copolymers**. *Journal of the American Chemical Society*, **125**(44):13366–13367, 2003. 31

[290] Rong-Ming Ho, Chun-Ku Chen, and Yeo-Wan Chiang. **Novel Nanostructures from Self-Assembly of Chiral Block Copolymers**. *Macromolecular rapid communications*, **30**(17):1439–1456, 2009. 31

[291] Hua-Yan Si, Jing-Sheng Chen, and Gan-Moog Chow. **A simple method to prepare highly ordered PS-b-P4VP block copolymer template**. *Colloids and Surfaces A: Physicochemical and Engineering Aspects*, **373**(1):82–87, 2011. 31

[292] AMIR WAGIH Fahmi, H-G Braun, and Manfred Stamm. **Fabrication of Metallized Nanowires from Self-Assembled Diblock Copolymer Templates**. *Advanced Materials*, **15**(14):1201–1204, 2003. 32

[293] Chanchayya Gupta Chandaluri, Gilad Pelossof, Ran Tel-Vered, Roy Shenhar, and Itamar Willner. **Block Copolymer Patterns as Templates for the Electrocatalyzed Deposition of Nanostructures on Electrodes and for the Generation of Surfaces of Controlled Wettability**. *ACS applied materials & interfaces*, **8**(2):1440–1446, 2016. 32

[294] Song-Zhu Chu, Kenji Wada, Satoru Inoue, and Sin-ichi Todoroki. **Synthesis and Characterization of Titania Nanostructures on Glass by Al Anodization and Sol- Gel Process**. *Chemistry of materials*, **14**(1):266–272, 2002. 32

[295] Marjorie Roulet, Marylène Vayer, and Christophe Sinturel. **A simple route to ordered metal oxide nanoparticle arrays using block copolymer thin films**. *European Polymer Journal*, **49**(12):3897–3903, 2013. 32, 33, 34

[296] Pavan S Chinthamanipeta, Qin Lou, and Devon A Shipp. **Periodic titania nanostructures using block copolymer templates**. *ACS nano*, **5**(1):450–456, 2010. 32

[297] Lixin Song, Yeng Ming Lam, Chris Boothroyd, and Puat Wen Teo. **One-step synthesis of titania nanoparticles from PS-P4VP diblock copolymer solution**. *Nanotechnology*, **18**(13):135605, 2007. 33

[298] Qin Lou, Pavan S Chinthamanipeta, and Devon A Shipp. **Mechanism of Titania Deposition into Cylindrical Poly (styrene-block-4 vinyl pyridine) Block Copolymer Templates**. *Langmuir*, **27**(24):15206–15212, 2011. 33

[299] Juan Peng, Wolfgang Knoll, Cheolmin Park, and Dong Ha Kim. **Two-dimensional arrays of strings of TiO2 nanoparticles via cooperative block copolymer self-assembly**. *Chemistry of Materials*, **20**(4):1200–1202, 2008. 33

[300] Bhanu Nandan, Biplab K Kuila, and Manfred Stamm. **Supramolecular assemblies of block copolymers as templates for fabrication of nanomaterials**. *European Polymer Journal*, **47**(4):584–599, 2011. 34

[301] Wonjoo Lee, Seung Yong Lee, Xin Zhang, Oded Rabin, and RM Briber. **Hexagonally ordered nanoparticles templated using a block copolymer film through Coulombic interactions**. *Nanotechnology*, **24**(4):045305, 2013. 35

[302] Zhicheng Liu, Tongxin Chang, Haiying Huang, and Tianbai He. **Gold nanoparticle arrays assembled on the reconstructed surface of block copolymer thin films**. *RSC Advances*, **3**(43):20464–20470, 2013.

[303] Bhanu Nandan, E Bhoje Gowd, Nadja C Bigall, Alexander Eychmüller, Petr Formanek, Paul Simon, and Manfred Stamm. **Arrays of inorganic nanodots and nanowires using nanotemplates based on switchable block copolymer supramolecular assemblies**. *Advanced Functional Materials*, **19**(17):2805–2811, 2009.

[304] Andriy Horechyy, Bhanu Nandan, Nikolaos E Zafeiropoulos, Petr Formanek, Ulrich Oertel, Nadja C Bigall, Alexander Eychmüller, and Manfred Stamm. **A Step-Wise Approach for Dual Nanoparticle Patterning via Block Copolymer Self-Assembly**. *Advanced Functional Materials*, **23**(4):483–490, 2013. 34

[305] Andriy Horechyy, Nikolaos E Zafeiropoulos, Bhanu Nandan, Petr Formanek, Frank Simon, Anton Kiriy, and Manfred Stamm. **Highly ordered arrays of magnetic nanoparticles prepared via block copolymer assembly**. *Journal of Materials Chemistry*, **20**(36):7734–7741, 2010. 34

[306] I Barandiaran and G Kortaberria. **Synthesis and characterization of nanostructured PS-b-P4VP/Fe 2 O 3 thin films with magnetic properties prepared by solvent vapor annealing**. *RSC Advances*, **5**(116):95840–95846, 2015. 34

[307] Gregory W Nyce, Joel R Hayes, Alex V Hamza, and Joe H Satcher. **Synthesis and characterization of hierarchical porous gold materials**. *Chemistry of materials*, **19**(3):344–346, 2007. 35

[308] Edward JW Crossland, Sabine Ludwigs, Marc A Hillmyer, and Ullrich Steiner. **Control of gyroid forming block copolymer templates: effects of an electric field and surface topography**. *Soft Matter*, **6**(3):670–676, 2010. 35

[309] Oleg Lupan, Thierry Pauporté, Tangui Le Bahers, Bruno Viana, and Ilaria Ciofini. **Wavelength-emission tuning of ZnO nanowire-based light-emitting diodes by Cu doping: experimental and computational insights**. *Advanced Functional Materials*, **21**(18):3564–3572, 2011. 35

[310] Oleg Lupan, Thierry Pauporté, and Bruno Viana. **Low-Voltage UV-Electroluminescence from ZnO-Nanowire Array/p-GaN Light-Emitting diodes**. *Advanced Materials*, **22**(30):3298–3302, 2010.

[311] Sang Wuk Lee, Hak Dong Cho, Gennady Panin, and Tae Won Kang. **Vertical ZnO nanorod/Si contact light-emitting diode**. *Applied Physics Letters*, **98**(9):093110, 2011.

[312] Min-Chang Jeong, Byeong-Yun Oh, Moon-Ho Ham, Sang-Won Lee, and Jae-Min Myoung. **ZnO-Nanowire-Inserted GaN/ZnO Heterojunction Light-Emitting Diodes**. *Small*, **3**(4):568–572, 2007.

[313] Xiao-Mei Zhang, Ming-Yen Lu, Yue Zhang, Lih-J Chen, and Zhong Lin Wang. **Fabrication of a High-Brightness Blue-Light-Emitting Diode Using a ZnO-Nanowire Array Grown on p-GaN Thin Film**. *Advanced Materials*, **21**(27):2767–2770, 2009.

[314] Sheng Xu, Chen Xu, Ying Liu, Youfan Hu, Rusen Yang, Qing Yang, Jae-Hyun Ryou, Hee Jin Kim, Zachary Lochner, Suk Choi, et al. **Ordered Nanowire Array Blue/Near-UV Light Emitting Diodes**. *Advanced Materials*, **22**(42):4749–4753, 2010. 35

[315] YR Ryu, TS Lee, JA Lubguban, HW White, YS Park, and CJ Youn. **ZnO devices: Photodiodes and p-type field-effect transistors**. *Applied Physics Letters*, **87**(15):153504, 2005. 35

[316] DJ Rogers, F Hosseini Teherani, A Yasan, K Minder, P Kung, and M Razeghi. **Electroluminescence at 375 nm from a Zn O/ Ga N: Mg/ c-Al 2 O 3 heterojunction light emitting diode**. *Applied Physics Letters*, **88**(14):141918, 2006. 35

[317] Sun-Hong Park, Seon-Hyo Kim, and Sang-Wook Han. **Growth of homoepitaxial ZnO film on ZnO nanorods and light emitting diode applications**. *Nanotechnology*, **18**(5):055608, 2007. 35, 36

[318] JJ Dong, XW Zhang, ZG Yin, JX Wang, SG Zhang, FT Si, HL Gao, and X Liu. **Ultraviolet electroluminescence from ordered ZnO nanorod array/p-GaN light emitting diodes**. *Applied Physics Letters*, **100**(17):171109, 2012. 37

[319] SG Zhang, XW Zhang, ZG Yin, JX Wang, JJ Dong, HL Gao, FT Si, SS Sun, and Y Tao. **Localized surface plasmon-enhanced electroluminescence from ZnO-based heterojunction light-emitting diodes**. *Applied Physics Letters*, **99**(18):181116, 2011.

[320] O Lupan, Th Pauporté, B Viana, IM Tiginyanu, VV Ursaki, and R Cortes. **Epitaxial electrodeposition of ZnO nanowire arrays on p-GaN for efficient UV-light-emitting diode fabrication**. *ACS Applied Materials & Interfaces*, **2**(7):2083–2090, 2010. 37

[321] JX Wang, XW Sun, Y Yang, H Huang, YC Lee, OK Tan, and Lionel Vayssieres. **Hydrothermally grown oriented ZnO nanorod arrays for gas sensing applications**. *Nanotechnology*, **17**(19):4995, 2006. 37, 41

[322] XD Wang, Jun Zhou, CS Lao, JH Song, NS Xu, and Zhong L Wang. **In situ field emission of density-controlled ZnO nanowire arrays**. *Advanced Materials*, **19**(12):1627–1631, 2007. 38

[323] Y-K Tseng, C-J Huang, H-M Cheng, I-N Lin, K-S Liu, and I-C Chen. **Characterization and field-emission properties of needle-like zinc oxide nanowires grown vertically on conductive zinc oxide films**. *Advanced functional materials*, **13**(10):811–814, 2003. 38

[324] Juncong She, Zhiming Xiao, Yuhua Yang, Shaozhi Deng, Jun Chen, Guowei Yang, and Ningsheng Xu. **Correlation between resistance and field emission performance of individual ZnO one-dimensional nanostructures**. *Acs Nano*, **2**(10):2015–2022, 2008. 41

[325] Q Zhao, HZ Zhang, YW Zhu, SQ Feng, XC Sun, J Xu, and DP Yu. **Morphological effects on the field emission of ZnO nanorod arrays**. *Applied Physics Letters*, **86**(20):203115, 2005.

[326] A Wei, Xiao Wei Sun, CX Xu, ZL Dong, MB Yu, and W Huang. **Stable field emission from hydrothermally grown ZnO nanotubes**. *Applied Physics Letters*, **88**(21):213102, 2006.

[327] Haibo Zeng, Xijin Xu, Yoshio Bando, Ujjal K Gautam, Tianyou Zhai, Xiaosheng Fang, Baodan Liu, and Dmitri Golberg. **Template Deformation-Tailored ZnO Nanorod/Nanowire Arrays: Full Growth Control and Optimization of Field-Emission**. *Advanced Functional Materials*, **19**(19):3165–3172, 2009. 38

[328] Matt Law, Lori E Greene, Aleksandra Radenovic, Tevye Kuykendall, Jan Liphardt, and Peidong Yang. **ZnO- Al2O3 and ZnO- TiO2 core- shell nanowire dye-sensitized solar cells**. *The Journal of Physical Chemistry B*, **110**(45):22652–22663, 2006. 39

[329] Yun-Ju Lee, Douglas S Ruby, David W Peters, Bonnie B McKenzie, and Julia WP Hsu. **ZnO nanostructures as efficient antireflection layers in solar cells**. *Nano letters*, **8**(5):1501–1505, 2008. 39

[330] Matt Law, Lori E Greene, Justin C Johnson, Richard Saykally, and Peidong Yang. **Nanowire dye-sensitized solar cells**. *Nature materials*, **4**(6):455–459, 2005. 39

[331] Punniamoorthy Ravirajan, Ana M Peiró, Mohammad K Nazeeruddin, Michael Graetzel, Donal DC Bradley, James R Durrant, and Jenny Nelson. **Hybrid polymer/zinc oxide photovoltaic devices with vertically oriented ZnO nanorods and an amphiphilic molecular interface layer**. *The Journal of Physical Chemistry B*, **110**(15):7635–7639, 2006. 39

[332] Lori E Greene, Matt Law, Benjamin D Yuhas, and Peidong Yang. **ZnO- TiO2 core- shell nanorod/P3HT solar cells**. *The Journal of Physical Chemistry C*, **111**(50):18451–18456, 2007. 39

[333] María Aymerich, Ana I Gómez-Varela, Ezequiel Álvarez, and María T Flores-Arias. **Study of Different Sol-Gel Coatings to Enhance the Lifetime of PDMS Devices: Evaluation of Their Biocompatibility**. *Materials*, **9**(9):728, 2016. 44

[334] B.D. Cullity and S.R. Stock. *Elements of X-ray Diffraction*. Prentice Hall, 2001. 46

[335] André Guinier. *X-ray diffraction in crystals, imperfect crystals, and amorphous bodies*. Courier Corporation, 1994. 46

[336] E.N. Kaufmann. *Characterization of Materials, 2 Volume Set*. Wiley, 2003. 47

[337] Challa SSR Kumar. *Transmission electron microscopy characterization of nanomaterials*. Springer Science & Business Media, 2013. 48

[338] DB Williams and CB Carter. **SpringerLink (Online service). Transmission Electron Microscopy: A Textbook for Materials Science**, 2009. 49

[339] Challa SSR Kumar. *UV-VIS and photoluminescence spectroscopy for nanomaterials characterization*. Springer, 2013. 50

[340] Jan Tauc. **Optical properties and electronic structure of amorphous Ge and Si**. *Materials Research Bulletin*, **3**(1):37–46, 1968. 50

[341] Sergei N Magonov and Myung-Hwan Whangbo. *Surface analysis with STM and AFM: experimental and theoretical aspects of image analysis*. John Wiley & Sons, 2008. 51, 52

[342] Pier Carlo Braga and Davide Ricci. *Atomic force microscopy: biomedical methods and applications*, **242**. Springer Science & Business Media, 2004. 52

[343] V Yu Davydov, VV Lundin, AN Smirnov, NA Sobolev, AS Usikov, and AM Emelyanov. **Electronic and optical properties of semiconductors**. *Semiconductors*, **33**(1):1, 1999. 55

[344] Deep Jariwala, Vinod K Sangwan, Lincoln J Lauhon, Tobin J Marks, and Mark C Hersam. **Carbon nanomaterials for electronics, optoelectronics, photovoltaics, and sensing**. *Chemical Society Reviews*, **42**(7):2824–2860, 2013. 55

[345] V Srikant and D R_ Clarke. **On the optical band gap of zinc oxide**. *Journal of Applied Physics*, **83**(10):5447–5451, 1998. 55

[346] Yunhua Huang, Xuedong Bai, and Yue Zhang. **In situ mechanical properties of individual ZnO nanowires and the mass measurement of nanoparticles**. *Journal of Physics: Condensed Matter*, **18**(15):L179, 2006. 55

[347] DS King and RM Nix. **Thermal stability and reducibility of ZnO and Cu/ZnO catalysts**. *Journal of Catalysis*, **160**(1):76–83, 1996.

[348] Yogendra K Mishra, Sören Kaps, Arnim Schuchardt, Ingo Paulowicz, Xin Jin, Dawit Gedamu, Stefan Freitag, Maria Claus, Sebastian Wille, Alexander Kovalev, et al. **Fabrication of macroscopically flexible and highly porous 3D semiconductor networks from interpenetrating nanostructures by a simple flame transport approach**. *Particle & Particle Systems Characterization*, **30**(9):775–783, 2013.

[349] Nastaran Faraji, Clemens Ulrich, Niklas Wolff, Lorenz Kienle, Rainer Adelung, Yogendra Kumar Mishra, and Jan Seidel. **Visible-Light Driven Nanoscale Photoconductivity of Grain Boundaries in Self-Supported ZnO Nano-and Microstructured Platelets**. *Advanced Electronic Materials*, **2**(9), 2016. 55

[350] Zhigang Li, Wenwu Zhong, Xiaoming Li, Haibo Zeng, Guping Wang, Weike Wang, Zhaorong Yang, and Yuheng Zhang. **Strong room-temperature ferromagnetism of pure ZnO nanostructure arrays via colloidal template**. *Journal of Materials Chemistry C*, **1**(41):6807–6812, 2013. 55

[351] Rajesh Kumar, O Al-Dossary, Girish Kumar, and Ahmad Umar. **Zinc Oxide Nanostructures for NO2 Gas–Sensor Applications: A Review**. *Nano-Micro Letters*, **7**(2):97–120. 55

[352] Dezhong Yu, Ruxiu Cai, and Zhihong Liu. **Studies on the photodegradation of Rhodamine dyes on nanometer-sized zinc oxide**. *Spectrochimica Acta Part A: Molecular and Biomolecular Spectroscopy*, **60**(7):1617 – 1624, 2004. 55

[353] Thomas Baird, Patrick J Denny, Robert Hoyle, Fiona McMonagle, Diane Stirling, and James Tweedy. **Modified zinc oxide absorbents for low-temperature gas desulfurisation**. *J. Chem. Soc., Faraday Trans.*, **88**(22):3375–3382, 1992. 55

[354] Ravindra P Singh, Vineet K Shukla, Raghvendra S Yadav, Prashant K Sharma, Prashant K Singh, and Avinash C Pandey. **Biological approach of zinc oxide nanoparticles formation and its characterization**. 2011. 55

[355] Yin Peng, An-Wu Xu, Bin Deng, Markus Antonietti, and Helmut Cölfen. **Polymer-controlled crystallization of zinc oxide hexagonal nanorings and disks**. *The Journal of Physical Chemistry B*, **110**(7):2988–2993, 2006. 55

[356] GC Chinchen, PJ Denny, DG Parker, MS Spencer, and DA Whan. **Mechanism of methanol synthesis from CO 2/CO/H 2 mixtures over copper/zinc oxide/alumina catalysts: use of 14 C-labelled reactants**. *Applied Catalysis*, **30**(2):333–338, 1987. 55

[357] Tim Reimer, Ingo Paulowicz, Robert RoÌĺder, SoÌĺren Kaps, Oleg Lupan, Steffen Chemnitz, Wolfgang Benecke, Carsten Ronning, Rainer Adelung, and Yogendra K Mishra. **Single step integration of ZnO nano-and microneedles in Si trenches by novel flame transport approach: whispering gallery modes and photocatalytic properties**. *ACS applied materials & interfaces*, **6**(10):7806–7815, 2014. 55

[358] Kun Ho Kim, Ki Cheol Park, and Dae Young Ma. **Structural, electrical and optical properties of aluminum doped zinc oxide films prepared by radio frequency magnetron sputtering**. *Journal of Applied Physics*, **81**:7764–7772, 1997. 55

[359] Zhong Lin Wang. **Zinc oxide nanostructures: growth, properties and applications**. *Journal of Physics: Condensed Matter*, **16**(25):R829, 2004. 55

[360] Xiaoming Li, Jizhong Song, Yanli Liu, and Haibo Zeng. **Controlling oxygen vacancies and properties of ZnO**. *Current Applied Physics*, **14**(3):521–527, 2014. 55

[361] Karin Keis, C Bauer, Gerrit Boschloo, Anders Hagfeldt, K Westermark, Håkan Rensmo, and Hans Siegbahn. **Nanostructured ZnO electrodes for dye-sensitized solar cell applications**. *Journal of Photochemistry and photobiology A: Chemistry*, **148**(1):57–64, 2002. 55

[362] Tapan K Gupta. **Application of zinc oxide varistors**. *Journal of the American Ceramic Society*, **73**(7):1817–1840, 1990. 55

[363] Daniele Costenaro, Fabio Carniato, Giorgio Gatti, Leonardo Marchese, and Chiara Bisio. **Preparation of luminescent ZnO nanoparticles modified with aminopropyltriethoxy silane for optoelectronic applications**. *New Journal of Chemistry*, **37**(7):2103–2109, 2013. 55

[364] Elisabetta Comini. **Metal oxide nano-crystals for gas sensing**. *Analytica Chimica Acta*, **568**(1):28–40, 2006. 55

[365] JX Wang, Xiaowei Sun, A Wei, Y Lei, XP Cai, Chang Ming Li, and Zhili Dong. **Zinc oxide nanocomb biosensor for glucose detection**. 2006. 55

[366] Thierry Pauporté and Daniel Lincot. **Electrodeposition of semiconductors for optoelectronic devices: results on zinc oxide**. *Electrochimica Acta*, **45**(20):3345–3353, 2000. 55

[367] V Parthasarathi and G Thilagavathi. **Synthesis and characterization of zinc oxide nanopartilce and its application on fabrics for microbe resistant defence clothing**. *International Journal of Pharmacy and Pharmaceutical Sciences*, **3**(4):392–398, 2011. 56, 59

[368] Shriwas S Ashtaputre, Aparna Deshpande, Sonali Marathe, ME Wankhede, Jayashree Chimanpure, Renu Pasricha, J Urban, SK Haram, SW Gosavi, and SK Kulkarni. **Synthesis and analysis of ZnO and CdSe nanoparticles**. *Pramana*, **65**(4):615–620, 2005. 56, 57

[369] SR Senthilkumar and T Sivakumar. **Green tea (Camellia sinensis) mediated synthesis of zinc oxide (ZNO) nanoparticles and studies on their antimicrobial activities**. *Int J Pharm Pharm Sci*, **6**:461–465, 2014. 57, 59

[370] Sulbha K. Kulkarni. *Nanotechnology: Principles and Practices*. Springer, Mahaveer Street, Darayagang, New Delhi, 1 edition, 2009. 57

[371] Fang Qian, Pui Ching Lan, Tammy Olson, Cheng Zhu, Eric B Duoss, Christopher M Spadaccini, and T Yong-Jin Han. **Multiphase separation of copper nanowires**. *Chemical Communications*, **52**(78):11627–11630, 2016. 58

[372] Anil Kumar, Lokesh Kumar Jangir, Yogita Kumari, Manoj Kumar, Vinod Kumar, and Kamlendra Awasthi. **Electrical behavior of dual-morphology polyaniline**. *Journal of Applied Polymer Science*, **133**(41), 2016. 58

[373] Mikiyasu Inoue and Izumi Hirasawa. **The relationship between crystal morphology and XRD peak intensity on CaSO 4· 2H 2 O**. *Journal of Crystal Growth*, **380**:169–175, 2013. 58

[374] JD Ye, SL Gu, F Qin, SM Zhu, SM Liu, X Zhou, W Liu, LQ Hu, R Zhang, Y Shi, et al. **Correlation between green luminescence and morphology evolution of ZnO films**. *Applied Physics A*, **81**(4):759–762, 2005. 65

[375] XL Wu, GG Siu, CL Fu, and HC Ong. **Photoluminescence and cathodoluminescence studies of stoichiometric and oxygen-deficient ZnO films**. *Applied Physics Letters*, **78**(16):2285–2287, 2001. 65, 80

[376] Sayan Bhattacharyya and A Gedanken. **Microwave-assisted insertion of silver nanoparticles into 3-D mesoporous zinc oxide nanocomposites and nanorods**. *The Journal of Physical Chemistry C*, **112**(3):659–665, 2008. 65

[377] Bharati Debnath, Ganga Halder, and Sayan Bhattacharyya. **One-step synthesis, structural and optical characterization of self-assembled ZnO nanoparticle clusters with quench-induced defects**. *Science of Advanced Materials*, **6**(6):1160–1169, 2014. 65, 68

[378] Yinyan Gong, Tamar Andelman, Gertrude F Neumark, Stephen OâĂŹBrien, and Igor L Kuskovsky. **Origin of defect-related green emission from ZnO nanoparticles: effect of surface modification**. *Nanoscale Research Letters*, **2**(6):297, 2007. 65, 68

[379] Cheol Hyoun Ahn, Young Yi Kim, Dong Chan Kim, Sanjay Kumar Mohanta, and Hyung Koun Cho. **A comparative analysis of deep level emission in ZnO layers deposited by various methods**. *Journal of Applied Physics*, **105**(1):013502, 2009. 65, 68

[380] SA Studenikin, Nickolay Golego, and Michael Cocivera. **Fabrication of green and orange photoluminescent, undoped ZnO films using spray pyrolysis**. *Journal of Applied Physics*, **84**(4):2287–2294, 1998. 65

[381] AB Djurišić, YH Leung, KH Tam, L Ding, WK Ge, HY Chen, and S Gwo. **Green, yellow, and orange defect emission from ZnO nanostructures: Influence of excitation wavelength**. *Applied Physics Letters*, **88**(10):103107, 2006. 68

[382] Tapas Kumar Kundu, Nantu Karak, Puspendu Barik, and Satyajit Saha. **Optical properties of ZnO nanoparticles prepared by chemical method using poly (vinyl alcohol)(PVA) as capping agent**. *International Journal of Soft Computing and Engineering*, **1**:19–24, 2011. 68

[383] A Oudhia, A Choudhary, S Sharma, S Aggrawal, and SJ Dhoble. **Study of defect generated visible photoluminescence in zinc oxide nano-particles prepared using PVA templates**. *Journal of Luminescence*, **154**:211–217, 2014. 68

[384] Ion Tiginyanu, Lidia Ghimpu, Jorit Gröttrup, Vitalie Postolache, Matthias Mecklenburg, Marion A Stevens-Kalceff, Veaceslav Ursaki, Nader Payami, Robert Feidenhansl, Karl Schulte, et al. **Strong light scattering and broadband (UV to IR) photoabsorption in stretchable 3D hybrid architectures based on Aerographite decorated by ZnO nanocrystallites**. *Scientific Reports*, **6**, 2016. 69

[385] Helena Brunckova, Lubomir Medvecky, Alexandra Kovalcikova, Martin Fides, Erika Mudra, Juraj Durisin, Jiri Skvarla, and Maria Kanuchova. **Structural and mechanical properties of lanthanide doped La1/3Nb0. 8Ta0. 2O3 thin films prepared by sol–gel method**. *Smart Materials and Structures*, **26**(4):045009, 2017. 69

[386] Chu-Chi Ting, San-Yuan Chen, Wen-Feng Hsieh, and Hsin-Yi Lee. **Effects of yttrium codoping on photoluminescence of erbium-doped TiO 2 films**. *Journal of Applied Physics*, **90**(11):5564–5569, 2001. 69

[387] Beatriz Julián, Rosa Corberán, Eloisa Cordoncillo, Purificación Escribano, Bruno Viana, and Clément Sanchez. **One-pot synthesis and optical properties of Eu3+-doped nanocrystalline TiO2 and ZrO2**. *Nanotechnology*, **16**(11):2707, 2005. 69

[388] Appl Polman. **Erbium implanted thin film photonic materials**. *Journal of Applied Physics*, **82**(1):1–39, 1997. 69

[389] C Falcony, Anibal Ortiz, M Garcia, and JS Helman. **Photoluminescence characteristics of undoped and terbium chloride doped zinc oxide films deposited by spray pyrolysis**. *Journal of applied physics*, **63**(7):2378–2381, 1988. 69

[390] A Ortiz, C Falcony, M Garcia, and A Sanchez. **Terbium-doped zinc oxide films deposited by spray pyrolysis**. *Journal of Physics D: Applied Physics*, **20**(5):670, 1987.

[391] Feng Gu, Shu Fen Wang, Meng Kai Lü, Guang Jun Zhou, Dong Xu, and Duo Rong Yuan. **Structure evaluation and highly enhanced luminescence of Dy3+-doped ZnO nanocrystals by Li+ doping via combustion method**. *Langmuir*, **20**(9):3528–3531, 2004. 69

[392] Dapeng WANG. **Fabrication and Characterization of ZnO Related Materials Thin Films for Optical Device Application**. 2012. 69

[393] S-K Lee, Shula L Chen, D Hongxing, L Sun, Z Chen, WM Chen, and Irina A Buyanova. **Long lifetime of free excitons in ZnO tetrapod structures**. *Applied Physics Letters*, **96**(8):083104, 2010.

[394] Vu Xuan Quang, Nguyen Quang Liem, Nguyen Cong Thanh, Truong Van Chuong, and Le Thi Le Thanh. **Photoluminescence of rare-earth centers in ZnO phosphors**. *physica status solidi (a)*, **78**(2), 1983. 69

[395] Rupali Das, Naveen Khichar, and Santa Chawla. **Dual mode luminescence in rare earth (Er3+/Ho3+) doped ZnO nanoparticles fabricated by inclusive co precipitation technique**. *Journal of Materials Science: Materials in Electronics*, **26**(9):7174–7182, 2015. 72

[396] Anukorn Phuruangrat, Oranuch Yayapao, Titipun Thongtem, and Somchai Thongtem. **Synthesis and characterization of europium-doped zinc oxide photocatalyst**. *Journal of Nanomaterials*, **2014**, 2014.

[397] Alireza Khataee, Atefeh Karimi, Mahmoud Zarei, and Sang Woo Joo. **Eu-doped ZnO nanoparticles: sonochemical synthesis, characterization, and sonocatalytic application**. *Ultrasonics sonochemistry*, 2015. 72

[398] Rita John and Rajaram Rajakumari. **Synthesis and characterization of rare earth ion doped nano ZnO**. *Nano-Micro Letters*, **4**(2):65–72, 2012. 72

[399] Srinivasan Anandan, Ajayan Vinu, Toshiyuki Mori, Narasimhan Gokulakrishnan, Pavuluri Srinivasu, Velayutham Murugesan, and Katsuhiko Ariga. **Photocatalytic degradation of 2, 4, 6-trichlorophenol using lanthanum doped ZnO in aqueous suspension**. *Catalysis Communications*, **8**(9):1377–1382, 2007. 72

[400] Václav Štengl, Snejana Bakardjieva, and Nataliya Murafa. **Preparation and photocatalytic activity of rare earth doped TiO 2 nanoparticles**. *Materials Chemistry and Physics*, **114**(1):217–226, 2009. 75

[401] Kuppulingam Thirumalai, Manohar Shanthi, and Meenakshisundaram Swaminathan. **Hydrothermal fabrication of natural sun light active Dy 2 WO 6 doped ZnO and its enhanced photo-electrocatalytic activity and self-cleaning properties**. *RSC Advances*, **7**(13):7509–7518, 2017. 75

[402] Sze-Mun Lam, Jin-Chung Sin, Ahmad Abdullah, and Abdul Mohamed. **Efficient photodegradation of resorcinol with Ag2O/ZnO nanorods heterostructure under a compact fluorescent lamp irradiation**. *Chemical Papers*, **67**(10):1277–1284, 2013. 78

[403] Lokesh Kumar Jangir, Purva Bansal, Yogita Kumari, Ghanshyam Singh, Manoj Kumar, K C Swami, and Kamlendra Awasthi. **Effective doping of Er(3+) in ZnO nanoparticles to control its luminescent properties**. *Macromolecular Symposia*, **masy.201700005.R1**(-):xxx, 2017. 80

[404] Qi Yu, Taotao Ai, Liyun Jiang, Yingtang Zhang, Chuang Li, and Xinqiang Yuan. **Efficient energy transfer in Eu-doped ZnO on diamond film**. *RSC Advances*, **4**(96):53946–53949, 2014. 80

[405] A Sharma, S Dhar, BP Singh, T Kundu, M Spasova, and M Farle. **Influence of Tb doping on the luminescence characteristics of ZnO nanoparticles**. *Journal of Nanoparticle Research*, **14**(2):676, 2012. 80

[406] BR Judd. **Optical absorption intensities of rare-earth ions**. *Physical Review*, **127**(3):750, 1962. 80

[407] Jiangtao Chen, Jun Wang, Fei Zhang, De Yan, Guangan Zhang, Renfu Zhuo, and Pengxun Yan. **Structure and photoluminescence property of Eu-doped SnO2 nanocrystalline powders fabricated by sol–gel calcination process**. *Journal of Physics D: Applied Physics*, **41**(10):105306, 2008. 80

[408] Yongzhe Zhang, Yanping Liu, Lihui Wu, Erqing Xie, and Jiangtao Chen. **Photoluminescence and ZnOâĘŠ Eu3+ energy transfer in Eu3+-doped ZnO nanospheres**. *Journal of Physics D: Applied Physics*, **42**(8):085106, 2009. 80

[409] Paul D Topham, Andrew J Parnell, and Roger C Hiorns. **Block copolymer strategies for solar cell technology**. *Journal of Polymer Science Part B: Polymer Physics*, **49**(16):1131–1156, 2011. 85

[410] Charles T Black, Ricardo Ruiz, Gregory Breyta, Joy Y Cheng, Matthew E Colburn, Kathryn W Guarini, H-C Kim, and Ying Zhang. **Polymer self assembly in semiconductor microelectronics**. *IBM Journal of Research and Development*, **51**(5):605–633, 2007.

[411] Almut Mecke, Christian Dittrich, and Wolfgang Meier. **Biomimetic membranes designed from amphiphilic block copolymers**. *Soft Matter*, **2**(9):751–759, 2006.

[412] Antonio Checco, Atikur Rahman, and Charles T Black. **Robust Superhydrophobicity in Large-Area Nanostructured Surfaces Defined by Block-Copolymer Self Assembly**. *Advanced Materials*, **26**(6):886–891, 2014. 85

[413] Frank S Bates and Glenn H Fredrickson. **Block copolymer thermodynamics: theory and experiment**. *Annual review of physical chemistry*, **41**(1):525–557, 1990. 85, 86

[414] DW Schwark, DL Vezie, JR Reffner, EL Thomas, and BK Annis. **Characterization of the surface morphology of diblock copolymers via low-voltage, high-resolution scanning electron microscopy and atomic force microscopy**. *Journal of materials science letters*, **11**(6):352–355, 1992. 85

[415] Ting Xu, AV Zvelindovsky, GJA Sevink, KS Lyakhova, H Jinnai, and TP Russell. **Electric field alignment of asymmetric diblock copolymer thin films**. *Macromolecules*, **38**(26):10788–10798, 2005. 85

[416] Eungnak Han, Karl O Stuen, Melvina Leolukman, Chi-Chun Liu, Paul F Nealey, and Padma Gopalan. **Perpendicular orientation of domains in cylinder-forming block copolymer thick films by controlled interfacial interactions**. *Macromolecules*, **42**(13):4896–4901, 2009.

[417] William A Phillip, Marc A Hillmyer, and EL Cussler. **Cylinder orientation mechanism in block copolymer thin films upon solvent evaporation**. *Macromolecules*, **43**(18):7763–7770, 2010. 85

[418] Shih-Huang Tung, Nisha C Kalarickal, Jimmy W Mays, and Ting Xu. **Hierarchical assemblies of block-copolymer-based supramolecules in thin films**. *Macromolecules*, **41**(17):6453–6462, 2008. 85, 90

[419] Jin Wook Lee, Chansub Lee, Su Yeon Choi, and Seung Hyun Kim. **Block Copolymer- Surfactant Complexes in Thin Films for Multiple Usages from Hierarchical Structure to Nano-Objects**. *Macromolecules*, **43**(1):442–447, 2009.

[420] Chih-Hung Lee and Shih-Huang Tung. **Microdomain control in block copolymer-based supramolecular thin films through varying the grafting density of additives**. *Soft Matter*, **7**(12):5660–5668, 2011.

[421] Junhuan Li, Yilin Li, Jun-Ting Xu, and Christine K Luscombe. **Self-Assembled Amphiphilic Block Copolymers/CdTe Nanocrystals for Efficient Aqueous-Processed Hybrid Solar Cells**. *ACS Applied Materials & Interfaces*, 2017. 85

[422] SG Zhang, XW Zhang, FT Si, JJ Dong, JX Wang, X Liu, ZG Yin, and HL Gao. **Ordered ZnO nanorods-based heterojunction light-emitting diodes with graphene current spreading layer**. *Applied Physics Letters*, **101**(12):121104, 2012. 85

[423] Jun Zhang, Xianghong Liu, Giovanni Neri, and Nicola Pinna. **Nanostructured Materials for Room-Temperature Gas Sensors**. *Advanced Materials*, **28**(5):795–831, 2016.

[424] Mohamed A Basyooni, Mohamed Shaban, and Adel M El Sayed. **Enhanced Gas Sensing Properties of Spin-coated Na-doped ZnO Nanostructured Films**. *Scientific Reports*, **7**, 2017.

[425] Matthew C Beard, Joseph M Luther, and Arthur J Nozik. **The promise and challenge of nanostructured solar cells**. *Nature nanotechnology*, **9**(12):951–954, 2014.

[426] Xi Qin, Yuxiu Sun, Naixin Wang, Qi Wei, Linhua Xie, Yabo Xie, and Jian-Rong Li. **Nanostructure array assisted aggregation-based growth of a Co-MOF-74 membrane on a Ni-foam substrate for gas separation**. *RSC Advances*, **6**(96):94177–94183, 2016. 85

[427] Massimo Lazzari, Carlos Rodríguez-Abreu, José Rivas, and M Arturo López-Quintela. **Self-assembly: a minimalist route to the fabrication of nanomaterials**. *Journal of nanoscience and nanotechnology*, **6**(4):892–905, 2006. 86

[428] Marek Grzelczak, Jan Vermant, Eric M Furst, and Luis M Liz-Marzán. **Directed self-assembly of nanoparticles**. *ACS nano*, **4**(7):3591–3605, 2010.

[429] Mariela J Pavan and Roy Shenhar. **Two-dimensional nanoparticle organization using block copolymer thin films as templates**. *Journal of Materials Chemistry*, **21**(7):2028–2040, 2011.

[430] Seok-Soon Kim, Chaemin Chun, Jae-Chul Hong, and Dong-Yu Kim. **Well-ordered TiO 2 nanostructures fabricated using surface relief gratings on polymer films**. *Journal of Materials Chemistry*, **16**(4):370–375, 2006. 86

[431] Ivana Vukovic, Gerrit ten Brinke, and Katja Loos. **Block copolymer template-directed synthesis of well-ordered metallic nanostructures**. *Polymer*, **54**(11):2591–2605, 2013. 86

[432] C Cummins, D Borah, Sozaraj Rasappa, A Chaudhari, T Ghoshal, BMD O'Driscoll, P Carolan, N Petkov, JD Holmes, and MA Morris. **Self-assembly of polystyrene-block-poly (4-vinylpyridine) block copolymer on molecularly functionalized silicon substrates: fabrication of inorganic nanostructured etchmask for lithographic use**. *Journal of Materials Chemistry C*, **1**(47):7941–7951, 2013. 86

[433] Siao-Wei Yeh, Kung-Hwa Wei, Ya-Sen Sun, U-Ser Jeng, and Keng S Liang. **CdS nanoparticles induce a morphological transformation of poly (styrene-b-4-vinylpyridine) from hexagonally packed cylinders to a lamellar structure**. *Macromolecules*, **38**(15):6559–6565, 2005. 86

[434] Bumjoon J Kim, Julia J Chiu, G-R Yi, David J Pine, and Edward J Kramer. **Nanoparticle-Induced Phase Transitions in Diblock-Copolymer Films**. *Advanced Materials*, **17**(21):2618–2622, 2005. 86

[435] Glenn H Fredrickson and Frank S Bates. **Dynamics of block copolymers: theory and experiment**. *Annual Review of Materials Science*, **26**(1):501–550, 1996. 91

[436] Ting Xu, Craig J Hawker, and Thomas P Russell. **Interfacial interaction dependence of microdomain orientation in diblock copolymer thin films**. *Macromolecules*, **38**(7):2802–2805, 2005. 93

[437] Jae Man Shin, YongJoo Kim, Hongseok Yun, Gi-Ra Yi, and Bumjoon J Kim. **Morphological Evolution of Block Copolymer Particles: Effect of Solvent Evaporation Rate on Particle Shape and Morphology**. *ACS nano*, **11**(2):2133–2142, 2017. 93

[438] Wendy van Zoelen, Evgeny Polushkin, and Gerrit Ten Brinke. **Hierarchical terrace formation in PS-b-P4VP (PDP) supramolecular thin films**. *Macromolecules*, **41**(22):8807–8814, 2008. 95

[439] Peter K Stoimenov, Rosalyn L Klinger, George L Marchin, and Kenneth J Klabunde. **Metal oxide nanoparticles as bactericidal agents**. *Langmuir*, **18**(17):6679–6686, 2002. 99

[440] Christine A Murray, Emma H Goslan, and Simon A Parsons. **TiO2/UV: Single stage drinking water treatment for NOM removal?** *Journal of Environmental Engineering and Science*, **6**(3):311–317, 2007.

[441] Bingshe Xu, Mei Niu, Liqiao Wei, Wensheng Hou, and Xuguang Liu. **The structural analysis of biomacromolecule wool fiber with Ag-loading SiO 2 nano-antibacterial agent by UV radiation**. *Journal of photochemistry and photobiology A: Chemistry*, **188**(1):98–105, 2007.

[442] Zhongbing Huang, Xu Zheng, Danhong Yan, Guangfu Yin, Xiaoming Liao, Yunqing Kang, Yadong Yao, Di Huang, and Baoqing Hao. **Toxicological effect of ZnO nanoparticles based on bacteria**. *Langmuir*, **24**(8):4140–4144, 2008. 99

[443] Krishna R Raghupathi, Ranjit T Koodali, and Adhar C Manna. **Size-dependent bacterial growth inhibition and mechanism of antibacterial activity of zinc oxide nanoparticles**. *Langmuir*, **27**(7):4020–4028, 2011. 99

[444] Loganathan Palanikumar, Sinna Nadar Ramasamy, and Chandrasekaran Balachandran. **Size-dependent antimicrobial response of zinc oxide nanoparticles**. *IET nanobiotechnology*, **8**(2):111–117, 2014. 99

[445] Mary Ellen Davey and George A O'toole. **Microbial biofilms: from ecology to molecular genetics**. *Microbiology and molecular biology reviews*, **64**(4):847–867, 2000. 99

[446] Ian W Sutherland. **Biofilm exopolysaccharides: a strong and sticky framework**. *Microbiology*, **147**(1):3–9, 2001. 99

[447] Lilia Fransisca, Bin Zhou, Heekyung Park, and Hao Feng. **The effect of calcinated calcium and chlorine treatments on Escherichia coli O157: H7 87–23 population reduction in radish sprouts**. *Journal of food science*, **76**(6), 2011. 99

[448] Rob Van Houdt and Chris W Michiels. **Biofilm formation and the food industry, a focus on the bacterial outer surface**. *Journal of applied microbiology*, **109**(4):1117–1131, 2010. 99

[449] Haibo Mu, Jiangjiang Tang, Qianjin Liu, Chunli Sun, Tingting Wang, and Jinyou Duan. **Potent antibacterial nanoparticles against biofilm and intracellular bacteria**. *Scientific reports*, **6**:18877, 2016. 99

[450] Tiina Mattila-Sandholm and Gun Wirtanen. **Biofilm formation in the industry: a review**. *Food Reviews International*, **8**(4):573–603, 1992. 99

[451] Manuel Simões, Lucia C Simoes, and Maria J Vieira. **A review of current and emergent biofilm control strategies**. *LWT-Food Science and Technology*, **43**(4):573–583, 2010. 99

[452] Jeffrey B Kaplan, Chandran Ragunath, Narayanan Ramasubbu, and Daniel H Fine. **Detachment of Actinobacillus actinomycetemcomitans biofilm cells by an endogenous β-hexosaminidase activity**. *Journal of bacteriology*, **185**(16):4693–4698, 2003. 99

[453] M Nitschke, LV Araújo, SGVAO Costa, RC Pires, AE Zeraik, ACLB Fernandes, DMG Freire, and Jonas Contiero. **Surfactin reduces the adhesion of food-borne pathogenic bacteria to solid surfaces**. *Letters in applied microbiology*, **49**(2):241–247, 2009. 100

[454] Ute Römling. **Rationalizing the evolution of EAL domain-based cyclic di-GMP-specific phosphodiesterases**. *Journal of bacteriology*, **191**(15):4697–4700, 2009. 100

[455] Olga E Petrova, Kathryn E Cherny, and Karin Sauer. **The diguanylate cyclase GcbA facilitates Pseudomonas aeruginosa biofilm dispersion by activating BdlA**. *Journal of bacteriology*, **197**(1):174–187, 2015. 100

[456] Davide Antoniani, Paola Bocci, Anna Maciąg, Nadia Raffaelli, and Paolo Landini. **Monitoring of diguanylate cyclase activity and of cyclic-di-GMP biosynthesis by whole-cell assays suitable for high-throughput screening of biofilm inhibitors**. *Applied microbiology and biotechnology*, **85**(4):1095–1104, 2010. 100

[457] Karthik Sambanthamoorthy, Rudolph E Sloup, Vijay Parashar, Joshua M Smith, Eric E Kim, Martin F Semmelhack, Matthew B Neiditch, and Christopher M Waters. **Identification of small molecules that antagonize diguanylate cyclase enzymes to inhibit biofilm formation**. *Antimicrobial agents and chemotherapy*, **56**(10):5202–5211, 2012. 100

[458] Lizziane Kretli Winkelströter and Elaine CP De Martinis. **Different methods to quantify Listeria monocytogenesbiofilms cells showed different profile in their viability**. *Brazilian Journal of Microbiology*, **46**(1):231–235, 2015. 100

[459] Stacy Sommer, Abdullah Ekin, Dean C Webster, Shane J Stafslien, Justin Daniels, Lyndsi J VanderWal, Stephanie EM Thompson, Maureen E Callow, and James A Callow. **A preliminary study on the properties and fouling-release performance of siloxane–polyurethane coatings prepared from poly (dimethylsiloxane)(PDMS) macromers**. *Biofouling*, **26**(8):961–972, 2010. 100

[460] Sylvie Miquel, Rosyne Lagrafeuille, Bertrand Souweine, and Christiane Forestier. **Anti-biofilm activity as a health issue**. *Frontiers in microbiology*, **7**, 2016. 100

[461] Kumud Kant Awasthi, Anjali Awasthi, Narender Kumar, Partha Roy, Kamlendra Awasthi, and PJ John. **Silver nanoparticle induced cytotoxicity, oxidative stress, and DNA damage in CHO cells**. *Journal of nanoparticle research*, **15**(9):1898, 2013. 100

[462] Anjali Awasthi, Ankita Dube, Yogita Kumari, Lokesh Kumar Jangir, Kumud Kant Awasthi, and Kamlendra Awasthi. **Toxicological Evaluation of TiO_2 Nanoparticles in Bacterial Cell**. In *Macromolecular Symposia*, **357**, pages 235–240. Wiley Online Library, 2015. 100

[463] Fidel Martinez-Gutierrez, Laura Boegli, Alessandra Agostinho, Elpidio Morales Sánchez, Horacio Bach, Facundo Ruiz, and Garth James. **Anti-biofilm activity of silver nanoparticles against different microorganisms**. *Biofouling*, **29**(6):651–660, 2013. 100

[464] Magdalena Lungu, Ştefania Gavriliu, Elena Enescu, Ioana Ion, Alexandra Brătulescu, Grigore Mihăescu, Luminiţa Măruţescu, and Mariana Carmen Chifiriuc. **Silver–titanium dioxide nanocomposites as effective antimicrobial and antibiofilm agents**. *Journal of nanoparticle research*, **16**(1):2203, 2014. 100

[465] Andreia Fonseca de Faria, Ana Carolina Mazarin de Moraes, Priscyla Daniely Marcato, Diego Stéfani Teodoro Martinez, Nelson Durán, Antônio Gomes Souza Filho, Adriano Brandelli, and Oswaldo Luiz Alves. **Eco-friendly decoration of graphene oxide with biogenic silver nanoparticles: antibacterial and antibiofilm activity**. *Journal of nanoparticle research*, **16**(2):2110, 2014. 100

[466] Shatavari Kulshrestha, Shakir Khan, Ramovatar Meena, Braj R Singh, and Asad U Khan. **A graphene/zinc oxide nanocomposite film protects dental implant surfaces against cariogenic Streptococcus mutans**. *Biofouling*, **30**(10):1281–1294, 2014. 100

[467] Prajna Jena, Soumitra Mohanty, Rojee Mallick, Biju Jacob, and Avinash Sonawane. **Toxicity and antibacterial assessment of chitosancoated silver nanoparticles on human pathogens and macrophage cells**. *International journal of nanomedicine*, **7**:1805, 2012. 100

[468] Varun Sambhy, Megan M MacBride, Blake R Peterson, and Ayusman Sen. **Silver bromide nanoparticle/polymer composites: dual action tunable antimicrobial materials**. *Journal of the American Chemical Society*, **128**(30):9798–9808, 2006. 100

[469] Justin T Seil and Thomas J Webster. **Reduced Staphylococcus aureus proliferation and biofilm formation on zinc oxide nanoparticle PVC composite surfaces**. *Acta biomaterialia*, **7**(6):2579–2584, 2011. 100

[470] Michal Eshed, Jonathan Lellouche, Shlomo Matalon, Aharon Gedanken, and Ehud Banin. **Sonochemical coatings of ZnO and CuO nanoparticles inhibit Streptococcus mutans biofilm formation on teeth model**. *Langmuir*, **28**(33):12288–12295, 2012. 100

[471] Annie Shrestha, Shi Zhilong, Neoh Koon Gee, and Anil Kishen. **Nanoparticulates for antibiofilm treatment and effect of aging on its antibacterial activity**. *Journal of endodontics*, **36**(6):1030–1035, 2010. 100

[472] Yi-Huang Hsueh, Wan-Ju Ke, Chien-Te Hsieh, Kuen-Song Lin, Dong-Ying Tzou, and Chao-Lung Chiang. **ZnO nanoparticles affect Bacillus subtilis cell growth and biofilm formation**. *PloS one*, **10**(6):e0128457, 2015. 100

[473] Qi Wang and Thomas J Webster. **Nanostructured selenium for preventing biofilm formation on polycarbonate medical devices**. *Journal of Biomedical Materials Research Part A*, **100**(12):3205–3210, 2012. 100

[474] Rene Hernandez-Delgadillo, Donaji Velasco-Arias, Juan Jose Martinez-Sanmiguel, David Diaz, Inti Zumeta-Dube, Katiushka Arevalo-Niño, and Claudio Cabral-Romero. **Bismuth oxide aqueous colloidal nanoparticles inhibit Candida albicans growth and biofilm formation**. *International journal of nanomedicine*, **8**:1645, 2013. 100

[475] Anja Kotiranta, Kari Lounatmaa, and Markus Haapasalo. **Epidemiology and pathogenesis of Bacillus cereus infections**. *Microbes and infection*, **2**(2):189–198, 2000. 101

[476] Hongbo Ma, Phillip L Williams, and Stephen A Diamond. **Ecotoxicity of manufactured ZnO nanoparticles–a review**. *Environmental Pollution*, **172**:76–85, 2013. 101

[477] George A O'Toole. **Microtiter dish biofilm formation assay**. *Journal of visualized experiments: JoVE*, (47), 2011. 101

[478] Manoranjan Arakha, Mohammed Saleem, Bairagi C Mallick, and Suman Jha. **The effects of interfacial potential on antimicrobial propensity of ZnO nanoparticle**. *Scientific reports*, **5**, 2015. 102

[479] Sangeetha Gunalan, Rajeshwari Sivaraj, and Venckatesh Rajendran. **Green synthesized ZnO nanoparticles against bacterial and fungal pathogens**. *Progress in Natural Science: Materials International*, **22**(6):693–700, 2012. 103

[480] Tadayuki Iwase, Akiko Tajima, Shinya Sugimoto, Ken-ichi Okuda, Ippei Hironaka, Yuko Kamata, Koji Takada, and Yoshimitsu Mizunoe. **A simple assay for measuring catalase activity: a visual approach**. *Scientific reports*, **3**:3081, 2013. 104

[481] Xiaogang Li, Zhun Yan, and Jianping Xu. **Quantitative variation of biofilms among strains in natural populations of Candida albicans**. *Microbiology*, **149**(2):353–362, 2003. 104

[482] Betsey Pitts, Martin A Hamilton, Nicholas Zelver, and Philip S Stewart. **A microtiter-plate screening method for biofilm disinfection and removal**. *Journal of microbiological methods*, **54**(2):269–276, 2003. 104

[483] Nicole Jones, Binata Ray, Koodali T Ranjit, and Adhar C Manna. **Antibacterial activity of ZnO nanoparticle suspensions on a broad spectrum of microorganisms**. *FEMS microbiology letters*, **279**(1):71–76, 2007. 104

[484] Justin T Seil and Thomas J Webster. **Antimicrobial applications of nanotechnology: methods and literature**. *International journal of nanomedicine*, **7**:2767, 2012. 104

[485] Bing Wang, Yuying Zhang, Zhengwei Mao, Dahai Yu, and Changyou Gao. **Toxicity of ZnO nanoparticles to macrophages due to cell uptake and intracellular release of zinc ions**. *Journal of nanoscience and nanotechnology*, **14**(8):5688–5696, 2014. 104

List of Publications related to research work

1. **Lokesh Kumar Jangir**, Yogita Kumari, Anil Kumar, Manoj Kumar and Kamlendra Awasthi, "Investigation of luminescence and structural properties of ZnO nanoparticles, synthesized with different precursors", Mater. Chem. Front., 2017, 1, 1413.
2. **Lokesh Kumar Jangir**, Yogita Kumari, Manoj Kumar and Kamlendra Awasthi, "Effective doping of Er^{3+} in ZnO nanoparticles to control its luminescent properties", Macromolecular Symposia", xxx (2017) xxx (accepted).
3. Yogita Kumari, **Lokesh Kumar Jangir**, Manoj Kumar, Kamlendra Awasthi, "Titania Nanodots Array using Self-Assembled poly(styrene)-*b*-poly(4- vinylpyridine) Block Copolymer Nanotemplates via ex-situ Approach", Materials Letters, 2017, 209, 365-368.
4. Yogita Kumari, **Lokesh Kumar Jangir**, Manoj Kumar, K. C. Swami and Kamlendra Awasthi, "Effect of volume fraction of minority block on the morphology of PS-*b*-P4VP nanotemplates, Macromolecular Symposia", xxx (2017) xxx (accepted).
5. **Lokesh Kumar Jangir**, Yogita Kumari, Manoj Kumar and Kamlendra Awasthi, "Enhanced optical properties of rare earth (Tb, Er, Eu) doped ZnO NP's ", RSC Advanced, (submitted).
6. Puja Sharma, **Lokesh Kumar Jangir**, Garima Awasthi, Kumud Kant Awasthi, Kamlendra Awasthi, Anjali Awasthi, "Effect of ZnO nanoparticles on biofilm activity of *Bacillus subtilis*", journal of colloid and interface science, (submitted).